Aspects de l'utilisation de fluides fluorocarbures saturées dans la physique des hautes énergies

G.D. Hallewell

CPPM-HDR-2011-001

UNIVERSITÉ DE LA MÉDITERRANÉE AIX-MARSEILLE II

FACULTÉ DES SCIENCES DE LUMINY
163 avenue de Luminy
13288 MARSEILLE Cedex 09

HABILITATION À DIRIGER DES RECHERCHES

Mention : Physique des Particules et Astroparticules
Specialité Physique et Sciences de la Matière

Mémoire présenté en vue de l'obtention de
l'Habilitation à Diriger des Recherches

par ***Gregory David HALLEWELL***

"Aspects de l'utilisation de fluides fluorocarbures saturées dans la physique des hautes énergies"

(Aspects of the use of saturated fluorocarbon fluids in high energy physics)

Soutenu le 15 février 2011 devant le jury composé de :

Eric Kajfasz :	**Directeur CPPM** **Directeur de Recherche : CNRS / IN2P3**	
José Busto :	**Professeur : Université de la Méditerranée** **Président du département de Physique**	
Mossadek Talby:	**Professeur : Université de la Méditerranée**	
Roger Forty :	**Physicien CERN :**	**Rapporteur**
Neville Harnew :	**Professeur : Université d'Oxford :**	**Rapporteur**
Christian Joram :	**Physicien CERN :**	**Rapporteur**

"Aspects de l'utilisation de fluides fluorocarbures saturées dans la physique des hautes énergies"

Gregory David Hallewell

Centre de Physique des Particules de Marseille (CNRS/IN2P3),

163 avenue de Luminy, Case 907, 13288 Marseille Cedex09, France

Habilitation à diriger des recherches

Université de la Méditerranée Aix-Marseille II, le 15 février 2011

Abstract

Les excellentes propriétés diélectriques des fluides fluorocarbures saturées (« SFCs » ; de forme $C_nF_{(2n+2)}$) ont permis leur utilisation comme fluides caloporteurs pour le refroidissement par immersion directe de l'électronique, par exemple, de la série de *supercomputers* Cray. Ces fluides sont aussi utilisées comme milieu pour le transfert de chaleur dans les processus de soudure « non-contact » en phase vapeur et pour le déverminage des circuits électroniques dans une atmosphère uniforme à température élevée.

Leurs grandes transparences aux ultraviolets, leur ininflammabilité et non-toxicité ont aussi permis leur utilisation comme radiateurs pour les détecteurs de rayonnements Tcherenkov ; ces fluides ont aussi servies comme radiateurs liquides et vapeurs dans nombreuses expériences en physique des particules et physique des astroparticules.

Les systèmes de circulation des fluides fluorocarbures empruntent souvent des cycles thermodynamiques similaires à ceux qui sont utilisés pour les fluides frigorifiques récemment développées pour remplacer des fluides CFC (chloro-fluoro-carbures). Cependant, ces nouveaux fluides sont conçus pour pouvoir se désintégrer facilement sous l'irradiation ultraviolette stratosphérique ; ils ne sont pas résistants aux radiations ionisantes, et ne peuvent donc pas être utilisés pour le refroidissement direct des détecteurs dans un environnement radioactif très important comme, par exemple, dans les expériences auprès du collisionneur LHC au CERN.

Les molécules de SFC pures sont par contre extrêmement résistantes aux radiations grâce à la présence de liaisons simples de type C-F. Leur utilisation comme fluides caloporteurs en régime évaporatif a été proposé et développé au CPPM pour le détecteur à pixels de l'expérience ATLAS au LHC. Plus tard, cette technique a été choisie aussi pour tout le trajectographe silicium de l'expérience ATLAS, ainsi que pour les trajectographes silicium des expériences ALICE et TOTEM au LHC. Les expériences ATLAS et CMS utilisent aussi les SFCs comme fluides caloporteurs sous forme liquide.

Le régime évaporatif exploite la chaleur latente de vaporisation et permet la circulation d'une masse moins importante de fluide que dans un système fonctionnant sous forme liquide. Grâce à une viscosité moins importante que celles de fluides caloporteurs à base de glycol-eau, une tuyauterie plus légère de diamètre réduit est possible, ce qui diminue - par conséquence – le bilan '$\%X_0$' du trajectographe.

Une technique ultrasonique pour l'analyse des mélanges de vapeurs SFC a été développée comme alternative à la réfractométrie UV pour les radiateurs Tcherenkov du détecteur SLD-CRID (« Cherenkov Ring Imaging Detector » : détecteur de rayonnement Tcherenkov par focalisation en anneau) à SLAC (Stanford Linear Accelerator Center, Californie, USA) pendant les années 1980. La technique a été utilisée plus récemment dans plusieurs détecteurs de rayonnement Tcherenkov, et a aussi trouvé des applications dans l'industrie pétrolière et dans la fabrication des semi-conducteurs par le processus MOCVD (« Metal-Organic Vapour Deposition ; fabrication par la déposition des vapeurs métallo-organiques). Cette technique a aussi démontré une sensibilité suffisante pour être utilisée dans l'analyse des mélanges de gaz utilisés dans l'anesthésie.

L'analyse des mélanges de vapeur par ultrasons est aujourd'hui sous évaluation pour le refroidissement du trajectographe ATLAS par mélanges de fluides SFCs.

Le travail de l'auteur dans plusieurs domaines d'application des ces fluides versatiles constitue le sujet de ce mémoire.

For Siân, Tom and Leona,

for putting up with me while I was writing this...

Aspects de l'utilisation de fluides fluorocarbures saturées dans la physique des hautes énergies

Aspects of the use of saturated fluorocarbon fluids in high energy physics

Contents

Aspects de l'utilisation de fluides fluorocarbures saturées dans la physique des hautes énergies

Aspects of the use of saturated fluorocarbon fluids in high energy physics

Gregory David Hallewell

Centre de Physique des Particules de Marseille (CNRS/IN2P3), Université de la Méditerranée, 13288 Marseille, France

Habilitation à diriger des recherches

Université de la Méditerranée Aix-Marseille II, le 15 février 2011

Abstract

The excellent dielectric properties of saturated ($C_nF_{(2n+2)}$) fluorocarbons have allowed their use in direct immersion liquid cooling of electronics, including the Cray series of supercomputers, and as heat transfer media in vapour phase soldering and burn-in testing of electronics. Their high UV optical transparency, non-flammability and non-toxicity have led to their use as liquid and gas radiator media for Cherenkov detectors: such fluids have been used as liquid and gaseous radiators in numerous particle physics and astroparticle physics experiments.

The systems used to circulate and purify fluorocarbon Cherenkov radiator fluids often rely on thermodynamic cycles similar to those of the refrigerants recently developed to replace chlorofluorocarbons. Since such new refrigerants are designed to disintegrate under UV exposure in the upper atmosphere, they are correspondingly not radiation-resistant, and cannot be used for direct cooling of particle detectors in demanding radiation environments, such as at the CERN Large Hadron Collider. However the pure saturated fluorocarbon molecules are extremely radiation resistant due to the presence of only single C-F bonds. Their use as evaporative refrigerants was pioneered at CPPM for the ATLAS pixel detector and has been chosen for the cooling of all the silicon detectors in the experiment, and also for cooling the semiconductor vertex detectors of the ALICE and TOTEM experiments at LHC. These fluids are also used as liquid phase cooling fluids in ATLAS and CMS.

The evaporative mode exploits the latent heat or enthalpy of vaporization, allowing the circulation of a lower coolant mass than in a monophase cooling system of the same refrigerative capacity. Coupled with the lower fluorocarbon viscosity - compared with aqueous antifreeze-based coolants - this permits the use of narrower delivery tubing to the detectors, resulting in a smaller '$\%X_0$'contribution to the detector material budget.

Ultrasonic techniques for the vapour phase analysis of fluorocarbon Cherenkov radiators were developed as an alternative to UV refractometry for the SLD Cherenkov Ring Imaging Detector at the Stanford Linear Accelerator Center during the 1980s. Subsequently the technique has been used in many other Ring Imaging Cherenkov Detectors and also in the petro-chemical industry and for MOCVD (metal organic chemical vapour deposition) manufacture of semiconductors. The technique has also been demonstrated to have possible application in the vapour phase analysis of gas mixtures used in clinical anesthesia. Such vapour phase analysis techniques are again under evaluation for the possible cooling of the upgraded ATLAS silicon tracker.

The work of the author related to various applications of these versatile fluorocarbon fluids is discussed in this *memoire.*

.

Introduction

Saturated fluorocarbon (SFC) - or perfluoro-carbon - fluids, of chemical structure $C_nF_{(2n+2)}$ - have been used in particle physics experiments for around 30 years thanks to their excellent dielectric properties, non-flammability, non-toxicity and radiation tolerance.

These desirable properties arise from the 'saturation' of all available sites along the singly-bonded carbon chain molecule with fluorine atoms, rather than other atomic species - notably hydrogen that might be left over from incomplete synthesis of a hydrocarbon precursor. Carbon-Fluorine bonds, with a typical length of around 130 pm, are the strongest known in chemistry.

1.1 Production of Saturated Fluorocarbons

The Fowler process [1], is commonly used in the synthesis of SFCs. In a two-stage process **c**obalt fluoride moderates a hydrocarbon ➔ SFC reaction;

$$\text{Stage 1: } 2CoF_2 + F_2 \rightarrow 2\ CoF_3$$

In stage 2 a hydrocarbon feed is introduced and fluorinated by CoF_3, which is converted back to CoF_2 in the process. In the example of hexane:

$$C_6H_{14} + 28\ CoF_3 \rightarrow C_6F_{14} + 14\ HF + 28\ CoF_2$$

Industrially, both steps are combined, for example in the manufacture of the 'Flutec®' range [2] of SFCs by F2 Chemicals Ltd, using a vertical stirred bed reactor, with hydrocarbon introduced at the bottom, and fluorine introduced half way up the reactor. The SFC vapor is recovered from the top. Another production technique, the Simons and Phillips Petroleum electrochemical process [3] using HF as a precursor, has been extensively used by 3M Corporation for the "Fluorinert" ® range of SFCs.

SFC molecules can exist in the n-state (linear) and, for n_{carbon} >3, also in the iso-configuration (branched), as illustrated in Fig 1.1. The figure also shows one configuration of a double carbon-bonded molecule. For each double carbon bond in the molecule, two less fluorine atoms can be accommodated.

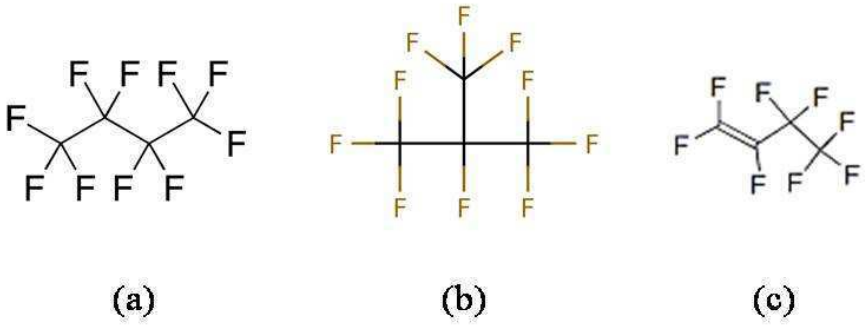

Fig.1.1. Examples of fluorocarbon molecules (carbon atoms not shown, by convention): (a) Saturated perfluoro-n-butane (n-C_4F_{10}); (b) Saturated perfluoro-iso-butane (i-C_4F_{10}), (c) Perfluoro-butene (C_4F_8)

1.2 Military and industrial uses

The dielectric properties and good heat transfer characteristics of SFCs liquids have allowed them to be used as immersion coolants in applications as diverse radar transmitters [4], (Figs. 1.2 & 1.3) and the Cray 2 supercomputer (Fig. 1.4, [5]) as well as hot contact environments for accelerated burn-in testing of electronic components (Fig 1.5, [6]). They are also extensively used in contactless vapour phase soldering of electronics onto printed circuits (Fig 1.6, [7]). SFCs, particularly octafluoropropane (C_3F_8) are also used for silicon oxide etching and the cleaning of semiconductor growth chambers [2].

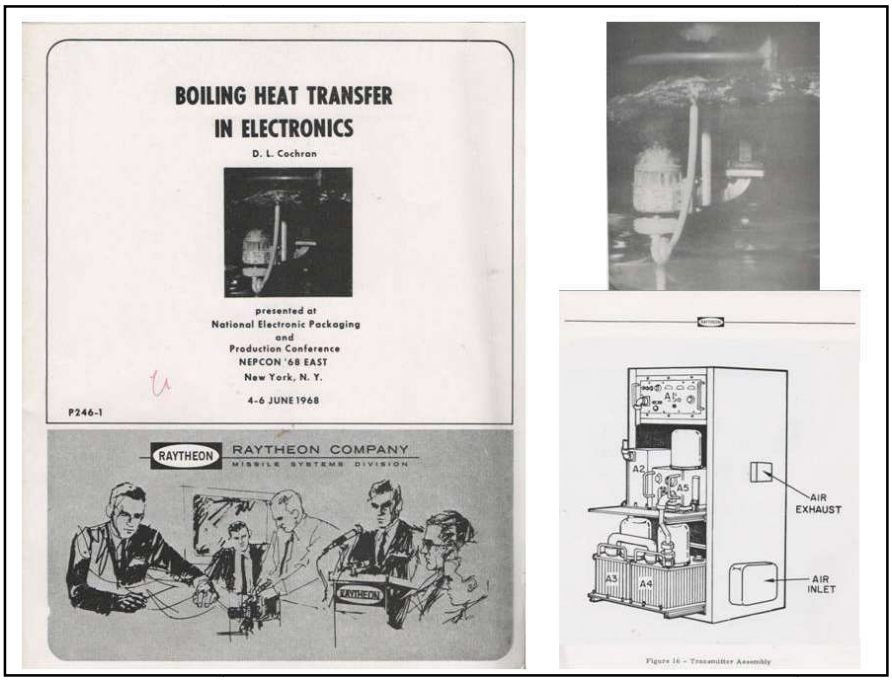

Fig.1.2. Illustration of an early application of liquid fluorinert immersion cooling of a radar klystron transmitter

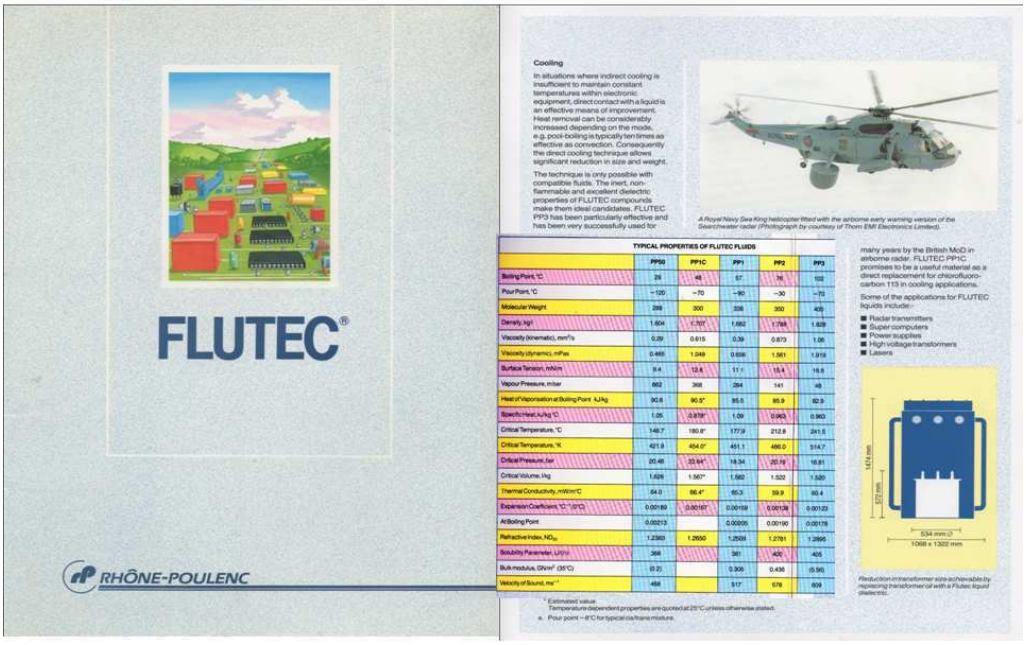

Fig.1.3. 1980's Publicity brochure for 'Flutec' fluids, which included the PP1(C_6F_{14}) and PP50 (C_5F_{12}) SFCs purchased for the SLD Cherenkov Ring Imaging Detector at SLAC.
The range was manufactured in the 1980s by Rhone Poulenc, Avonmouth, U.K..
Production has since been transferred to F2 Chemicals Ltd, Warrington, UK.

SYSTEMS PACKAGING

Cooling a Superfast Computer

Heat is removed from the CRAY-2 supercomputer by a cooling fluid that flows over each component.

By Richard D. Danielson, 3M Commercial Chemicals Div., St. Paul, Minn., Nick Krajewski and Jerry Brost, Cray Research, Chippewa Falls, Wisc.

A new generation supercomputer, the CRAY-2, uses a novel approach to cooling which will very likely influence computer construction in the future. Made by Cray Research Inc., the supercomputer combines diminutive physical size with very high speed and memory capacity.

The new supercomputer is cooled by immersing the entire computer — power supplies, memory boards, logic circuits and main processors — in an inert, high-dielectric liquid bath. CRAY-2 works sit in a sealed 155-gal tank of 3M's Fluorinert perfluorocarbon, electronic liquid FC-77.

Supercomputer packaging

The CRAY-2 design makes use of significant technological innovations, with capabilities which are an order of magnitude greater than those of its predecessor. These include a clock cycle of 4.1 ns, four background processors for independent or combined tasking, high-speed local random-access memory of 256 million words, and an effective throughput six to 12 times that of the physically larger CRAY-1.

In dramatic counterpoint to its expanded speed and capacity, the CRAY-2 is only about half the size of Cray's earlier system, standing approximately 45-in. high with a diameter of less than 5 ft.

The CRAY-2's relatively small size is a necessity for its blazing speed. Signal propagation times from point-to-point within the system must be extremely short, or the exotic processor and memory circuits cannot do their job. But physical compactness creates enormous heat buildup problems. At very high computer speeds,

1. Circuit modules are immersed in a non-conductive, circulating, fluorocarbon liquid to remove heat from the CRAY-2 supercomputer. Transparent circuit module towers are in the foreground, while a coolant storage tower is in the background with cabinets containing pumps and heat exchangers on both sides.

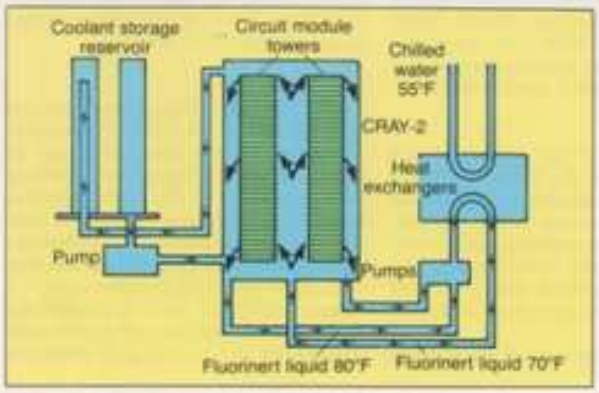

2. Cooling fluid is pumped through the circuit module towers and heat exchangers.

Fig.1.4. Application for the direct immersion cooling of a Cray-2 supercomputer using FC-77, a blend of C_8F_{18} saturated fluorocarbon with cyclic - $C_8F_{16}O$

ELECTRICAL/ELECTRONIC ASSEMBLY

Condensation/Vapor-Phase Reflow Soldering

A High Quality, High Yield, Economical Process

Recent technological innovations are the key to more widespread and economical applications of the condensation heat transfer method.

Terrence Thompson
Associate Editor

Condensation/vapor-phase reflow soldering is a unique process which uses the latent heat of a hot condensing saturated vapor on an assembly to provide precise temperature control and high heat transfer rates for soldering assemblies. The vapor is produced by boiling a suitable inert fluid at atmospheric pressure. This high quality, high yield process was originally developed by Western Electric's Engineering Research Center in Princeton, NJ as a technique for the mass soldering of terminal pins in the plated-through-holes of multilayered printed circuit boards.

Condensation soldering offered many advantages over existing soldering methods such as (1) rapid heating with the precise temperature control that protects heat sensitive components from thermal damage, (2) even heating of the entire assembly surface regardless of parts geometry and (3) an inherently clean operation since only continuously distilled vapor contacts the assembly. Although Western Electric initiated production with the process in 1973, it was not until two recent breakthroughs occurred that the technique became economically attractive and commercially available. The first breakthrough was provided by the availability of a suitable inert liquid in production quantities.

Working Primary Fluids

Selecting the appropriate working fluid is critical, as its characteristics determine the maximum temperature to which the assembly will be exposed. The first breakthrough that helped make condensation soldering a commercial and industrial reality was the 3M Company's introduction of the "Fluorinert" family of electronic liquids in production quantities. The FC-70 Fluorinert liquid in particular is especially well suited for electronic applications as its boiling point is 419 F which is ideal for most electronic soldering applictions. The availability of the FC-70 liquid was crucial because the only liquid available prior to its introduction was DuPont's Freon E5 which was made exclusively for Western Electric and was not avail-

Figure 1 Schematic representation of the basic condensation soldering system is shown in (a) and the modified system with a secondary vapor blanket in (b). In both systems, the assembly is lowered into the saturated reflow vapor where the latent heat of vaporization is quickly transferred to the assembly as the vapor condenses on the part surfaces. With the secondary vapor blanket shown in (b), the losses of the expensive primary vapor are minimized. After a brief immersion in the reflow vapor, the assembly is lifted out to the upper condensing coil area and allowed to cool and drain before removal.

Surface Mount

Fluxless SMD Soldering

one of the happier solder stories

by Hendrik B. Hendriks and Bruce E. Ingyn, Product Design Engineers Ordnance Systems Div., General Electric Co., Pittsfield, MA

Figure 2 To ensure sufficient solder fillets, LamCore boards are selectively plated during manufacture to add an additional 3.5 to 4 mils of tin/lead. This close-up shows an array of five as-plated tin/lead termination pads.

The need for leadless ceramic chip carriers has grown substantially in the past few years. These carriers significantly increase packaging density on printed wiring — including multilayer — assemblies. The LCCs are more reliable, have greater resistance to vibration than do conventional integrated circuits, and have shorter signal paths, which result in faster circuits. Other approaches to mounting LCCs have been open to question, but today vapor phase soldering is recognized as one of the most reliable solutions.

VPS is an application of condensation heating that uses the latent heat of 3M's Fluorinert FC-70 vapors to reflow preapplied solder. Every surface is enveloped by the condensing vapor, so the entire board is rapidly and uniformly heated. Besides assuring uniform heat, VPS provides a controlled, inert, and low temperature (215°C) soldering environment.

Even with the advantages inherent in the VPS process, flux residue can be difficult to clean from finished boards. If not completely removed, flux can cause outgassing or contamination when the board is in use. Flux can also cause voids in solder joints because of outgassing during the reflow process. After initial investigation, engineers determined that instead of developing a method for removing flux, the best solution was to eliminate its use altogether.

A Flux Shun

The engineering development group then set out to develop an LCC/MLB packaging technique with a fluxless assembly process. Besides designing a reliable process, an overall goal was to incorporate standard materials and techniques for cost containment and higher yields.

The cost of glass-epoxy printed wiring boards is considerably less than that of ceramic boards, so the group first tried standard glass-epoxy boards in

Figure 1 To lower the coefficient of thermal expansion of glass-epoxy multilayer boards, engineers at GE bonded alloy 42 — an eonvinciet mixture with 42% nickel — between board layers, as illustrated in this cross section of a LamCore MLB connector frame assembly.

Fig.1.5. Vapour phase application of SFCs for vapour phase soldering of components to printed circuit boards

PRODUCTION TECHNIQUES

Liquid Burn-In Testing Cuts TWT Supply Failures

Teledyne MEC in Palo Alto, Calif. is saving production time using liquid burn-in testing to detect traveling wave tube power supply failures before encapsulation.

By N.A. Kramer, Teledyne MEC, Palo Alto, Calif.

A liquid burn-in testing system employed prior to encapsulating units in silicone has reduced failure rates dramatically in high-voltage power supplies at Teledyne MEC in Palo Alto, Calif. In some units the failure rate has fallen from ninety to five percent.

The liquid used for testing is 3M's Fluorinert electronic liquid FC-43. It combines very low solvent action, high chemical inertness, high dielectric strength, and excellent heat transfer characteristics. It also is non-flammable, non-explosive, and essentially non-toxic.

The company relies on liquid burn-in for testing all new designs and for troubleshooting high-voltage power supply modules or packages which are experiencing an unacceptably high failure rate. The test enables location and correction of any problems that may be encountered before encapsulation, when they can be corrected at minimal cost.

Quick and inexpensive

Liquid burn-in testing is a quick and easy way of providing the temporary equivalent of encapsulation through immersion in a special liquid. While immersed in this liquid, the units are tested electrically. If defective, they are easily repaired and retested. If the burn-in test is passed, the units are then encapsulated in their permanent silicone coatings, and tested one last time before shipment.

Until the advent of liquid burn-in testing at Teledyne, high-voltage power supply modules were open-air bench tested. With this method, voltages had to be held to a minimum if the unit was unencapsulated, to avoid arcing and possible destruction. As a result, the unit's reaction to maximum load was left undetermined. In the event of failure, the encapsulating material had to be removed manually to locate and correct the problem. In addition to extra expense, there was an ever-present danger of causing greater damage in picking silicone out of the extremely compact power supply package.

To attain the high-voltage burn-in capabilities the company wanted—that is, subjecting unencapsulated units to maximum operating voltages—Teledyne engineers experimented first with a plastic battery case filled with FC-43. Units were immersed in the electronic liquid to prevent arcing, but it was soon discovered that the liquid was a good insulator and also helped cool the units under test through excellent heat transfer properties.

Excessive evaporation rate

Although this arrangement, which one engineer described as "jerry-rigged," worked fairly well, it did not permit extended burn-in of 24 to 48 hours at normal operating temperatures of 71° C to 105° C. At these temperatures, the evaporation rate of FC-43 liquid

1. In preparation for a burn-in test, a Teledyne technician connects a power supply to the unit under test. The liquid is then pumped into the liquid bath cabinet for full voltage tests. After testing, the liquid is recovered for reuse.

Fig.1.6. Liquid phase application of SFCs as a hot contact medium for accelerated thermal stress testing of electronic circuits.

2 Saturated fluorocarbon Cherenkov radiators in high energy physics

2.1 Cherenkov radiation

In the early years of the 20th century, an unexplained faint blue luminescence was frequently seen in transparent materials in the presence of radioactive sources. By 1938, studies had shown that the light exhibited a continuous spectrum, most intense in the blue and ultraviolet, without the discrete line structure associated with atomic fluorescence.

P.A. Cherenkov shared the 1958 Nobel prize for his demonstration [8] that the effect was due to the passage of fast charged particles, giving rise to a relativistic 'sonic boom' that occurs when a charged particle traverses a transparent dielectric medium (the '*radiator*') with refractive index *n* exceeding unity - i.e. *other than a vacuum* - with a velocity, βc[1], exceeding the phase velocity of light *in that medium*. Figs. 2.1, 2.2 & 2.3 illustrate the phenomenon. Cherenkov furthermore proposed that the effect could be useful for the identification of the type of emitting particle.

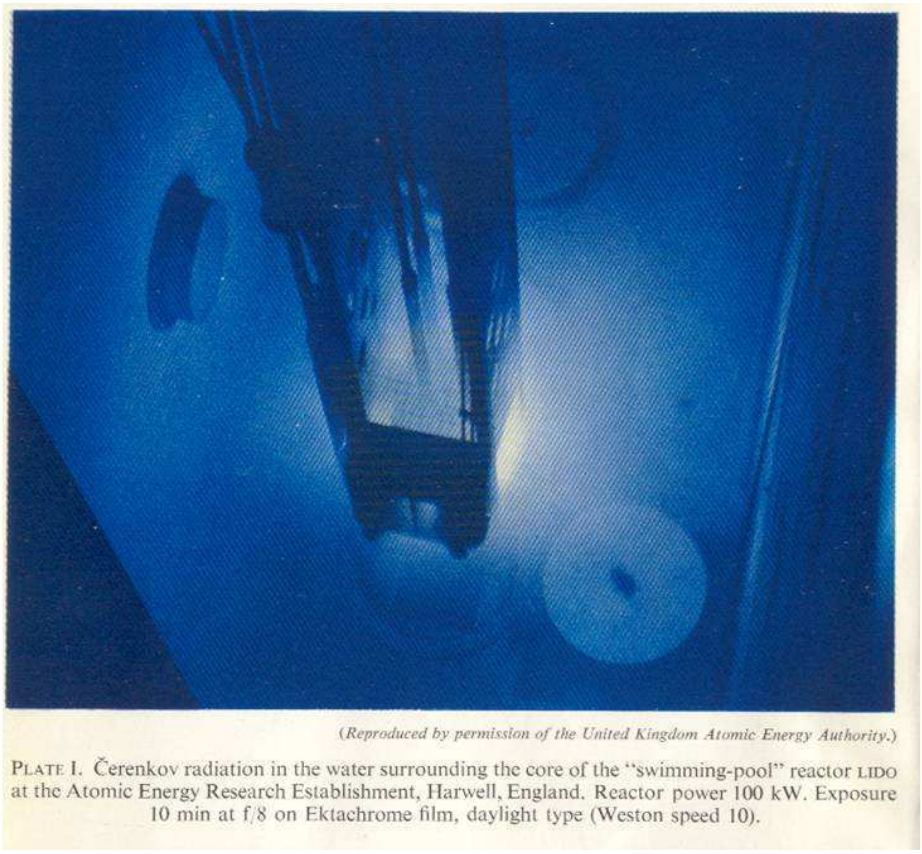

(*Reproduced by permission of the United Kingdom Atomic Energy Authority.*)

PLATE I. Čerenkov radiation in the water surrounding the core of the "swimming-pool" reactor LIDO at the Atomic Energy Research Establishment, Harwell, England. Reactor power 100 kW. Exposure 10 min at f/8 on Ektachrome film, daylight type (Weston speed 10).

Fig. 2.1. Cherenkov radiation in the water moderated LIDO reactor at AERE Harwell, UK. This photograph and caption was used as the beautiful frontispiece to the classic 1958 monograph on Cherenkov Radiation by J. V. Jelley [9]

Molecules in the medium are polarised by the passage of the charged particle. This polarisation is transient and after the passage of the charge, the polarised molecules relax by emitting a short pulse of electromagnetic radiation. In general, the wavelets of radiated energy interfere destructively due to the symmetrical distribution of the polarisation field (fig 2.2a). However, when the particle velocity exceeds the phase velocity of light in the medium, the effective shape of the polarisation field is asymmetrical with regard to the particle flight direction (fig 2.2b). The de-excitation of dipoles from this asymmetrical field results in a detectable, coherent wave front of electromagnetic radiation, known as Cherenkov radiation after its discoverer.

[1] Using notation where particle velocity, β, is expressed as a fraction of the speed of light, c, *in vacuo*; $\beta = v/c$

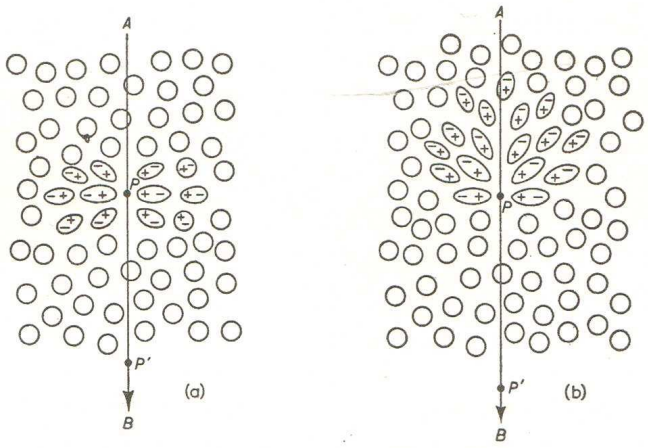

Fig.2.2. The molecular excitation and de-excitation phenomenon giving rise to the emission of Cherenkov radiation by a medium traversed by relativistic charged particles (after [9])

Although this electro-magnetic phenomenon arises at the molecular level, from the polarisation and depolarisation of the medium by the passing charge, the build-up of a coherent detectable wave front is susceptible to Huygens analysis in the same way as the shock wave produced by an aircraft exceeding the speed of sound.

Fig. 2.3 illustrates, with a Huygens construction, that the coherent wave front built by constructive interference of the different wavelets is projected as a cone - analogous to the supersonic *Mach* cone - having a specific opening angle, θ_c, with respect to the particle trajectory. The cone angle depends on the ratio of the particle velocity βc to the speed of light, c/n in the medium of refractive index n.

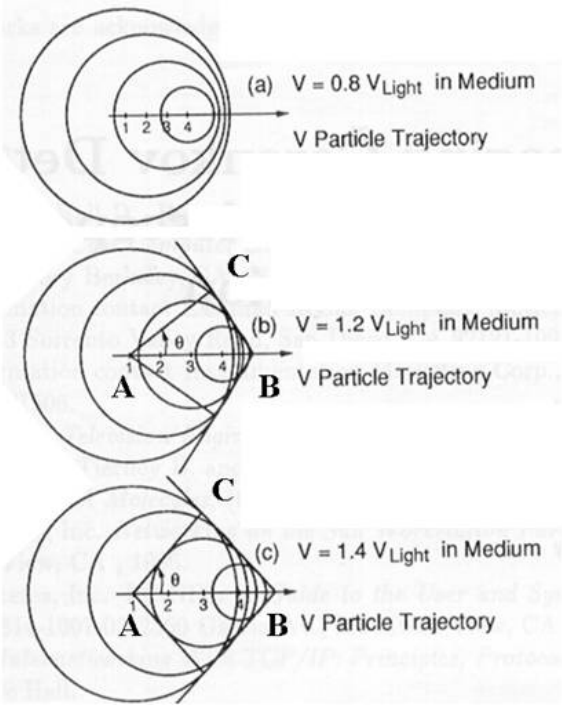

Fig. 2.3: Cherenkov radiation from a fast charged particle in a transparent medium.
*In (a), where the particle velocity = 0.8*c/n, no Cherenkov shock wave can develop. When the local light velocity is exceeded however, the radiated waves (shown only for four points along the particle trajectory) stack up into a wave front at an angle θ_c to the trajectory, which increases with velocity, (b) and (c) illustrating the cases for 1.2*c/n and 1.4*c/n respectively.*

The particle travels the distance AB in the same time, *t*, that the light takes to reach point C with speed *c/n*.

Therefore $\cos\theta_c$ = AC/AB

$$\cos\theta_c = (ct/n) / (\beta ct)$$
$$= 1/\beta n. \quad (2.1)$$

It can be seen that the greater the particle velocity the greater the Cherenkov cone angle.

The threshold above which Cherenkov radiation is produced occurs when;

$$\beta c = c/n,$$
$$\rightarrow \beta = 1/n \quad (2.2)$$

The limiting value of Cherenkov cone angle is given when the particle approaches the speed of light *in vacuo*.

In the limit;

$$\theta_c = \arccos(1/n). \quad (2.3)$$

For many years after the pioneering work of Cherenkov, studies of the radiation were mainly concerned with photographic measurement of its emission angles in a variety of 'radiator' media of relatively high refractive index transparent liquids and solids in which the light emission is relatively large – typically in excess of 2000 visible photons/cm. These early data were compared with the theory of energy loss by Cherenkov radiation formulated in the 1930's by Frank and Tamm [10]..

The mean number of Cherenkov photons $<N\gamma>$; emitted with energy $\hbar\omega$ is given from the theory:

$$< N_\gamma > = \frac{\alpha L Z^2}{c} . \int \left(1 - \frac{1}{\beta^2 n^2(\omega)}\right) dw \quad (2.4)$$

Where Ze is the particle charge, L is the radiator length, and α ($\approx 1/137$) is the fine structure constant.

Recasting eq. (2.4) in more convenient units;

$$<N\gamma> = N_o.Z^2 L \sin^2\theta c \quad (2.5)$$

where

$$N_o = 370\ cm^{-1}eV^{-1}\int_{E1}^{E2} \varepsilon(E)\, dE. \quad (2.6)$$

N_o is referred to as the global 'quality parameter' of a Cherenkov detector over the energy band (E_1-E_2) of detected Cherenkov photons (eV), and is an important yardstick for judging its performance. $\varepsilon(E)$ is a photon energy dependent efficiency for their detection which we shall discuss in more detail later.

Fig. 2.4 shows the variation of the Cherenkov light emission angle with particle velocity (here in 'everyday units' of km/sec) up to the vacuum limit c. Denser radiator materials (solids or liquids) are useful for measuring the velocities of slower particles, but it becomes more difficult to measure differences in angle and hence velocity when this exceeds ~0.98c. Aerogel or, for higher energies, a lower density (gas) radiator is necessary to measure the velocities of faster particles; Fig. 2.4 shows the velocity thresholds and ranges of response of gases of four different refractive indices. Two of these are SFCs.

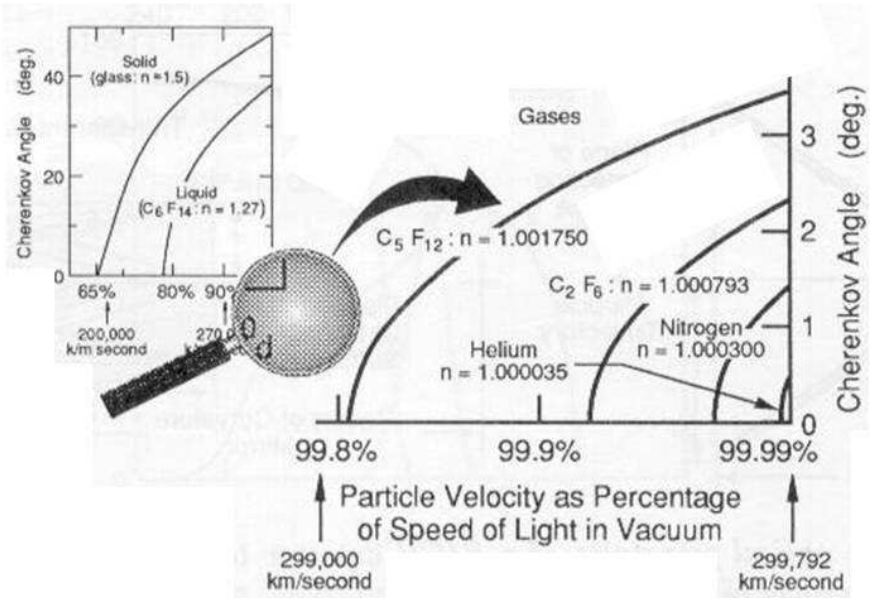

Fig. 2.4. The threshold velocities and angular range for the emission of Cherenkov radiation in a variety of materials.

In a transparent gas, the very low yield - typically less than 10 photons/cm at atmospheric pressure - proportional to the square of the small Cherenkov angle (eq. 2.5) - requires a long sample of gas, usually more than 50cm. Since Cherenkov light is produced with equal intensity along the whole radiator however, a concave mirror will collect and focus light from all points onto the detector, as illustrated in fig. 2.5.

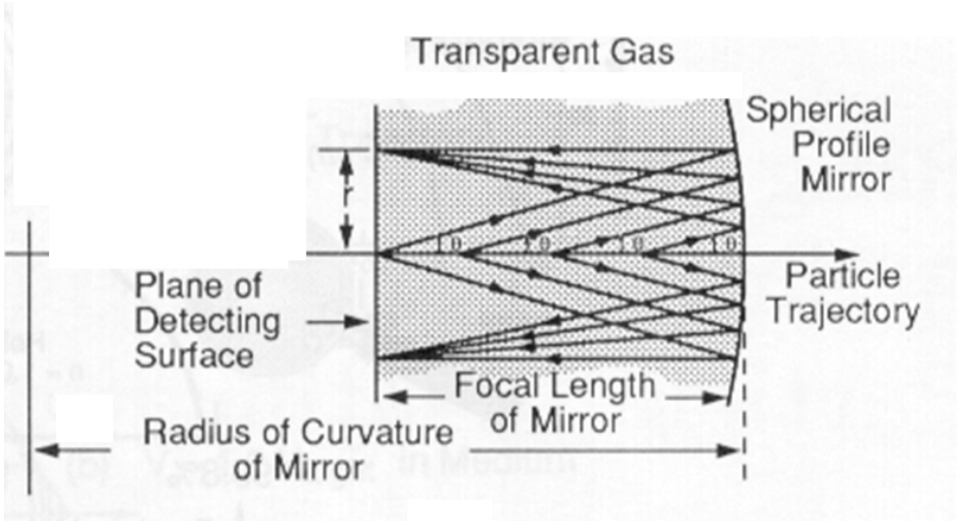

Fig. 2.5. Illustration of the imaging of Cherenkov radiation produced in a gas radiator using a spherical surface mirror with radius of curvature equal to twice the focal length.

For a Cherenkov angle θ_c in a gas, the radius, *r*, of the Cherenkov ring seen at the light detecting surface depends on the focal length of the mirror;

$$r = f \tan\theta_c \qquad (2.7)$$

While most Cherenkov detectors use spherical mirrors for ease of fabrication, the DELPHI ring imaging Cherenkov detector at the CERN LEP e^+e^- collider [11] used parabolic mirrors which offered improved focussing over a wider range of light incidence angles in a short gas radiator.

From eq. (2.2) we can deduce that the threshold energy *E* or momentum *p* for a particle to produce Cherenkov radiation depends on its rest mass. The relativistic energy of a particle is related to its normalised velocity β , *(v/c) – here also defined to be the normalised velocity (c/n) threshold for the production of Cherenkov light* - and rest mass m_0 via the Lorentz transform;

$$E = \frac{m_0 c^2}{\sqrt{1 - \beta^2}} \tag{2.8}$$

Where we may express the particle energy E as;

$$E = \gamma m_0 c^2 \tag{2.9}$$

with γ defined as:

$$\gamma = \frac{1}{\sqrt{1 - \beta^2}} \tag{2.10}$$

Using the conventional abbreviated relativistic formalism;

$$E^2 = p^2c^2 + m_0^2c^4 \tag{2.11}$$

and setting c = 1, we find a Cherenkov momentum threshold p_{th} (GeV/c) for a charged particle species as

$$p_{th} = \gamma m_0 \tag{2.12}$$

for $\gamma^2 >> 1$.

Figure 2.6 is an example illustrating the ring radii and number of detected photoelectrons on Cherenkov rings as a function of particle momentum for the 5 lightest charged particle species in the 5 m Cherenkov radiator of the CERN OMEGA RICH-1[12] as operated in 1984/5 with a radiator gas mixture of $50\%C_2F_6/50\%N_2$ with refractive index 1.00056.

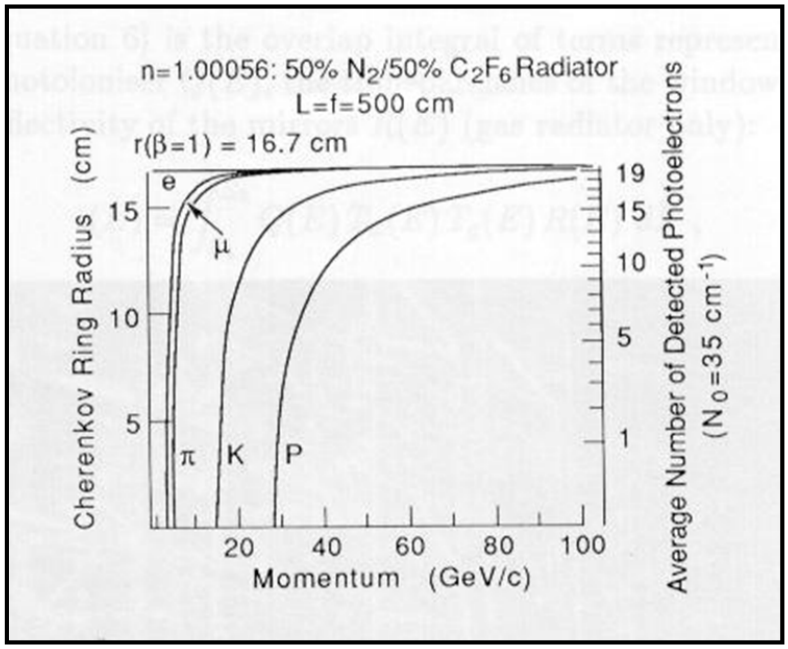

Fig. 2.6. Cherenkov ring radii & number of detected photoelectrons vs particle momentum: CERN OMEGA RICH-1 5 m gas radiator ($50\%C_2F_6/50\%N_2$, n = 1.00056).

When the refractive index of a Cherenkov radiator is high enough (as in the case of a solid or liquid), the light produced in a thin sample is bright enough to detect without elaborate optical focussing. In Fig. 2.7 a cone of Cherenkov light is projected onto a detecting surface where it is seen as a ring. A disadvantage of this "proximity focussing" is the parallax effect where the Cherenkov ring is still expanding as it passes through the detector of Cherenkov light; this detector thus needs to either be itself very thin or to have depth sensitivity to resolve the Cherenkov angle, and hence the particle mass to the required precision.

Liquid perfluoro-hexane (C_6F_{14}) was used as a thin shell proximity-focussing radiator in the DELPHI RICH [11] and SLD barrel CRID detectors at the SLAC e^+e^- Linear Collider (SLC) [13]. It continues this application in the STAR RICH [14] at Brookhaven National Laboratory (BNL), USA, in the NA35 heavy ion experiment at CERN [15] and in the ALICE High Momentum Particle Identification Detector (HMPID) [16].

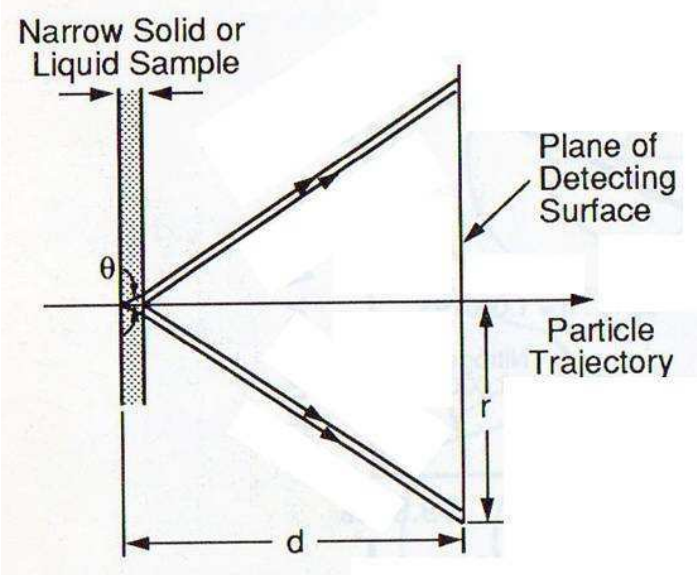

Fig. 2.7. Illustration of the imaging of Cherenkov radiation produced in a thin liquid or gas radiator with projective or 'proximity' focussing onto a light detector.

2.2 The progression toward Cherenkov ring imaging detectors

Although, as can be seen from Figs. 2.5 – 2.7, the general principles of the Ring Imaging Cherenkov (RICH) detector are quite simple, its technology required to progress toward the detectors described in refs [11-16] turned out to be extremely complex and took many years to mature. Since the early 1980's however, a number of large RICH detectors were commissioned at electron-positron colliders (LEP at CERN and the SLAC Linear Collider: SLC) and also in fixed target experiments. RICH detectors have also flown suspended below high altitude balloons. More recently RICH detectors have been commissioned for experiments at LHC. Examples from the diverse assortment of RICH detectors with fluorocarbon radiators will be explored in section 2.4, while details of the fluorocarbon radiator systems of two RICH detectors on which the author has worked are examined in more detail in section 2.5.

Turning the clock back to the early days of Cherenkov detectors in particle physics can reveal the lineage of RICH detectors. In a transparent gas, the very low yield - typically less than 10 photons/cm at atmospheric pressure – meant that the emission of Cherenkov radiation in gases was not observed conclusively until the 1950s when photomultipliers became widely available. Since these were incapable of spatially reconstructing or 'imaging' the ring of photons, detectors operated only in 'threshold' mode; a signal being seen only when the particle velocity exceeded that of light in the radiator gas. By increasing the gas pressure or filling with a denser gas, the refractive index could be increased, making the detector sensitive to slower-moving particles. As the need arose for Cherenkov detectors to surround the collision points of particle beams and targets, from which particles of several species might be ejected at various angles, multiple detectors appeared, containing up to a hundred photomultiplier/mirror threshold 'cells'. The rather large mirrors (typically about 100 sq cm) gathered light from a wide area onto a single photomultiplier, often making the light from two adjacent particles indistinguishable. The limit on the number of cells and their smallness was economic; the high cost of photomultipliers.

Following the 1960 proposal by Arthur Roberts [17], it was not until 1962 that technology had advanced sufficiently in the form of position-sensitive electronic image intensifiers, that an image of spatially-separated
single Cherenkov photons from the passage of a single particle was seen in any medium [18]. Since image intensifiers were also expensive and had a very limited field of view, there was a clear need for large area, inexpensive detectors of

Cherenkov light coupled to imagers which would allow the positions and radii of many (often overlapping) rings to be measured.

High precision gas-filled two-dimensional imagers had already been developed in the early 1970's to measure trajectories to $\sigma < 1$mm. In these devices, clouds of ionisation electrons – ejected from gas molecules by an incoming particle are 'drifted' in an electric field toward a grid of accurately positioned thin wires (typically 20 μm diameter) held at a positive voltage of several kilovolts. In the high electric field surrounding each wire, drifting electrons acquire enough kinetic energy to ionise additional gas molecules through bombardment, leading to a greatly multiplied and electronically-detectable signal. The trajectory of the traversing particle is recorded using the locations of the wires at which the signals are detected, and from the measured time of ionisation drift.

A major breakthrough came in 1977 with the suggestion of Jacques Seguinot and Thomas Ypsilantis of College de France, Paris, for the addition of a small amount of photosensitive vapour to the passive filling gas of a drift chamber to make an inexpensive Cherenkov light imager with an area of several square metres [19]. Two photosensitive molecules – with the colourful acronyms TEA (Tri-Ethyl-Amine) and TMAE (Tetrakis[di-Methyl-Amino]Ethylene) were found, with very high photoelectron conversion efficiencies, *Q(E)*, at UV wavelengths where Cherenkov radiation is at its most intense.

In Fig. 2.8 we see that the window separating the Cherenkov radiator medium from the photon detection and imaging region must be transparent to the photons that ionise the photosensitive molecule. The wavelength-dependent term $\varepsilon(E)$

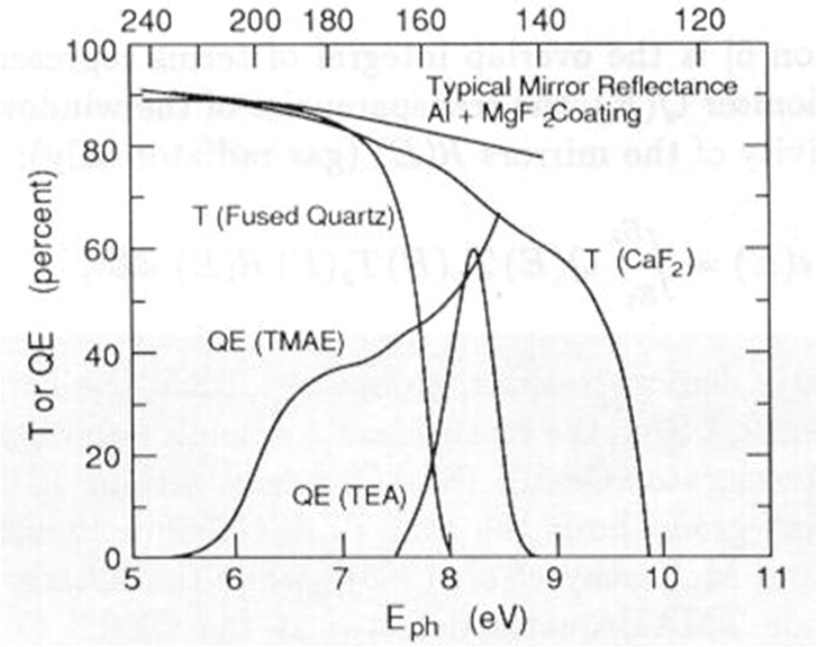

Fig. 2.8. TEA is well matched to the transmittance of Calcium Fluoride (CaF_2), while TMAE is matched to that of quartz, which is much less expensive. The TMAE/quartz combination made possible very large area RICH detectors at CERN and SLAC.

of the efficiency parameter N_0 (eq. 2.5, 2.6) is the overlap integral of terms representing the quantum efficiency of the photo ionizer *Q(E)*, the transparencies of the radiator medium, T_R, and the window, T_W.

$$\varepsilon(E) = Q.T_R.T_W.R_M.\eta \qquad (2.13)$$

Converted single photoelectrons are registered in the electronics chain with single electron detection efficiency, η, itself a product of electrostatic and electronics efficiencies. Should the detector use a mirror to focus the Cherenkov light onto the photo-converter, an additional wavelength-dependent reflectivity R_M; comes into play.

Shortly after the early demonstrations, groups at CERN, the Fermi National Accelerator Laboratory (Illinois, USA), the Rutherford Appleton Laboratory (UK) and the Stanford Linear Accelerator Laboratory (SLAC) began serious RICH/CRID research programs., The Fermilab group built the first TEA /Calcium Fluoride RICH detector [20]], while the RAL group – with which the author was associated - commissioned the first very large scale TMAE/quartz detector at the CERN Omega spectrometer [21]

Fig. 2.9 shows the 5 x 3 m mirror array of the CERN Omega RICH, containing 80 hexagonal mirror elements of 70 cm diameter and 5m focal length. The mirror coatings of evaporated aluminium with a top layer of magnesium fluoride were chosen to have high reflectance in the wavelength range 160-220 nm, the TMAE/quartz detection bandwidth and for tolerance to the radiator gas, which could contain up to 50% perfluoro-ethane (C_2F_6). Cherenkov light from the mirror array was reflected onto a focal surface of 16 quartz-windowed Time Projection Chambers (TPCs, Fig. 2.10) containing a hydrocarbon gas (doped with 0.1% TMAE). The single photoelectrons ejected from the TMAE molecules were drifted in a uniform electric field up to 20 cm in gas at atmospheric pressure to be detected and localized in two dimensions on an array of 3000 electronically-instrumented 20 μm sense wires operating in proportional mode.

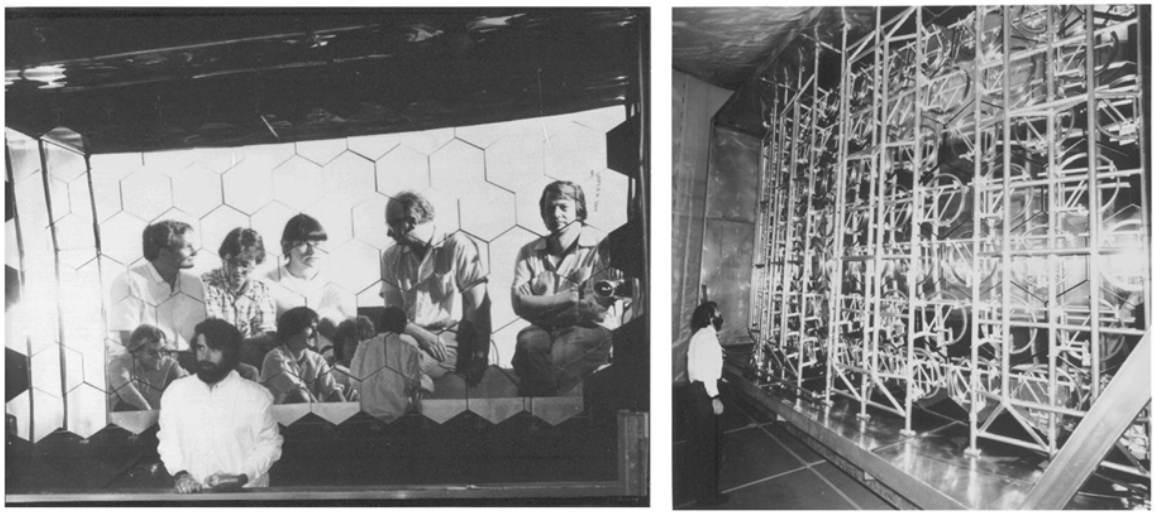

Fig. 2.9. Front and rear view of the 5x3 m mirror array of the CERN Omega RICH (1982-85 version)

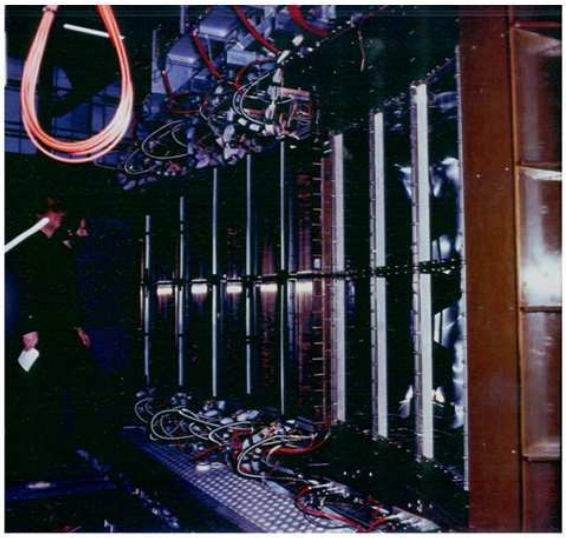

Fig. 2.10. Focal plane array of Time Projection Chambers at the CERN Omega RICH (1982-85 version)

Fig. 2.6 showed the threshold and ranges of particle identification achieved in the Omega RICH, operating with a 5m gas radiator of refractive index 1.00056, corresponding to a typical mixture of 50%C_2F_6 & 50% nitrogen. The Cherenkov ring radius and the number of photons on a ring are shown as a function of particle momentum at the typical achieved performance of $N_0 = 35$ cm^{-1}.

Small-scale prototype detectors operating the TMAE/quartz imaging tube combination achieved N_0 values as high as 90. Such performance was mainly the result of a very careful choice of materials allowed to come into contact with the highly reactive TMAE. The Omega RICH amassed a large body of operation experience that demonstrated that a full scale instrument would only be operated with long term stability (months at a time), even at more modest N_0 values, if great attention was also paid to the purity of the radiator gas and the TMAE dopant entering the detector. Details of the recirculation system for the gas mixture used in the OMEGA RICH are discussed in Section 2.5.1. These experiences prompted the inclusion of extensive fluid monitoring and purification systems in the second generation of RICH/CRID detectors constructed at CERN and SLAC.

2.3 The arrival of Cerenkov ring imaging detectors with 4π solid angle coverage.

It was quickly realised that large RICH detectors would be needed to completely investigate the new physics expected at the Large Electron Positron (LEP) collider at CERN and at the SLAC linear collider (SLC). One experiment at each collider - DELPHI at LEP [11, 19] and SLD at SLC [13] - was equipped with a ring imaging Cherenkov detector. The SLD Cerenkov Ring Imaging Detector (CRID) and DELPHI RICH detectors were designed to provide almost complete particle identification over greater than 90% of the solid angle, and to identify electrons, muons, pions, kaons and protons at momenta up to 30GeV/c.

Fig. 2.11 shows the layout of the SLD CRID with which the author was associated. The detector contained 'barrel' and 'end-cap' sections, within a 0.6 T solenoidal magnetic volume. In the barrel CRID Cerenkov photons were either projected [from a 1 cm layer of liquid perfluoro-n-hexane (C_6F_{14})[2]] or focused [from a 50 cm gas radiator of 70% perfluoro-n-pentane (C_5F_{12})[3] in nitrogen] into rings with maximum (β=1) radii of 17 and 2.8 cm respectively, allowing π/K/p separation up to 30 GeV/c, and e/π separation up to 6 GeV/c. In the end cap CRID only a perfluoro-butane (C_4F_{10})[4] gas radiator was employed, giving a π threshold of 2.5 GeV/c and π/K/p separation for momenta up to about 30 GeV/c.

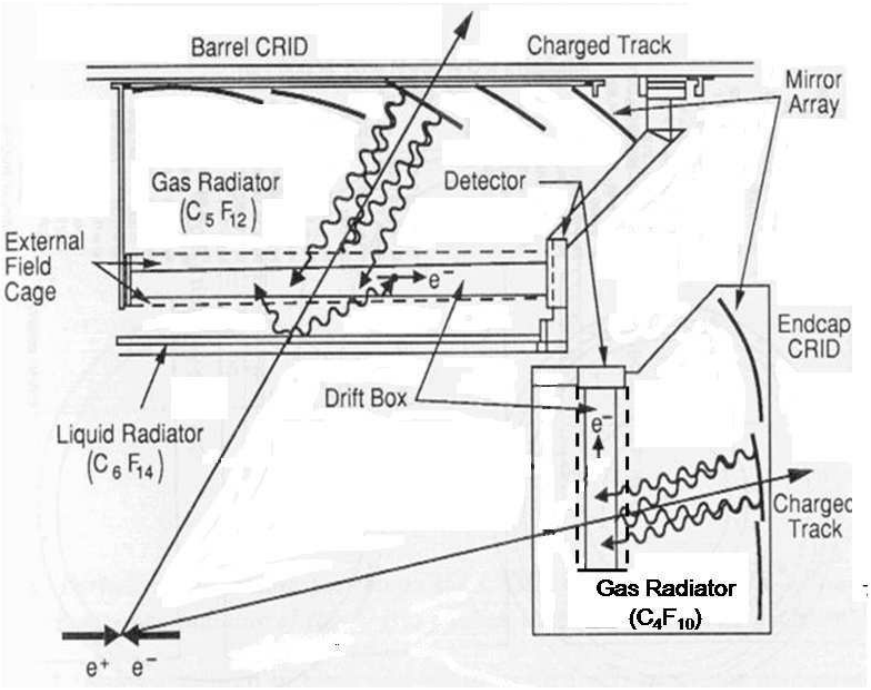

Fig. 2.11. The barrel and end-cap layout of the SLD CRID, showing the liquid and gaseous fluorocarbon radiators.

Cherenkov photons entered an array of imaging Time Projection Chambers (TPCs or "drift boxes") through quartz windows on their imaging surfaces. These presented a combined area for single photons of more than 40m^2. Once inside, the photons ionised TMAE molecules present in a carrier gas at atmospheric pressure. In the barrel CRID the carrier gas was ethane (C_2H_6) while in the end caps, 15%CO_2 was added to C_2H_6 to reduce the Lorentz angle for photoelectrons drifting perpendicular to the 0.6T solenoidal field. The photoelectrons drifted in a uniform electronic field of several hundred volts per cm towards anode wires. Fig. 2.12 shows the principle of operation of an SLD CRID drift box. One coordinate of each detected Cerenkov photon was given by the position of the wire at which an electron was detected; the second (perpendicular) by the time that the electron drifted (up to 1.2 m) before detection (measured by a fast electronic clock with a 65 ns 'tick'); and the 3rd coordinate - the 'depth' along the 7 μm carbon anode wire – was given by the ratio of electrical signals seen in sensitive amplifiers connected to its two ends.

[2] Flutec PP1: ISC Chemicals Ltd, Avonmouth, Bristol UK. Now produced by F2 Chemicals Ltd, Preston, UK.
[3] Flutec PP50: ISC Chemicals Ltd, Avonmouth, Bristol UK. Now produced by F2 Chemicals Ltd, Preston, UK.
[4] PF-5040: Mfr: 3M Speciality Chemicals St Paul, MN, USA

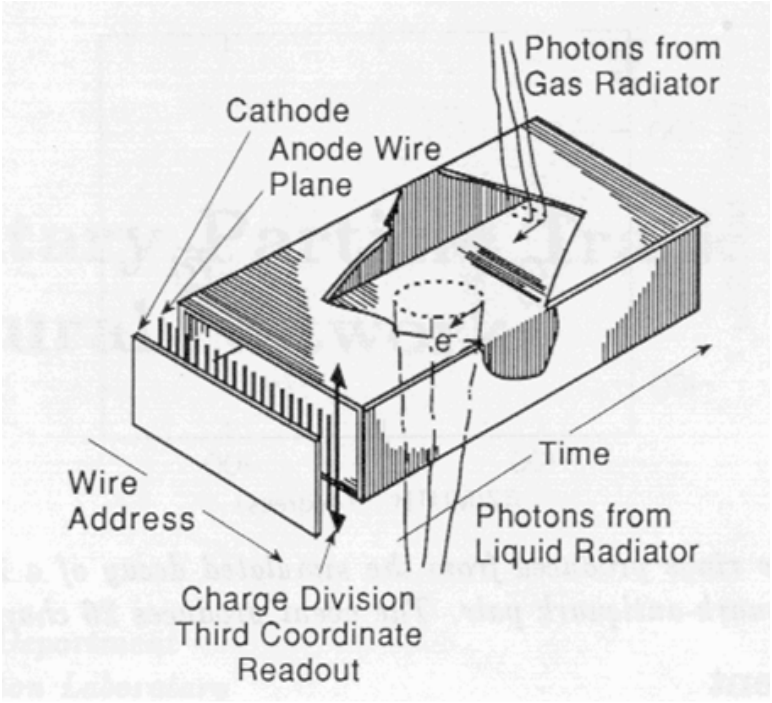

Fig. 2.12. Three coordinate localisation of Cherenkov photons in a drift tube of the SLD CRID detector operating with C_2H_6/TMAE at atmospheric pressure.

Figure 2.13 shows a quadrant view of the DELPHI barrel and forward RICH detectors. Unlike in the SLD end cap CRID the DELPHI forward RICH detector used C_6F_{14} liquid radiators, and consequently had better low momentum particle identification. Fig 2.13 also illustrates a time projection chamber/drift box within the DELPHI barrel RICH detector. In this device the 3rd (depth) coordinate is given by the ratio of electrical signals seen in cathode 'pads'; electrodes etched into the cathode plane and dividers around each anode wire, while the photoelectrons produced by the conversion of Cherenkov photons can drift up to 1.6 m before detection at the anode wires.

The major technical achievement of this second generation of RICH detectors was their ability to measure the position of each single photoelectron ejected from a TMAE molecule. Many of these photoelectrons were drifted more than one metre through the atmospheric pressure (or $1.3bar_{abs}$) carrier gas in a highly uniform electric field before being detected; a requirement that placed even greater demands on the purity of the TMAE and drift gas than in the Omega RICH with its much shorter drift distance. In particular, electronegative impurities (which can absorb the electrons before detection) must be carefully removed and the gas frequently monitored. With these precautions each Cerenkov photon could be located with a precision of 1 mm^3, enabling the radius of the ring, and hence the velocity and mass of the particle that produced it to be determined very accurately.

The technological feat of this single-photon RICH detection technique – manifested in this most extreme way in the 1.6m long drift TPCs of the DELPHI barrel RICH detector – remains unmatched in any other detection technology.

From figures 2.11 and 2.13 we can begin to appreciate the excellent dielectric properties of SFC fluids: the central (x=0) cathodic dividers of the SLD CRID and DELPHI RICH operated at voltages around 80kV and 160kV respectively to set up starting potential for the long drift field for photoelectrons. The uniform electric fields in the TPCs/drift boxes were established with resistively-degraded parallel conductors deposited or stretched across their quartz windows, aided by external field cages. In all cases naked HV conductors were exposed to SFC fluids; the problem in maintaining a discharge-free uniform electric field was determined by the surface cleanliness of the insulators and the quality of the resistive voltage degraders which prevented static charge accumulation.

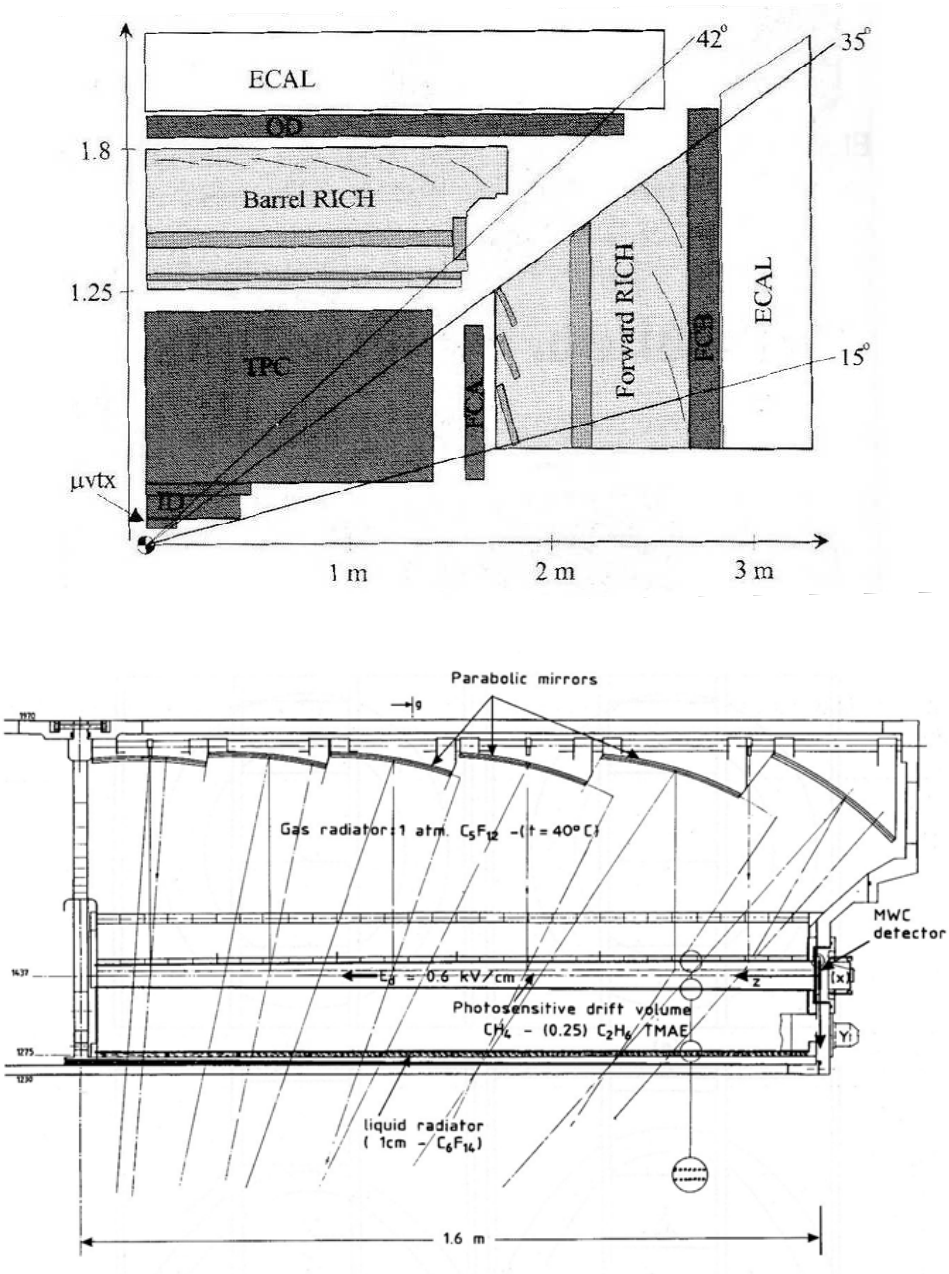

Fig. 2.13 Quadrant view of the DELPHI barrel and forward RICH detectors (above) and a view of the parabolic mirrors and a 1.7m long drift TPC the barrel RICH showing the external field shaping cage and the multi-wire proportional detector.

In the following sections we consider some representative examples of saturated fluorocarbon radiators in use in various experiments. For some of these the radiator circulation system and analysis technology are examined in detail. It will be seen that these systems have been built on the experiences gained and lessons learned in the handling of saturated fluorocarbons in the DELPHI RICH detector, some elements of which are also discussed.

2.4 Cherenkov Radiators in particle physics and astroparticle physics experiments.

Table 2.1 - including data from [22] - details the refractivity and energy thresholds of saturated fluorocarbons used as vapour or liquid Cherenkov radiators in current and previous experiments. Examples of operational details of some of these detectors are detailed in subsequent chapters.

Table 2.1. Molecular weight, refractivity & Cherenkov threshold for several SFCs, with RICH detectors.

SFC	Mol. Wt.	(n-1) x10^{-6} average 4-7eV	γ_{th}	RICH Detector
CF_4	88	488	32	LHCb[23]-R2, PHENIX[24]
C_2F_6	138	793	25	OMEGA (with 50% N_2)[12]
C_5F_{12}	238	1750	17	DELPHI [11] (barrel), SLD [13] (barrel + 30%N_2)
C_4F_{10}	188	1500	18	DELPHI & SLD (forward), CAPRICE [25] Swordy [26] balloon gondolas, LHCb-R1, COMPASS[27] HADES [28], HERMES [29], HERA-B[30], DIRAC [31]
C_6F_{14} (liq)	288	2.78 x10^5	1.6	DELPHI, SLD, STAR[14], NA35[15], ALICE HMPID[16]

Several of the RICH detectors indicated in Table 2.1 use SFC radiators in unusual ways or in combination with each other or with other gases. Some examples from Table 2.1 are considered in this section.

2.4.1 Fluorocarbon radiators in suspended balloon gondolas.

Remarkably sophisticated instruments have been flown in balloon missions from the late 1980s to the present day. The CAPRICE98 gas RICH [25] flew as part of a package containing a superconducting tracker at an altitude of 37 km over New Mexico during May 1998 in a mission to measure the antimatter component in the primary cosmic ray flux. The RICH (illustrated in Fig 2.14) used a 1 metre C_4F_{10} radiator and a MWPC with a

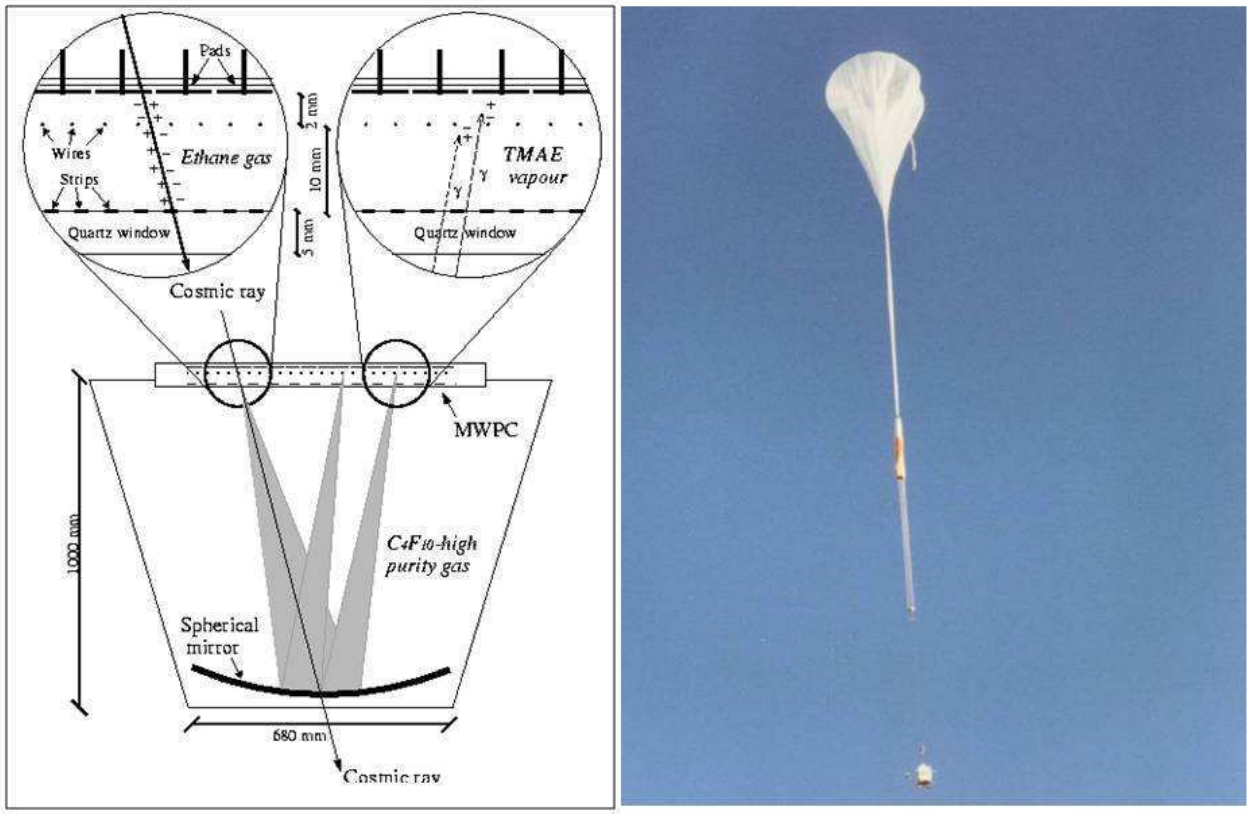

Fig. 2.14 The CAPRICE98 C_4F_{10} gas radiator RICH detector

quartz UV window and a TMAE in ethane (C_2H_6) for photon detection. Two-dimensional readout used sense wires and cathode pads. A RICH detector with a 3m C_4F_{10} gas radiator [26] was flown during 1996/7 by a Chicago University group in an experiment to directly identify primary cosmic rays consisting of light nuclei. The imaging drift chamber used a fused silica UV window with C_2H_6/TMAE. The proportional wire plane and cathode segmentation resembled those used in the OMEGA and DELPHI RICH detectors, and the SLD CRID. To ensure good transparency below 1900 nm oxygen and water vapour contamination were removed by circulating the radiator gas through an Oxisorb[5]® chromium filter. Since it was impractical to flush the radiator volume during the balloon flight the radiator was sealed shortly before launch.

2.4.2. The LHCb RICH detectors.

The LHCb experiment is a forward spectrometer covering the angular range of 20 to 300 (250) mrad in the horizontal (vertical) plane and designed to exploit the large production cross section of b-quarks at LHC for the study of CP-violating asymmetries and rare decays of B hadrons - probes of new physics beyond the Standard Model. Excellent particle identification is required for LHCb. Two RICH detectors [23] are employed to distinguish between kaons, pions and protons traversing the detectors in the momentum range 1 to 100 GeV/c.

The RICH1 detector employs atmospheric pressure C_4F_{10} gas and aerogel as Cherenkov radiators while RICH2 uses an atmospheric pressure gaseous CF_4 radiator. Cherenkov photons, emitted in the three radiator media, are focused via an optical system of spherical and flat mirrors onto the photon detector planes which are equipped with a total of 484 Hybrid Photon Detectors (HPDs). In RICH1 (RICH2) the photon detector planes are split into a top and bottom (left and right) panels, shown in Fig. 2.15. An HPD consists of a pixellated silicon sensor, bump-bonded to a readout chip and encapsulated within a vacuum photon detector. Photons enter the HPDs through quartz windows coated with S20 photocathode sensitive in the visible wavelength range 200 nm - 600 nm {~10% (~30%) at λ =200nm (300nm)}. Photoelectrons are accelerated through 20 kV and cross-focused with demagnification onto the silicon sensors.

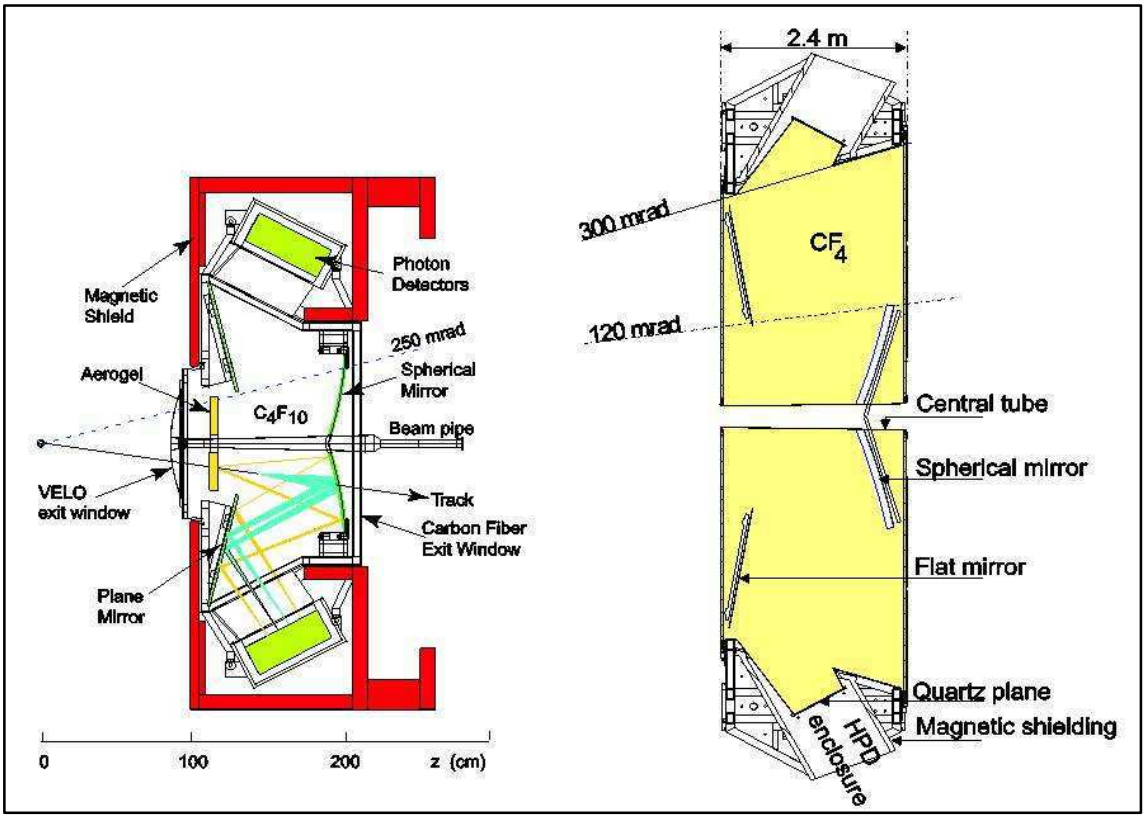

Fig 2.15. Schematic views of the LHCb RICH1 (aerogel and C_4F_{10} radiators) and RICH2 (CF_4 radiator) detectors

The LHCb RICH radiator systems [23,32] are illustrated in Fig 2.16. The operational difference between the two

[5] Chemical O_2 removal via the reaction $2Cr + 3O_2 \rightarrow 2CrO_3$, water removal via 5Å molecular sieve.
Mfr: Messer Spectron D-65933 Frankfurt, Germany
http://www.spectron.de/spectron_de/en/produkte/spectromol/oxisorb/Oxisorb.php?navanchor=1710047

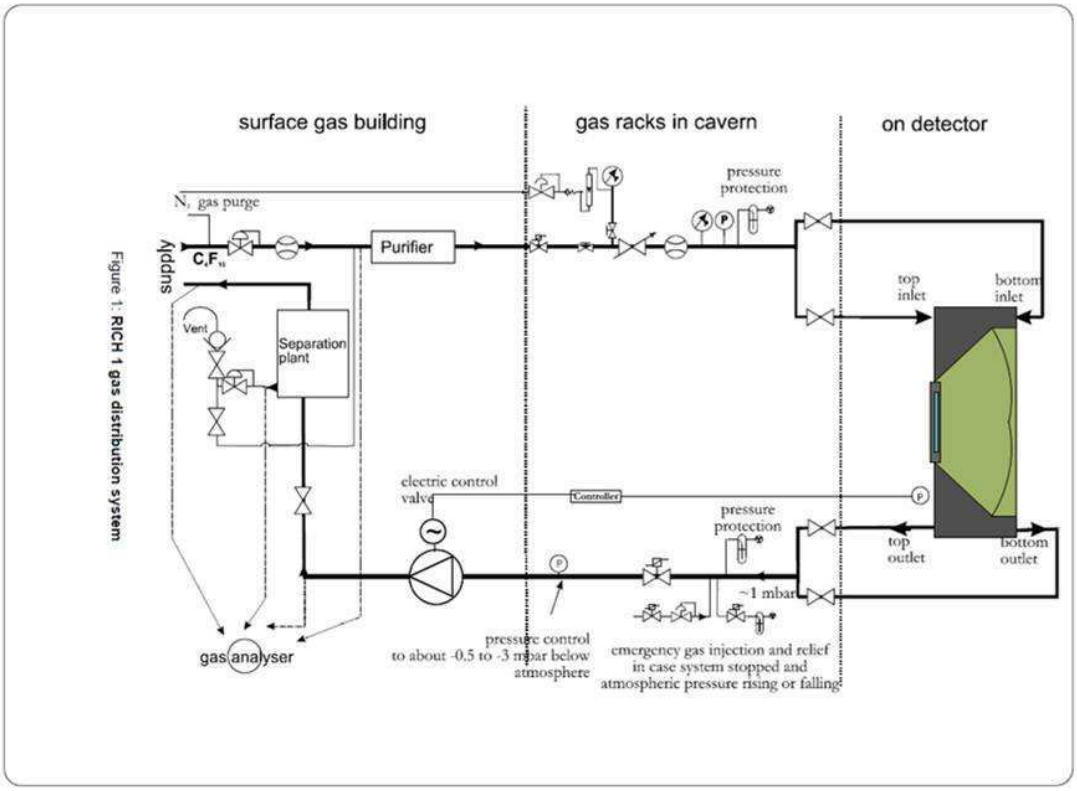

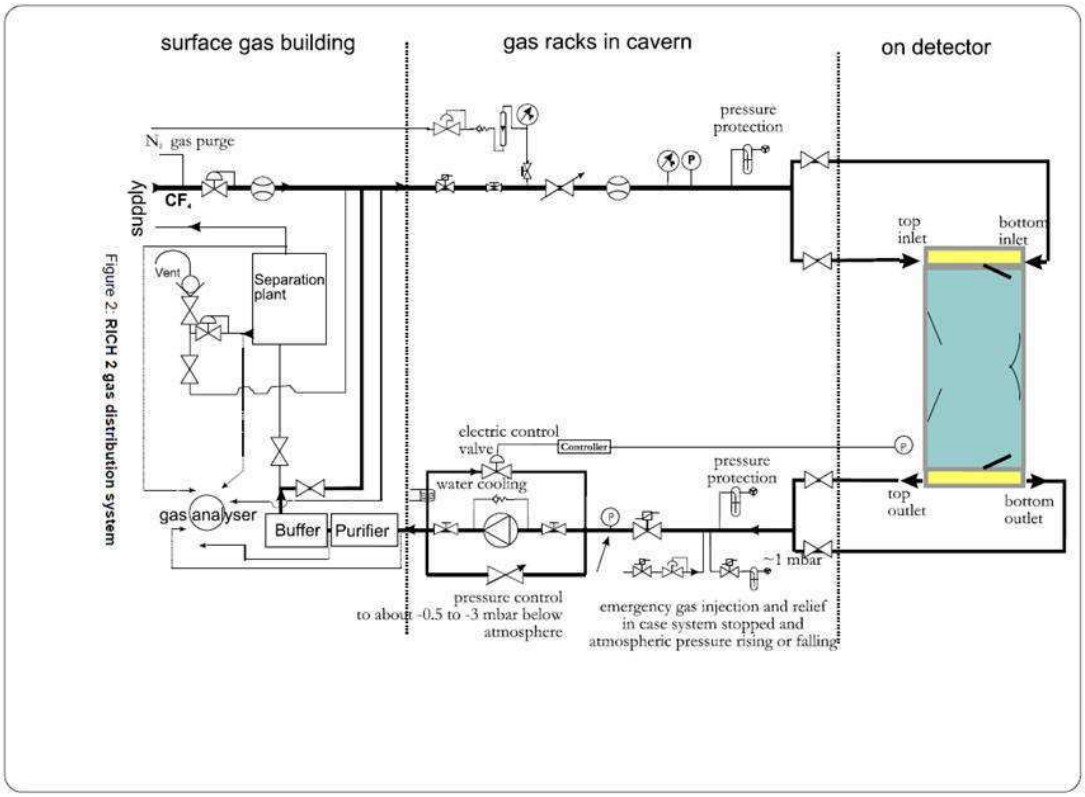

Fig. 2.16 Schematics of the radiator recirculators of the LHC RICH1 & RICH2 detectors (after [32]).

systems stems from the higher volatility of CF_4 compared to C_4F_{10}, as illustrated in Fig 2.17, which compares the

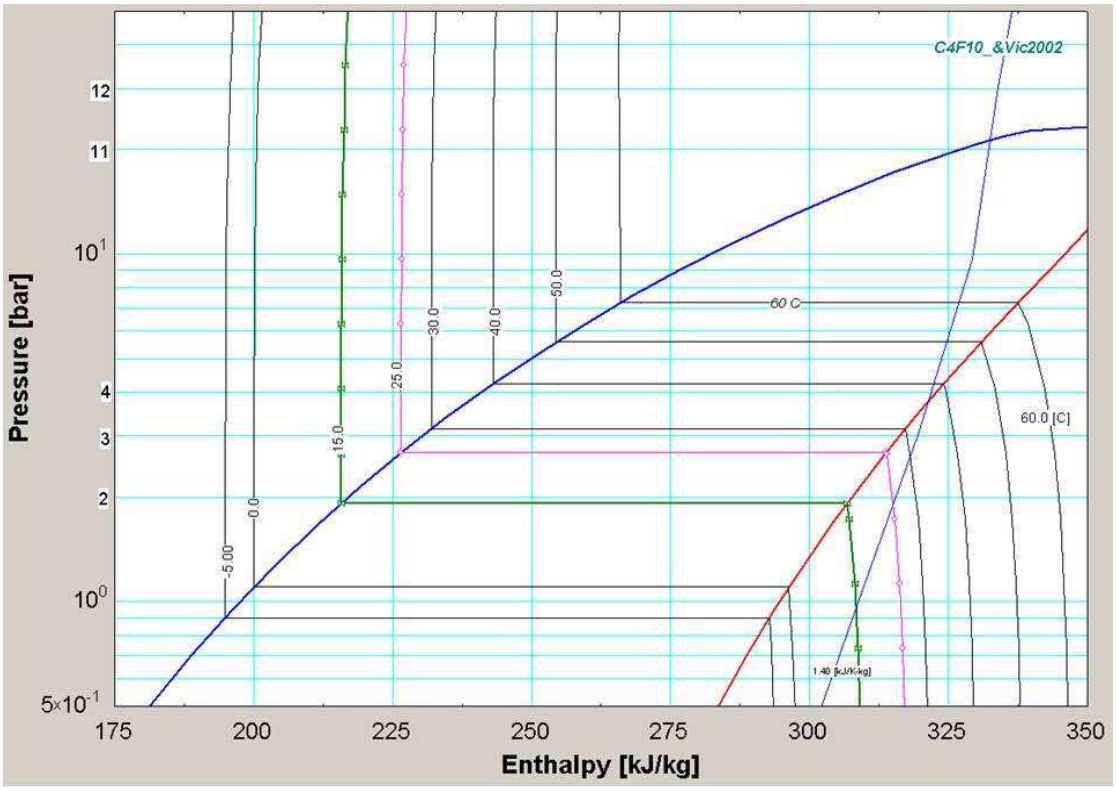

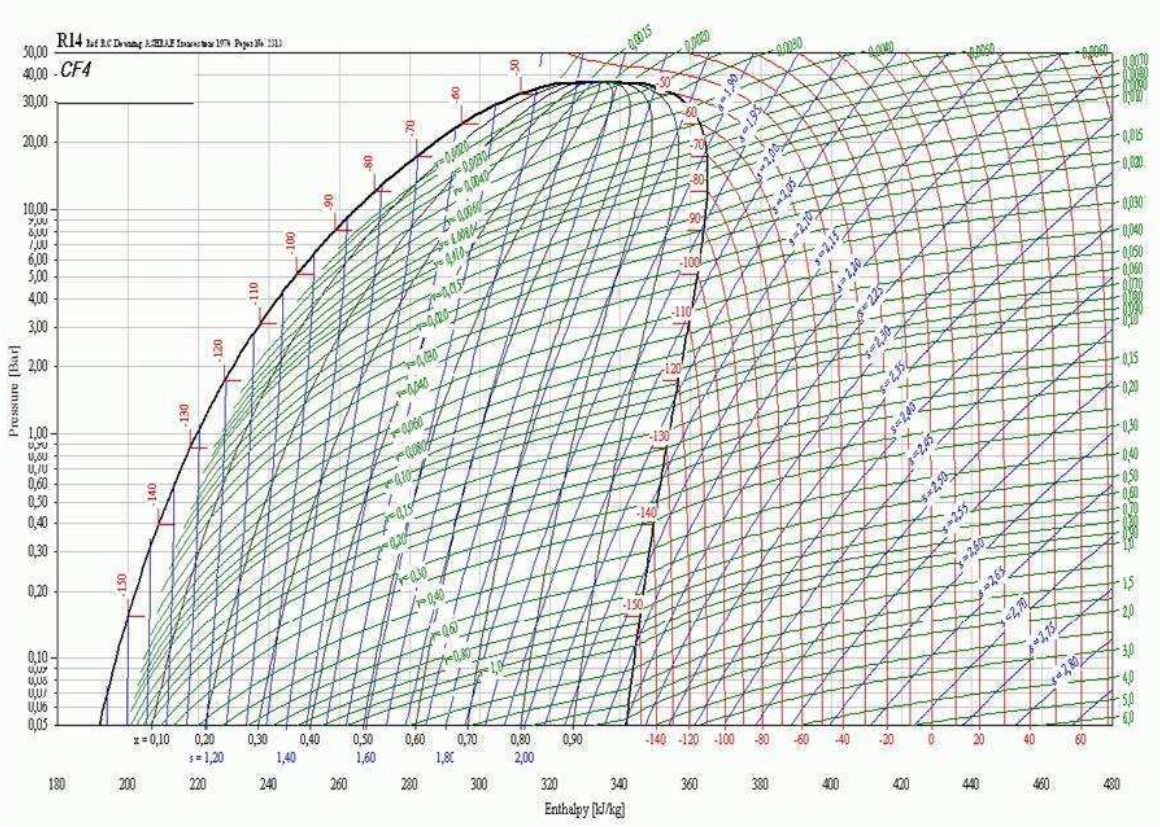

Fig 2.17 Pressure-Enthalpy curves for C_4F_{10} and CF_4

pressure-enthalpy diagrams of the two fluids. It can be seen that while C_4F_{10} has a boiling temperature of around -3ºC at atmospheric pressure, CF_4 requires liquid nitrogen temperatures to arrive at a saturated vapour of 1 bar $_{abs}$. In the absence of copious amounts of liquid nitrogen, long-term liquefaction-circulation is impractical, though it is necessary for economic and environmentally-responsible recovery of CF_4 at the end of operation and also briefly during filling, when CF_4 is introduced at the bottom of the radiator vessel gradually displaces nitrogen (with a small admixture of CF_4) from the top.

Before the start up and during shutdown periods both RICH detectors will be filled with nitrogen gas. Both radiator volumes have two gas inlets and two gas outlets, one of each at the bottom and on top of the vessel; the high density SFC vapour can be filled from the bottom as the lower density nitrogen is purged from the top.

The RICH1 C_4F_{10} system is designed to circulate 0.4m^3/hr in a closed loop and can exploit thermodynamic liquefaction of the return gas to -50ºC to liquefy the C_4F_{10} and allow volatile impurities to escape. The return gas is compressed in the return line before entering the separation plant. Behind the compressor the C_4F_{10} is liquid and for this reason the compressor is placed at the surface. The purification by liquefaction is complimented by molecular sieve filters to remove water vapour.

The RICH2 system is designed to circulate 10m^3/hr of CF_4 with purification by passage through oxygen and water vapour filters. Liquid nitrogen driven liquefaction is only used during CF_4 recovery, and briefly during filling, as mentioned above.

Both RICH radiator gas systems incorporate UV gas transmission monitoring and water vapour and oxygen measurements before and after the purifiers. The specification for residual O_2 and water vapour contamination in the radiator gases is < 100-200 ppm. This is more generous than in the case of a CsI or TMAE photocathode (for example) where the quantum efficiency of the photocathode is rising at UV wavelengths below 200 nm where H_2O and O_2 absorption is more severe. Water can be removed to a level well below 0.1 ppm using molecular sieve. 13X molecular sieves, together with activated carbon, have been used successfully in the DELPHI RICH fluid system (section 2.4.6) to remove trace gases that absorb photons in the wavelength window above 170 nm. Molecular sieves (4Å and 3Å pores for the removal of O_2 & H_2O from C_4F_{10} & CF_4) and 13X (for the removal of all molecules of kinetic diameter < 10Å, including O_2 {@3.46Å} & H_2O {@2.65Å} from C_4F_{10})) are presently implemented in the LHCb RICH gas systems. Activated carbon can be introduced if needed: its advantages are discussed in sections 2.4.4 and 2.4.6..

2.4.3 The PHENIX hadron-blind RICH detector at Brookhaven

Figure 2.18 illustrates the hadron-blind RICH in the PHENIX experiment [24]. This detector has demonstrated

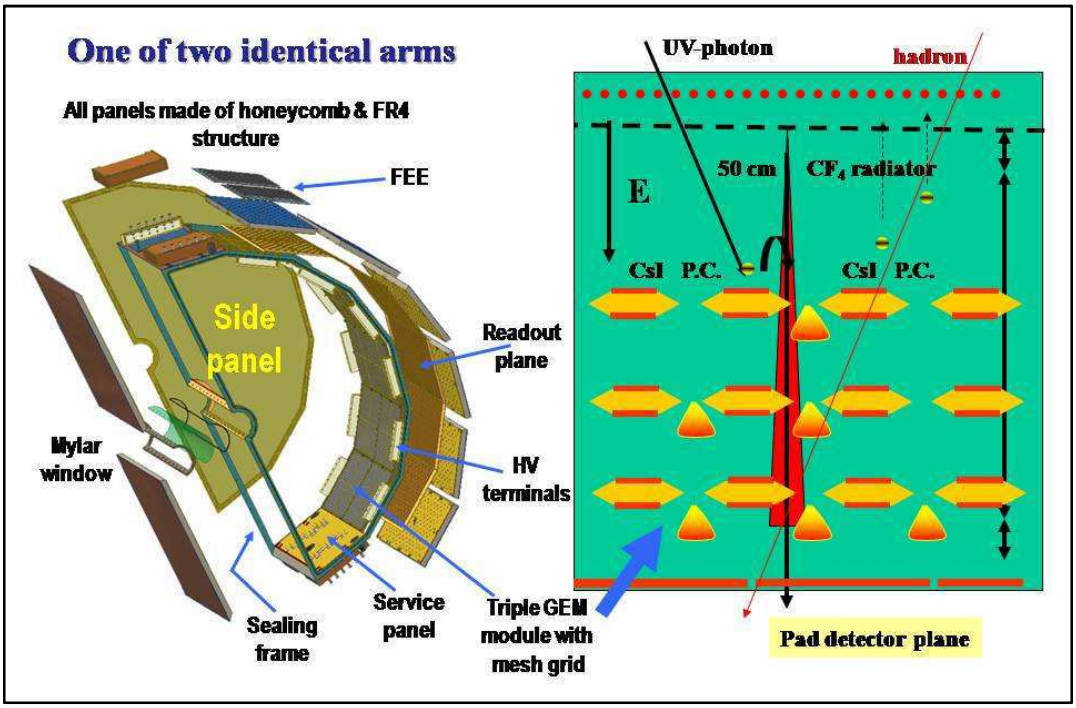

Fig. 2.18. Construction and principle of the PHENIX hadron-blind RICH detector.

extremely high efficiency for Cherenkov photon detection (N_0 ~ 800) in windowless operation with CF_4 serving as radiator and for photoelectron detection in a Gas Electron Multiplier (GEM) device with a CsI photocathode and a gain of around 5.10^3. Ionization from passing hadrons is trapped on electrodes in the GEM allowing for clean electron

identification in gold-gold collisions at the Brookhaven Relativistic Heavy Ion Collider. Each of the two arms that clamshell the RHIC beam pipe contains 12 (23x27cm^2) triple GEM stacks with a mesh cathode. The topmost of the three gold-plated, perforated GEM layers has a Caesium Iodide photocathode deposited. Since the photocathode is reflective there is no photon feedback. The photon detector is hadron-blind since most of the ionization charge in the drift region is repelled away from the GEM stack and collected on the cathode mesh. Proximity focussing in the 50 cm deep CF_4 gas radiator gives rise to a 'blob' of Cherenkov photons on the photocathode. Readout is via ~ 2000 hexagonal anode pads of diameter 15.5 mm and area 6.2 cm^2; which are comparable in size to the typical Cherenkov 'blob' size (2-3 pads hit, average size 10.2 cm^2).

2.4.4 The COMPASS RICH Cherenkov radiator system and the purification of C_4F_{10}

The COMPASS RICH-1 uses a 3m C_4F_{10} radiator operating at atmospheric pressure to provide hadron identification in the range from 3 to 55 GeV/*c*, in the COMPASS wide-acceptance spectrometer at the CERN SPS. It has a 21 m^2 VUV mirror array and a total of 5.5m^2 of photon detectors in two varieties; multi-anode PMTs in the central region and MWPCs with CsI photocathodes elsewhere (determinant to the C_4F_{10} purity requirement). The radiator volume of around 80m^3 is continuously swept with C_4F_{10} gas at a rate of about 2 m^3/h. Water vapour and oxygen contaminations are removed by Cu catalyst filters (operated at 40ºC) and 5Å molecular sieves (at 15ºC); the resulting levels of contamination are below 1 ppm for H_20 and below 3 ppm for O_2.

Light transmission values larger than 88% in the VUV wavelength domain of the CsI-based photon detectors (165-210 nm) are routinely obtained. Such high levels are required through the use of a CsI photocathode whose quantum efficiency is rising at the shorter UV wavelengths. The achievement of such high transmissions in C_4F_{10} (for an average Cherenkov photon transit distance of ~4.5m) was more exacting than in previous C_4F_{10} forward radiator systems at DELPHI and SLD, where the Cherenkov photon distances were much shorter.

It was found, from earliest running in 2000/2001, that a dedicated cleaning procedure needed to be applied before usage of the commercially available C_4F_{10}, which could contain UV-absorbing impurities, particularly O_2. [33]. This pre-use purification procedure went through several iterations before arriving at the present configuration in which C_4F_{10} is pumped in a closed loop through activated carbon and 3Å molecular sieves to condense in a cold trap at -45ºC from which the gas component is vented away, carrying with between 10 and 20% C_4F_{10}. Figure 2.19 shows this pre-purification system.

In initial testing during 2001 silica gel, activated carbon, molecular sieve 13X and copper filters were used. After several tests it was decided to use the (BASF R3-11G) copper catalyst for the chemical removal of oxygen via:

$$2\,Cu + O_2 \rightarrow 2\,CuO$$

UV transparency measurements (in 1 cm liquid samples) from the first 20 bottles of C_4F_{10} (around 100m^3 vapour equivalent at 1 bar $_{abs}$) received from the manufacturer[6] indicated that there were two qualities in the delivery:

- nine bottles showing an initial transparency of 95% at 230 nm could be cleaned up to 65% at 165 nm (cut-off at 150nm) for a loss in material of ~ 7% ;
- eleven bottles showing an initial transparency of < 70% at 230 nm for which the pre-cleaning by circulating the material through a set of filters in liquid phase required several weeks with a loss of material close to 50%, giving finally 80% transparency at 200 nm (still with a rather poor N_0-limiting cut-off at 190nm).

For the latter group, the performance of the pre-cleaning was clearly inadequate: an additional low temperature cleaning step was tested: C_4F_{10} was cooled down and liquefied at -40ºC, while oxygen and other dissolved gases could be removed with an inert flushing gas such as argon. Using this procedure the oxygen content could be reduced by a factor of 10 to 40 and the remaining C_4F_{10} rendered usable.

[6] PF5040 performance fluid: 3M Corporation

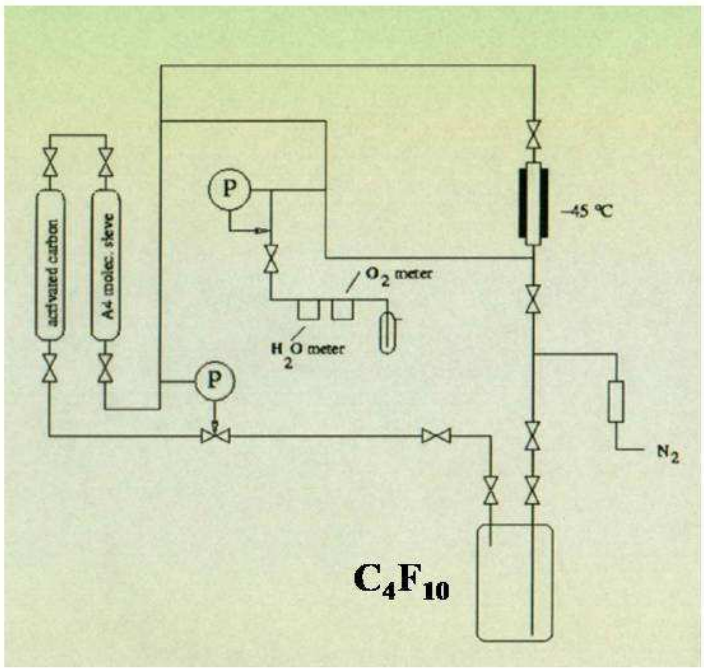

Fig 2.19: Schematic of the COMPASS RICH C_4F_{10} pre-cleaning system, based on that used for the DELPHI forward RICH

The ongoing successful operation of the COMPASS RICH1 radiator requires two cleaning steps: the pre-cleaning - performed in a dedicated laboratory with frequent transmission measurements on liquid samples using a VUV monochromator - followed by low temperature cleaning in the experimental area using the purification unit installed in the radiator gas system (Fig. 2.20).

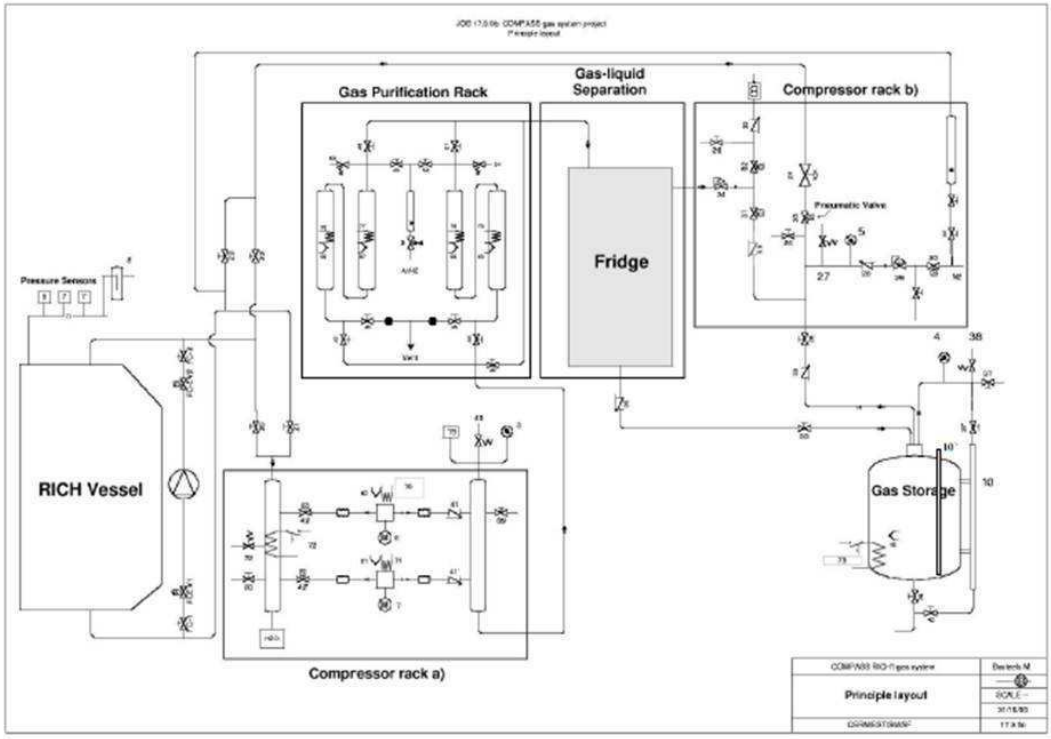

Fig 2.20: Schematic of the COMPASS RICH C_4F_{10} radiator recirculator with cartridge and low temperature purifiers and parallel stirring loop (see text)

In the COMPASS RICH radiator recirculator, part of the C_4F_{10} charge is kept in liquid phase inside a storage buffer, allowing automatic headspace buffering of variations in atmospheric pressure and the compensation of leaks (which typically are at the level of 80 l/day). Before and after COMPASS RICH running periods all the C_4F_{10} is recovered into the storage tank, in liquid phase. To avoid the formation of thermal gradients inside the radiator vessel a parallel, compressor driven loop was installed in 2009 and provides a 20 m^3/h circulation flow.

The levels of O_2 and H_2O contamination in the radiator are continuously monitored while the UV transparency is frequently checked in an automated system based on a UV lamp, grating monochromator, sample cell and PMTs.

The pre-cleaning setup has evolved from that used for the preparation of the gas for the 2001 run. Due to rapid saturation a change of the copper catalyst filter material was needed on a two-day basis. The regeneration procedure consisted of flushing with argon for 12 hours at 200ºC followed by flushing with "Noxal" (97%Ar/3%H_2 mixture) for a further 8 hours at 200ºC and terminating with a 12 hour argon flush at room temperature. Although spare cartridges could be regenerated in parallel with the purification, the procedure was very time consuming and manpower intensive, and triggered a search for a different approach.

For the 2002 and 2003 runs, the additional radiator gas needed was pre-cleaned using the refurbished DELPHI pre-cleaning system, where the raw material is filtered in gas phase (Fig 2.19). This system consists of a set of interchangeable filters of 5Å, 13X molecular sieve and activated carbon, a pump for circulation and a cooling unit for gas-liquid separation. The C_4F_{10} gas is circulated in a closed-loop or transferred from the initial delivery bottle into a second bottle for storage of clean C_4F_{10} gas. The process is controlled via a PLC-unit, including readout of water and oxygen analyzers. While the overall losses were still in the order of 20%, the amount of time needed was significantly reduced. Figure 2.21 illustrates the C_4F_{10} pre-cleaning for the 2002 run. Three different qualities of raw material are shown together with the final transparency after pre-cleaning. In all cases the design value of 80% at 165 nm was reached.

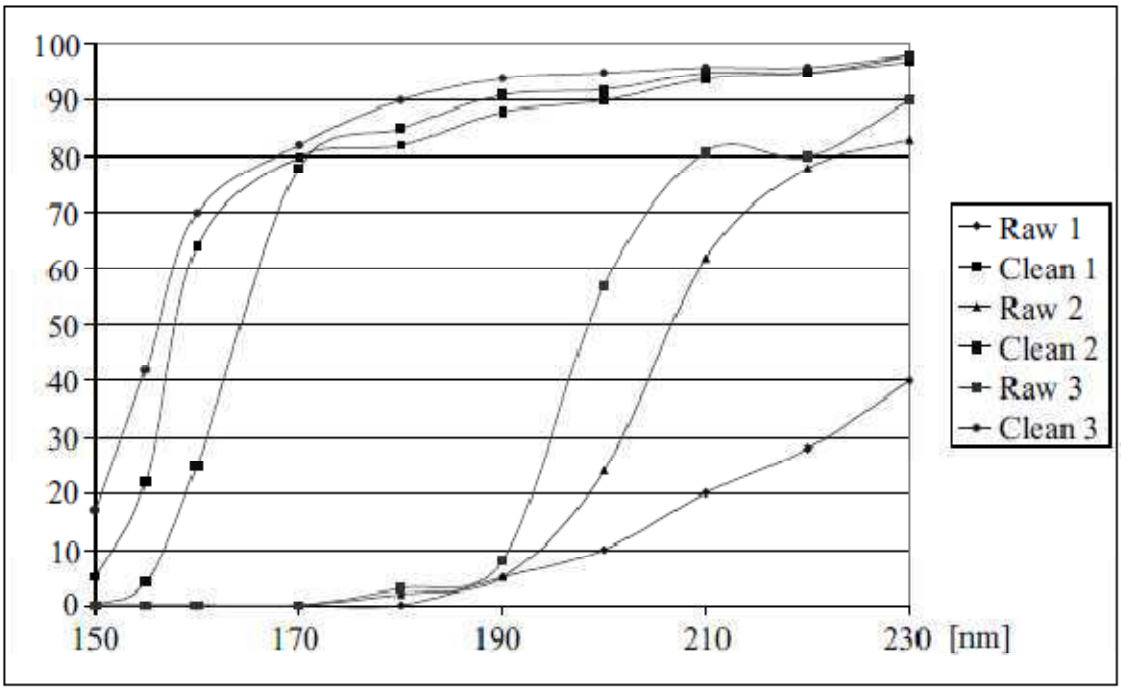

Fig 2.21 Percentage transparency in a 1 cm sample of liquid C_4F_{10} before and after cleaning of three bottles of C_4F_{10} for use in the 2002 run of COMPASS RICH1, using the pre-cleaning procedure described in the text: acceptance criterion $T \geq 80\%$ at 165nm

2.4.5 The ALICE High Momentum Particle Identification Detector (HMPID)

The High Momentum Particle Identification Detector (HMPID) in ALICE [16, 34] is composed of 7 (1.5 x 1.5) m^2 modules, a 15mm C_6F_{14} liquid radiator and photon imaging via 10m^2 of reflective CsI photocathode operating in quartz-windowed MWPCs filled with methane (CH_4) at atmospheric pressure. The MWPCs have a 4mm sensitive gap and analog pad readout. The detector has already demonstrated π/K separation up to 3 GeV/c and proton identification up to 5 GeV /c; a future upgrade should extend the momentum range to 30 GeV/c by means of 1 m of C_5F_{12} gas radiator, with a mirror focussed configuration.

Each HMPID module is equipped with three liquid radiator trays of 1330 (l) x 413 (w) x15 (t) mm^3 made of 4mm thick Neoceram ® glass-ceramic material, closed by three 5mm thick glued fused silica plates forming a UV-transparent window. Silica rods glued between the bottom plate and the windows provide the necessary strength to withstand the hydrostatic load. The tray elements are glued together with Araldite ® 2011.

Liquid circulation is via a closed, pressure-regulated system which continuously purifies, fills, re-circulates and empties the twenty-one radiator vessels independently. The system consists of

- a surface station with purification, UV transparency monitoring and a fridge to condense any C_6F_{14} returning to the surface as vapour;
- a distribution station located on the HMPID cradle, inside the ALICE solenoid magnet;
- a pumping station located in the ALICE cavern, outside the experiment, to return liquid C_6F_{14} to the surface.

The hydraulics and operating scheme of the liquid circulation system is shown in Fig. 2.22. Similar gravity cascades were used previously in the C_6F_{14} radiator trays of the DELPHI RICH, the SLD CRID and the STAR RICH at Brookhaven.

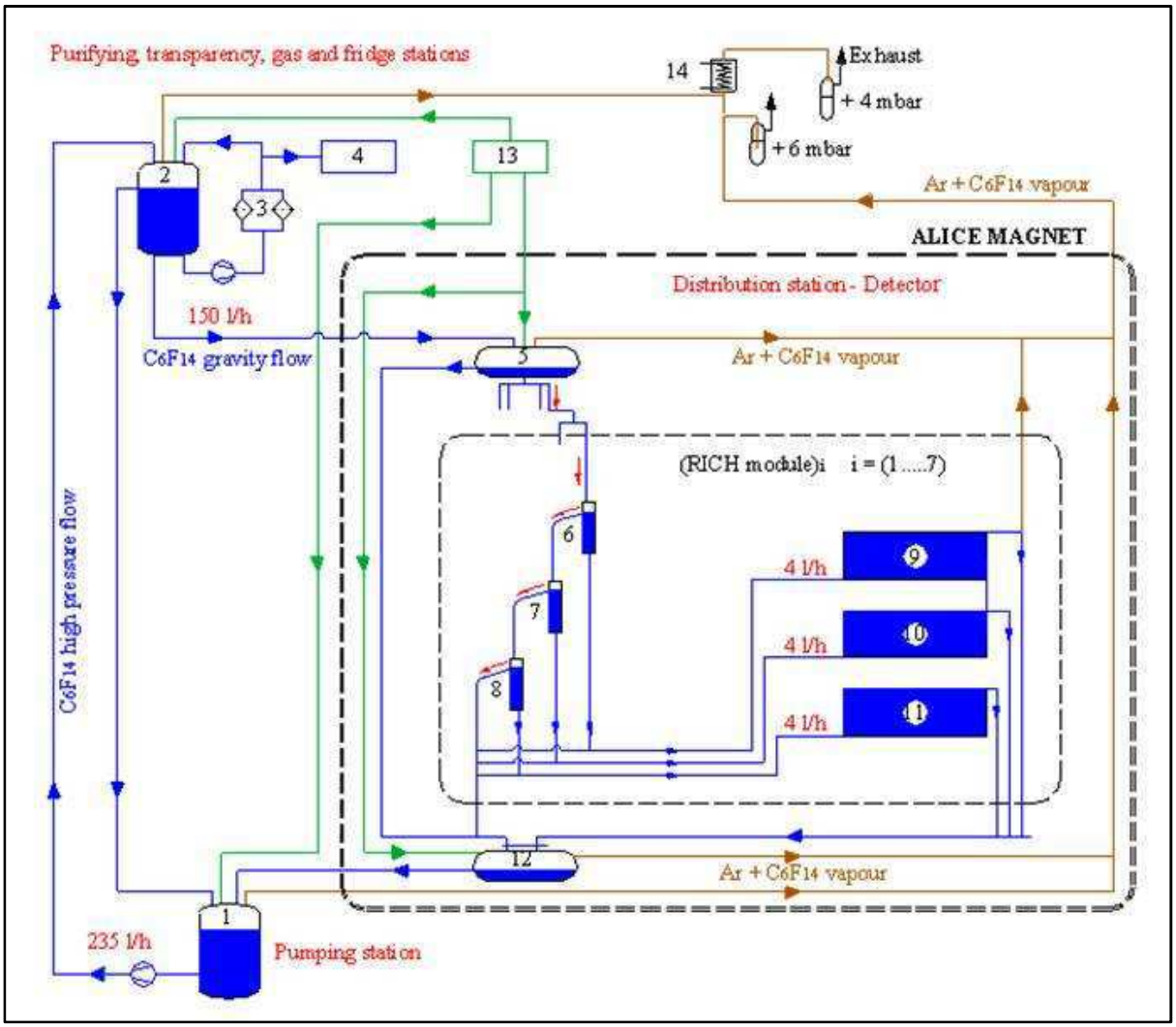

Fig 2.22. The C_6F_{14} liquid radiator circulation system of the ALICE HMPID

The liquid is continuously pumped at a constant flow rate of 235 l/h @ 6.3 bar from the ALICE cavern (1) up to a surface collection tank (2) from where it passes through a purifying station (3) where 13X molecular sieve and regenerable (at 180 °C) carbon active filters remove O_2 and H_2O contaminants to maintain liquid transparency (to better than 80% at λ = 170 nm). Sampling lines connected to the purifying station send liquid to a monochromator station (4) for real-time transparency measurement.

From the surface station the liquid flows by gravity, at fixed flow rate of 150 l/h, into the tank of the distribution station (5). The C_6F_{14} flows from (5) to the seven groups of 3 small header tanks (6, 7, 8) supplying - via independent lines - the 21 radiator vessels (9, 10, 11) by cascade. The header tank cascade system defines and limits the hydrostatic loading of each radiator tray, guaranteeing a laminar flow of 4 l/h through each tray without exceeding its maximum working pressure of 140 mbar above atmospheric pressure. The liquid returns through a vapour separation tank (12) into the main storage tank (1) of the pumping station from where the cycle starts again.

The liquid circulation system has an argon purge system to eliminate air before the trays are filled, and to prevent air collection. Argon is flushed at a flow rate of 30 l/h and along its return lines it collects evolved C_6F_{14} vapour channelling it to the surface fridge station (14), where it is condensed at – 40 °C for re-use, the gaseous argon being allowed to vent.

2.4.6 Technological feed-forward from the DELPHI RICH fluorocarbon radiator experience

In this section I highlight a few more of the "*retours d'expérience*" from the enormous DELPHI RICH experience that the detectors previously mentioned sections 2.4.1 to 2.4.5 have built upon. It is far beyond the scope of this *memoire* to enter into detailed descriptions of all the DELPHI subsystems, nor of the radiator performance, including Cherenkov angle resolution etc. of DELPHI or the other RICH detectors mentioned, so I focus instead on SFC radiator-related techniques of interest to future applications, including the use of SFCs as coolants for silicon trackers.

(i) Purification of SFCs to remove oxygen and water vapour contamination

The DELPHI RICH collaboration probably expended more effort studies of the compatibility of materials with SFCs and in the development and understanding of techniques for the removal of oxygen and water vapour impurities from Cherenkov radiators than any other collaboration. The benefit of this study to other users was illustrated in the previous sections. A summary of the present state of the art is given collectively in [35] - [37]. This is impossible to emulate: however it is necessary to consider the unsuitability of some methods of purification in the context of imperfect fluorocarbon molecules and the constraints of high radiation, as discussed in the following sections.

(ii) Elimination of 'defective' fluorocarbon molecules

In addition to the need to remove O_2 and H_2O contamination from SFCs to maximize their UV transparency in the sensitive range of the photocathode, care is also necessary to verify that the fluorocarbon molecules are indeed fully saturated and do not contain residual chemically-attached hydrogen in molecules of the form $C_nF_{(2n+2-x)}H_x$ or doubly-bonded fluorocarbon molecules of the form C_nF_{2n}. While the elimination of these molecular types was important for the radiator performance of the DELPHI RICH – for which the chemical methods discussed below were developed – it is even more important in tracker cooling applications where SFCs must be ducted through the high radiation areas near LHC collision points.

The removal of intrinsic or extrinsic hydrogen (respectively from non-fully fluorinated molecules of the form $C_nF_{(2n+2-x)}H_x$. or residual water vapour) – is necessary to eliminate a source for hydrofluoric acid (HF) generation under ionizing radiation. Also the exposure of these molecules to Oxisorb ® chromium or activated copper catalysts can provoke violent exothermic reactions which can destroy accompanying 'good' saturated fluorocarbon molecules while transforming residually-hydrogenated molecules into weaker double carbon-bonded ($C_nF_{(2n)}$) species [35], [36], which are more likely to polymerise under irradiation.

Residually hydrogenated and double carbon-bonded FC molecules can both be identified in Fourier Transform Infra Red (FTIR) spectroscopy via their respective characteristic absorptions near 3000 and 1784 cm^{-1}. Double carbon-bonded molecules of the form C_nF_{2n} also exhibit strong absorption in the UV range 190–200nm, allowing fairly straightforward batch qualification, as carried out for the DELPHI RICH detector [35].

Techniques for the catalytic modification of C_nF_{2n} molecules were extensively investigated for DELPHI [35]: double carbon-bonded molecules were reformed using a permanganate (MnO_4) catalyst with the removal of the MnO_2 precipitated in the process [35]. Figure 2.23 illustrates the recovery of optical transmission in a 1cm sample of C_6F_{14} purified by this technique to remove double carbon-bonded impurity molecules. (Note that this procedure does not remove O_2 and H_2O contamination which are still present afterward.)

The lack of inertness of the residually-hydrogenated molecules of the form $C_nF_{(2n+2-x)}H_x$ necessitated development of less aggressive methods than activated metal catalysts, for O_2 and H_2O removal, through the use of activated carbon and porous membranes [35,36]. More recent techniques to remove hydrogenated molecules have centred on the use of activated carbon [36, 38] as for example in the COMPASS RICH. Activated carbon[7] is an adsorption material with a less specific surface geometry which has proven particularly efficient in removing various geometries of hydrocarbon molecules from process fluids. Many types exist, adapted to different requirements. In an example of the use of activated carbon [36] ("Filtracarb FY5") it was found that some C_4F_{10} batches destined for the COMPASS RICH detector were contaminated with benzene (C_6H_6), as well as other alkanes and alkenes during the production process [33], [36]. Benzene has a maximum absorption coefficient around 180 nm such that a 10^{-8} concentration would reduce the UV transparency of the C_4F_{10} by 5% over a 4 m path length. benzene has a kinetic diameter of 5.85Å compared with 5.6Å for C_4F_{10}. While 13X (10Å pore size) molecular sieves can clearly trap C_6H_6, they will also do the same for C_4F_{10}, resulting in unacceptable losses of the Cherenkov fluid. The C_4F_{10} was therefore purified using techniques developed for the DELPHI forward RICH, using a combination of activated carbon and 4Å molecular sieve for the light alkanes ($C_nH_{(2n+2)}$) and alkenes (C_nH_{2n}). The liquid C_4F_{10} was held in a -50°C cold trap and the oxygen purged with an argon flush to prevent it saturating the 4Å molecular sieve, which was left available for water and the lighter alkanes and alkenes. The larger hydrocarbons were trapped on the carbon with only a trivial loss of the C_4F_{10} radiator fluid [33], [36].

[7] See for example: http://www.activated-carbon.com/

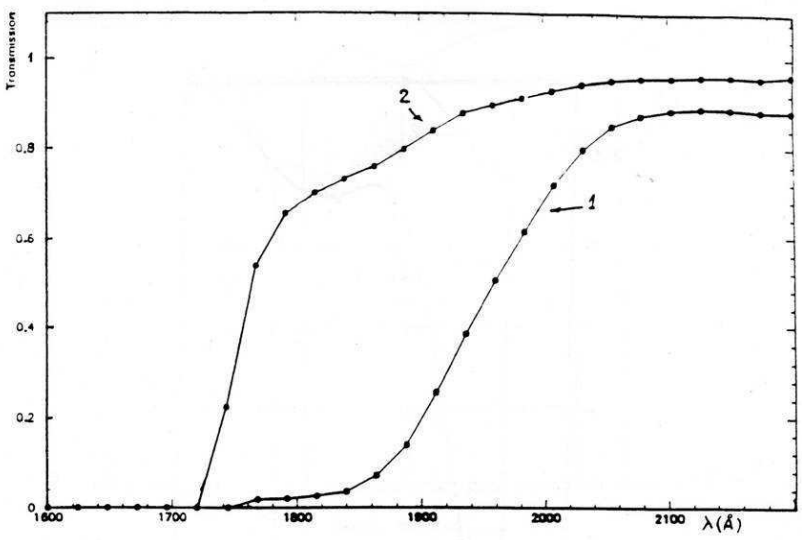

Figure 2.23 Recovery of optical transmission (2) in a 1cm sample sample of C_6F_{14} purified by a permanganate technique to remove double carbon-bonded impurity molecules (after[36]).

Membrane filters have also been investigated within the DELPHI RICH collaboration, with excellent results. [35-37] Thin film membrane development was mainly driven by industrial interest in separating H_2 (kinetic diameter 2.89Å) from CH_4, CO and N_2 (respectively 3.8, 3.76 & 3.8 Å) gas streams. Two main categories of membrane systems can be identified; zeolite molecular sieve films and composite hollow fibre membranes. In [35] a study was made of the efficacy of hollow fibre membranes for the cleaning of C_6F_{14} liquid radiator (molecule kinetic diameter 7Å). The liquid to be cleaned was continuously passed through the capillaries. The permeating molecules with small kinetic diameters (< 4Å) including O_2 and H_2O were removed by pumping the space surrounding the capillaries. The typical gain in UV detection starting from a point of around 70% transparency at 185nm was between 0.08 (start) and 1 Å (finish) for each hour of circulation through the membrane. Fig 2.24 illustrates the use of the membrane to clean the previously chemically treated C_6F_{14} liquid ($Mn0_4$ catalytic treatment for double carbon-bonded molecules), where excellent transparency was recovered after the removal of O_2 and H_2O by the membrane. The membrane does not need regeneration as in the case of a chemical O_2 and H_2O scrubber.

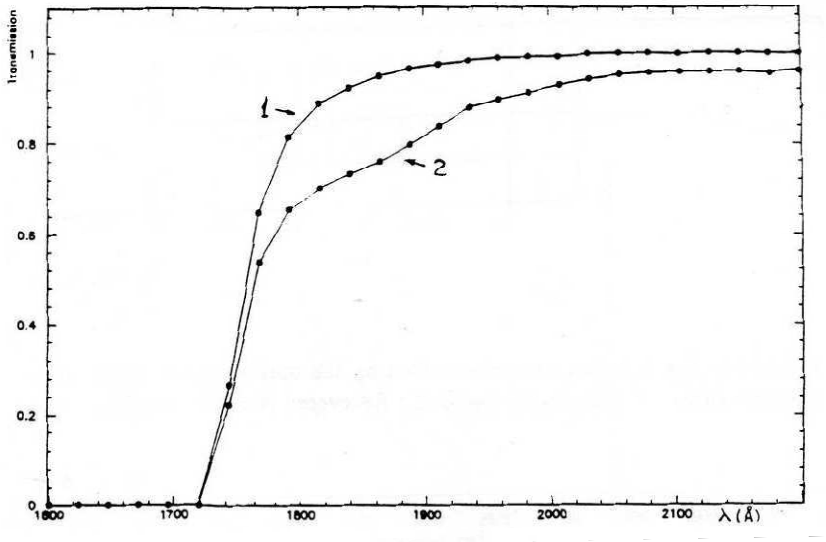

Figure 2.24 Recovery of optical transmission (1) in a 1cm sample sample of C_6F_{14} using membrane filtration following purification by a permanganate technique (2) to remove double carbon-bonded impurity molecules (after[36]).

(iii) Distillation separation of SFC species differing by 50 units of molecular weight.

During the long lifetime of the DELPHI Barrel RICH the mild solvent activity of the C_6F_{14} in the liquid radiator trays and the C_5F_{12} in the gas radiator gradually degraded some of the glue and elastomer barriers that separated them, leading to a progressive cross-contamination which threatened to compromise the refractive indices of both radiators. In collaboration with an industrial laboratory[8] a 7.6 m high distillation column (Fig 2.25) was designed and constructed [39] for the separation of C_5F_{12} and C_6F_{14}. Contaminated (mixed) liquids were collected in a common mixing tank and fed into a 7.6 metre high distillation column capable of separating 150-200 kg/hr of the two fluids to a separated purity better than 95%. The homogeneously-packed[9] column operated according to the McCabe –Thiele method. The C_5F_{12}/C_6F_{14}mixture was introduced roughly half way up the column. Predominantly C_6F_{14} liquid exited near the 12kW boiler at the bottom and predominantly C_5F_{12} and from the 5kW capacity C_5F_{12} condenser at the top. With a column operating pressure 125Pa above atmospheric pressure and the boiler (C_5F_{12} condenser) operating at 57°C (31°C), 98.4% C_6F_{14} was extracted from the bottom, and 96.7% C_5F_{12} from the top.

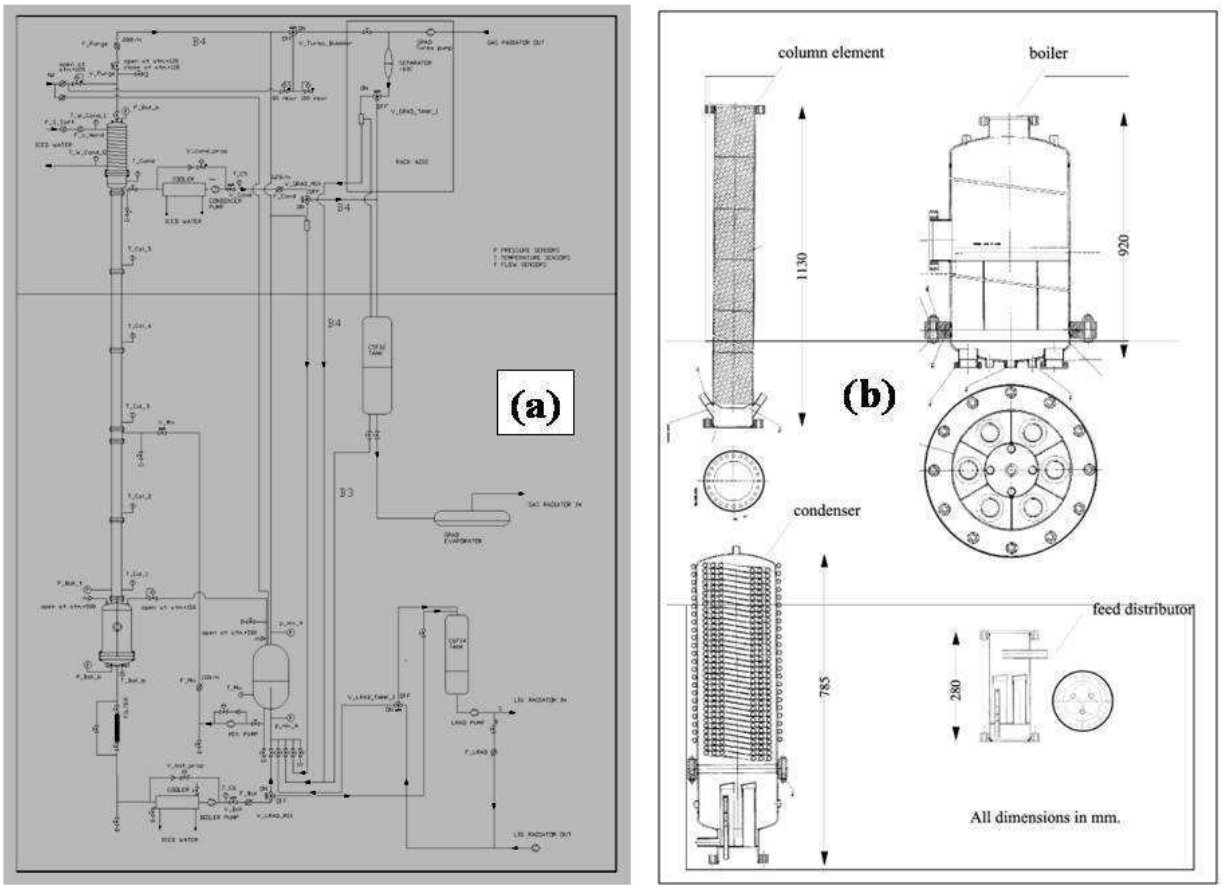

Fig 2.25 Schematic of the vertical column installation for C_5F_{12}/C_6F_{14} separation at the DELPHI barrel RICH. Mixed liquid feed and purified liquid extraction points (a); internal details of the column, bottom boiler and top condenser.

Such separation technology is likely to be needed again soon, in the context of the ATLAS evaporative cooling studies with mixtures of C_2F_6 and C_3F_8 (section 5.1) should these blends need to be unmixed for storage or recycling. It is interesting to note that these fluids also differ from each other by 50 units of molecular weight. The future column may need to be developed with a higher operational pressure in mind, given the greater volatility of the two components.

[8] Bayer AG, Zentrale Forschhung ZF-TVG 4, D-51368 Leverkusen, Germany, (Messrs H. Steude & H-W Kramer).
[9] Rombopak ® 9M structured large surface area packing; Mfr: Kühni AG, Basel, Switzerland.

2.5 Cherenkov radiator systems on which the author has collaborated

The author has been involved in Cherenkov radiator systems where, in addition to their use in pure mode, SFC vapours have been mixed with non-fluorocarbon gases (usually N_2) as pragmatic responses to (surprisingly) mechanical concerns:

- Omega RICH with 50%N_2/50%C_2F_6 [12]: hydrostatic loading of a thin radiator window originally designed for lighter (N_2) gas;
- SLD CRID with 30%N_2/70%C_5F_{12} [13]: risk of condensation of pure C_5F_{12} in the event of vacuum failure in the liquid argon calorimeter (LAC) cryostat forming the outer wall of the barrel radiator.

2.5.1 The OMEGA RICH C_2F_6/N_2 radiator recirculator system

Fig 2.26 illustrates the OMEGA RICH radiator recirculator system used with C_2F_6/N_2 between 1984 & 1986.

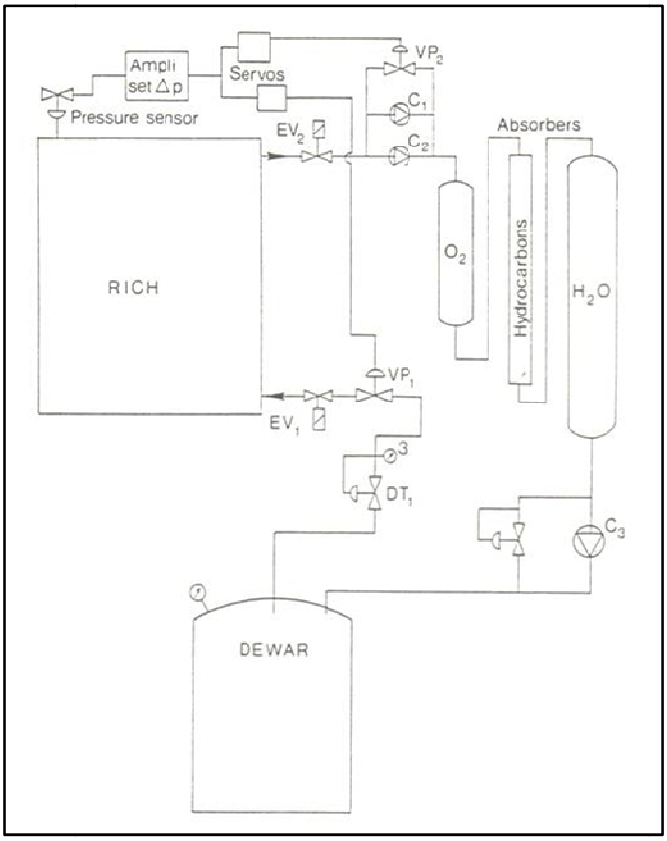

Fig. 2.26 OMEGA RICH radiator recirculator system used with C_2F_6/N_2 between 1984 and 1986.

The circulator was not *completely thermodynamic* in operation (i.e. it did not implement an evaporation-condensation cycle during radiator circulation in run conditions). Condensation was only used to recover the C_2F_6 during end-of-operation changeover to a passive N_2 filling of the radiator vessel. The three distinct phases of operation - all of which were required to maintain a pressure of 1bar abs ±1mbar in the 120m^3 OMEGA RICH radiator vessel - were:

- **Filling from an inert N_2 precursor**: C_2F_6 was introduced at bottom of the radiator vessel at a rate of around 5m^3/hr displacing N_2 from the top through a vent valve opened only during this procedure. C_2F_6 gradually mixed with the N_2 remaining in the vessel. During the fill gas was extracted from monitor ports at the top and bottom of the radiator vessel and sent to a Fabry-Perot interferometer, for (visible wavelength) refractive index measurement. It was found that the displacement technique could achieve up to 70% C_2F_6 concentration, beyond the 50% concentration needed from physics requirements;

- **Circulation**: C_2F_6/N_2 left the radiator vessel and was passed through O_2, H_2O (activated copper and 3Å molecular sieve) filters boosted by a pair of oil-free compressors[10] C1&C2 (compression to ~ 3 bar_{abs}). A 600 l Dewar serves as gas buffer volume during this purely mechanical circulation;
- **C_2F_6 recovery and radiator passivation with N_2 gas**: C_2F_6 was recovered from the bottom of the radiator vessel and liquefied at -70ºC in a Dewar cooled by cold N_2 gas from liquid boil-off. During this procedure N_2 gas was injected into the top of the radiator vessel. During C_2F_6 recovery the Dewar headspace gradually pressurized with incondensable N_2, returning at a low concentration with the C_2F_6 from the bottom of the radiator vessel. The Dewar could be pressurized to a maximum of 16 bar_{abs}: incondensable N_2 was periodically "burped" out, without serious loss of C_2F_6 whose saturated vapour pressure (s.v.p.) was around 150 $mbar_{abs}$, as illustrated in Fig. 2.27.

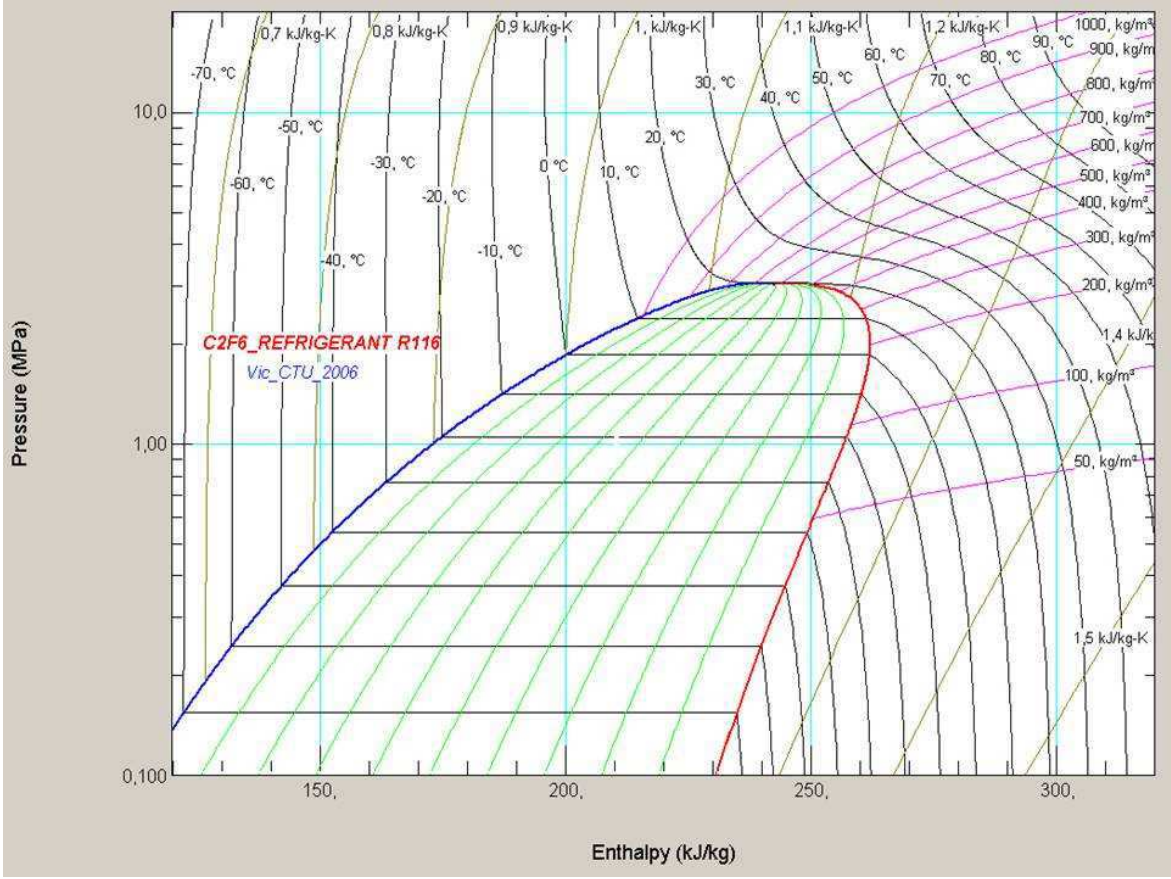

Fig. 2.27. Presssure-Enthalpy diagram for C_2F_6.

[10] Haug SOGX 50-D4 Dry Piston Compressor (rated 3.6 m^3hr^{-1} air, P_{in} 1 bar_{abs}; P_{out} = 9 bar_{abs} limit)

2.5.2 The SLD Cherenkov Ring Imaging Detector radiator recirculator systems

The SLD barrel Cherenkov Ring Imaging Detector (CRID) system was designed to provide particle identification in the study of Z^0 physics at the SLAC Linear Collider (SLC). The performance specification was outlined in section 2.3. Fig 2.11 illustrated the SLD Cherenkov Ring Imaging Detector. The detector was divided in to three main elements, a central barrel and two forward endcaps.

In the barrel region a combination of liquid (C_6F_{14}) and atmospheric pressure gas (70% C_5F_{12} in N_2) fluorocarbon radiators were used, while in the end caps a simpler system employed only a C_4F_{10} gas radiator. All three radiator vessels operated at a temperature of 40ºC, above the saturation temperature of the TMAE photo-ionizer in the TPC drift gases. The temperature control systems were based on highly redundant multi-channel networks of Kapton heater pads and temperature sensors bonded to the walls of the radiator vessel and also on the external end surfaces of the TPCs.

The radiator of the barrel CRID was chosen to be a mixture of 70% C_5F_{12}/30% N_2 due to concerns on the risk of condensation of pure C_5F_{12} in the event of a failure of the radiator vessel temperature control system. Even in the unlikely event of such a failure, nitrogen gas could enter the radiator vessel to maintain the overpressure of around 1mbar relative to the atmospheric pressure reference [40].

A particular concern was a possible vacuum failure in the liquid argon calorimeter (LAC) cryostat which formed the outer wall of the barrel CRID radiator and the surface onto which the mirror support frames were attached. In fact such a vacuum failure did occur due to a split which developed in a bellows fitting delivering liquid N_2 to the cooling loop of the liquid argon cold mass. This bellows was situated in the vacuum space around the cold mass. The barrel CRID mirrors had been installed but the radiator was still filled with N_2 during its pre-commissioning phase. It was considered impractical to empty the liquid argon and warm up the cold mass, so instead the vacuum was spoiled to allow an access hole to be cut in the end wall of the cryostat for the bellows to be replaced. During this operation, the inside wall of the cryostat was exceptionally heated with around 15kW with all circuits of Kapton heater pads powered, instead of the few normally required to keep the wall at 40ºC to counter the few hundred watts of cold leakage across the vacuum space. The repair was a complete success, and in spite of the safety factor given by the (70% C_5F_{12}/30%N_2) mixture, no further problems were encountered with the cryostat. The temperature control system continued to work reliably throughout the life of the detector, accumulating more than 4 million channel hours of operation (see also section 4.4.2).

The maintenance of the (70% C_5F_{12}/30%N_2) radiator mixture to avoid unacceptable drifts in the refractive index resulted in the development of a novel instrument for the continuous on-line ultrasonic analysis of the radiator gas mixture as an alternative to difficult direct measurements of refractive index with extraction to an interferometer. This instrument, which has been adopted by all major RICH detectors since, is discussed in section 3.2.

Figure 2.28 illustrates the final circulation system of the SLD barrel CRID, which operated with a mixture of 70% C_5F_{12}/30% N_2 in a unique (to this day) *continuous*, *cryo*-thermodynamic circulation cycle (condensation/evaporation at temperatures derived from the evaporation of liquid nitrogen, rather than SFC condensation during recovery only - as in other RICH radiator recirculators), resulting in reduced consumption of oxygen and water vapour removing filters (Oxisorb ® + activated copper and silica gel, respectively). C_5F_{12} in the radiator mix was condensed in a vacuum jacketed counter-current heat exchanger cooled with cold N_2 gas coming from liquid N_2 boiloff (A) and held in a vacuum-insulated cold tank (B) while N_2 and other incondensable impurities - for example from dissolved or ingressed air - escaped from the tank headspace. The C_5F_{12} storage tank was kept at -80°C through heat exchange with cold N_2 gas evolving from the cooling loops of the SLD LAC cold mass. With a s.v.p. of only a few mbar at -80°C, C_5F_{12} loss was negligible.

Fig 2.29 illustrates the thermodynamic cycle on a C_5F_{12} pressure-enthalpy diagram. The circulator operated in a "*thermo-siphon*" mode (characterised by a clockwise progression on the P-h diagram) with cold C_5F_{12} liquid draining from the condenser (a visible pressure rise in the liquid phase) into an electrically heated evaporator (C), the liquid column from the condenser being sufficient to maintain the evaporation pressure a few hundred mbar above atmospheric pressure.

The C_5F_{12} vapour exiting the evaporator was mixed with new warm N_2 gas (also derived from N_2 boil-off) in a 70%/30% ratio by mass flow controllers (D) for re-injection into the radiator vessel at a flow of 30-40 litres.min^{-1}. The thermal motor for this system was provided by the abundant liquid N_2 use of the SLD liquid argon calorimeter. For example the cold N_2 gas used to condense the C_5F_{12} was itself pre-cooled in heat exchange with liquid N_2 in an upstream counter flow heat exchanger.

The C_5F_{12}/N_2 mixture being injected into the barrel CRID radiator was monitored and corrected with feedback from a custom combined ultrasonic analyzer/flow-meter instrument described in sections 3.2 & 5.2.

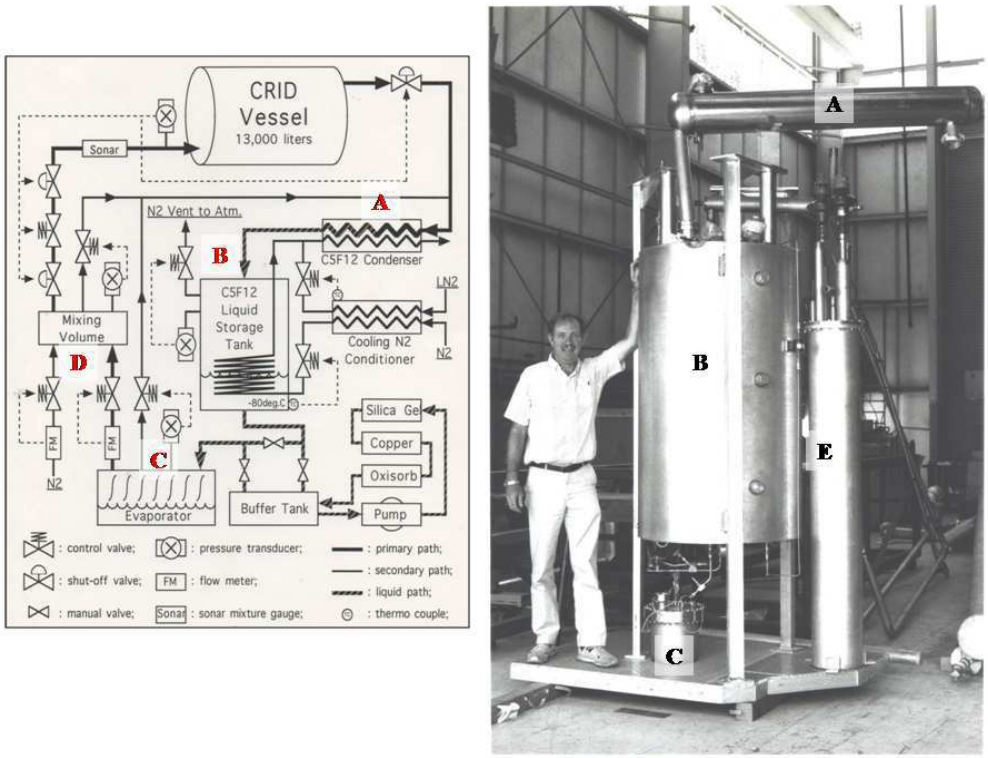

Fig 2.28. Schematic and photo of the thermodynamic elements of the SLD barrel CRID C_5F_{12}/N_2 recirculator: indexing corresponds to text.

The combination of a low temperature condenser with gravity liquid feed to an evaporator and an ultrasonic instrument for fluid flow and mixture analysis has recently assumed great importance in the context of evaporative SFC cooling of the ATLAS silicon tracker (Chapter 5).

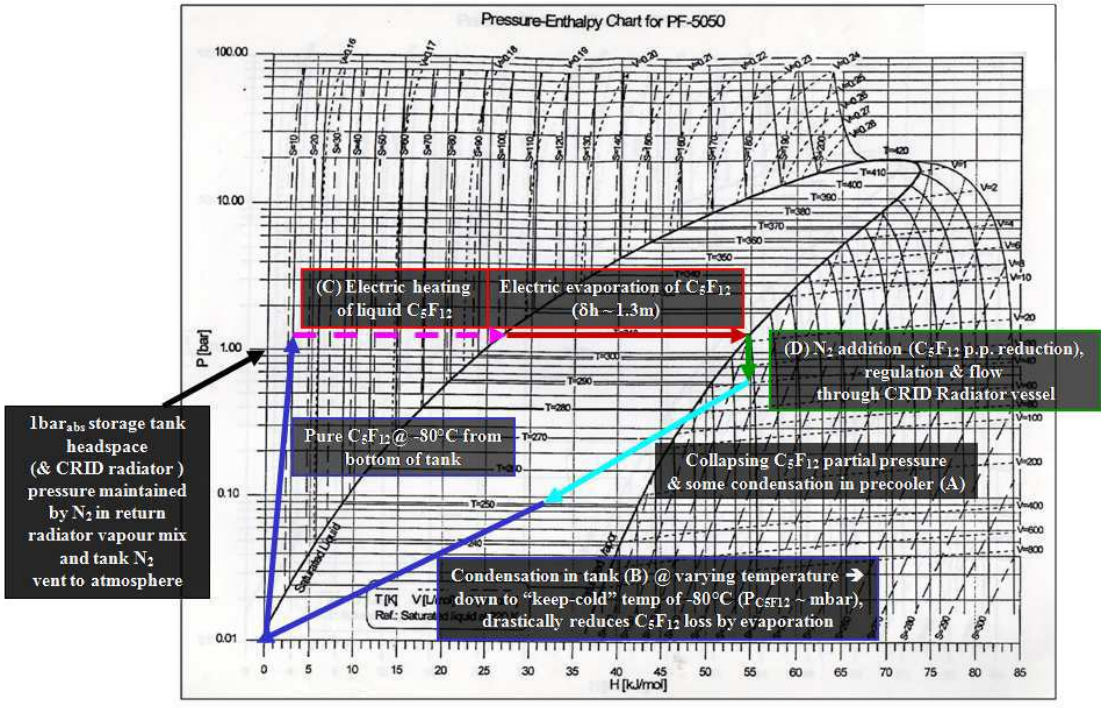

Fig 2.29. Thermodynamic cycle of the SLD barrel CRID C_5F_{12}/N_2 recirculator: indexing corresponds to fig. 2.27 and text.

Thermodynamic circulation in the SLD barrel CRID radiator was not the first approach considered. Believing that the DELPHI RICH group was successfully using an axial oil-less turbocompressor to circulate C_5F_{12} we initially began to study circulation using a Paxton RU80 automotive supercharger, belt- driven by an electric motor (Figs. 2.30 & 2.31). The device gave us months of grief. Drive belts frequently broke with the turbine turning at very high speeds (up to 13000 rpm) and the pressure rise could barely be controlled by a parallel 6" bypass with a butterfly valve. Around 90% of the total flow was directed around the bypass, resulting in progressive heating of the gas stream, which had to be cooled by a water heat exchanger located in a buffer tank.

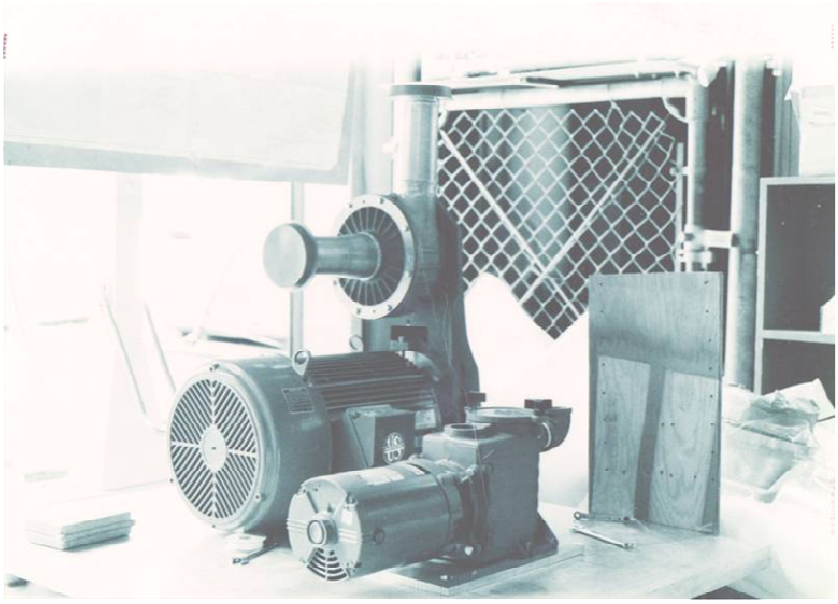

Fig. 2.30. Sepia of Paxton RU80 supercharger (horizontal input, tangential exit), drive motor & belt housing (behind). The pump alongside was for water cooling the gas, which was heated by repeated passages through the by-pass.

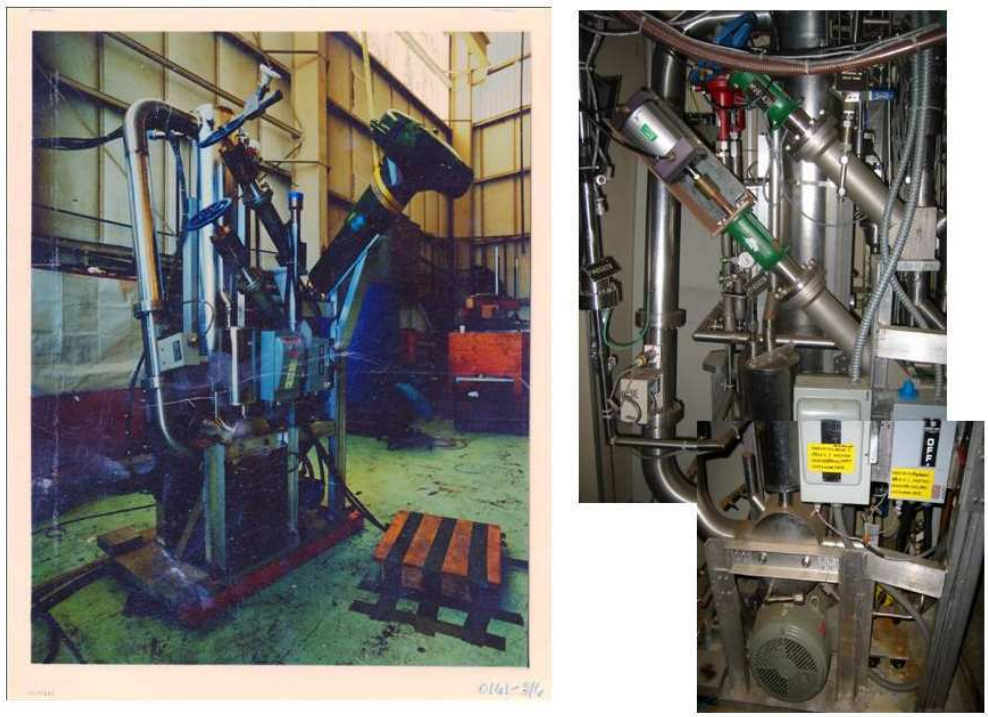

Fig. 2.31. Two views of the Paxton RU80 supercharger assembly: Left - the high flow bypass with high Cv butterfly valve; Centre rear - 300 litre aspiration buffer tank; Centre above electric motor - the water cooled output buffer tank

Start up and shutdown sequences were also problematic, as at that time we were unfamiliar with the developing technology of variable frequency motor speed controllers coupled to Proportional, Integral and Derivative (PID) controllers now extensively used, for example, in LHC experiment cooling systems. We employed a rather crude 'soft start' motor controller and started and shut down with the bypass butterfly valve fully open. After initial tests with air we made further studies with Freon 13B1 ($CBrF_3$), left over from the SLAC LASS threshold Cherenkov detector. Dramatic heating around the bypass tubing and repeated heat-related failures of the butterfly valve electronics eventually led us to abandon this approach in favour of that of Fig 2.27.

The SLD end-cap CRID detectors [41] used gaseous C_4F_{10}, and as in the case of the Barrel CRID, circulation was thermodynamic (figs 2.32 & 2.33), using a condenser tank operating around -2ºC (where the C_4F_{10} vapour

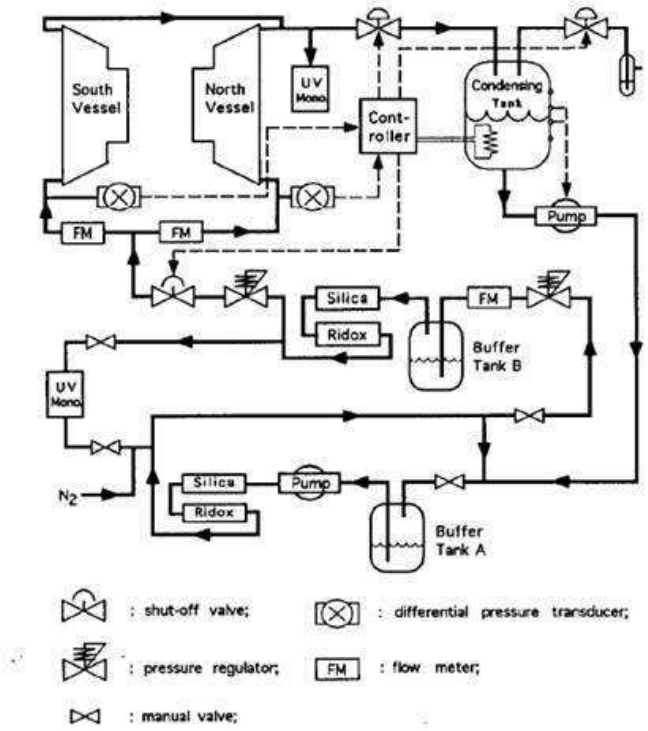

Fig. 2.32. The SLD End-cap CRID C_4F_{10} radiator recirculation system- schematic

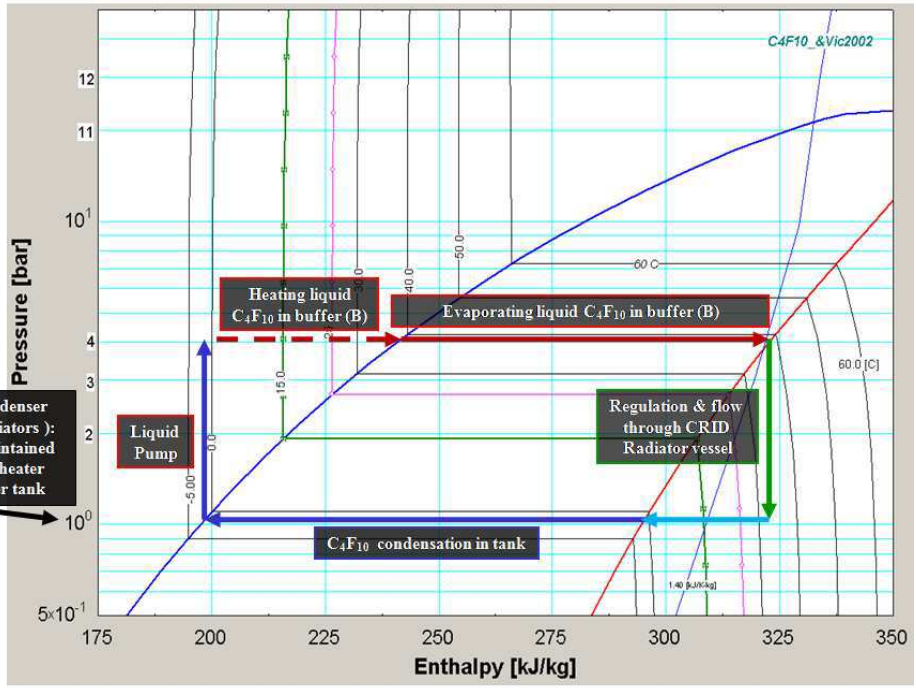

Fig. 2.33. The SLD End-cap CRID C_4F_{10} radiator recirculation system- thermodynamics

pressure is around $1bar_{abs}$) to define the radiator vessel pressures. The condenser tank was cooled with a standard R134A freezer circuit. Accurate control of the condenser tank (and radiator vessel) pressure (to around 0.2 Torr) was handled via immersed heaters in the C_4F_{10} liquid controlled in response to variations in the sensed tank pressure. Typical flow rates were quite low, around 2.5 l/min per end cap, giving a volume change every 18 hours. The condenser headspace could be briefly 'burped' from time to time to vent ingressed air, but this resulted in loss of some C_4F_{10}. Unlike the barrel radiator recirculator, this warmer-operating system was obliged to continuously pump the circulating SFC fluid through O_2 ('Ridox'® activated copper[11]) and H_2O (silica gel[12]) filtering devices, using gear pumps.The filtration through Tank A was continuous, with a small flow extracted for evaporation in Tank B. By contrast, the filtration system of the barrel recirculator - with its much lower condenser temperature and more efficient venting of incondensibles - could be operated periodically in a parasitic loop (fig 2.28).

Figure 2.34 illustrates the principal components affecting differential pressures in the barrel CRID radiator system.

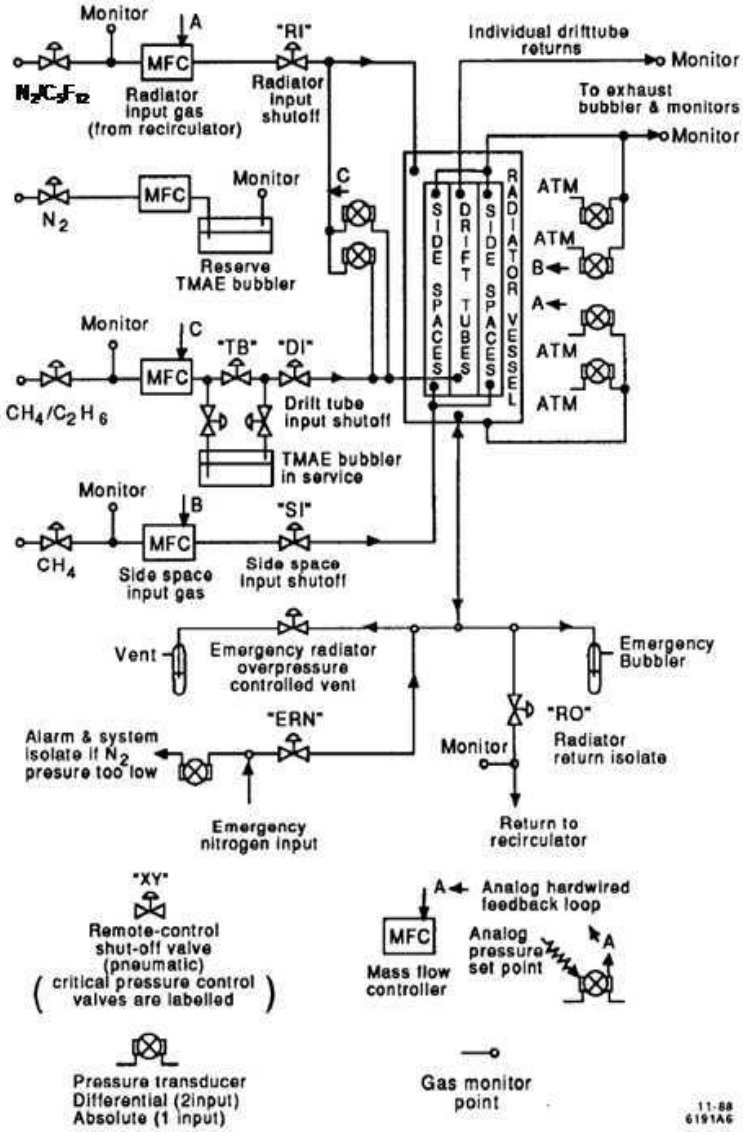

Fig 2.34 Principal components affecting differential pressures in the barrel CRID radiator system.

[11] Ridox Q5 reactant. Engelhard Co. Elyria, OH44035, USA
[12] Sorabead ws: Costal Chemical Co. Pasadena TX 77503, USA

To minimize stress on the fragile CRID TPCs the differential pressure across the quartz windows was controlled by a triple-layered safety system [42] powered from an uninterruptable power supply (UPS):

- In normal operation, with analog feedback from sensitive pressure transducers[13] the gas delivery mass flow controllers (MFCs[14]) maintained[15] the correct differential pressure by analog variation of the flow of the input gases. Redundant pairs of pressure sensors measured the differential pressure between the drift tube common supply manifold and the radiator vessel, and between the radiator vessel and the external atmospheric pressure;
- Outside the normal operating bands, signals from pressure transducers were used in a custom processor, containing a FPGA[16] programmed as a finite state machine, to sequentially open or close a series of input flow and overpressure or underpressure relief valves, based on a comparison of sensed pressure readings and stored reaction thresholds;
- In the event of failure of both electronic systems, a bidirectional passive pressure relief bubbler allowed excess gas to leave the radiator vessel in the event of an overpressure or to admit air in the event of an underpressure.

The normal operating condition was one in which the pressure in the TPCs was ≤ 1 mbar higher than the radiator vessel pressure, which was itself ≤ 1 mbar higher than atmospheric pressure. Unlike in the DELPHI RICH there was no absolute radiator pressure reference, so refractive index could vary with atmospheric pressure. Figure 2.35 shows the safety system reaction philosophy with the action thresholds. Fig 2.36 illustrates the reaction matrix in its full 2-dimensional implementation, receiving stimuli and giving responses to variations in differential pressure between the TPCs and radiator vessel, and between the radiator and atmosphere. The valve nomenclatures correspond to those of fig 2.34. In addition to the radiator and TMAE-laden drift gas delivery systems a third system was used to purge the 'side spaces' of the TPCs. The side walls of the drift tubes were of a two layer construction with a purge space between the layers, which was continuously purged with methane (CH_4), supplied by a MFC. Although leak communication between the highly electronegative radiator gas and the TMAE-laden UV-absorbing drift gas through the two series glue joints was expected to be minimal, the sidewall exhaust gas was regularly monitored for evidence of leakage in either direction. The robust nature of the side spaces (width < 1cm) meant that it was not necessary to relate their pressure to the radiator vessel pressure with a resonse matrix in the same way as the main TPC gas circuits which acted on the full quartz surface area – a reference to atmospheric pressure through a bubbler was sufficient protection.

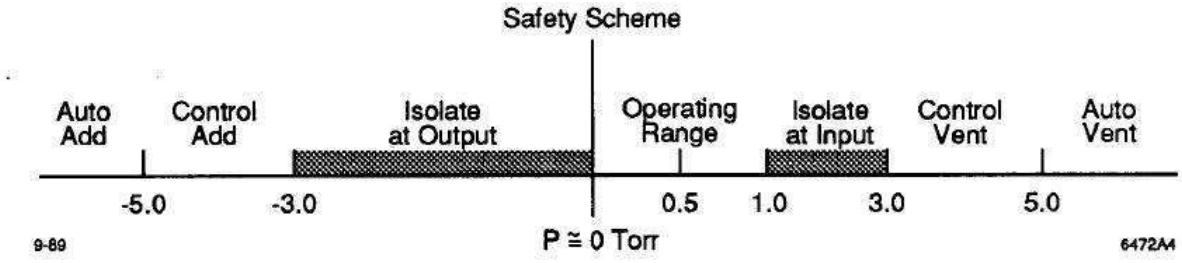

Fig. 2.35. SLD barrel CRID pressure safety system reaction philosophy and action thresholds

[13] MKS Model 262 Capacitance Manometer ± 10 Torr full scale – capable of functioning in the 0.6T solenoidal field.
[14] Model 258B, MKS Inc., Burlington, MA 01803, USA
[15] Via MKS Model 260 PID controller
[16] Altera EP1800

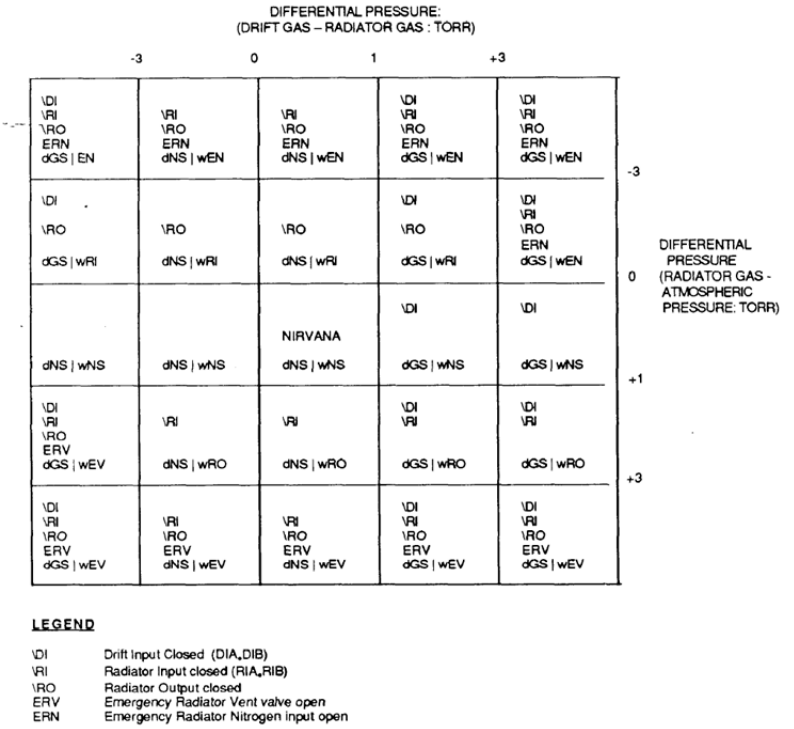

Figure 2.36. SLD barrel CRID gas pressure safety system response matrix

The barrel CRID C_6F_{14} liquid radiator system is shown in Fig. 2.37. The system used only gravity to move the

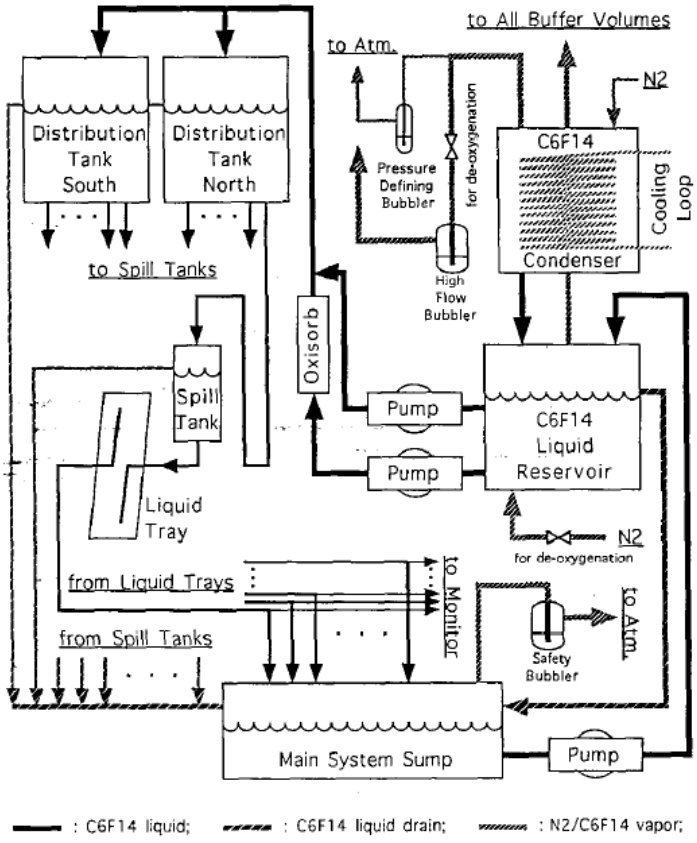

Fig 2.37. The barrel CRID C_6F_{14} liquid radiator system.

liquid through quartz-windowed radiator trays. C_6F_{14} stored in a reservoir tank was elevated by gear pump through Oxisorb filters to a pair of distribution tanks located above the CRID at the ends of the SLD detector. From these distribution tanks liquid C_6F_{14} cascaded under gravity to spill tanks (overflow devices), most of which fed only a single tray by gravity. The pressure heads in the liquid trays were defined and limited by the liquid levels in the corresponding spill tanks. The liquid from the trays and the spill tanks drained into to a lower collection sump from which it was elevated once more to the main reservoir. A safety bubbler on the sump protected the quartz windows on the liquid trays from overpressure.

C_6F_{14} liquid was initially deoxygenated by bubbling boiloff N_2 through it. This reduced the O_2 concentration of 250 l of liquid from an initial level of 133000 ppm to ~20 ppm in around 24 hours. At this point N_2 bubbling was stopped and normal circulation through Oxisorb commenced.

The radiator trays, reservoirs and all tubing were filled with N_2 before startup. This N_2, together with that used to purge the liquid in the reservoir was allowed to escape to atmosphere through a vertical condenser which recondensed any entrained C_6F_{14} to reduce the loss.

The SLD radiator and drift gas systems were equipped with an extensive series of monitor devices. Figure 2.38 illustrates the schematic of one of the three monitor racks (1 barrel + 2 end cap).

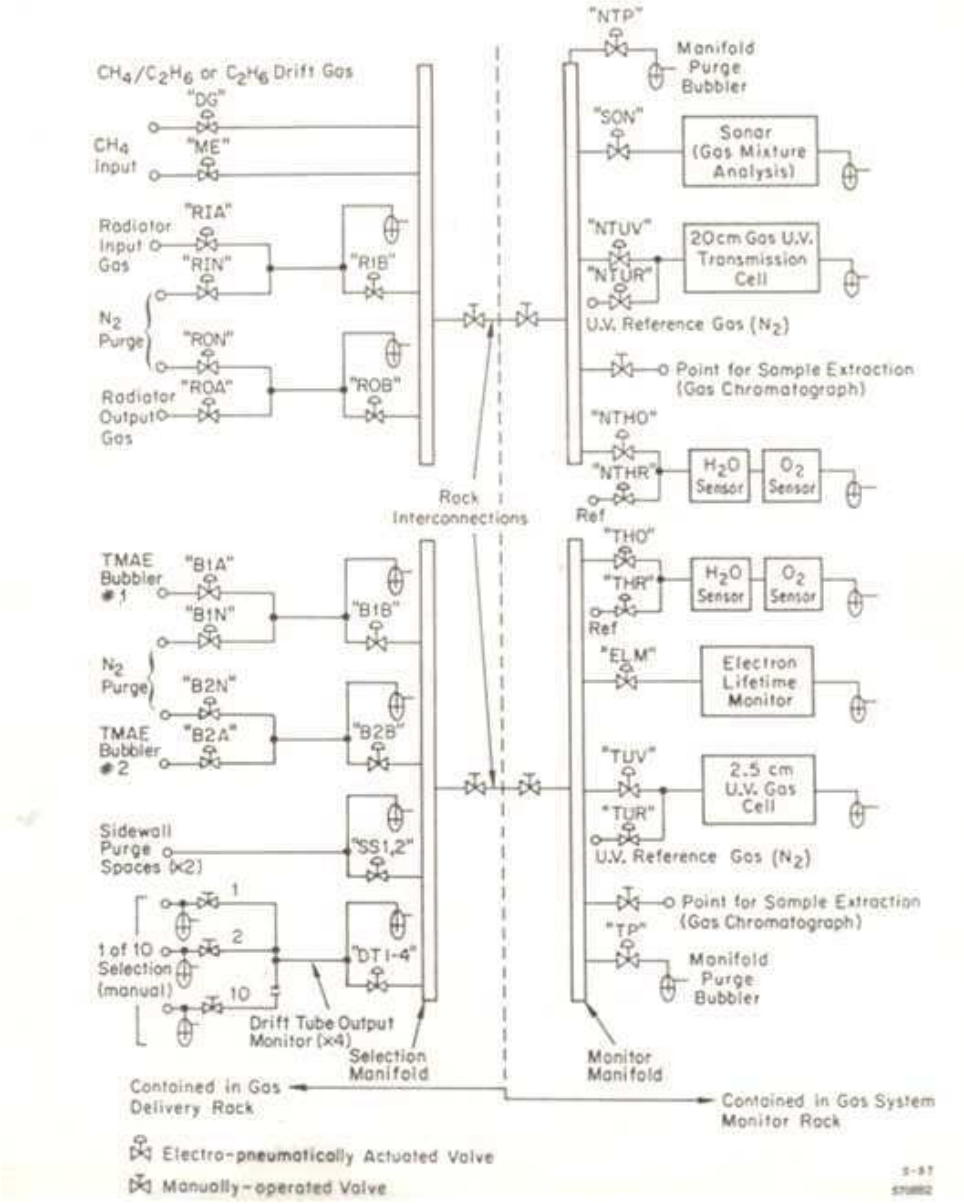

Figure 2.38 SLD gas systems monitor rack (1 of 3)

The gas monitoring was divided into two separated zones by necessity: electronegative radiator gas streams could not be allowed to mix with TMAE laden gas streams. Also since the TMAE was much more reactive than the fluorocarbon radiator gas component, all stream selection valves in the 'TMAE' monitoring section (the lower half of Fig 2.38) were of all stainless steel construction with welded bellows seals and stainless steel stem tips. In the 'NON-TMAE' section (the upper half of Fig. 2.38) valve stems could be of Kel-F elastomer. Drift gases were also tested in this section before passing through the TMAE bubblers.

Stream selection was automated and regular: a FPGA[17] programmed as a finite state machine selected one stream at a time in the TMAE or NON-TMAE sections to be sent to monitoring instruments. Purging of the stream selection and monitor instruments manifolds with N_2 gas interleaved measurements. UV gas cell and O_2[18], H_2O[19] monitoring instruments could be baselined with N_2 reference gas as necessary. All pneumatic valves were piloted directly from TTL open-collector logic using miniature solenoid valves.[20]

The UV transmission cells of the TMAE and NON-TMAE sections were mounted in tandem on a N_2-purged UV monochromator[21] illuminated with light from a deuterium lamp[22] (Fig. 2.39). Both cells were equipped CaF_2 windows, and were preceeded by a CaF_2 beam splitter plate for lamp intensity normalization. Both the transmission and reference arms used PMTs[23] with wavelength shifted windows for UV sensitivity. Clearly when one cell was in use the other had to be under N_2 purge; this was sequenced by the FPGA finite state machine.

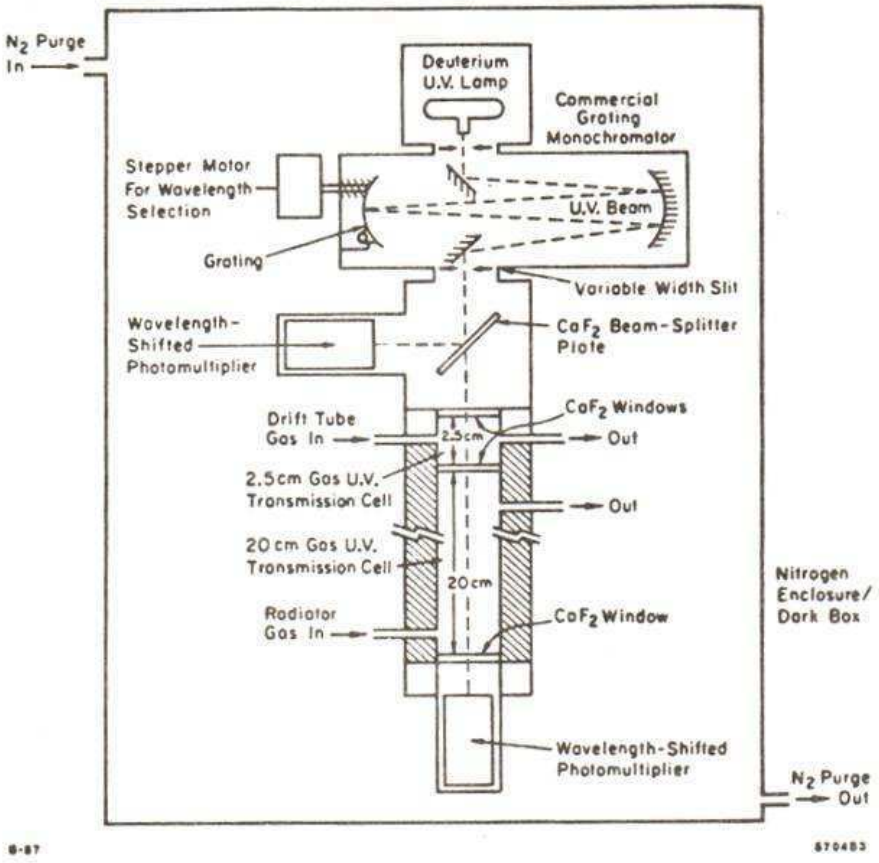

Fig 2.39: the tandem UV cell arrangement of the SLD gas monitoring system.

It was found that the 2.5cm UV cell for TMAE-laden gases was quite well matched to the expected absorption length at the TMAE bubbler operating temperature of around 40°C. However a longer cell than the 20cm foreseen for the fluorocarbon monitoring UV cell would have given higher precision (unlike the DELPHI RICH UV cells, these cells at

[17] ALTERA EP1800
[18] Trace Oxygen Analyzer (disposable fuel cell), Teledyne Analytical Instruments, City of Industry, CA, USA
[19] System 5 Hygrometer, Panametrics Inc., Waltham, MA, USA
[20] Honeywell/Skinner K3P2LO; 0.5 Watts (100mA @ 5VDC), 8 bar compressed air switching
[21] 77250 Monochromator, Oriel Corp., Stratford, CT, USA
[22] L879-01, Hamamatsu Photonics, Hamamatsu 430, Japan
[23] RCA Quanticon C31000N

SLD were of fixed length, requiring N_2 normalization for the transparency measurements). Additional UV monochromator/cells were later installed in the recirculation plant parallel liquid purification loops (Figs 2.28 & 2.37) to monitor the radiator fluids in liquid phases for higher precision.

The NON-TMAE section of the monitor rack shown in Fig. 2.38 also contained an ultrasonic cell for analysis of the gas radiator mixture by speed of sound measurement at known temperature at atmospheric pressure [43]. This cell was an adjunct to the in-situ radiator monitoring system discussed in section 3.2.

3 Ultrasonic Cherenkov radiator gas analysis

3.1 Introduction: sound velocity in gases

The velocity of sound, V_s, in a pure gas at temperature absolute T (Kelvin) is given by

$$V_S = \sqrt{\left[\frac{RT}{m}\left(f + \frac{gR}{C_V}\right)\right]} \tag{3.1}$$

where

$$g = \left[\frac{V}{R}\left(\frac{\partial P}{\partial T}\right)_V\right]^2 \tag{3.2}$$

and

$$f = -\frac{V^2}{RT}\left(\frac{\partial P}{\partial V}\right)_T \tag{3.3}$$

R is the universal gas constant (8.314 $JK^{-1}mol^{-1}$), m is the molar mass in kg, C_v is the specific heat at constant volume ($JK^{-1}mol^{-1}$), P is the pressure (Nm^{-2}) and V is the molar volume (m^3).

Taking an ideal gas assumption for the equation of state (EOS) of one mole of gas, viz;

$$PV = RT \tag{3.4}$$

and taking partial derivatives, we arrive at the familiar form ;

$$V_S = \sqrt{\left[\frac{\gamma RT}{m}\right]} \tag{3.5}$$

where $\gamma = C_p/C_v$ and use has been made of the identity linking the molar specific heats at constant pressure and volume:

$$C_p = C_v + R \tag{3.6}$$

Since it neglects both molecular size and intermolecular attractions, the ideal gas law is most accurate for monatomic gases – the noble gases (He, Ne, Ar, Kr and Xe) at low densities, which includes the range of pressure and temperature conditions seen in Cherenkov radiators. The simple diatomic species (H_2, N_2, O_2…) approximate ideal gas behavior over familiar conditions. However as gas molecules become larger, molecular size, intermolecular attractions and more complex internal oscillation modes cause their behavior to deviate more from that of an ideal gas, requiring more sophisticated descriptions, such as the Van der Waals EOS.

$$\left(P + \frac{a}{V^2}\right)(V - b) = RT \tag{3.7}$$

where a is a measure of the attractive force between the molecules and b is due to their finite volume and general incompressibility. For any pure gas a and b can be expressed in terms of the critical temperature T_c and pressure P_c, T_c being the temperature above which the material exists only in gaseous form, whatever the pressure:

$$a = \frac{27R^2\,T_c^2}{64P_c},\ b = \frac{RT_c}{8P_c} \tag{3.8}$$

$$V_S = \sqrt{\frac{RT}{m}\,\frac{PV}{RT}\left(\left(1 - \frac{a}{PV^2} + \frac{b}{V}\right) + \frac{R}{C_V}\left(1 + \frac{2b}{V}\right)\right)} \tag{3.9}$$

Figure 3.1 illustrates the variation of sound velocity *vs.* molecular weight for a number of common gases and fluoroalkanes currently in use as Cherenkov radiators.

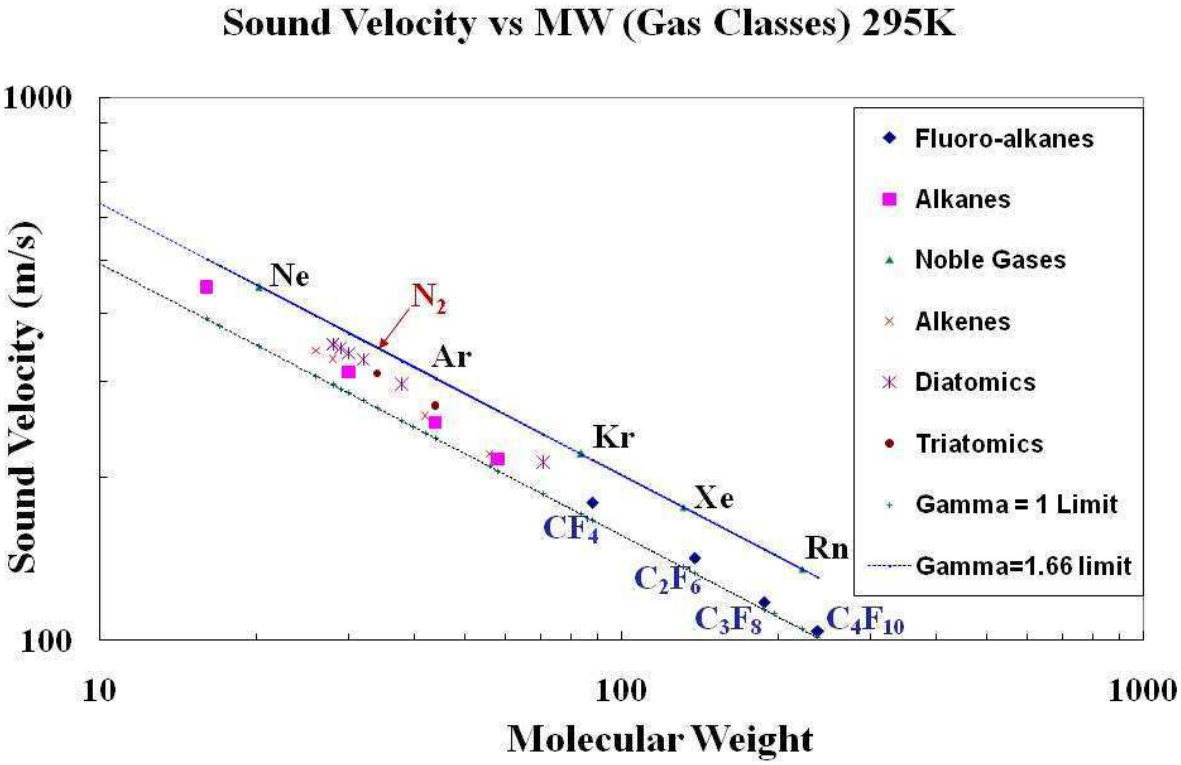

Figure 3.1 Sound velocity vs. molecular weight for various common gases and fluoroalkanes

It can be seen that all gases are constrained in velocity/MW space by the upper and lower bounds on the ratio of specific heats Cp/Cv; 1.66 and 1. The expected index is $m^{-0.5}$ eq. (3.5) for gases exhibiting ideal behavior - approximated by the noble gases (including helium, not shown on the plot) and the diatomics. However as the gas molecules get more complex they tend toward the unity Cp/Cv limit with a steepening velocity/MW index; visible in Fig. 3.1 for the alkanes and their fluoroalkane analogs, which have indices approximating -0.55 and -0.56 respectively.

A number of more complex EOS have been developed to model the behavior of specific vapours or groups of vapours to high precision. These include the Benedict-Webb-Rubin (BWR) and more recently the PC-SAFT[24] EOS, both of which have been used in this context.

In the BWR EOC (in common other EOS models of real gases) it is conventional to define a "compressibility factor", Z;

$$Z = \frac{PV}{RT} \tag{3.10}$$

where Z = 1 is the definition of an ideal gas. The BWR EOS extends the definition of compressibility in terms of dimensionless "reduced" temperatures, pressures and molar volumes T_r,P_r,& V_r;

$$Z(T_r, P_r) = \frac{P_r V_r}{T_r} \tag{3.11}$$

where

$$T_r = \frac{T}{T_c}, \quad P_r = \frac{P}{P_c} \text{ and } \quad V_r = \frac{P_c V}{R T_c}$$

[24] Perturbed Chain-Statistical Associating Fluid Theory – see also Appendix 1.

and T_c and P_c are the critical temperature and pressure respectively. The right hand side of eq. (3.11) may be expanded in terms of a series of empirical constants. In [43] these constants were used to predict sound velocities in pure hydrocarbons and mixtures of hydrocarbons (CH_4, C_2H_6, C_4H_{10}) as at that time the drift gas for the imaging TPCs of the SLD CRID had not been decided upon (it subsequently stabilized for the barrel on the choice of C_2H_6 and for the end cap CRID to 85%C_2H_6 /15%CO_2 , a mixture not amenable to ultrasonic analysis due to the high absorption of CO_2 around 50kHz). Drift gas extraction (prior to TMAE addition via bubble-through) was anticipated as the electron drift velocity was expected to be strongly dependent on mixture ratio.

An EOS of the form of eq. 3.11 is said to be "generalized" since it is applicable to almost any gas whose critical temperature and pressure are known. Generalized EOS are based on the "principle of corresponding states" wherein all gases, measured at the same reduced temperature and pressure deviate from ideal gas behaviour to the same degree and have roughly equal compressibility factors. This principle has found wide application and is reasonably accurate. It has been further improved however with the introduction of an "acentric" factor w:

$$Z(T_r, P_r) = Z^{(0)} + wZ^{(1)} \tag{3.12}$$

Where $Z^{(0)}$ is the compressibility factor for an ideal gas (from example a noble gas) and $Z^{(1)}$ is the deviation of the real gas from the simple gas approximation. $Z^{(0)}$ and $Z^{(1)}$ are similarly tabulated for a wide variety of gases. To facilitate sound velocity calculations using the BWR EOS, [43] used the formulation

$$V_s = \sqrt{\frac{C_p}{C_v}\frac{ZRT}{m}\left(1 - \frac{P_r}{Z}\left(\frac{\delta Z}{\delta P_r}\right)_{T_r}\right)^{-1}} \tag{3.13}$$

where the parameters Z, C_p, C_v and $(\delta Z/\delta P_r)_{Tr}$ were calculated for each gas from its critical temperature, pressure and acentric factor w. Figure (3.2) compares the speed of sound predictions in isobutane (C_4H_{10}) for the Ideal Gas (X), Van der Waals (◊) and BWR (□) EOSs with measurements made at 1 bar_{abs} between 25 and 40°C. It can be seen that the BWR EOS sound velocities predictions for this relatively complex alkane molecule are closest to the measurements made with an ultrasonic device described in section 3.2.

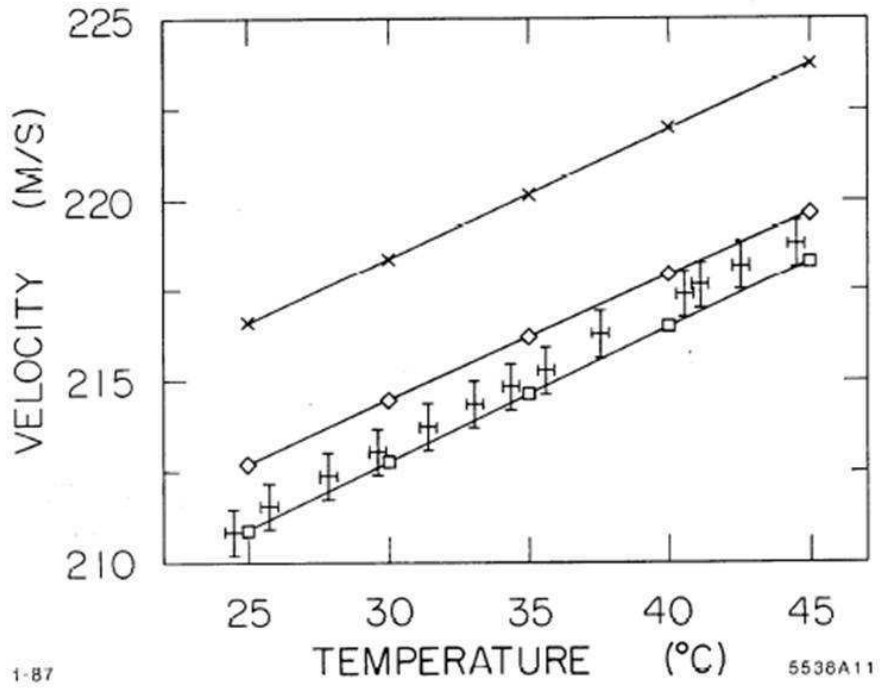

Fig. 3.2.Speed of sound predictions in isobutane (C_4H_{10}) for the Ideal Gas (X), Van der Waals (◊) and BWR (□) EOSs with measurements made at 1 bar_{abs} between 25 and 40°C (after [43]).

Unfortunately at the time (mid 1980's) the Van der Waals and BWR empirical constants for the fluorocarbon vapours were largely unknown, and our guess uses of constants for CFC freons or (better) hydrocarbons of similar geometry to predict sound velocities in C_5F_{12} vapour were less than successful in reconciling with our measurements, as illustrated in Fig. 3.3 [43]. In this situation the measurements had to be taken as definitive.

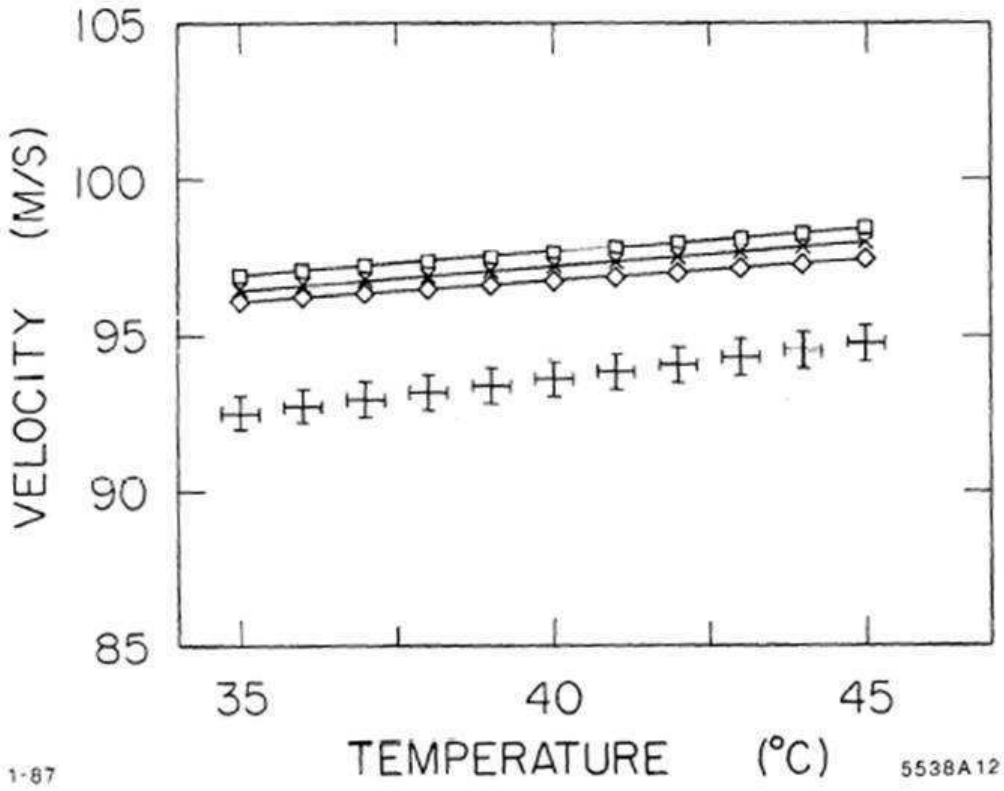

Fig. 3.3. Speed of sound predictions in perfluoro-pentane (C_5F_{12}) vapour for the Ideal Gas (X), Van der Waals (◊) and BWR (□)EOSs with measurements at 1 bar_{abs} between 35 and 45°C (after [43]).

To predict the speed of sound V_m in a mixture of gases the simplest approximation is perhaps to assume that the velocity is proportional to the concentration by weight of the components:

$$V_m = \frac{\sum_i X_i \ \rho_i V_i}{\sum_i X_i \ \rho_i} \tag{3.14}$$

where X_i, ρ_i and V_i are the fractional concentration, density and the sound velocity (tabulated or measured) in the pure i^{th} component respectively. This formula has the advantage of simplicity and freedom from dependence on tabulated thermodynamic data. The formula is accurate (~0.1%) for sufficiently ideal gas mixtures, for example air (considering the three principal components N_2, O_2 and Ar), but is much less accurate (error ~ l-3%) in predicting the velocities in non-ideal hydrocarbon or fluorocarbon mixtures.

It is possible also to construct a mixture velocity formula from more rigorous considerations and using tabulations of specific heat data where these can be found. In this way the ratio of specific heats for the mixtures can be expressed as:

$$\gamma_m = \frac{C_{P_m}}{C_{V_m}} = \frac{\sum_i X_i \; C_{P_i}}{\sum_i X_i \; C_{V_i}} \tag{3.15}$$

Where, to reasonable approximation in the absence of detailed C_v data, use can be made of the identity (based on eq. (3.6));

$$\gamma_m = 1 + \frac{R}{C_{P_m} - R} \tag{3.16}$$

The results for pure gases in [43] suggested that more accurate velocity predictions can be achieved with the use of realistic gas EOS in which the sound velocity in a pure gas could be predicted from its critical temperature and pressure, under both the VDW or BWR EOS. The Lee and Kesler three-parameter correlation scheme, in which empirical mixing rules determine a "pseudocritical" temperature and pressure and "pseudoacentric" factor was invoked in [43] for mixtures of light hydrocarbons of potential interest to the SLD CRID.

In this scheme the critical volume, V_{Ci}, of the ith component were given by

$$V_{Ci} = Z_{Ci}\, RT_{Ci} / P_{Ci} \tag{3.17}$$

where
$$Z_{Ci} = 0.2905 - 0.085 w_i \tag{3.18}$$

The first numeric factor in eq (3.18) represents the compressibility factor of an ideal gas at its critical point, while the second is the average empirical compressibility deviation for the light hydrocarbons.

The pseudo-critical volume of the gas mixture, V_{Cm}, is given by a molar concentration weighted summation over all component combinations:

$$V_{C_m} = \tfrac{1}{8} \sum_{i=1}^{n} \cdot \sum_{j=1}^{n} X_i \, X_j \left(V_{C_i}^{1/3} + V_{C_j}^{1/3} \right)^3 \tag{3.19}$$

while the three correlation parameters are defined by;

$$T_{C_m} = \frac{1}{8\, V_{C_m}} \sum_{i=1}^{n} \cdot \sum_{j=1}^{n} X_i \, X_j \left(V_{C_i}^{1/3} + V_{C_j}^{1/3} \right)^3 \left(T_{C_i} \, T_{C_j} \right)^{1/3} \tag{3.20}$$

$$w_m = \sum_{i=1}^{n} X_i \, w_i$$

$$P_{Cm} = (0.2905 - 0.085 w_m) RTC_m / V_{Cm}$$

The pseudocritical temperature and pressure can be applied to the BWR EOS (eq. (3.11)) and to the Van der Waals EOS (eq. (3.7)) using eq. (3.8).

Figure 3.4 compares the sound velocity measurements over the full dynamic range of methane (CH_4) in isobutane (C_4H_{10}) – a combination of interest as a possible drift gas for the SLD barrel CRID - with the almost identical predictions of the BWR and Van der Waals EOS (solid line) and density weighting (dashed line). The agreement of the BWR and Van der Waals predictions was unsurprising since they used the abundant thermodynamic parameters that existed for hydrocarbons. Figure 3.5 compares the sound velocity measurements over the full dynamic range of perfluoro-pentane (C_5F_{12}) in nitrogen (N_2) that could be encountered in the SLD barrel CRID radiator with the predictions of the BWR and Van der Waals EOS and density weighting. The lack of agreement with the measurements was unsurprising due to the lack of thermodynamic parameterizations for SFCs during the mid 1980s. This situation has considerably improved in recent years for the BWR EOS, while more recently the PC-SAFT EOS has been found to be very precise, and is now used for SFC mixture predictions in the current context of ATLAS evaporative cooling.

.

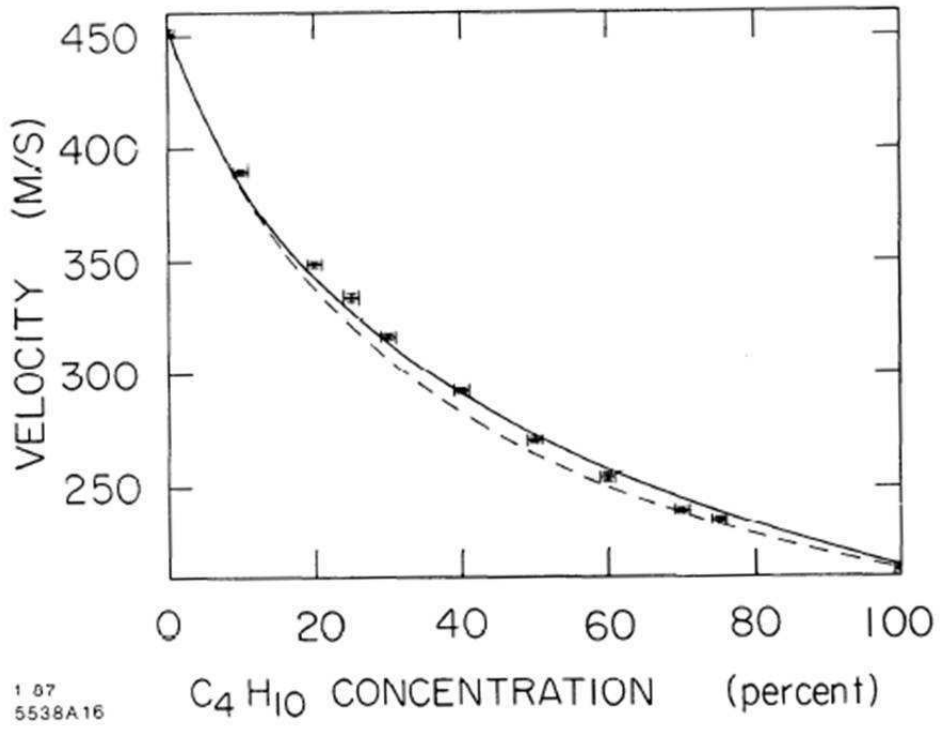

Fig. 3.4. Comparison of sound velocity measurements at 30ºC in methane(CH_4)/isobutane(C_4H_{10}) with predictions of the BWR & Van der Waals EOS (solid line) and density weighting (dashed line) (after [43]).

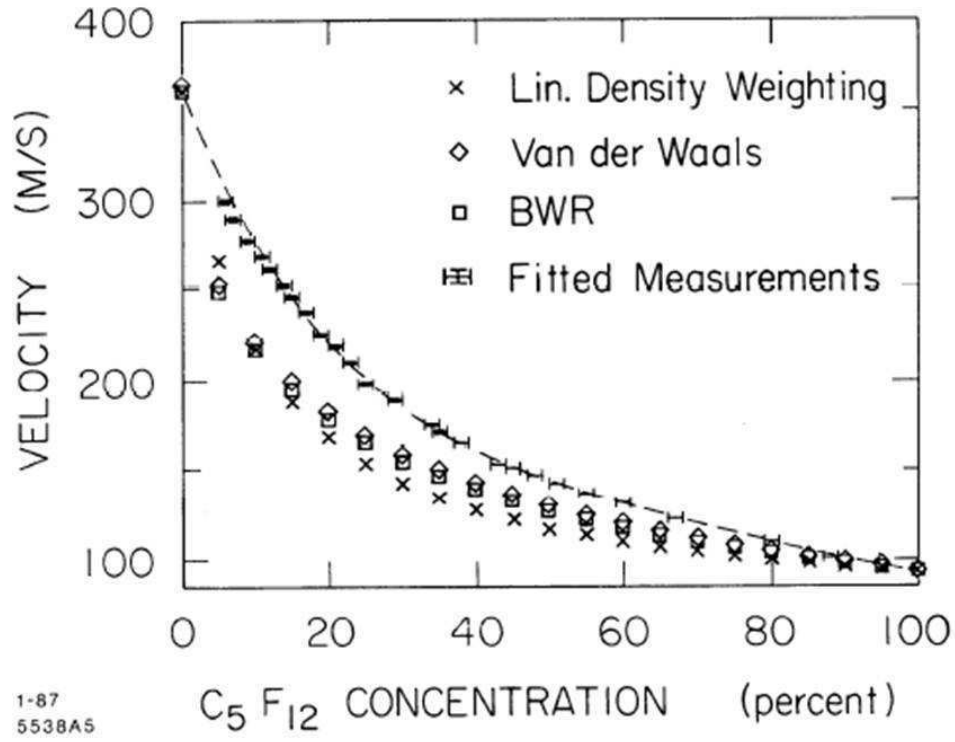

Fig. 3.5. Comparison of sound velocity measurements at 41ºC in perfluoro-pentane(C_5F_{12})/nitrogen(N_2) with predictions of the BWR EOS (˙) & Van der Waals(◊) EOS and density weighting (X) (after [43]).

3.2 Ultrasonic gas analysis developments for the SLD barrel CRID radiator

In the SLD CRID - as a rapid, on-line, ring data-independent alternative to the difficult measurement of refractive index via vapour extraction to an interferometer - a network of 6 pairs of ultrasonic transducers was installed at 3 different heights in the barrel radiator vessel using lines of sight existing between the rows of mirrors, as illustrated in Fig. 3.6.

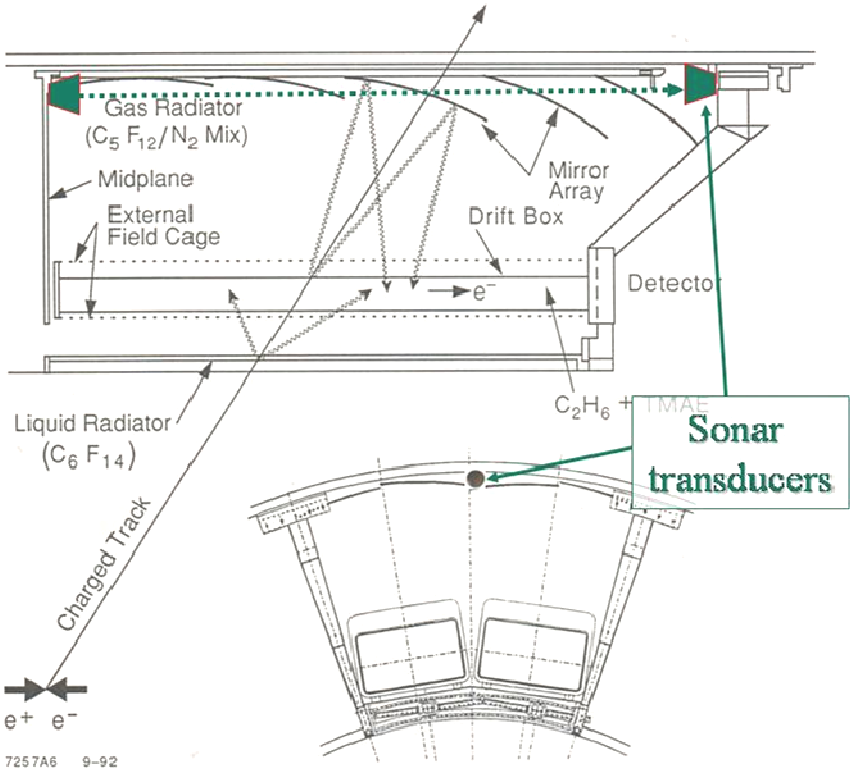

Fig. 3.6. Ultrasonic lines of sight in the SLD barrel gas radiator vessel (one of 6 such pairs)

The system was based on the Polaroid 600 instrument grade 45kHz ultrasonic transducer[25] developed for auto-focus cameras during the early 1980s – a very successful development that also has found use in robotic and production line position sensing applications. We were also very surprised that this transducer could withstand evacuation and pressurization to more than 6 bar_{abs} without loss of repeatability of operation.

Figure 3.7 illustrates the main components of the electrostatic transducer. The rear plate with the spiral groove allows gas to enter and leave from behind the diaphragm, equalizing the pressure and allowing operation over the wide pressure range.

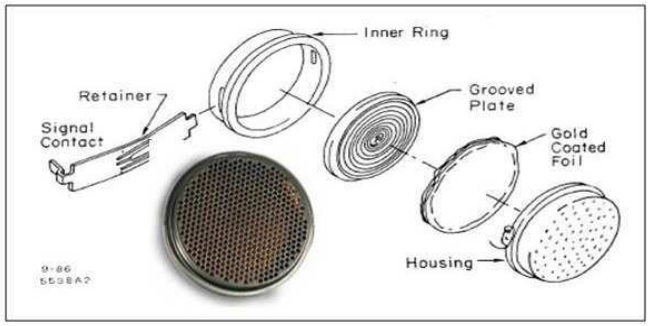

Fig. 3.7. Exploded view of the Polaroid 6000 instrument grade ultrasonic transducer

[25] Now marketed by SensComp, Inc. 36704 Commerce Rd. Livonia, MI 48150 USA http://www.senscomp.com

Figure 3.8 illustrates the frequency range and directionality of the transducer. In the SLD application the directionality was not particularly important since the device was operated in a non-resonant time-of-flight mode with straight-forward detection of the first arriving pulse.

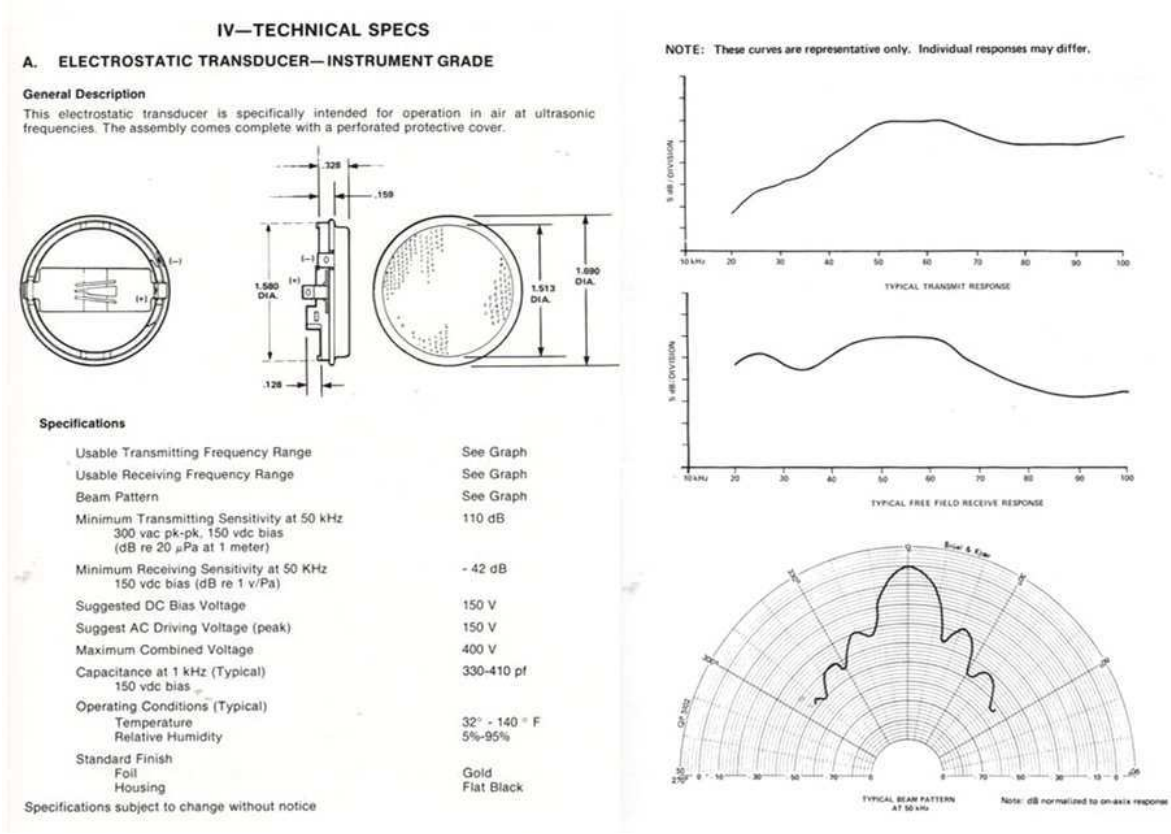

IV—TECHNICAL SPECS

A. ELECTROSTATIC TRANSDUCER—INSTRUMENT GRADE

General Description

This electrostatic transducer is specifically intended for operation in air at ultrasonic frequencies. The assembly comes complete with a perforated protective cover.

Specifications

Usable Transmitting Frequency Range	See Graph
Usable Receiving Frequency Range	See Graph
Beam Pattern	See Graph
Minimum Transmitting Sensitivity at 50 kHz 300 vac pk-pk, 150 vdc bias (dB re 20 μPa at 1 meter)	110 dB
Minimum Receiving Sensitivity at 50 KHz 150 vdc bias (dB re 1 v/Pa)	- 42 dB
Suggested DC Bias Voltage	150 V
Suggest AC Driving Voltage (peak)	150 V
Maximum Combined Voltage	400 V
Capacitance at 1 kHz (Typical) 150 vdc bias	330-410 pf
Operating Conditions (Typical)	
Temperature	32° - 140 ° F
Relative Humidity	5%-95%
Standard Finish	
Foil	Gold
Housing	Flat Black

Specifications subject to change without notice

NOTE: These curves are representative only. Individual responses may differ.

TYPICAL TRANSMIT RESPONSE

TYPICAL FREE FIELD RECEIVE RESPONSE

TYPICAL BEAM PATTERN AT 50 kHz

Fig. 3.8. Frequency range and directional sensitivity of the Polaroid 6000 ultrasonic transducer

The original Polaroid 6000 transducer was purchased as part of an application kit which included identical electronics to that used in the commercialized camera. The transducer was driven with a 'chirp' of 8 sinusoidal pulses of 45kHz sound through a transformer coupling. Since the camera autofocus system relied on acoustic echo timing, the read-out electronics was blanked for a period of 1.5ms starting from the first cycle.

Since it was anticipated in SLD to mount transducers in a complicated volume, echo timing was replaced with line of sight transit time measurement with distinct transmit and receive transducers. This had the advantage of allowing the transmit and receive transducers to be individually biased with DC voltages up to a maximum of ~360V, the high bias being particularly useful in increasing the sensitivity of the receiving transducer for absorptive gases, particularly CH_4.

Local driver and amplifier/discriminator boxes were mounted as close as possible to each transducer pair, and connected via short coaxial cables. The drivers of all transducer pairs were simultaneously sent trains of 8 ECL pulses at 45kHz; bi-polar ECL being chosen to allow long transmission distances of up to 50m from a central multi-channel clock module implemented in CAMAC. Figure 3.9 illustrates the local drive circuit and packaging together with the 8 cycle 'chirp' generated in response to the ECL drive signal.

The capacitor C2 is charged between chirps and provides the energy storage for the chirp duration. The voltage decay superimposed on the square wave chirp (top scope trace in fig. 3.9) allows more energy to be put into the first sound cycle – hopefully the first to cross the receiver threshold - and less to subsequent cycles, helping to reduce amplifier saturation effects.

Figure 3.10 illustrates the sonar timing cycle: synchronous with the emission of the first sound cycle a fast (4MHz) readout clock is started. The clock is stopped by when the threshold of the receiving amplifier/discriminator is crossed and the number of counted pulses and the inter-transducer distance used to calculate the sound velocity. The amplifier/discriminator, shown in Fig. 3.11, was similarly packaged to the driver and connected to the receiving transducer via a short coaxial cable. Analog threshold and bias voltage were sent via a screened multi twisted pair cable and the 'threshold crossed' signal returned as an ECL signal to stop the channel's transit time clock in the central clock module.

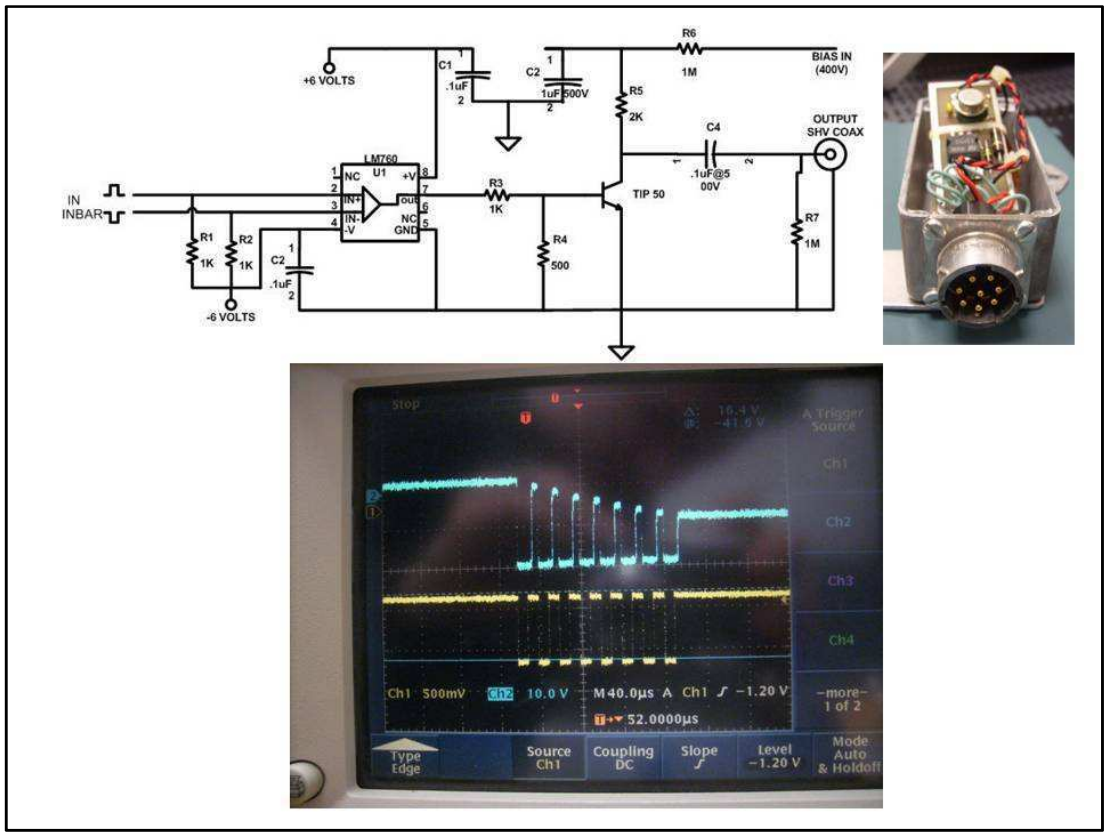

Fig. 3.9. Local ultrasonic drive circuit and packaging.
Driver response (blue trace) to 45kHz ECL pulse train (yellow trace)

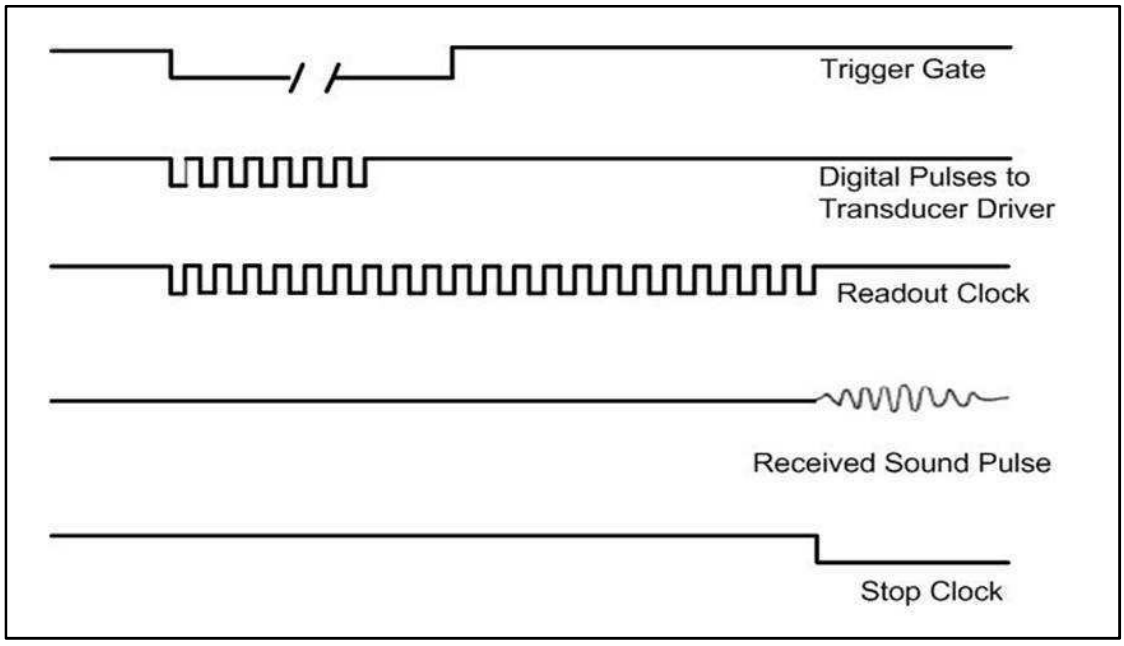

Fig. 3.10. Sonar Timing Diagram (one channel of a multiple channel implementation)

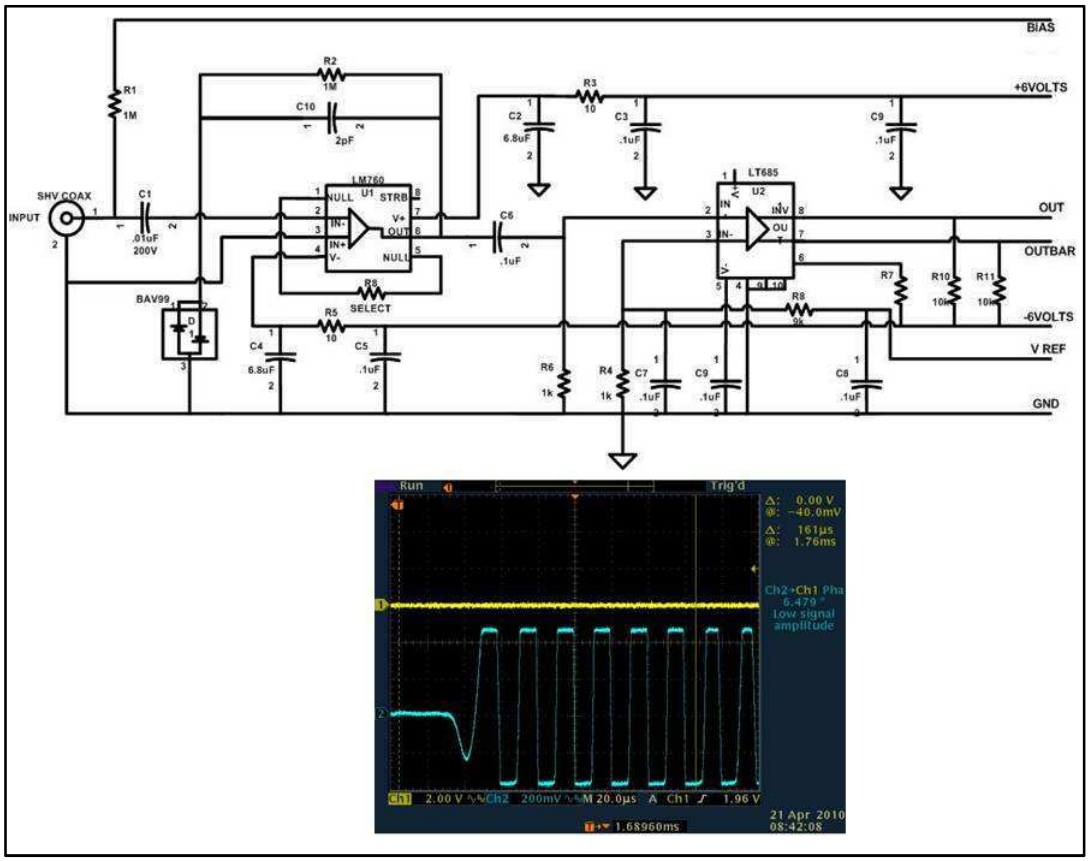

Fig. 3.11 Local amplifier/discriminator schematic with typical pre-comparator amplifier output: receiving transducer at ~80V bias in air at 1 bar_{abs} (blue trace).

The ultrasonic channels installed in the SLD barrel CRID 13m^3 radiator vessel revealed significant stratification effects during the replacement of the N_2 passivation gas with the 70% C_5F_{12}/30%N_2 radiator mix and also later during C_5F_{12} recovery to the storage tank (and refilling the radiator vessel with N_2).

The example in Fig 3.12 illustrates the homogenization in the radiator vessel during replacement of the N_2 passivation gas with the first fill of the 70% C_5F_{12}/30%N_2 during the SLD 'engineering run' of August 1991. The colour highlighting of the plots in the *vignettes* of sound velocity *vs*. elapsed time for the 5 operating sonar pairs (scanned from the engineering run logbooks and now the only CRID radiator documentation surviving from that event) corresponds to the indexing of the ultrasonic channels in the figure.

The vignettes illustrate how the middle and bottom regions of the radiator vessel homogenize within around 8 hours while the upper region requires a further 74 hours (> 15 volume changes at a nominal flow of 40l/min).

In August 1991 the radiator vessel was supplied with gas through four 1½" tubes at the South end and exhausted through six 1½" tubes at the North end. The initial hydrostatics was very efficient at displacing N_2 by the heavy mixture in the lower half of the vessel, but much less so for the upper half, where there was no 'high-up' exhaust pipe for hydrostatically advantageous N_2 expulsion.

Later, during the replacement of the radiator mix with N_2 passivation gas the lower pairs of sonars did not indicate the nominal speed of sound for nitrogen until more than two weeks after the start. The hydrostatics of injecting N_2 at 'middle and low' was inefficient at displacing the much heavier C_5F_{12}/N_2 mixture; N_2 tended to skip over the surface of the cloud of heavy C_5F_{12}/N_2 mixture, only slowly depleting the C_5F_{12} concentration.

Following the 1991 engineering run the entry and exit tubing was reconfigured; two entry tubes and two exhaust tubes being moved from their irrelevant mid positions to new high entry and exhaust points, with additional external valves added to define the flow configuration for a light➔ heavy or heavy➔ light gas replacement.

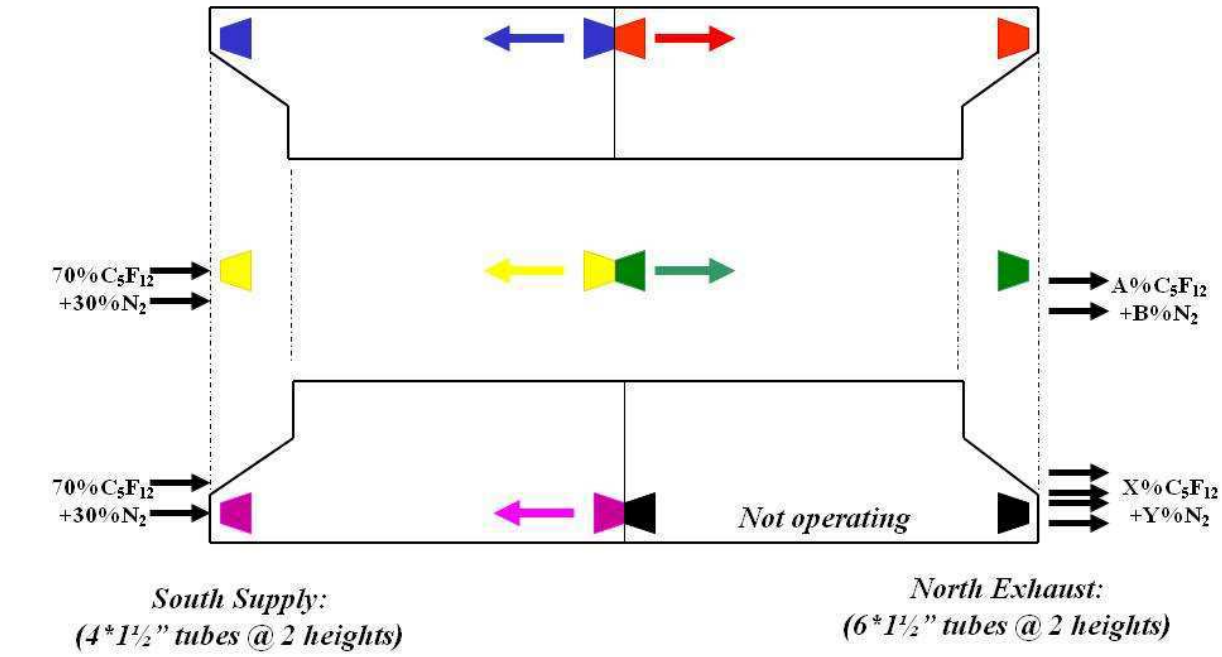

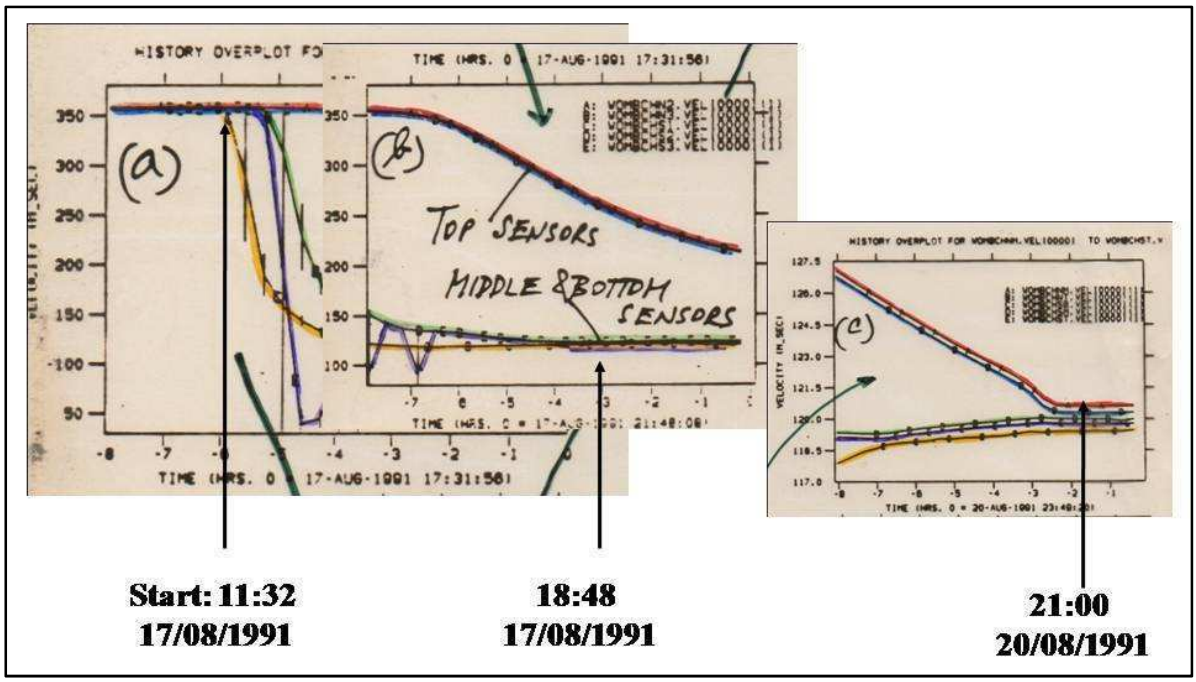

Fig. 3.12. Homogenization of the radiator gas mixture in the SLD barrel CRID during the replacement of the N_2 passivation gas with the active 70% C_5F_{12}/30%N_2 radiator mix during the 1991 SLD-CRID engineering run. The input and output tubing were subsequently reconfigured to reduce these stratification effects.

While the value of the sonar radiator gas analysis became apparent during the SLD engineering run, its potential was exploited further during the operation of the detector as an on-line monitor of refractive index. Starting from a look up table of C_5F_{12}/N_2 mixture ratio *vs.* sound velocity based on the fitted measurements[26] shown in Fig 3.5 [43] and using this in conjunction with the known refractive indices of the two pure components at the operating temperature, n_{C5F12} =

[26] As previously mentioned, the thermodynamic parameters for use with the Van der Waals and Benedict Webb Rubin equations of state for fluorocarbons were incomplete during the 1980s, (by comparison with those of hydrocarbons); we considered our own measurements therefore as definitive for radiator analysis. Today the thermodynamic parameters for fluorocarbons are much better known.

1.00176, n_{N2} = 1.000298, the refractive index of the radiator gas mixture could be determined for any measured mixture ratio;

$$(n)_{rad} = \sum_{i=1}^{2}(n_i * m_i) \tag{3.21}$$

Where m_i is the sonar-measured fractional concentration of i^{th} component in the mixture *(i = 2)*

From this plot of the Cherenkov threshold for each particle species could be determined as a function of the sound velocity measured in the radiator gas, as illustrated in Fig 3.13.

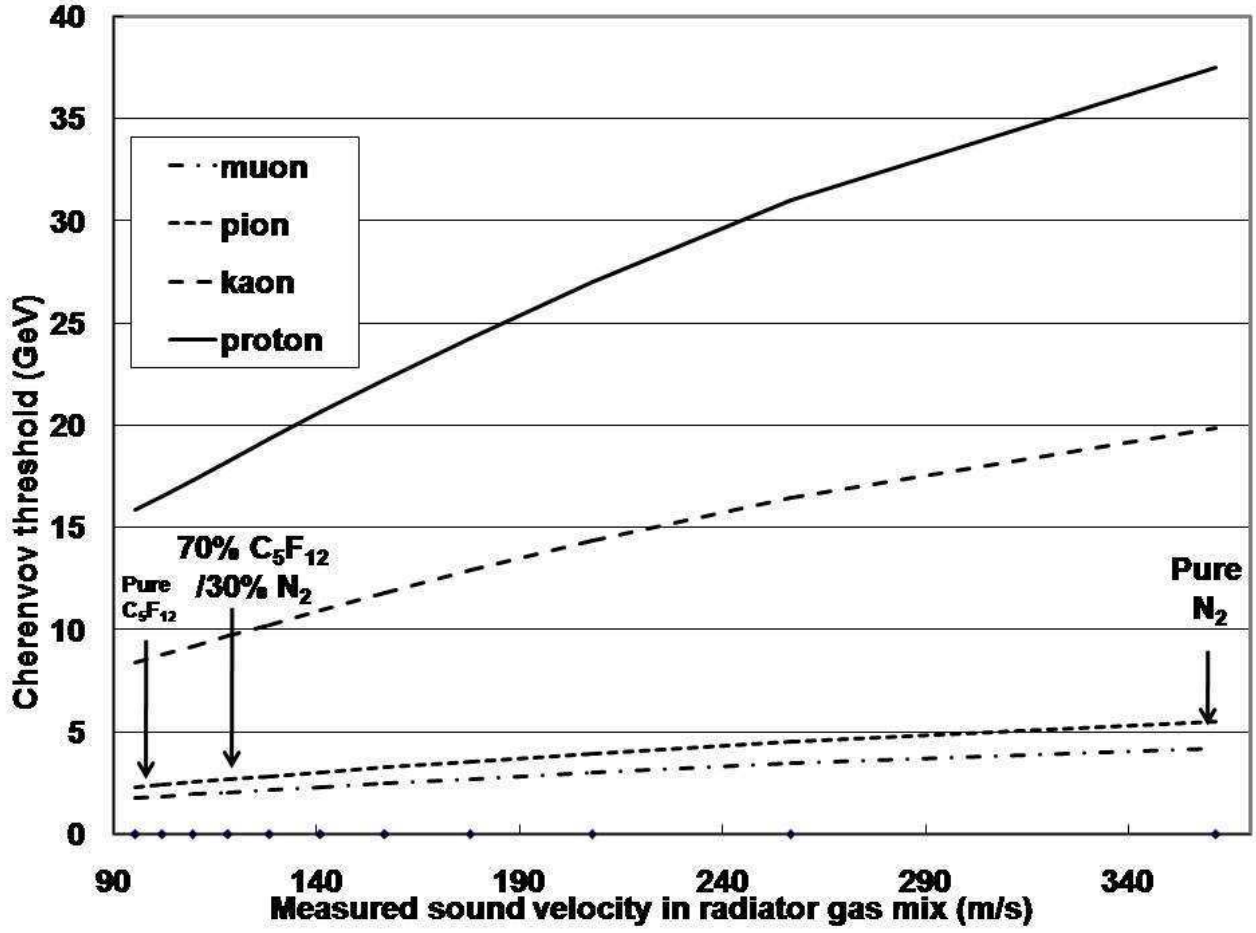

Fig.3.13. Cherenkov thresholds for particle species vs measured sound velocity in a C_5F_{12}/N_2 radiator gas at 40ºC (SLD CRID operating mix = 70%C_5F_{12}/30%N_2).

Sonar radiator analysis was continuously used as an independent check on refractive index. As data taking progressed and confidence with the SLD barrel CRID radiator recirculator and the vessel temperature control system grew, the C_5F_{12} concentration in the radiator gas was progressively increased to beyond 87%C_5F_{12}. Fig 3.14 illustrates the $\beta = 1$ Cherenkov angle comparison [44] over data taking runs in 1995 and 1996 between $\beta = 1$ reconstructed ring data from Z^0 events (□) and predicted angles from the average sonar-deduced refractive index corrected for atmospheric pressure (●).The agreement between the two datasets was encouraging and on this basis it was decided to rely on the sonar to monitor the refractive index during periods of SLC luminosity lacking high statistics in Z^0 events.

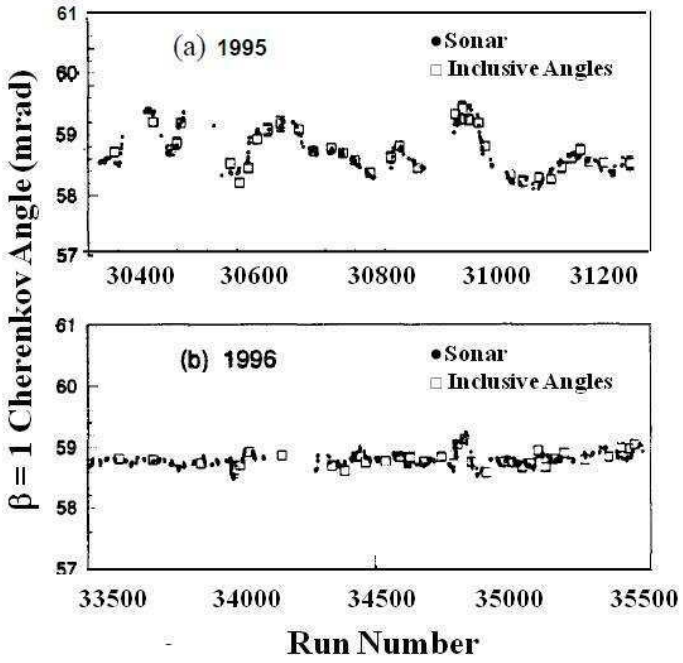

Fig 3.14. β = 1 Cherenkov angle comparison (1995-6 runs) between reconstructed ring data (□) in the SLD barrel CRID and angles from sonar-deduced refractive index corrected for atmospheric pressure(●) – after [44]

Today fluorocarbon thermodynamic data are much better known and new equations of state - for example the PC-SAFT[27] approach based on perturbation theory [APPENDIX 1] - allow much better agreement between theory and experimental measurement in fluorocarbon mixtures and mixtures with certain other non-fluorocarbon gases. This can be of interest in the operation of the current generation of RICH detectors as it is in the context of C_2F_6/C_3F_8 fluorocarbon mixtures foreseen for upgrading the present ATLAS silicon tracker C_3F_8 evaporative coolant are discussed in section 5.2

[27] Perturbed-Chain Statistical Associating Fluid Theory

3.3 Radiator ultrasonic gas analysis in other RICH detectors.

Since its first use for the analysis of the N_2/C_5F_{12} radiator of the SLD barrel CRID [43], as a continuously-sensitive on-line refractive index monitor, all the major RICH detectors, including DELPHI [45], COMPASS [46] and LHCb [47] have employed radiator gas analysis.

In the DELPHI forward RICH detectors a single 50kHz ultrasonic transducer was used with a custom-triggered Polaroid 6500 ranging board [45] to measure the echo delay over a fixed acoustic path length in a vessel into which radiator gas can be extracted. The system was installed in the DELPHI forward RICHs (side A and side C) and ran continuously since 1994. Figure 3.15 illustrates the measurement-based look up table fit of sound velocity *vs* concentration (at 25°C) of N_2 in C_4F_{10} that was used for radiator gas analysis in the DELPHI forward RICH detectors [45].

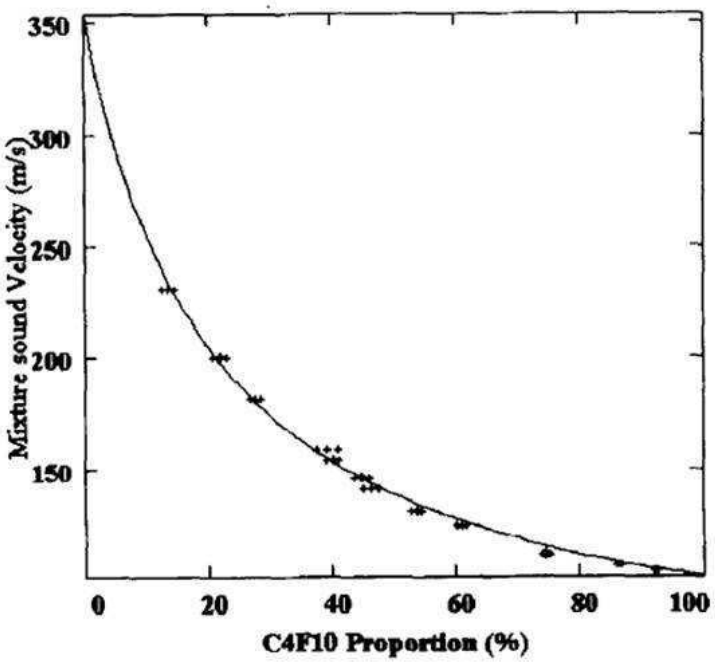

Fig 3.15. Measurement-based look up table fit of sound velocity vs concentration (at 25°C) of N_2 in C_4F_{10} used in the DELPHI forward RICH detectors(after [45]).

In the Compass RICH a similar approach has been used, with a temperature controlled tube and a Polaroid 6500 ranging board with a single transducer [33, 46], aimed the analysis of N_2/C_4F_{10} mixtures that will be encountered in the filling and recovery of C_4F_{10} from the radiator vessel.

In the LHCb RICH detectors a single 50kHz ultrasonic transducer is used with a recycled (DELPHI forward RICH [47]) Polaroid 6500 ranging board to measure the echo delay over a fixed acoustic path length in a vessel into which extracted gas from the RICH-1 and RICH-2 radiators can be directed. A path length of 30cm (60cm round trip) was used with extracted C_4F_{10} gas streams. A calibrated mixture containing 1% N_2 was found to change the measured echo transit time by 30σ [47]. Considerable absorption was noted in CF_4 however (as is common in light triatomic and pentatomic molecules including CO_2 and CH_4) and the echo distance had to be reduced from 60cm to 40cm to discern an echo. With this modification a calibrated mixture $CF_4/N_2$with 1% N_2 was found to change the measured echo transit time by 20σ compared to that seen in pure CF_4. It was planned to make a production system where systematic effects could be better controlled allowing comparisons with theoretical predictions for fluorocarbon gases and mixtures.

4 Development of the ATLAS Fluorocarbon evaporative cooling system

4.1 Early developments leading to the acceptance of evaporative fluorocarbon as the ATLAS silicon tracker baseline cooling system.

Based on the author's experience with the use of SFC fluids as Cherenkov radiators in the SLD CRID detector, the study of SFCs as potential coolants for the ATLAS (ex-EAGLE) pixel detector, (itself also proposed by the EAGLE CPPM pixel group [48]) began in 1993, with studies of evaporation of C_6F_{14} entrained as an aerosol mist in N_2 carrier gas into a 750mm long evaporator tube containing a capillary wick. The N_2/C_6F_{14} exhaust was captured in a low temperature condenser which allowed the N_2 to vent from the headspace [49].

Around this time other phase-change alternatives for the cooling of silicon detectors were being proposed, including an 'open' system with the evaporation of highly flammable butane (C_4H_{10}) into the tracker environmental space from capillary wicks in contact with the heat-generating areas of silicon microstrip modules [50]. This proposition was quickly eliminated, despite its previous proposal for use for the GEM silicon tracker at SSC, due to concerns over the evolution of a highly flammable gas used in a 'secondary activity' such as cooling, and also the previous problems with wick 'de-priming' (dry-out and localized boiling) seen in R&D for GEM. No 'open' evaporative cooling system has been proposed since.

Another alternative phase-change system was based on the melting of a slurry of 3-8% microscopic (50- 500 μm) ice crystals ("*Binary Ice*" ®[28]) [51], circulated through a closed tube circuit in a (highly toxic) methanol antifreeze carrier. In this system, sub-atmospheric or 'leakless' operation was mandatory due to the toxicity of the methanol and the conductive nature of any coolant leaks onto detectors or electronics.

Leakless water cooling had been developed for water cooling of LEP electronics racks and also for some detectors [52], including first generation silicon microstrip vertex detectors at LEP where heat-generating electronics was concentrated around end rings rather than dispersed throughout the whole surface area, as was being proposed for LHC.

Liquid C_6F_{14}, presently used to cool the CMS silicon tracker, has a heat capacity, C_p of around $1000 Jkg^{-1}K^{-1}$. The mass flow, $\dot{m}$, required to evacuate a given power, Q, for a given acceptable rise in the coolant temperature, δT, is given by;

$$\dot{m} = Q / (C_p \,.\, \delta T) \tag{4.1}$$

Considering equation (4.1) for the case of a hypothetical 10kW tracker and allowing a temperature rise of 4°C in the C_6F_{14} coolant, a high mass flow of $\sim 2.5 kgs^{-1}$ (or in units often used in the refrigeration industry; 9 tonnes per hour) would be required. To give a sense of scale, if the tracker could be operated at temperatures high enough for water ($C_p \sim 4200 Jkg^{-1}K^{-1}$) to be used, the mass flow would be reduced by around a factor of four.

In general, phase change cooling systems allow for significantly lower mass flow of the coolant than in uniphase cooling with the same fluid. If all the delivered coolant could be *evaporated* however, the latent heat or *enthalpy*, *H*, of evaporation of the coolant could be employed to extract the heat. Taking the example of C_6F_{14} as an evaporative coolant ($H \sim 100 Jg^{-1}$) we see that a mass flow of only around $0.1 kgs^{-1}$ would be required to extract 10kW of heat. In practice due to various factors, such as the pick-up of heat by the liquid coolant on its way to the tracker (as discussed in following sections) not all the enthalpy is always exploitable. However at the exploitation figures of 50-60% typical of the current ATLAS tracker, the fluorocarbon coolant mass flow is still more than a factor 10 lower than it would be in liquid phase, allowing for thinner coolant liquid delivery tubing and coolant exhaust tubing filled with vapour rather than liquid; both of which contribute to a lower *%X0* tracker material budget.[29]

Other important factors in the choice of coolant are its viscosity and the pressure drop that this contributes in a given length and diameter of delivery or recovery tubing that must navigate through other detectors to reach the tracker.

The pressure drop δP (Pa) in a liquid of (temperature-dependent) density ρ and absolute viscosity n (in units of Pa.s or equivalently $kg.m^{-1}s^{-1}$) flowing at a mass flow rate $\dot{m}$ (kgs^{-1}) through a tube of hydraulic diameter D, area S and length L at linear velocity V (ms^{-1}), is given by;

$$dP = \frac{K.L.\rho.V^2}{D} \tag{4.2}$$

[28] Trade mark of Integral Technologie GmbH, Flensberg, Germany; at that time a manufacturer of ice slurry cold plants for applications such as supermarket cold stores.

[29] The assiduous reader might question why not to use water as an evaporant, given its exceptionally high enthalpy of evaporation of $2.5 kJg^{-1}$. Unfortunately, at typical tracker operating temperatures the evaporation pressure of water is only a few $mbar_{abs}$.

where a dimensionless empirical flow regime factor[30], *K*, relates the pressure drop to the dimensionless Reynolds number Re where;

$$Re = \frac{\dot{m}.D}{S.n} \tag{4.3}$$

Re < 2320 is a common definition of laminar flow. In this region the factor *K* of eq. (4.2) is conventionally expressed as {64/Re}. Pressure drop is linear with mass flow in this regime.

In the turbulent regime, conventionally defined for Re > 2320, *K* is taken as;

- $\{0.316*Re^{-0.25}\}$ for $(2320 \leq Re \leq 10000)$;
- $\{0.184*Re^{-0.2}\}$ for $(10000 \leq Re \leq 100000)$.

Pressure drop increases exponentially with mass flow in the turbulent flow regions.

Although the C_p of C_6F_{14} is only around a quarter that of water – its much lower viscosity (0.00075 $kgm^{-1}s^{-1}$ at -20°C) and non-conductivity offer critical advantages.

Table 4.1 indicates the viscosity and density of the various cooling fluids under consideration in 1997/8 for the ATLAS silicon tracker. Of particular interest are the viscosities of the SFC liquids, which are numerically similar to that for methanol, but at a temperature 20ºC colder! Also the SFCs have a viscosity a factor of ~ 10 less than *binary ice* ® at temperatures below ~ -14ºC**.**

Operating temperature specification for silicon substrates

Early studies based on LHC operation at $L = 10^{34}cm^{-2}s^{-1}$ suggested [53], that substrate operating temperatures around -7ºC were needed to guard against thermal runaway by minimizing leakage current under silicon irradiation and also to sufficiently slow depletion voltage growth (on assumed 300μm substrates) to assure all tracking layers (with the exception of the pixel B-physics layer) a 10 year operational life. Under the hypothesis of 10 years' operation @ T_{Si} ~ -7°C with 2 days/year @ 20°C (breakdowns of cooling etc.) and 14 days/year @ 17°C (maintenance), the depletion voltage growth would be limited to 600V. The -7ºC temperature figure was endorsed for both the pixel and SCT (**S**emi **C**onductor **T**racker – the non-pixel (microstrip) elements of the silicon tracker of the ATLAS inner detector).

The expected 10-year fluences (normalised to 1MeV equivalent. neutrons) by tracking layer were:

- SCT layers (average): 2.10^{14} n cm^{-2};
- Pixels (layer 1, r = 11.5cm): 6.10^{14} n cm^{-2}; (layer 2, r = 13.7cm + disks): 4.10^{14} n cm^{-2};
- Pixel B layer (r = 4.7cm) : ~10^{15} n cm^{-2} (after 5 years) (600V V_{dep} limit reached after 5 years)

Studies with evaporative cooling continued at CPPM. The injection of an entrained C_6F_{14} mist was considered impractical, owing to the difficulty of maintaining a constant C_6F_{14} mist concentration in the N_2 carrier. Instead, evaporation with perfluorobutane (C_4F_{10})[31] was extensively studied; the motivation being the perceived requirement for a sub-atmospheric pressure cooling system no matter what coolant used, which was at that time being imposed by the known success of "leakless" room temperature water-based cooling systems and the choice by the ATLAS ID community of *Binary Ice* ® as the *de facto* cooling system for the entire silicon tracker. It should be noted in this context that at that time only two institutes, Rutherford Appleton Laboratory (SERC, UK) and INFN *Sezione di Genova* had signed the ATLAS memorandum of understanding to provide cooling system 'deliverables'. CPPM-IN2P3 considered other aspects of the pixel system (together with liquid argon calorimetry and real time DAQ) the priorities. The prevalent attitudes of '*it's not sexy; it's only cooling; anyone can do it - as long as it's not us'* and '*anti-freeze protects my car engine and stops it boiling when I go skiing, what's the big deal?*' remained major obstacles to overturning the *Binary Ice* 'baseline' which, despite having difficulty in meeting the -7ºC target temperature, was being strenuously supported by its main proposer (RAL) as an 'off the shelf' industrialised solution.

[30] ASHRAE (American Society of Heating and Refrigerating and Air-Conditioning Engineers)
[31] Mfr: 3-M Corp. Specialty Chemicals Division, St. Paul, MN55113-3223, USA

Table 4.1. Density & Viscosity for fluids considered for ATLAS silicon tracker cooling (various temperatures)

Fluid	**Density (kgm^{-3} @ T (°C))**	**Absolute viscosity ($kgm^{-1}s^{-1}$ @ T (°C))**
Water	~ 1000 (5°C)	0,00135 (5°C)
Methanol	791.8 (5°C)	0,00082(0°C)
Ethylene glycol	812 (20°C)	0,00179 (0°C)
Propylene glycol	1036 (20°C)	0,243 (0°C)
Binary Ice® (5% ➔ 2% ice in methanol)	826.2 (-14°C)	0.009 (-14°C)
C_6F_{14}	1680 (25°C)	0,00075 (-20°C)
C_4F_{10} (liquid)	1668 (-20°C)	0.00056 (-20°C)
C_4F_{10} (vapour)	6.53 (-20°C)	$1.1 . 10^{-5}$

Despite the combination of a highly toxic methanol freezing point depressant and a total pressure budget of less than 1bar of driving pressure, requiring the circulation of a viscous sub-zero coolant mixture in relatively large diameter tubes, *Binary Ice* was considered the baseline choice for the *whole* ATLAS silicon pixel and SCT tracker [54] while the evaporative fluorocarbon alternative using C_4F_{10} was a possible back-up only for the pixel detector [55] at the time of the ATLAS inner detector TDR. In some sense the pixel system benefitted from being an 'immature' system meriting only a 'provisional' chapter[32] in the inner detector TDR; the fluorocarbon evaporative cooling could be presented again in the definitive ATLAS pixel TDR[33] [56]. However, by this time the advantages in reduced tracker material had already become apparent. Figure 4.1 compares the radiation length contributions of *Binary Ice* an evaporative fluorocarbon cooling in a pixel detector with 3 barrel layers and endcaps [57].

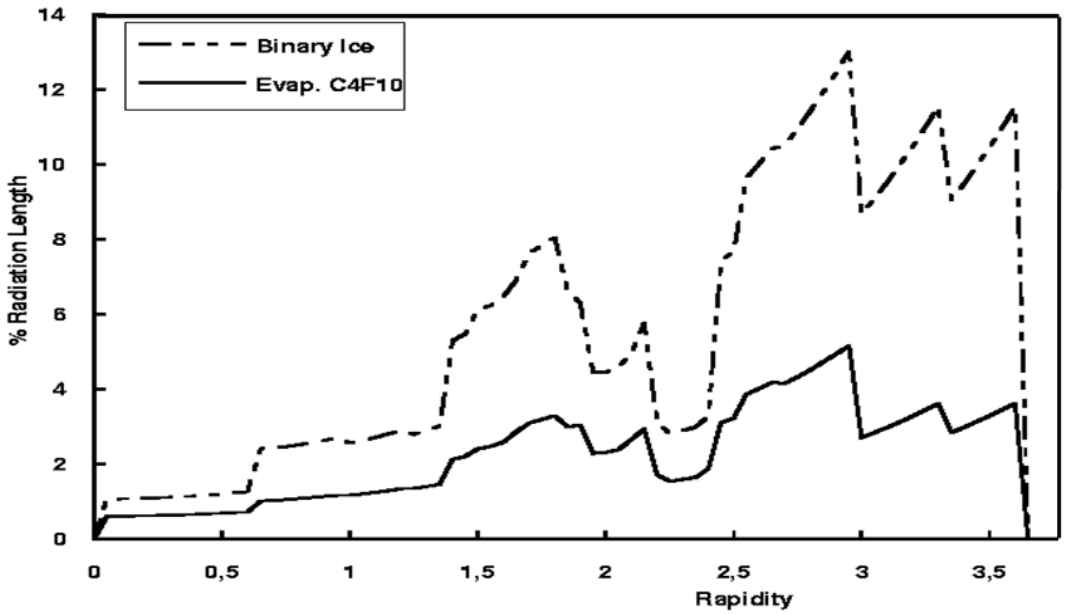

Fig. 4.1 Radiation length comparison of the contribution of binary ice and fluorocarbon cooling to a three layer barrel pixel detector (radii 4.7, 10.5 & 13.7cm) with four end-caps (z = 49.0 ,60.8, 75.9 & 103.5 cm). Coolant and service tubes only – no pixel modules, cabling or support structures.

The comparison is made on the basis of 75W to be evacuated from each independent longitudinal pixel "barrel stave" circuit (13 pixel modules) and 58 W from each disk sector (10 pixel modules) – the then-current design.

Figure 4.2 is a more recent (approximating the actually built) representation of the ATLAS pixel detector illustrating the relative positions of the various tracking surfaces.

[32] Editors: M. Gilchriese (LBNL) and G. Hallewell (CPPM)
[33] Editors: G. Hallewell (CPPM) and N. Wermes (Bonn University)

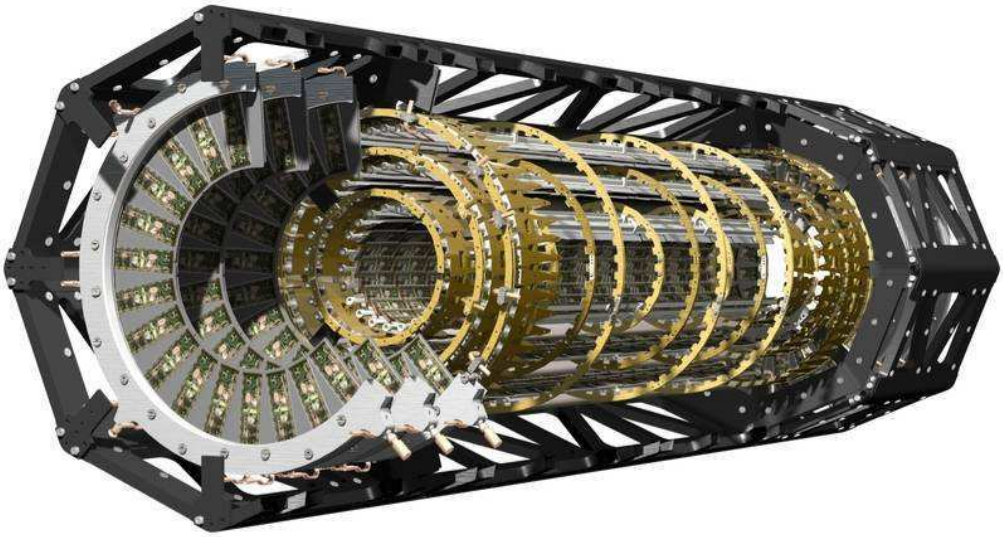

Fig.4.2. Illustration of the ATLAS pixel detector and its support structures: the three barrel layers and the end cap disks are shown, together with full length cooling tubes (l~ 80cm) of the barrel pixel layers.

For the $\%X_0$ calculations of fig 4.1 the densities and viscosities of the two fluids are assumed at -15ºC, with tube diameters sized for comparable pressure drops, particularly in the exhaust tubing to the circulator. On-detector tubing was assumed to be in 200 μm wall aluminium tube with 3.6 mm inner diameter for the barrel layers and 3.2 mm for the end caps. Off-detector tubing was assumed to be 550 μm wall aluminium with diameter increasing in two steps over the 10.5 m total length considered to lie within the rapidity bite of the electromagnetic calorimeter surrounding the inner tracker volume. In the evaporative case the liquid coolant could be delivered in a much thinner tube due to the lower flow rate and viscosity. Coolant is assumed to pass through the on-detector tubes in bi-phase state and through the off-detector exhaust tubing in the vapour state.

The dramatic reduction in the radiation length contribution at low radius for the evaporative coolant and its tubing was instrumental in the movement toward evaporative fluorocarbon cooling as the final baseline choice.

4.2 The CPPM development evaporative fluorocarbon tracker cooling system

The C_4F_{10} circulation system used at CPPM to study pixel barrel staves (of various constructions but typically featuring straight tubes 80cm length with hydraulic diameters in the range 3-4 mm) and disk sectors (of various constructions but typically featuring triple-bend tubes around 30cm length with hydraulic diameters in the range 3-4 mm, tested in the 'W', 'M', 'E' and '3' fluid flow configurations) is shown in Figure 4.3.

The system was composed of four main elements;

- A delivery system to inject liquid coolant simultaneously in up to four parallel pixel or SCT structures under test, in which it evaporates at a controlled pressure (and temperature);
- a system for regulating evaporation pressure and returning the evaporated coolant to the condenser;
- a combined condenser and cold coolant storage reservoir;
- a liquid pump and cooled liquid delivery tubing to deliver cold liquid to the structures under test in a cold N_2 gas-filled environment.

Liquid C_4F_{10} leaving a cold (-20ºC) condenser under gravity descended 1.5m to gear pump which pressurised the liquid to around $5bar_{abs}$ and distributed it to up to four parallel channels where pixel and SCT test structures could be accommodated.

We consider these elements in detail in the following sections.

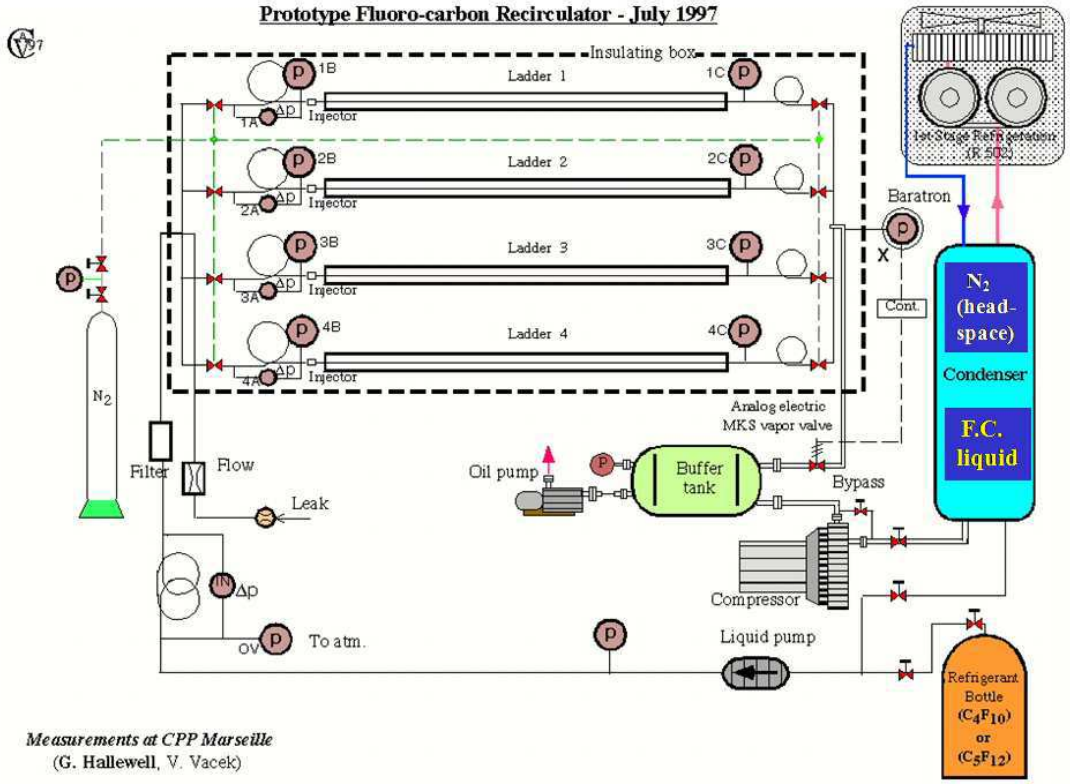

Fig. 4.3. The CPPM developmental fluorocarbon evaporative cooling test stand.

4.2.1. The injection system

The flow to each of four parallel cooling channels could be selected by a remote control pneumatic valve and manually adjusted with a needle valve. Liquid coolant entered the test structures through injectors based on 'orifice plates'. Three types of injectors were studied;

- ***drilled injectors***: holes drilled in 6 mm aluminium bar inserted into a 6mm Swagelok union. This type was soon abandoned due to the fragility of the drills, dictating a minimum possible diameter of 300 μm and the inconsistent diameter from injector to injector;
- ***copper tipped injectors***: soft copper was crimped around a thin tungsten wire mandrel of the required diameter (200 -300 um). The seam of the copper was silver-solder closed and the tip was soldered into a 6mm brass or copper tube for insertion into a 6mm Swagelok union. The tungsten wire was then withdrawn;
- ***ruby injectors***: aluminium spool pieces machined from 6mm bar into which inexpensive synthetic ruby watch bearings, typically 1mm thick with pre-machined holes diameters of 200, 250 and 300 μm were inserted.

Of these, the ruby injectors were considered the most reliable and repeatable; the needle valves which had been needed for flow balance with the previously-studied injectors could be eliminated if ruby injectors of the same diameters were used on the parallel circuits[34]

[34] In an interesting development at this time, CMS was deliberating on the coolant to use for its silicon microstrip and pixel tracker. The community wanted a non-conductive coolant in the event of leaks, so the natural choice was a fluorocarbon. However a senior CMS figure stated he wouldn't want to use an evaporative system based on injectors, since his father had been a heating contractor, who had often told him how heating oil injectors on furnaces were renowned for blocking up. CMS chose a pressurized C_6F_{14} liquid cooling system instead.

4.2.2. The evaporation pressure control and vapour recovery system

The various ATLAS pixel and SCT structures (evaporators) tested in the cooling plant all exhibited a common limitation to varying degrees: the evaporation temperature in the on-detector cooling tube needed to be substantially cooler than the required -7ºC silicon operating temperature, due to the thermal impedances between the silicon substrates and the tube wall. These impedances were due in varying proportions to the glue or thermal grease coupling of the coolant tube to heat-spreader tiles to which the silicon modules (or simulated modules) were attached. In some structures real heat spreader plates of carbon-carbon (of exceptional longitudinal thermal conductivity around 1000 $Wm^{-1}K^{-1}$, but poorer transverse conductivity (10-40 $Wm^{-1}K^{-1}$) were used, while some early pixel disk sectors used 'hairy' carbon tubes in which the radial fibres were bonded to carbon-carbon faceplates. A detailed description of these structures and their thermal performances is not within the scope of this report, some details can be found in [56]. In some test structures in-tube evaporation temperatures as low as -25ºC were required. It was becoming clear however in concurrent testing elsewhere (1997-98) with *binary ice* that the exponentially rising viscosity at lower in-tube temperatures was proving a potential show-stopper for many of the structures under test. The evaporation pressure control had therefore to maintain evaporation temperatures significantly below -7ºC for real structures tested.

Vapour leaving the test structures passed through a buffer tank and a vacuum pump on its way to the condenser. The evaporation pressure in the structures under test was determined by the pressure in the buffer tank, P_{buffer}. This pressure was maintained near a set point value by constantly adjusting the vapour pumping speed through the buffer by variation of the aperture of a high C_v butterfly valve[35]. The valve was adjusted in real time on the basis of the instantaneous sensed pressure[36] by a commercial Proportional, Integral and Derivative (PID) analog process controller[37].

Defining $V(t)$ as the controller pressure command DAC voltage output, the PID algorithm was of the form:

$$V(t) = K_p e(t) + K_i \int_0^t e(\tau)\,d\tau + K_d \frac{d}{dt} e(t) \qquad (4.4)$$

where the tuning parameters, K_p, K_i and K_i are the proportional, integral and derivative gains respectively and $e(t)$ is the time-dependent offset between the sensed parameter (pressure) and its set point..

Note:

- Large values of proportional gain, K_p, usually mean faster response, since the larger the error the larger the proportional term compensation. Excessive proportional gain can lead to process instability and oscillation;
- Large values of integral gain, K_i, imply steady state errors are eliminated more quickly. The trade-off is larger overshoot: any negative error integrated during transient response must be integrated away by positive error before reaching a steady state;
- Large values of derivative gain, K_d decrease overshoot, but slow down transient response and can lead to instability due to signal noise amplification in the differentiation of the error.

In practice modern PID controllers, as in the case of the model used here, have an 'autotune' algorithm that temporarily freezes two of the three gain terms while the effect of variation of the remaining gain is studied, then permutes the active gain before converging to (usually) optimal values of all three. Section 4.4.3 discusses the rejected proposal of the author to incorporate PID algorithm in the ATMEL microcontroller chip of ATLAS E-LMB (Embedded Local Monitor Box: [58]) for active control of coolant mass flow based on the sensed exhaust temperature.

It was known that conventional refrigeration compressors for refrigerants including R22, R134a and R404 conventionally operate with synthetic lubricating oils. Since these oils were considered unlikely to be radiation resistant – with a probable risk of polymerisation - and since the oil was likely to plate out around the entire coolant circuit, affecting the efficiency of heat extraction, it was decided to use an oil-free vacuum pump[38] acting as a compressor of ratio ($Pc_{ondenser}$ /P_{buffer}). It was quickly realised that the vacuum pump could not be operated at an output pressure less than $1bar_{abs}$ without significant ingress of air from the surroundings. Nor could it generate output pressures significantly in excess of 1 bar_{abs}. It was thus necessary to operate the condenser at 1 bar_{abs} with the difference between the s.v.p. of the C_4F_{10} liquid in the condenser and atmospheric pressure being made up with an inert headspace gas – in this case N_2, as discussed in the following section.

[35] MKS model 653A-1-40-1: 400 mm aperture
[36] Measured with a MKS 'Baratron' model 122B, 0-5000$Torr_{abs}$ pressure range: 1Torr resolution.
[37] MKS 600 series pressure controller.
[38] Edwards ESDP30 Rotary Scroll Type: $30m^3hr^{-1}$ air

4.2.3 The low temperature condenser

The Armalex® foam-insulated condenser (fig. 4.4) could be maintained in the temperature range -25ºC ➔ -35ºC (depending on laboratory ambient temperature and C_4F_{10} condensation load) by a 2KW compressor/ refrigerator[39]. C_4F_{10} vapour entered the condenser through two parallel plate heat exchangers[40], cooled by R404A counter-evaporation at a typical temperature set point of -30º C. Condensed C_4F_{10} liquid leaving the heat exchangers accumulated in the bottom of the condenser and the liquid level was determined before start-up, with the aid of four float-switch depth gauges, to be high enough to maintain a good 'keep-cold' contact with the outside of the parallel plate heat exchangers.

Figure 4.5 shows the corresponding thermodynamic cycle for the circulator for the example of -25ºC evaporation temperature. The cycle **ABCDE** is unconventional, not only because it does not rotate in a counter-clockwise direction as in a 'usual' refrigeration cycle characterised by;

{evaporation ➔ compression ➔ condensation ➔ liquid detente}

nor in a purely clockwise cycle;

{evaporation ➔ vapour pressure collapse ➔ condensation ➔
liquid pump/gravity pressure gain ➔ liquid detente}

as for example in the SLD CRID radiator recirculator (§2.5.2), but dissociates the C_4F_{10} +N_2 entry isobar from the C_4F_{10} condensation isobar and its corresponding low partial pressure isotherm. This dissociation, by virtue of the extra headspace pressure of N_2 gas means that although C_4F_{10} condenses in an ambient pressure of $1bar_{abs}$ it does so at a low partial pressure and a corresponding temperature in the range (-25ºC ➔ -35ºC).

The condenser headspace was referenced to atmospheric pressure via a vent. A pressure sensor triggered the opening of a pneumatic valve in the N_2 supply (or vent line) if the headspace pressure dropped below (or rose above) the permitted band of ± 50 mbar w.r.t. atmospheric pressure.

In this way a fluorocarbon with a relatively low (~350 $mbar_{abs}$) sub-atmospheric s.v.p. at the necessary in-tube evaporation temperature of -25ºC required for -7ºC silicon temperature in certain prototype thermo-mechanical structures could be circulated with only half of the cooling loop being below atmospheric pressure. The liquid leaving the condenser had to be forced around the system with a pump and/or the gravitational head of en elevated condenser, as will be seen in the following section.

The system clearly has shortcomings;

- the vapour extraction side (**A**) is below atmospheric pressure and so prone to leak ingress from air or the environmental gas surrounding the silicon tracker (later chosen to be N_2 for ATLAS, an alternative candidate being CO_2);
- ingressed non-condensable gas must be vented from the headspace of the condenser where it will tend to accumulate. Some of the C_4F_{10} vapour above the liquid in the condenser be lost in this operation;
- the low evaporation pressure of the C_4F_{10} in the structures being cooled (350 $mbar_{abs}$ or lower) makes it difficult to return vapour through long tubing to the compressor (vacuum pump) input;
- the heat transfer coefficient of C_4F_{10} with dissolved N_2 will be less than in C_4F_{10} starting from the uncontaminated state.

[39] Danfoss Model SC18/18 CLX T2
[40] ALFA LAVAL type CB 26 H

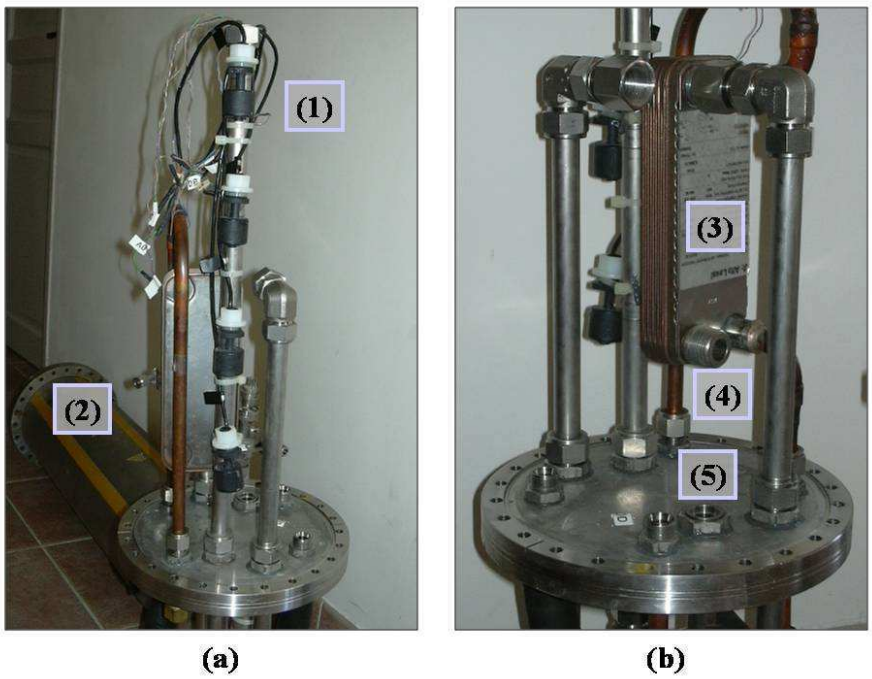

Fig 4.4. Condenser internals; photo(a): C_4F_{10} level float-switches (1) and pressure dome (2): photo (b) 1 of 2 heat exchangers (3), condensate exit from heat exchanger to liquid reservoir (4) C_4F_{10} exit to liquid pump (5)

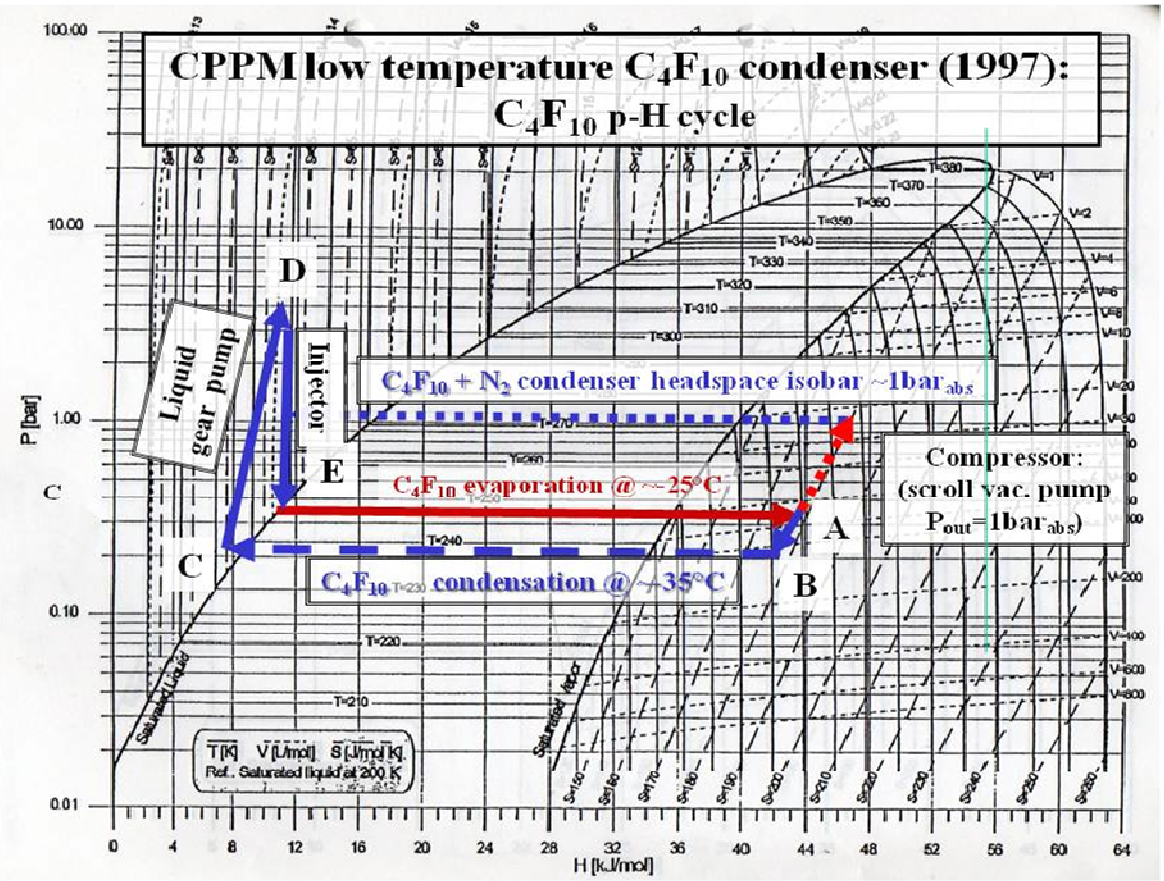

Fig. 4.5. Thermodynamic cycle in the CPPM evaporative cooling test stand with a low temperature condenser.

It should be remembered however that this system was built at a time when it was still being demanded that any competing cooling system be 'leakless' to the exterior, as was required for *binary ice*. With a dielectric non-

toxic, non-flammable fluid for which there was plenty of circulation experience from the world of RICH detectors, this demand was clearly unfounded. However with the re-baselining in favour of SFC evaporative cooling, other SFC fluids with higher operating pressures could start to be considered, as discussed in later sections.

In the CPPM C_4F_{10} test circulator two conditions were necessary to assure circulation in the most general conditions;

- overcoming the ($P_{condenser} - P_{buffer}$) 'potential barrier': the necessity of the vacuum pump upstream of the condenser;
- maintaining the pressure of the C_4F_{10} liquid greater than the s.v.p. at the condenser temperature, to help maintain the pump 'primed'.

4.2.4 The liquid pump and liquid circulation piping

To deliver a volatile coolant as liquid (at any temperature below its critical temperature), its pressure everywhere in the liquid supply tubing must exceed its s.v.p. at the local ambient temperature. The higher the temperature of the local liquid tubing, the higher the required pressure; the limit being the critical temperature at the top of the 'dome' in the pressure-enthalpy diagram for the coolant – see for example Fig 4.5. Above this temperature the fluid cannot be delivered in liquid form whatever the pressure. Throttling devices in the tubing can introduce pressure drops, causing the liquid pressure to drop to the s.v.p. threshold, provoking evaporation. Also heat can be absorbed from devices like liquid pumps, with the same effect.

In the CPPM test system cold C_4F_{10} liquid leaving the compressor tended to be warmed by the pump, which was placed in a styrofoam cold box. The tubing from the condenser to the pump and downstream of the pump until the entry point of the cold enclosure containing the structures under test were also insulated, the latter also being jacketed in a coaxial tube through which cold C_6F_{14} liquid was counter-circulated.

To prevent local boiling at the pump, the combined ρgh pressure of the liquid column from the condenser (h being the sum of the liquid level in the condenser and the condenser height above the pump), and the condenser 1 bar_{abs} operating pressure were set to exceed the local s.v.p. at the pump.

The cold enclosure containing the test structures was a foam-insulated Plexiglass glovebox purged with cold gas from liquid N_2 evaporation and operating in the range -5º ➔ 0ºC.

At the time of the ATLAS inner detector TDR (April 1997: [56]), no definitive pixel or SCT structures (with silicon detector modules) were available. Instead, approximate thermal interface structures linked dummy silicon pixel modules (of the same overall dimension but with deposited platinum heater resistances) to 200 μm wall aluminium tubes of 3.6 mm inner diameter for the barrel pixel 'staves' and 3.2 mm for the pixel end cap sectors.

4.3 Rebaselining the ATLAS silicon tracker cooling to evaporative fluorocarbon

The first review of the ATLAS cooling systems was held on October 30, 1997[59]. The review expressed a marked preference for evaporative fluorocarbon cooling for the following reasons:

- the lower material budget;
- the much greater safety of the cooling medium;
- the less drastic consequences of a leak;
- fewer components;
- the routing of the pipes being more likely to fit in the available space due to the lower viscosity of the coolant and the correspondingly smaller diameter tubes.

The review recommended further study of;

- injectors – specifically could orifice injectors be replaced with something else?
- effectiveness of refrigerant flow through vertical and radial orientations;
- control aspects using a full scale representative prototype;
- radiological aspects;

The ATLAS inner detector community was asked to nominate a person to develop a project plan to address the above issues before the end of 1997 for the issues to be addressed over a ~ 12 month timescale.

These recommendations resulted in the author coming to work at CERN full time for the period September 1998-February 2001 in close contact with the CERN group of Michel Bosteels and in close collaboration with Vaclav Vacek and associates of the Czech Technical University, Prague.

4.3.1 Evaporative fluorocarbon cooling in the ATLAS Pixel TDR

In the spring of 1998 the ATLAS pixel TDR [56] was published. This document detailed the converging mechanical designs for barrel pixel linear arrays ('staves') and disk sectors including the thermal drains between the silicon pixel substrates and the cooling channels. Fig 4.2 gave a general view of the pixel detector. Figure 4.6. illustrates the construction of a pixel barrel 'stave' of 13 linearly-arranged pixel detector modules with

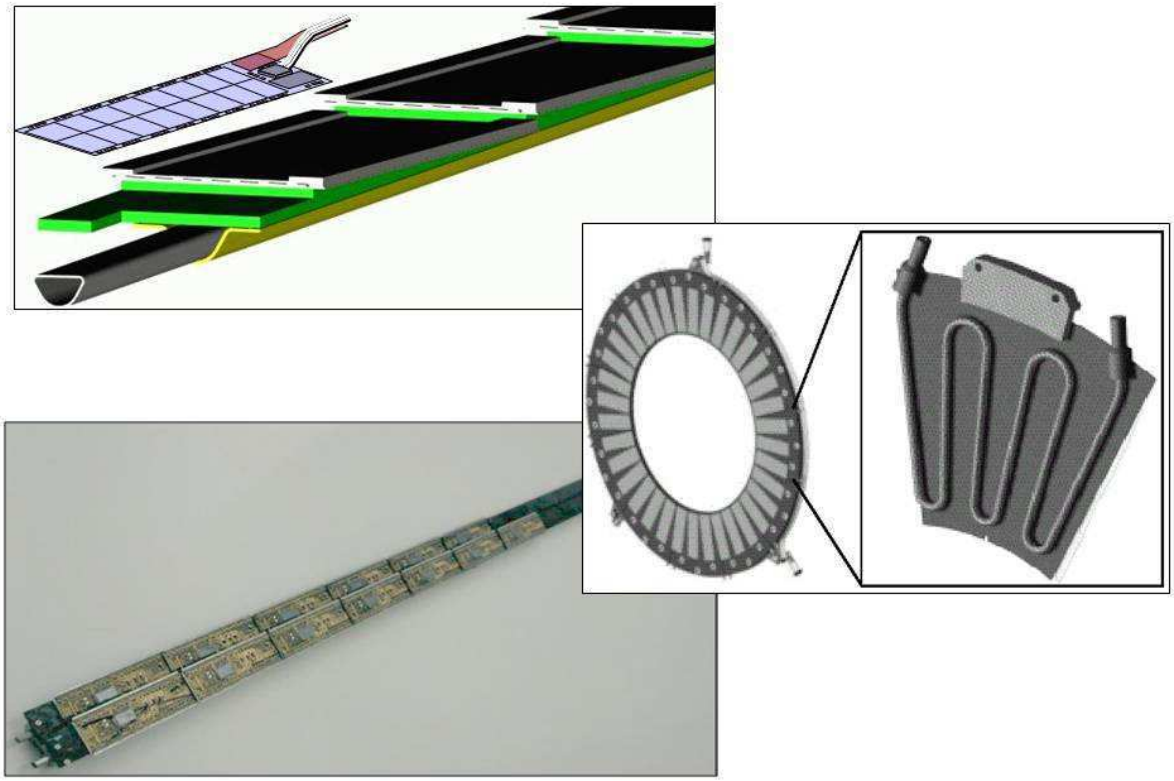

Fig. 4.6. Illustration of ATLAS pixel barrel ('stave') and end cap (disk sector) support and cooling structures.

overlap in z. (ϕ overlap with their neighbours is assured by their positioning in the end-ring support structure of Fig 4.2). The major components are a 80cm long 'shingled' heat spreader plate in graphite which channels the heat dissipated in the pixel substrate with its bump-bonded readout chips into a 'D' profile aluminium cooling tube with 200 μm wall and 3.6mm equivalent hydraulic diameter. The difference in thermal expansion between the tube and the heat spreader is accommodated in a sliding grease joint. The contact between tube and heat spreader is maintained by a preformed carbon fibre reinforced plastic (CFRP) 'Omega' form, glued to the outer edges of the heat spreader plate.

In the pixel disk sectors 1.5mm thick carbon-carbon heat spreader plates are glued directly to a 5-bend serpentine ('VW' geometry) circular section 200 μm wall aluminium tube of 3.2 mm inner diameter. Eight such sectors form each of the six disks. Earlier versions of disk sectors had two concentric rings of pixel modules and serpentine tubes in a 'W', 'E', 'M' or '3' orientation with respect to gravity.

By the time of the ATLAS Pixel Detector TDR $C_4F_{10.}$ evaporative cooling had relegated binary ice to back up status - *for the pixel detector cooling system only* - and had demonstrated successful cooling of prototype pixel barrel staves and disk sectors. Examples of this cooling effectiveness are illustrated in Figs 4.7 and 4.8.

Fig 4.7 illustrates temperatures at the input and output ends of the cooling tube and the temperature distributions along the 13 thermally-simulated silicon modules of a thermo-mechanical prototype pixel barrel stave cooled with evaporating C_4F_{10}. Each tile is attached to the heat spreader plate as illustrated in Fig. 4.6. Some general trends are apparent with increasing power, in particular the inefficient thermal heat sinking of modules 2, 9 & 13 and the temperatures of the modules at the output end being lower than those nearer the input. This latter phenomenon is due to the progressive pressure drop in the tube due to the presence of vapour produced by the heat input of the downstream modules; the upstream modules have a slightly higher evaporation pressure (and hence temperature) than their downstream neighbours.

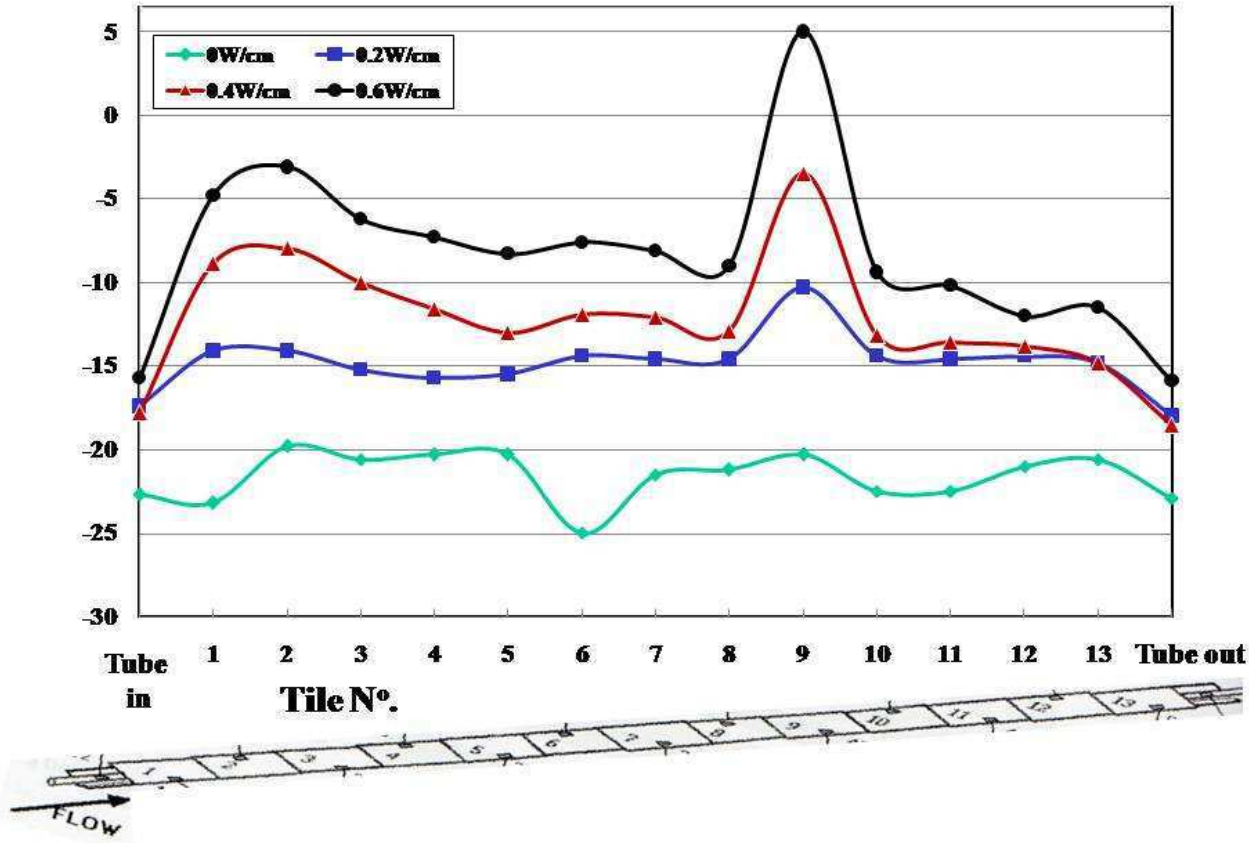

Fig 4.7 Illustration of the cooling of a thermo-mechanical ATLAS pixel barrel 'stave' with evaporative C_4F_{10} and increasing module power: 0.2, 0.4 and 0.6 Wcm^{-2} - respectively 26, 52 and 79 Watts total dissipation.

There was considerable interest to know whether evaporative cooling could cope with tubes bent in compound shapes, with liquid injection (and vapour extraction) in all clock positions including those opposed by gravity. This "all-orientation" cooling was successfully demonstrated with a prototype pixel end cap sector (in this case with a 3.2mm ID "hairy" carbon tube attached to carbon-carbon faceplates, as illustrated in Fig. 4.8. The evaporation pressure and the pressure upstream of the ruby injector (located in the boil-off N_2-chilled glove box) were logged together with temperatures on the dummy pixel modules and the carbon-carbon faceplates at a power dissipation of 40W. Fig 4.8 demonstrates the wide safety margin available at 250Torr evaporation pressure; increasing the evaporation pressure from 250 to 350 Torr ('M' configuration) caused the average module temperature to rise to an average of no more than -7.9ºC, below the temperature specification of -7ºC.

4.3.2. Toward evaporative cooling with C_3F_8 for the pixel and SCT detectors

Despite this success it was becoming clear that the low evaporation pressures (300-400 $mbar_{abs}$) of C_4F_{10} for in-tube evaporation at temperatures in the range -16º➔-20ºC necessary to cool some of the less thermally-efficient pixel and SCT barrel and end cap structures would be a limiting factor in sending the exhaust vapour back to the condenser through the long trans-detector tube runs of > 30 metres due to:

- the relatively large liquid-gas expansion factor of C_4F_{10} at these low pressures;
- the higher pressure drop in the exhaust tubing provoked by this higher vapour volume flow;
- the reduced pumping speed of vacuum pumps/compressors with declining input pressure;

- the lower heat transfer coefficient between the evaporant and the tube wall at lower pressure.

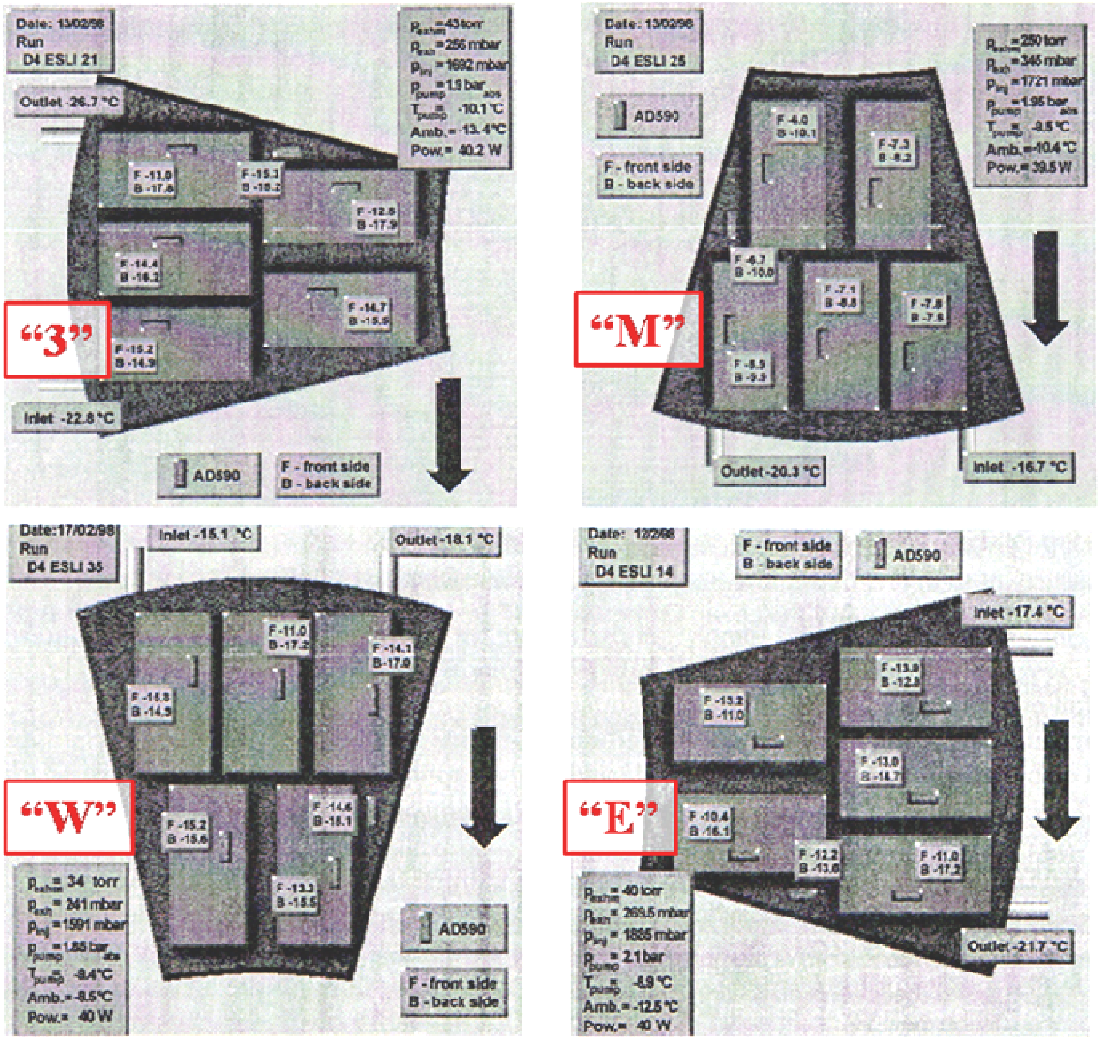

Fig 4.8 Illustration of all-orientation cooling of an early ATLAS thermo-mechanical prototype end-cap pixel sector using evaporative C_4F_{10} (after [56]: pp 212,213).

It was considered important therefore to begin a study of the next lightest of the SFCs: perfluoro-propane (C_3F_8): Some pertinent parameters for comparison between C_4F_{10} and C_3F_8 are listed in table 4.2 for example at a temperature of -10ºC.

Table 4.2 Comparision of evaporation parameters for C_4F_{10} and C_3F_8: an example at T = -10ºC .

SFC fluid	**C_4F_{10}**	**C_3F_8**
Molecular weight	238	188
Temperature for evaporation at 1 bar abs (ºC)	-2	-37
Vapour pressure @ -10ºC (Bar_{abs})	0.723	2.894
Liquid density at -10ºC ($g.cm^{-3}$)	1.638	1.510
Enthalpy of vaporisation ($J.gm^{-1}$) at -10ºC	115	95
Mass flow in a pixel stave dissipating 72 Watts, using assuming the use of all available enthalpy at -10ºC ($gm.s^{-1}$)	0.63	0.76
Liquid flow to a pixel stave dissipating 72 Watts, assuming the use of all available enthalpy at -10ºC (cm^3s^{-1})	0.384	0.503
Liquid-vapour expansion factor for evaporation at -10ºC	210	60
Vapour flow in exhaust tubing following a pixel stave dissipating 72Watts	59.6	30.2

Of particular interest in Table 4.2 is the liquid➔gas conversion rate for the two fluids at the same evaporation temperature. The increased s.v.p. of C_3F_8 can confer a two-fold advantage:

- a higher evaporation pressure to allow conventional gas compressors operating at input pressures around $1bar_{abs}$, with vapour condensation in a warm condenser – as in a "conventional" refrigeration cycle;
- a lower volume flow of vapour - promising lower pressure drops in the exhaust tubing returning vapour to the compressor aspiration manifold.

Despite this, the proposal provoked some shock in a community still believing that on-detector coolant pressures should be around $1bar_{abs}$ or less, as characteristic of "leakless" aqueous systems. The request came to study also fluids with a higher (lower) evaporation pressure than C_4F_{10}, (C_3F_8) – a mixture of the two. Also proposed were studies of a new refrigerant trifluoro-iodomethane (CF_3I) - a combined inerting/firefighting vapour for fuel tanks of military aircraft, with the combined environmentally friendly properties of being non ozone-depleting and very rapid photo-disintegration under UV irradiation so as not to be a greenhouse gas. Table 4.3 compares of relevant evaporation parameters for these vapours at -15ºC.

Table 4.3: Comparision of evaporation parameters for C_4F_{10}, C_3F_8, 50% C_3F_8/50% C_4F_{10}, CF_3I, at -15ºC.

Fluid [ref for calcn]	L (Jg^{-1})	cm^3 Vol(vap) /cm^3(liq)	S.V.P (bar a) @ -15º C
C_3F_8[41]	97.0	71.4	2.46
C_4F_{10}[42]	101.1	242.6	0.58
CF_3I[43]	100.8	176.3	1.33
50%C_3F_8/ 50%C_4F_{10} [60],[61]	98.3	147.6	$1.01P_{SV}$ ➔$1.65\ P_{SL}$

Given this impetus, it was decided to modify the CPPM circulator of Fig 4.2 to allow operation with the above fluids for further thermal studies of pixel and SCT prototype thermo-mechanical test structures [62], and to make measurements of heat transfer coefficient. The adapted circulator is illustrated in Fig. 4.9.

Higher pressure operation with C_3F_8 required an oil-less compressor able to accept input vapour at or above atmospheric pressure – a problem solved using a recycled piston compressor[44] originally used to circulate C_2F_6 in the OMEGA RICH radiator vessel during the 1980s (§2.5.1) – the recirculator having been constructed by the CERN group of Michel Bosteels. The first stage scroll vacuum pump was used only with the lower pressure vapours, C_4F_{10} & C_3F_8/C_4F_{10}, since the pumping speed of the piston compressor was insufficient at input pressures below 1 bar_{abs}.

The most flexible condenser solution was the replacement of the cold condenser with a new version able to operate at higher pressures using water heat exchange at ~ 15ºC(55ºC) for C_3F_8 (C_4F_{10}) operation, with a typical condensation pressure around 6.5(1.9) bar_{abs}.

At around the same time, a decision was made to replace the orifice type injectors with long capillaries having internal diameters as small as 0.6mm; it this way it was planned to verify that liquid coolant could be delivered at the required mass flows through the thinnest types of commercially available tubing to further reduce *%X0* in the most critical inner zones of the inner tracker volume.

Figure 4.10 illustrates the thermodynamic cycle for C_3F_8 with rotation in the "conventional" anti-clockwise sense on the pressure-enthalpy diagram. The evaporator➔condenser pressure increase is given by the vapour compressor while the condenser➔evaporator pressure detent is given by a combination of a delivery capillary and a flow-determining pressure regulator. The importance of precooling the supply liquid before the capillary input will be discussed in §4.4.

With the modified circulator particular attention was paid to the cooling of SCT end cap and barrel structures which had higher power and longer cooling channels than the pixel structures.

[41] Mfr: Astor Chemical Co., 14 Dobrolubov Avenue, 197198 St. Petersberg, Russia
[42] Mfr: 3-M Corp. Specialty Chemicals Division, St. Paul, MN55113-3223, USA: PF5040 grade
[43] Mfr: Ajay North America Inc. Powder Springs, GA, 30127-0127, USA
[44] Haug SOGX 50-D4 Dry Piston Compressor (rated 3.6 m^3hr^{-1} air, P_{in} 1 bar $_{abs}$; P_{out} = 9 bar $_{abs}$ limit)

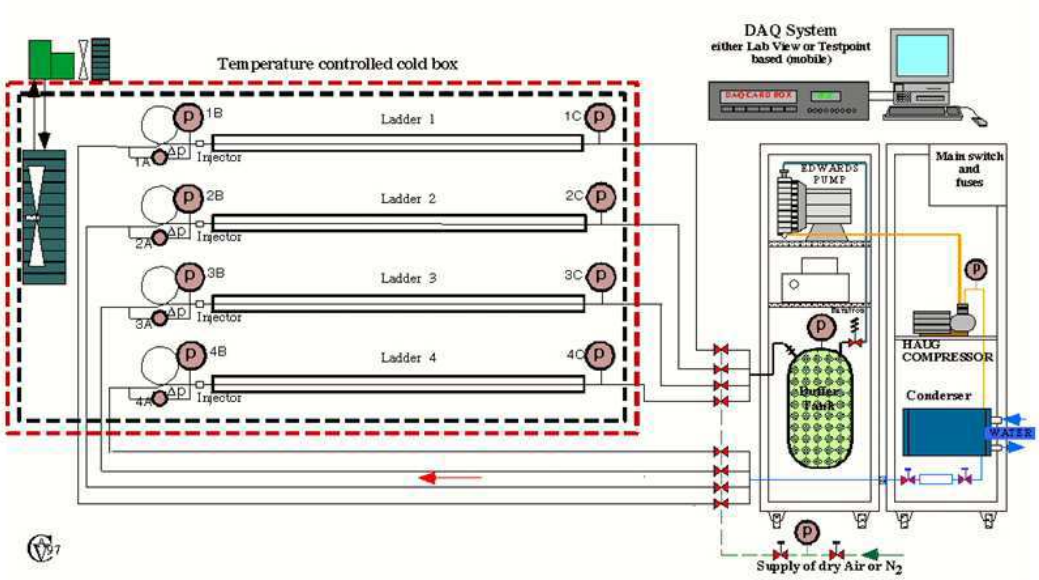

Fig 4.9. The C_3F_8-adapted developmental fluorocarbon evaporative cooling test stand.

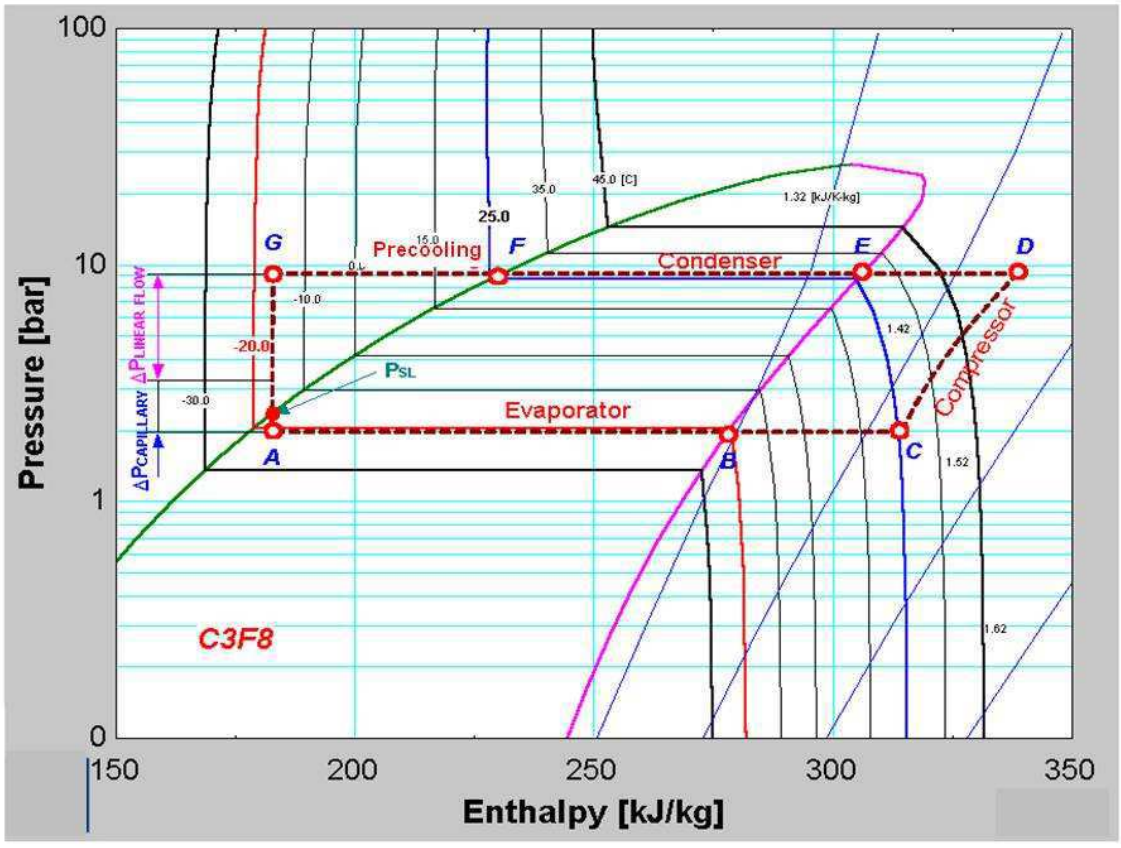

Fig 4.10. The C_3F_8 cooling cycle on the pressure-enthalpy diagram; modified recirculator with warm condenser, vapour compressor, liquid precooling and variable flow regulator.

Figure 4.11a illustrates a thermo-mechanical model for the on-detector cooling for a quarter disk of the ATLAS forward SCT, supporting 33 silicon micro-strip modules and dissipating 400W. On the "front", heat from two arcs of silicon modules (simulated with resistive heaters) was conducted to the coolant via attachment blocks glued to the 3.6mm ID cooling tubes (Fig. 4.11b). On the "rear" of a real quadrant a third arc of modules provides tracking hermeticity through overlap. A full (4-quadrant) SCT disk would contain 132 silicon modules.

To accommodate thermal expansion effects, each quadrant has two serpentine circuits with 3.6 mm ID tubes, and lengths 2.5 & 3.5m ("A"&"B"), respectively cooling 14 and 19 modules. Each circuit first cools the inner front arc of modules, follows an arc at the outer radius, and then cools the modules on the rear of the panel. Thermal connections to the cooling tube are of several types: some attachment blocks evacuate the simulated 7W power of the module readout electronics ("E"): those along the front outer arc evacuate only ~ 2W of substrate ("S") dissipation (the expected substrate dissipation after 10 year's LHC operation at $10^{34}cm^{-2}s^{-1}$). The innermost front blocks traverse the support, and evacuate, in addition to the 9W (E+S) dissipation of the front inner modules, ~2W from the simulated substrates ("S") of the rear modules. Blocks were of several different heights, and some spanned a gap between joined tubes, presenting lower impedance for heat conduction into the fluid.

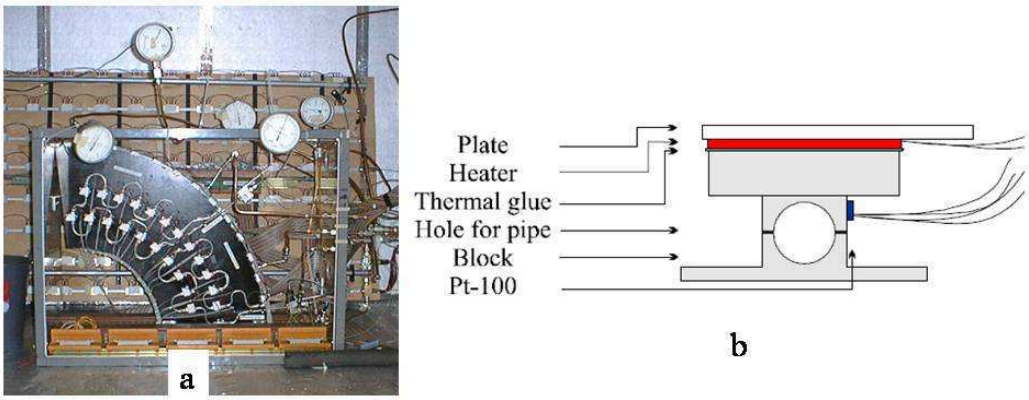

Fig. 4.11a,b. Thermo-mechanical model for on-detector cooling of a quadrant of an ATLAS SCT disk (b) example of simulated silicon microstrip module (electronics or substrate- see text) heat sink to cooling tub

Figure 4.12 illustrates the temperature profile along the 250cm "A" tube and the cooling blocks associated with it, for C_3F_8 cooling at full power dissipation (7W (E); 2W (S)) and a boiling pressure 2.3 bar_{abs}. The

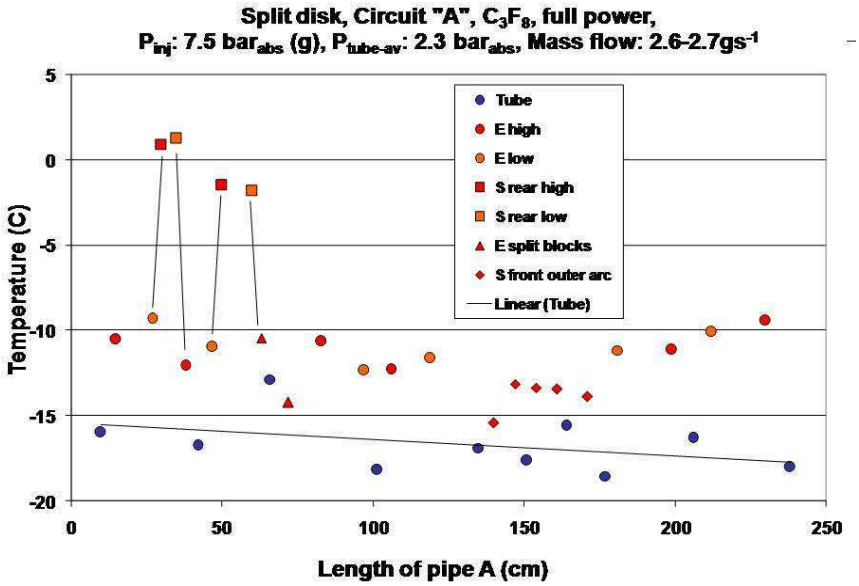

Fig. 4.12. Temperature profile along "A" tube and associated cooling blocks of a thermo-mechanical prototype SCT disk sector: C_3F_8 cooling at full power dissipation (7W (E); 2W (S)) with a boiling pressure 2.3 bar_{abs}.

temperature of all blocks, with the exception of the rear "S" side of the double block (since redesigned) were below –7ºC, and the temperature gradient along the tube was only ~2ºC. By decreasing this boiling pressure, the temperature of the test structure could be further, uniformly, reduced. C_4F_{10} cooling showed inferior performance: at full power dissipation the "A" tube structure could not reach the target temperature of –7ºC due to the large pressure gradient along the 3.6 mm ID tube, generated by the relatively large volume of vapour produced at low boiling pressures of around 500 $mbar_{abs}$. The situation in the longer (350 cm) "B" circuit was correspondingly worse.

The SCT barrel was also a demanding cooling requirement, with pairs of 160 cm barrel staves connected in series and then in parallel to form "quartets" as shown in Fig. 4.13. Coolant is injected through a capillary to a series pair of staves with a total tube length of 3.2m. A common exhaust is shared with a second series pair of staves mounted in parallel. This manifolding is presently used in the 44 quartets of the 4 tracking layers of the operational SCT barrel.

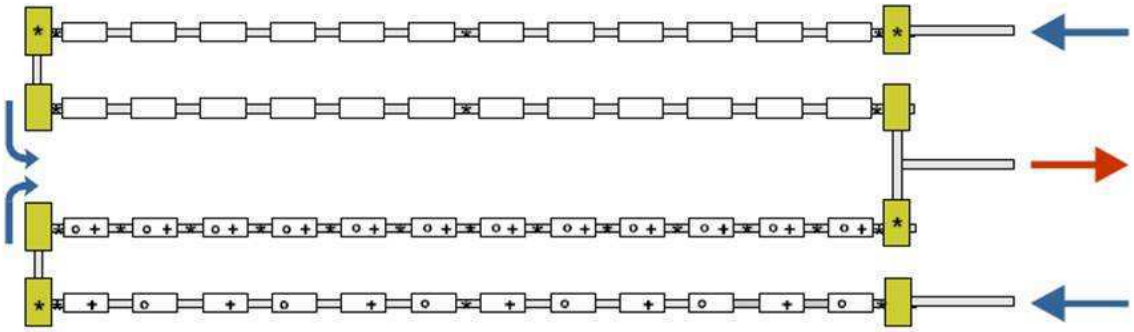

Fig. 4.13. Thermo-mechanical model for the on-detector cooling of an ATLAS SCT barrel shared-output series- parallel "quartet" of 160 cm long 'staves', each stave carrying 12 simulated modules, each dissipating 9.2W .

In the prototype thermo-mechanical structure, each stave carried 12 heater plates attached with thermally conductive glue to one 7.2 mm side of a flat-walled oval tube having an equivalent I.D. of 2.7mm. A total of 64 temperature sensors are attached to the plates and on the tubes between them. Plates were laminated from two (60 x 20 mm) pieces of aluminum with thermally conductive glue, to investigate the layering of the detector module, in which the hybrid supporting the readout electronics ("E") is mounted on top of the silicon substrate ("S"), which has closer attachment to the cooling tube. Temperature sensors are mounted on the E and S sides of the blocks.

Figure 4.14 shows sample data taken with C_3F_8 at 10W/block. The temperature (pressure) gradient between the input of the first series stave and the output of the second is ~7°C (1.1 bar). Block temperatures vary between

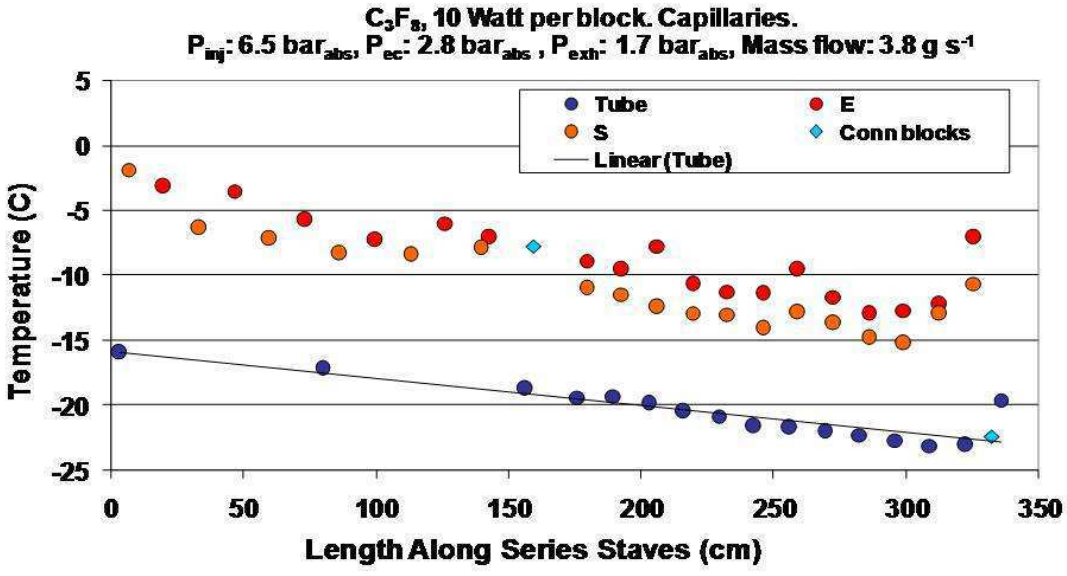

Fig. 4.14. Temperature profile along two series staves of a thermo-mechanical prototype SCT barrel quartet C_3F_8 cooling at full power dissipation (220 W) with average boiling pressure ~ 2.3 bar_{abs}.

-2°C and -15°C. Although the target (S) temperature of -7°C is not met on the first four blocks at the beginning of the upstream stave the majority of the 24 simulated modules on the two series staves were within the temperature specification. It was concluded that the 2.7 mm ID of the cooling tubes in the thermo-structure was insufficient to evacuate the vapour produced from ~240W dissipation of two staves in series. The tube internal diameter was increased to 4 mm equivalent in the production SCT staves.

The good results with SCT structures were followed by a discovery that the dissipation in pixel barrel staves was likely to increase to around 100Watts for staves in layers 1 & 2 and 144W for staves in the B layer. Studies were made with the modified circulator of Fig. 4.9 using both C_3F_8 and C_3F_8/C_4F_{10} mixtures as illustrated in Fig. 4.15.

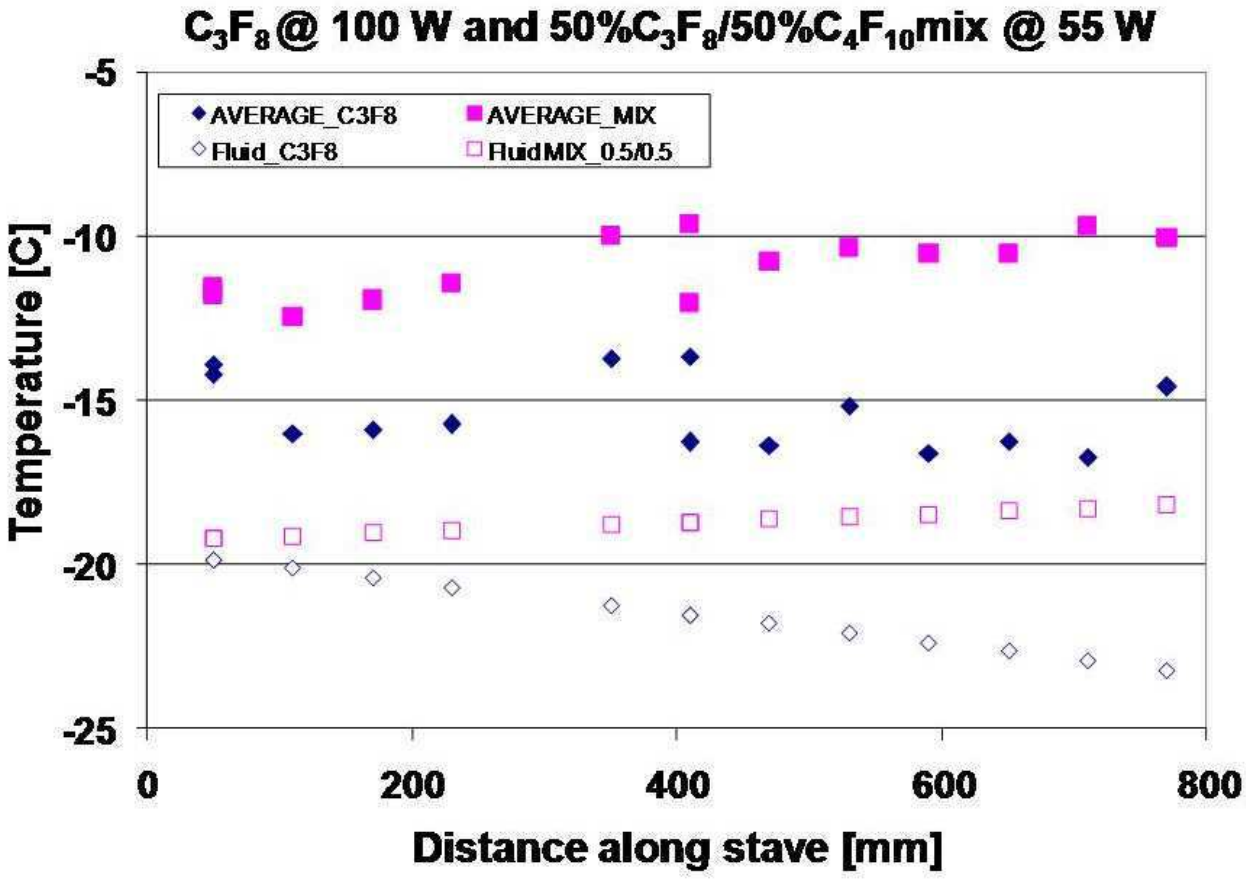

Fig. 4.15. Temperature profile along a thermo-mechanical prototype pixel stave with C_3F_8 (◊) and 50%C_3F_8/50% C_4F_{10} (□)cooling at 100W and 55W dissipation respectively.

It was found that the ID of the prototype pixel stave tube was insufficient to maintain the -7°C silicon temperature with the 50%C_3F_8/50%C_4F_{10} mixture at dissipations exceeding ~60W, but that cooling to the target temperature was possible at the highest envisaged dissipation using C_3F_8. It was subsequently required that pairs of pixel staves be connected in series to halve the number of supply and return lines to entering from each end of the tracker volume. It proved possible to accommodate this requirement, also, keeping the warmest module (ie. that nearest the input capillary - in the absence of poor thermal contact elsewhere) below -7ºC using C_3F_8 cooling.

It was important to study the efficiency of heat transfer between the evaporating coolant and the wall of the cooling tube independently of effects related to bad thermal coupling of the tube to the structures to be cooled; often a problem at the module level in prototype SCT and pixel thermo-mechanical prototypes.

The heat transfer coefficient (HTC), h ($Wm^{-2}K^{-1}$) is related to ΔQ , the power to be evacuated into the coolant through a contact area A(m^2) via

$$h = \frac{\Delta Q}{A \cdot \Delta T \cdot} \tag{4.4}$$

where ΔT is the measured temperature difference between the heated surface and the cooling fluid.

Heat transfer coefficients were measured on a 1.6m long simplified SCT stave with 12 copper blocks soft-soldered onto a 1.6 m long cupronickel tube of 3.6mm ID. On each block were a ceramic heater and a PT100 sensor. PT100's were

also fitted to the coolant tube near each block, allowing *h* to be measured at 12 positions from (block-tube) temperature differences and knowledge of the dissipation at each block and its contact area with the tube. Typical measurements for the different fluids in this tube are shown in Fig. 4.16, and varied in the range 2➔5.10^3 $Wm^{-2}K^{-1}$ depending on power dissipation. The highest HTCs were seen in the case of C_3F_8, which was expected due to its higher s.v.p. – there being more molecular collisions with the tube wall in a given time interval - while the lowest were seen with 50%C_3F_8/50%C_4F_{10} mixture, which was initially a surprise since its s.v.p. was higher than pure C_4F_{10}. Additional mixtures in different ratios of C_3F_8 and C_4F_{10} were made to further investigate this effect, confirming (in Fig. 4.17) reduced HTCs for mixtures relative to those of their pure components. This phenomenon has, however, been reported elsewhere [63], [64].

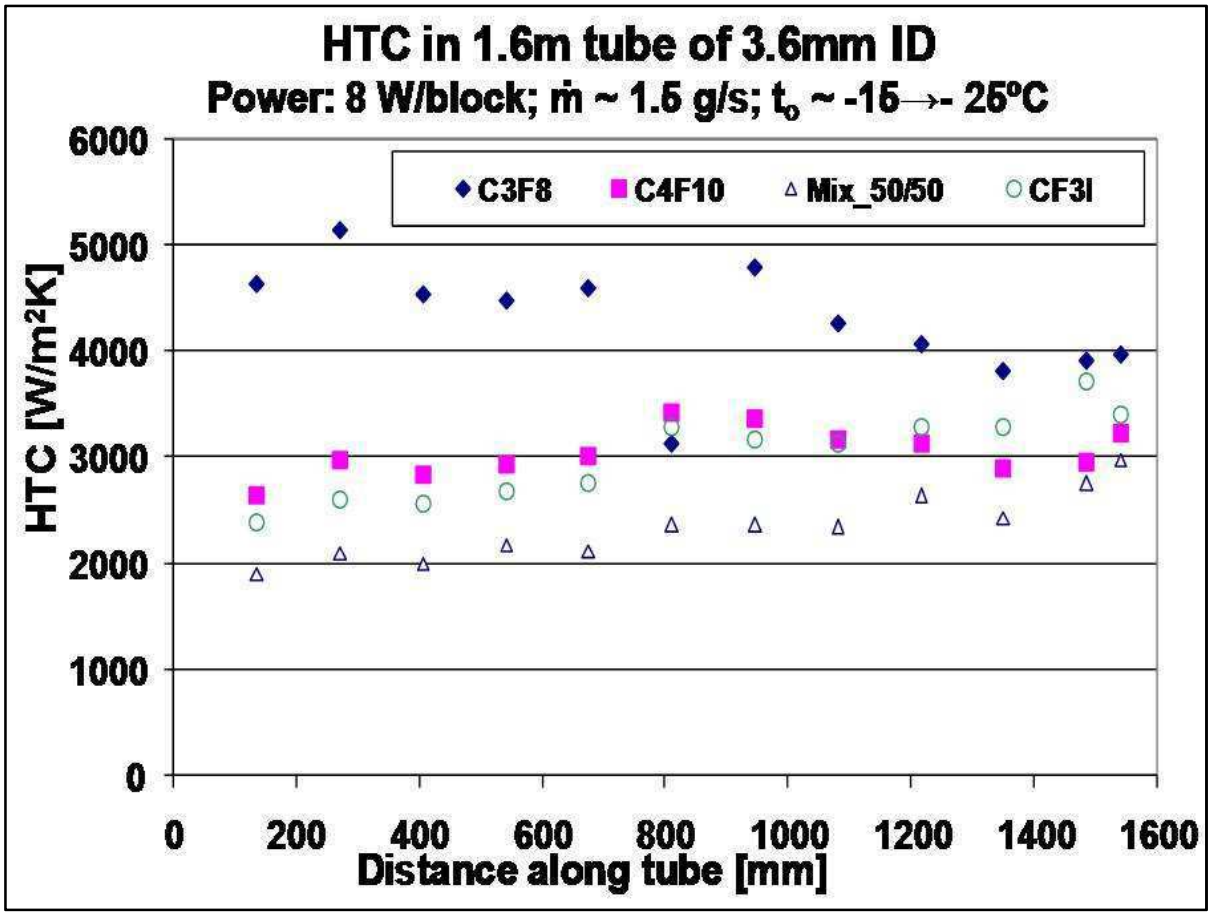

Fig. 4.16. Measured Heat Transfer Coefficient in various evaporative refrigerants, including C_3F_8, C_4F_{10} and 50%C_3F_8/50%C_4F_{10} (after [65]).

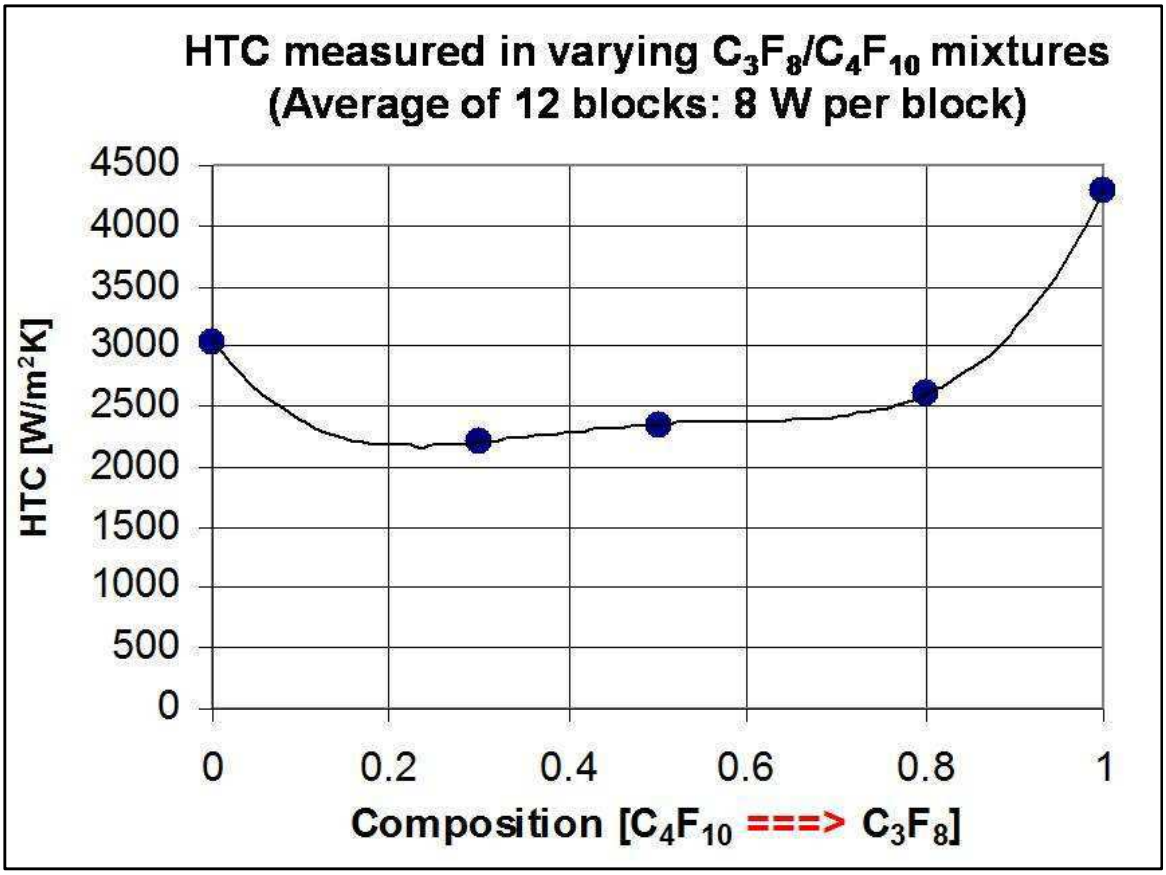

Fig. 4.17. Measured heat Transfer Coefficients in a 3.6mm in varying mixtures of C_3F_8 and C_4F_{10} (after [65]).

4.3.3. Sonar analysis of C_3F_8/C_4F_{10} mixtures

It was realised that sonar gas analysis as used in the SLD CRID could be useful in the verification of C_3F_8/C_4F_{10} blends of interest as evaporative coolants with evaporation pressures around 1 bar_{abs} in the range -15➔ -25°C.
A temperature-controlled tube was built to allow measurements of sound velocity in C_3F_8/C_4F_{10} vapour mixtures at temperatures from -20➔+40°C and pressures in the range 1-5bar_{abs}. Original SLAC driver, amplifier/receiver and timer electronics were used in conjunction with a National Instruments multi-function card which acquired temperature data and counted the number of 4MHz clock pulses counted during the sound flight time through the gas. Look up tables of sound velocity *vs.* C_3F_8/C_4F_{10} relative composition were created at various temperatures and pressures [65] from sound velocity measurements made in calibration mixtures covering the full C_3F_8/C_4F_{10} dynamic range. A Labview ® graphical user interface compared the on-line measured velocity with the look-up table to yield the concentration in real time, as illustrated in Fig 4.18 [66].

The sonar tube enabled us to demonstrate the use of sound velocity to find the saturation line of single fluids, or of the lower boiling component in the binary mixture. The procedure is demonstrated in Fig. 4.19 [67] for a 60%C_4F_{10}/40%C_3F_8 mixture at -18°C. The sound velocity falls as the pressure (density), is increased towards 0.05MPa, beyond which the C_4F_{10} condenses, leaving a mixture progressively enriched in lighter C_3F_8. The pressure of the saturation cusp at this temperature is in good agreement with the predictions of the NIST REFPROP package [66].

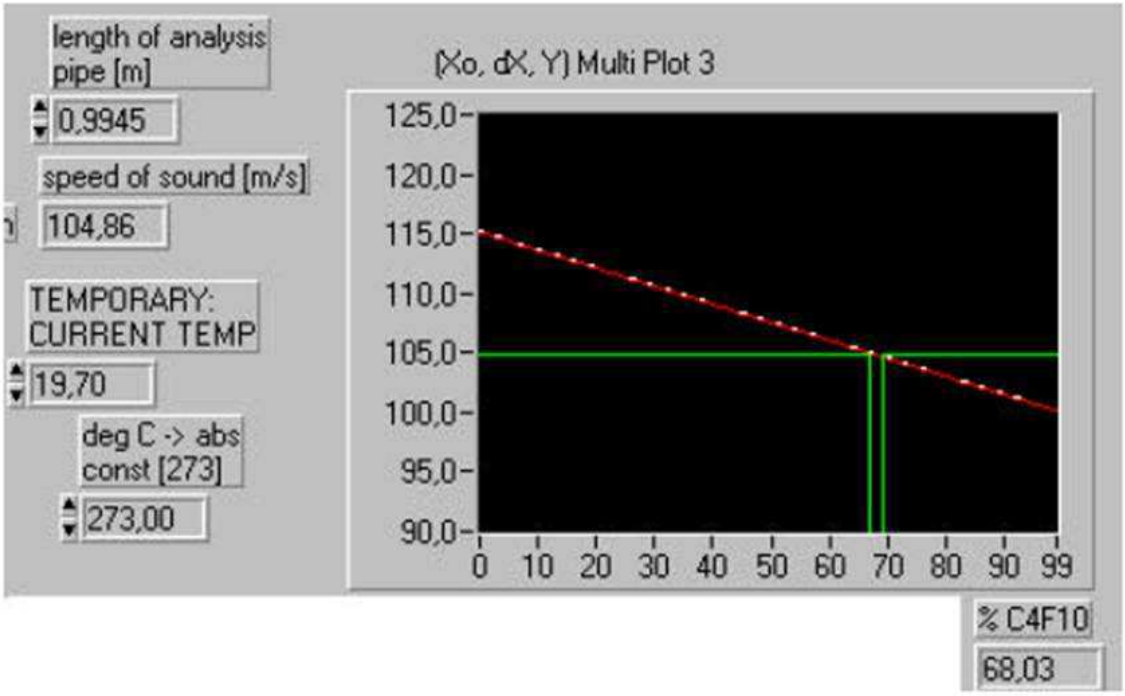

Fig. 4.18. Labview ® graphical user interface for real time presentation of C_4F_{10}/C_3F_8 mixture ratio by comparison of measured sound velocity(here at 1 bar abs and 19.7°C with stored calibration table.

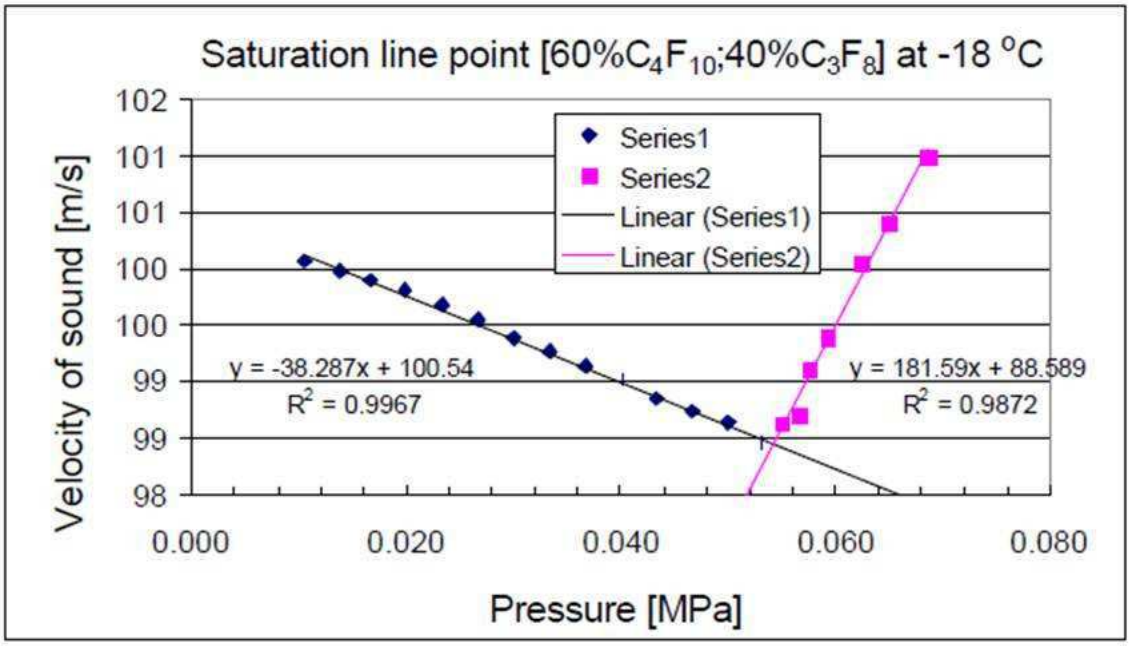

Fig 4.19 Sound velocity determination of the condensation pressure of the heavy component in a C_4F_{10}/C_3F_8 mixture. (after[65]).

4.4. Progression towards a dynamically flow-controlled multi-channel cooling system

In a second cooling review in May 1999 [68] the pixel and SCT communities were encouraged to find a common coolant compatible with the then existing mechanical designs for the structures and to create a substantial 'demonstrator' system of parallel cooling circuits with a representative compressor/condenser circulator, flow and evaporation pressure control and tube runs in realistic diameters and lengths.

The natural candidate coolant was C_3F_8 since neither C_4F_{10} nor mixtures of C_3F_8/C_4F_{10} were adequate due to the high vapour volume flow and large pressure drops in the exhaust tubing produced at the lower evaporation pressure.

CF_3I, though a capable coolant with an attractive evaporation pressure of around 1 bar abs at -25ºC, was found to be very unstable under irradiation and was for this reason abandoned. The choice of C_3F_8 also allowed a simplification of the cooling circuit of fig 4.9, with the suppression of the scroll vacuum pump first stage, since the C_3F_8 vapour arriving at the piston compressor input had a pressure in the range 1-2 bar_{abs} depending on evaporation temperature. A much larger capacity piston compressor was purchased for the demonstrator; capable of handling a vapour flow equivalent to at least 6KW of heat absorption, evaporating C_3F_8 at a temperature of around -25ºC. Other developments included the use of a dome-loaded pressure regulator[45] to set the flow of coolant, and a dome-loaded back-pressure regulator (BPR) to set the evaporation pressure (and hence the evaporation temperature) in each circuit. These devices respectively regulate their output or input pressure to follow an analog air command pressure applied to the opposite side of the diaphragm to the process fluid.

Table 4.4 details the configuration (power, # inputs & outputs) of parallel C_3F_8 evaporative cooling circuits in a 6KW multichannel demonstrator built at the request of the May 1999 ATLAS ID cooling review, for control system studies. The demonstrator cooling circuits used simple thermo-mechanical models of 6 SCT 480W 'quartets', 9 pixel 208W series stave pairs and sectors of SCT and pixel disks. All these structures were housed in a cold box which could be cooled to ~ -8ºC with an internal R404A refrigeration pack to simulate the cold N_2 environment planned to surround the SCT and pixel detector in the final installation.

Table 4.4 configuration of parallel C_3F_8 evaporative cooling circuits in the 6KW multichannel demonstrator

Layer	Cooling Circuits	Staves /Circuit	Capillaries / circuit	Power/ Cct (W)	Regulated Input Flows	Regulated Exhausts (Boiling Pressure)
Part of SCT 4 layer	2	4 (2 series pairs in parallel)	2	480	4	2
Part of SCT 3 layer	2	4 (2 series pairs in parallel)	2	480	4	2
Part of SCT 2 layer	1	4 (2 series pairs in parallel)	2	480	2	1
Part of SCT 1 layer	1	4 (2 series pairs in parallel)	2	480	2	1
Part of Pixel 2 layer	4	2 (series)	1	208	4	4
Part of Pixel 1 layer	3	2 (series)	1	208	3	3
Part of B layer	2	2 (series)	1	208	2	2
SCT disk/4	1	3 arcs in parallel (2 front 1 back)	3	110	3	1
Pixel disk/6	2	2 arcs in parallel (1 front 1 back)	2	96	2	1
TOTALS				5274	26	17
Comparison for SCT 4 full size layer 4				6720	28	14

Coolant was delivered through copper capillaries of typical length 0.8 m and internal diameter 0.8 mm. The pixel series stave and disk sectors were "one-in one-out", while the SCT quartets and disk quadrant were "two–in one-out" and "three-in one-out" respectively, reflecting a decision taken by the SCT to reduce pipework and services cross sections. The total power dissipation, numbers of capillaries and exhausts was similar to that of the outermost SCT layer illustrated with its services in figure 4.20. In all cases (pixel and SCT) capillary fluid delivery and vapour exhaust were arranged to be on the same end of each cooling circuit, with half the circuit tubing connecting to each side of the detector. Fig 4.21 illustrates the simple series pixel staves used in the demonstrator cold box: the 'one-in one-out' geometry is visible. Figs. 4.22 & 4.23 illustrate the 3-D

[45] An analog to the dome loaded pressure regulator is the SCUBA diving regulator which delivers breathing air at the ambient pressure: the demand pressure on the diaphragm being determined by the local ρgh hydrostatic column of sea water.

nature of the demonstrator which, in addition to simulating the lengths and inner diameters of the coolant tubing (including capillaries), also reproduced the relative heights of coolant delivery and recovery hardware on the ATLAS service platforms and the detailed routing of services through the magnet to the inner detector.

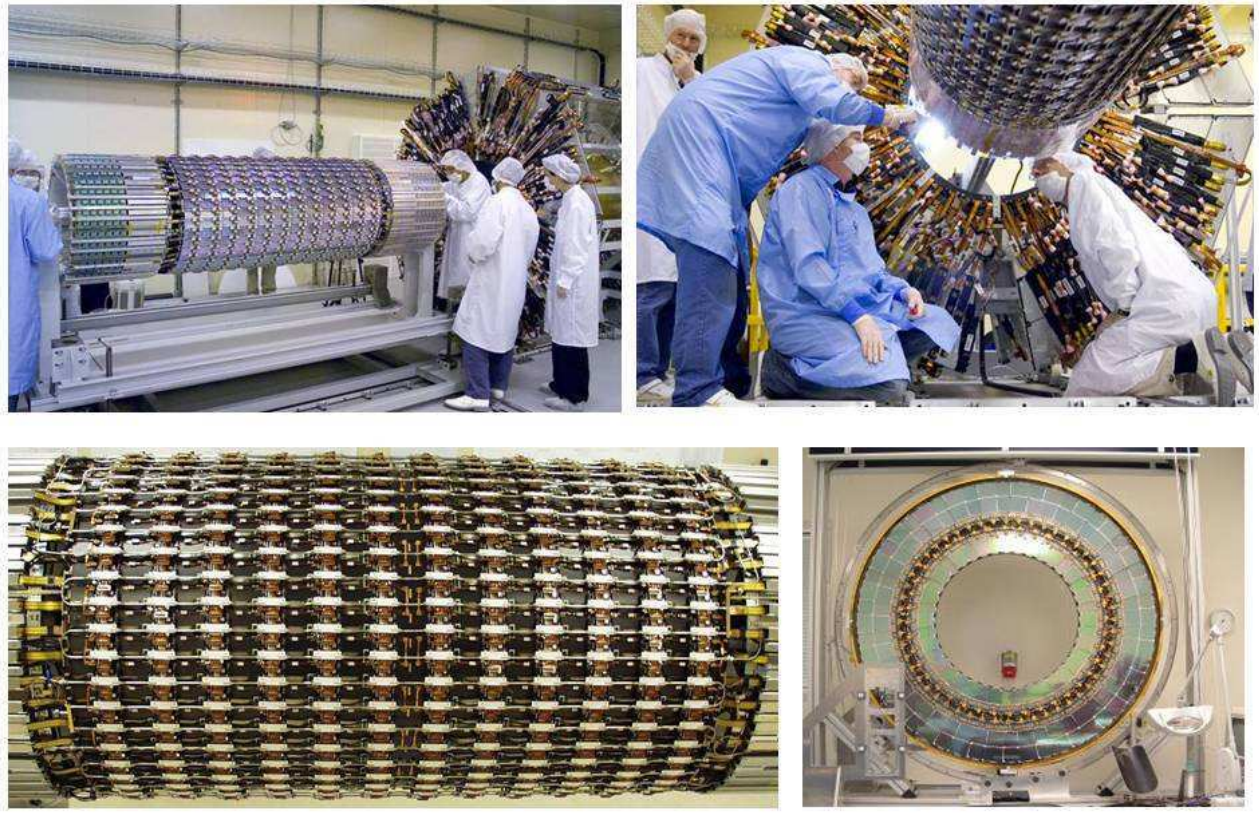

Fig. 4.20 Illustration of the SCT on detector evaporative cooling channel 'quartets' on the outermost SCT layer 4, together with one half of the coolant delivery and exhaust tubing cooling. Complete SCT forward disk for comparison.

Fig. 4.21 Pixel dummy thermal series staves built for 6kW evaporative cooling demonstrator

Fig 4.24 illustrates the piston compressor and condenser. This compressor was a single stage multi-cylinder oil-less device capable of compressing C_3F_8 from a minimum input pressure of around 800 $mbar_{abs}$ to a maximum output pressure of ~ 9 bar_{abs} (a similar compression range to the much lower capacity single cylinder compressor used in the preliminary studies). The buffer tank at the input to the compressor was the lowest pressure point in the circuit. The pressure of the superheated (i.e. without accompanying unevaporated liquid)

C_3F_8 vapour in the aspiration buffer was controlled through variation of the suction speed of the compressor, varying the frequency of the 3-phase AC sent to compressor motor between 20 and 60Hz[46]. The flow of coolant to each circuit was controlled in proportion to the circuit heat load to be evacuated using a pressure regulator[47]

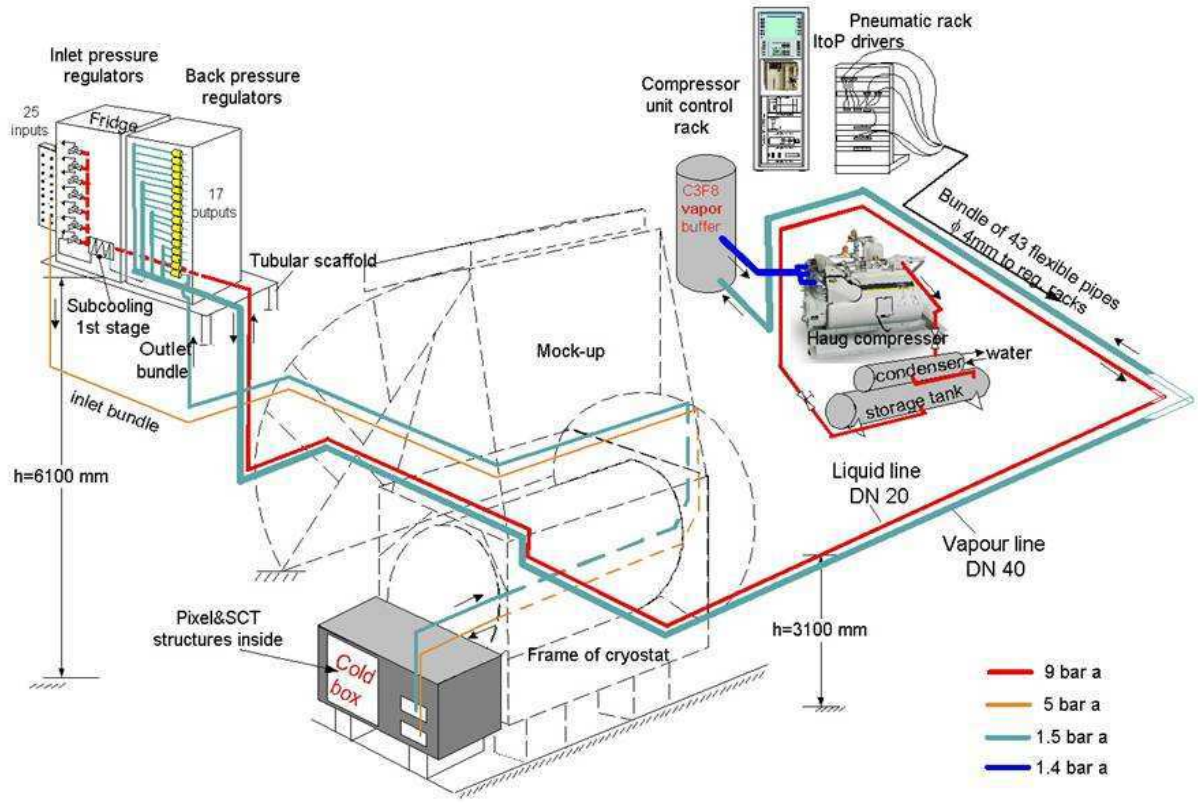

Fig. 4.22. 6kW evaporative cooling demonstrator: three dimensional routings of tubing in the demonstrator between compressor/condenser, flow and exhaust regulator racks and SCT and pixel thermo-structures in cold

Fig. 4.23. 6kW evaporative cooling demonstrator and service model: arrival at the cold box of insulated coolant delivery and exhaust tube bundles from the flow and exhaust regulator racks (CERN Building 175).

[46] Via Motor Speed Controller CIMR-XCAC41P5, Yaskawa Co., 1-16-1 Kaigan, Minato-Ku, Tokyo, 105-6891 Japan
[47] Model 44-2211-242-1099: Mfr: Tescom, Elk River MN 55330, USA

Fig. 4.24. Piston compressor (oil-less, single stage, maximum output pressure 8bar$_{abs}$) and condenser (foreground) used in multi-channel C_3F_8 evaporative cooling demonstrator tests; aspiration buffer tank behind.

with "dome-loading"; one side of the regulator membrane was exposed to the process fluid (liquid C_3F_8) while the other was pressurized (inside a brass dome) with N_2 gas of variable pressure. The liquid C_3F_8 pressure at the regulator output – and hence at the capillary input - tracked the varying pressure of the N_2 'command' gas applied to the dome. This analog command pressure was varied in the range 1-9 bar $_{abs}$ using a DAC-controlled "***I2P***" or "***E2P***" actuator[48]. The control strategy was to maintain the temperature at a point downstream of each thermostructure a few degrees above the evaporation temperature selected for the circuit. This evaporation temperature was itself set using a dome-loaded BPR[49] in the exhaust of the cooling circuit, the command pressure also set using a DAC and intermediate V2P actuator. The BPR regulated the (ingoing) pressure of exhaust C_3F_8 vapour ***upstream*** of its membrane to correspond to the analog command pressure; in contrast to the flow regulator which regulated the (outgoing) liquid pressure ***downstream*** of its membrane. In practice the evaporation pressure in each circuit was chosen from knowledge of the desired temperature of the simulated silicon modules, taking into account the offsets occurring in the intermediate material linking them to the cooling tubes. It was almost a 'set and forget' parameter, unlike the flow rate which was intended to be dynamically varied.

The coolant flow strategy was to always deliver enough - but not too much - fluid (which would otherwise flood and chill the exhaust tubing passing other moisture-sensitive detectors) to cool the required heat load, which in the final system could vary according to the number of powered modules attached to the cooling tube. All silicon real (and most simulated) microstrip and pixel modules are equipped with individual thermal interlocks between their on board NTC (Negative Temperature Coefficient) thermistor and their individual module power supply providing the substrate depletion voltage and front end LVDC. Power ON/OFF could be by operator intervention, with automatic power off in

[48] "Volts to Pressure" or "Current to Pressure" acronyms. E.g. Model PS111110-A: Mfr Hoerbiger Origa GmbH, A-2700 Wiener-Neustadt, Austria: Input 0-10V DC, Output pressure 1-11 bar$_{abs}$: also 4➔20mA input for long distance signalling

[49] Model 26-2310-28-208: Mfr: Tescom Corp., Elk River, MN 55330, USA

the case of over-temperature for reasons independent of the activity of the cooling circuit, for example to a de-lamination of the module from its cooling attachment. The cooling system had, therefore, be able to react to such spontaneous effects.

The flow control strategy was similar to that used in refrigerators where a flow control valve is located on the input to the evaporator with mass flow regulated via feedback from a sensor on the exhaust downstream of the evaporator. The sensor on the exhaust may be a mechanical device such as a vapour pressure bulb activating the flow control valve through a capillary (dome loading) - as shown in Fig. 4.25 - or an electrical probe (RTD, NTC or equivalent) with electronic control of the valve. Such on-evaporator devices were completely excluded in the ATLAS application owing to the extra material they would introduce and also due to the lack of serviceability in the innermost regions of the tracker. Flow and evaporation temperature control devices could only be accommodated in accessible locations on external service platforms, as simulated in the demonstrator. In ATLAS these are 30 metres from the inner tracker silicon, *as the tubes run*.

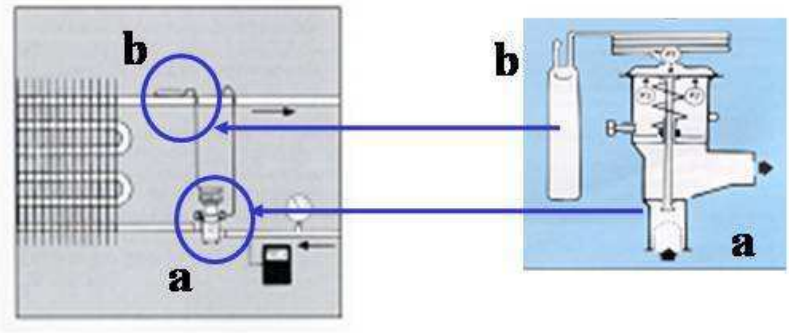

Fig. 4.25. On-evaporator dynamic flow regulation with dome-loaded flow valve and vapour pressure bulb; a combination excluded in the ATLAS application due to $\%X_0$ considerations at the on detector evaporators.

Figure 4.10 illustrated the C_3F_8 thermodynamic cycle used in the small scale and demonstrator tests. Of considerable interest is the high pressure liquid region beyond the left extent of the thermodynamic "dome". In this region, if the liquid leaving the condenser is precooled before injection into the capillary, more of the available enthalpy of evaporation (the available width of the bi-phase "dome") at the evaporation temperature can be used. The ideal is to cool the liquid down to the (vertical extension of the) evaporation isotherm before injection through the capillary, so that all of the enthalpy at the evaporation temperature (around 100J / gm of injected liquid) can be used, minimizing the required mass flow. The demonstrator was intended to fully exploit this precooling with the liquid flow regulators kept cold and the tubing between the regulators and the local capillaries in the ID volume held within cooled insulated bundles, as visible in the photographs of Fig. 4.23.

Fig 4.26 illustrates the racks containing the manifolded liquid flow regulators (a) and the evaporation pressure-controlling back pressure regulators (b). The liquid flow regulators were housed in a freezer cabinet with the liquid from the condenser precooled in a concentric heat exchanger before entering the manifold supplying the flow regulators. An interesting feature of this precooling was that it used a counterflow of evaporating C_3F_8 in the outer concentric jacket of a coiled copper heat exchanger, the central tube containing the C_3F_8 liquid to be sent to the thermostructure cooling circuits. The mass flow and evaporating temperature of this precooling loop were controlled by the same types of liquid flow and vapour BPRs as on the thermostructures themselves with the precooling loop evaporation pressure set to a similar value as that on the thermostructures.

Needless to say, the bundles of cooling tubes between the cooled liquid regulator rack and the cold box which simulated the cold nitrogen environment around the SCT and pixel detectors of the final installation needed to be insulated to prevent the liquid warming up on its simulated path through the ATLAS magnets. In practice passive foam insulation was found to be insufficient for this. A pair of additional 'tracer' cooling tubes was incorporated with the C_3F_8 liquid delivery tubes to the thermostructures under the insulation of each tube bundle. As with the precooling heat exchanger in the regulator freezer cabinet, these tracers were cooled with counter-evaporating C_3F_8, one tube in each delivery tube bundle being the C_3F_8 liquid delivery and the other the evaporator return. At the cold box, the two tracer tubes for each bundle were linked with a capillary in a technique called '*cold nosing*'. The configuration of a typical C_3F_8 liquid delivery bundle and its capillaries is shown in Fig 4.27.

Since in the real experiment the coolant tubes pass between other humidity-sensitive detectors and their readout electronics an additional skin of active insulation was also foreseen. This would have added very little extra volume, being only a thin aluminium or copper foil overcoat with Kapton foil heaters and associated temperature sensors bonded

Fig. 4.26. Precooled C_3F_8 liquid flow regulators (a) and evaporation pressure defining back-pressure regulators (b) in the multi-channel demonstrator.

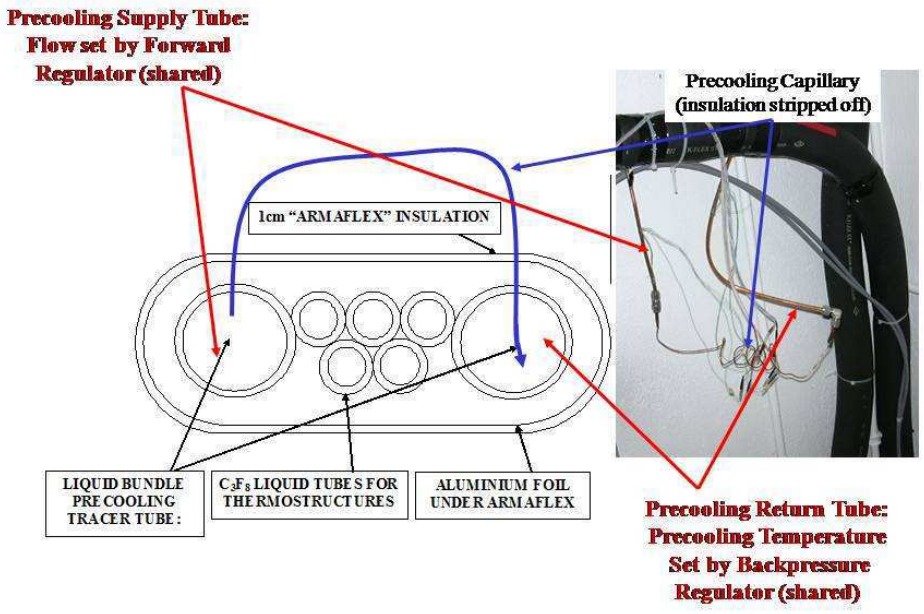

Fig. 4.27.Cross section of an insulated and pre-cooled C_3F_8 liquid delivery tube bundle following the flow regulators in the multi-channel demonstrator. Pre-cooling in the tracer tubes is achieved by counter-evaporation of C_3F_8 using a delivery-point capillary (the 'cold nose') with evaporation pressure defined by a remote BPR.

to the outside. The purpose would have been to compensate any cold leak through the Armaflex® insulation[50] and maintain the other tubes bundle surface above the estimated local dew point of ~18ºC, thereby preventing the formation of surface condensation. This was not installed on the demonstrator system, but was considered a simple system which could wait; similar systems having been employed in multi-tube bundles in the SLD and DELPHI RICH detectors to keep tubes containing TMAE-laden drift gas warm to prevent TMAE condensation.

4.4.1. Demonstration of the dynamic regulation of coolant flow

The combination of pre-cooling the C_3F_8 liquid flow right through to the point of use at the simulated inner detector cold volume allowed the pressure upstream of the capillaries to be varied over a wide dynamic range. The flow through the capillaries was expected to be approximately proportional to their upstream pressure as long as this did not drop so far as to cross the saturated liquid line – the left boundary of the bi-phase "dome" region in fig 4.10.

The " enough - but not too much" coolant delivery strategy was tested using three control system variants discussed below [69]. In each study the temperature of the exhaust tube relative to the evaporation set point temperature was an important indicator that sufficient coolant was being delivered. Temperature sensors and analysing heaters were mounted on the exhaust tubing downstream of a single thermostructure together with a pair of transparent, coaxial vacuum-insulated Plexiglass tubes (Fig. 4.28) to observe whether and how far unevaporated liquid was entering the exhaust.

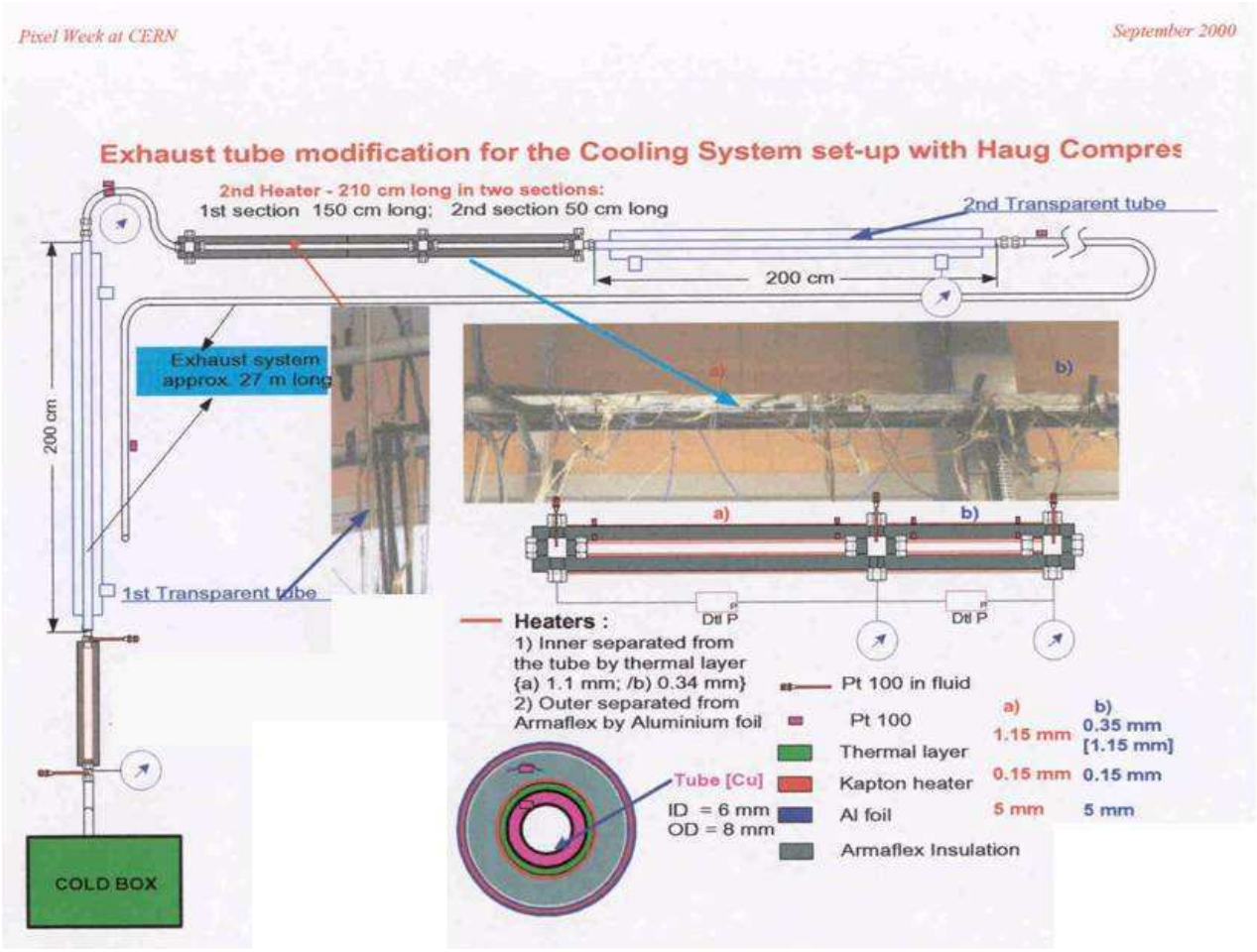

Fig. 4.28.Exhaust tube diagnostics applied to a single cooling circuit to investigate dynamic flow control and to investigate the passage of unevaporated liquid C_3F_8 into the exhaust tube.

[50] Alternative insulation materials with better performance were being considered, including Cryo-Gel® silica aerogel. Mfr: Aspen Aerogels Inc. Northborough MA 01532, USA

Figure 4.28 illustrates the configuration of the test exhaust tube with a two-metre vertical transparent tube followed by a section of tube with heaters and a second two-metre transparent tube. The geometry was intended to model the most defavourable cooling tube run from the ATLAS inner detector volume; specifically whether backed up unevaporated C_3F_8 liquid in the vertical section of the exhaust could increase the evaporation pressure (and temperature) in the theromstructure under test. Two main variants of dynamic flow control were tested, as follows [69]:

(i) Dynamic flow algorithms based on powered modules

Dummy silicon modules with resistive heaters were equipped with indicating relays to communicate their ON/OFF power status to a bit pattern reader. A DC voltage proportional to the number of powered modules was generated and sent from a DAC, through a V2P actuator to apply a proportional pressure P_{CAP} to the dome-loaded liquid flow regulator (and thereby a C_3F_8 pressure P_{CAP} at the capillary input), according to the algorithm:

$$P_{CAP} = P_{EVAP} + m*(\#\text{powered modules}) \quad \text{(i)}$$

where P_{EVAP} is the evaporation pressure and m is $1/9^{th}$ the pressure necessary to remove the heat from 10 modules (around 100 Watts), determined from previous measurements;

Results were good over a wide range of circuit power (varying number of powered modules), and indicated that very little un-evaporated liquid was entering the exhaust. This was manifested by it being possible to maintain the temperature at a point ~50 cm downstream of the evaporation zone a significant margin (>10 °C) above the evaporation temperature T_{EVAP}, over the most of the possible range of circuit power: i.e. from one module powered to all modules powered.

A small heater wound on the tube downstream of the final simulated silicon module , of power 5-10 Watts, sufficed to provide the 'analyzing' heat at the end of a thermo-structure, the aim being to maintain the temperature, T_{EVAP} , corresponding to the maintained evaporation pressure (via the BPR) upstream of this heater and a temperature of (T_{EVAP} +~10 °C) after it (i.e. for the liquid run out to occur under this heater rather than under the last silicon module).

Unevaporated C_3F_8 was seen to bubble up into the first transparent exhaust tube to a distance of around 30 cm only during short transients (around 30 seconds) during rapid simultaneous transitions from all modules powered (around 120W total dissipation on the 12 simulated modules in the thermostructure) to zero dissipated power with no modules powered. Importantly, in all cases, temperatures on powered modules stayed below the upper allowable temperature of -7ºC during the transient (ramp-up/ramp-down of varying numbers of powered modules on the cooling circuit).

Interestingly, when the module dissipation was set to zero and the feedback to the liquid flow regulator disabled with the regulator set to high flow, the vertical column of boiling C_3F_8 (of ascending, foamy appearance) seen in the transparent exhaust did not seem to affect the boiling pressure temperature in the thermostructure, since the foamy liquid in the exhaust was boiling under the defining suction from the compressor input through the BPR, even though this was more than 25 metres away, as in the final installation. (It was commented that "Torricelli had triumphed over the leaning tower of Pisa".)

Nonetheless, a protocol sensing only on the *presence* of power to a module is vulnerable to variations in the individual module power draw, unless adapted to:

$$P_{CAP} = P_{EVAP} + m'* \Sigma_i (POWER_{module(i)}) \quad \text{(ii)}$$

where m' is the pressure/power conversion constant ($mbarW^{-1}$).

This protocol was tested with a high current DC power supply serially-powering dummy silicon modules with its 0-10VDC analog monitoring output (proportional to output current) used as a direct input to the V2P actuator. The results were very similar to those seen in configuration (ii), a short (20-30cm) column of foamy evaporant being seen in the vertical exhaust only under rapid full➔ zero power transitions.

Although performing similarly to configuration (i) above, this configuration would require (in a multi-rail power supply providing the substrate depletion voltage and LVDC for the front end electronics):

- control system access to the monitored and summed currents on several supply rails per module;
- the power supplies to continuously provide this information.

Since this information is computer dependent, being created in the processors of multichannel power supplies and then passed through a communication network, this algorithm is vulnerable to communications failures. A preferred option

was a local flow control system in which the temperature sensors bracketing the analyzing heater on the exhaust tube fed back to the flow regulator with the minimum of intermediate electronics and – more importantly - without the need to communicate with remote computers.

(ii) Direct Proportional, Integral and Derivative control of Fluid Flow.

Direct PID control of circuit flow on the basis of sensed exhaust temperature proved an effective means of control. In a first study, a commercial PID controller[51] directly piloted the V2P driver to keep the temperature at a point ~50 cm downstream of the evaporation zone a significant margin (>10 °C) above the evaporation temperature T_{EVAP}, over the full range of circuit power: i.e. from one module powered to all modules powered. No unevaporated C_3F_8 was seen to bubble up into the first transparent exhaust tube, even in rapid full power ➔ zero power transitions, unlike in the earlier tests.

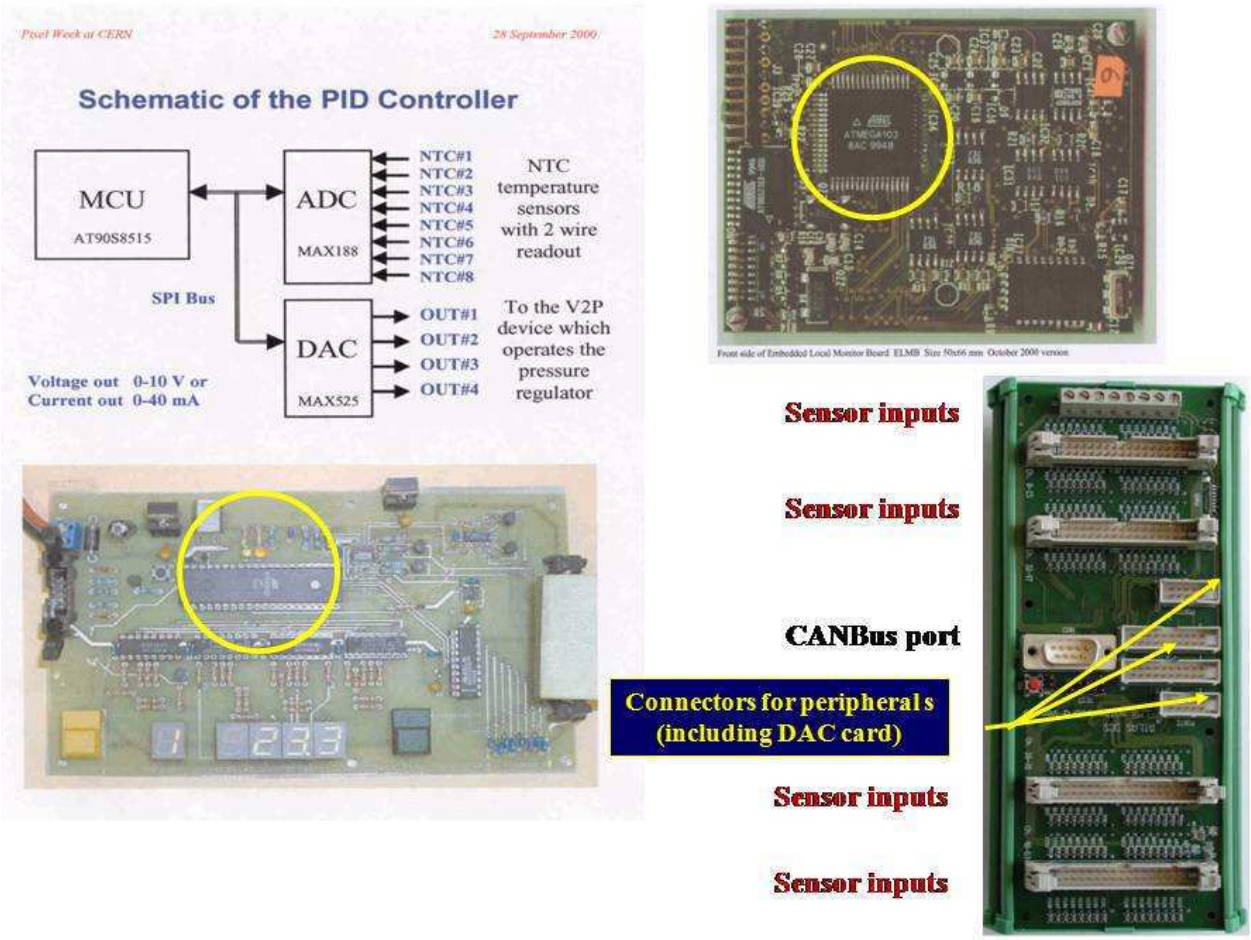

Fig. 4.29. (Left) PCB with AT90S8515 microcontroller incorporating a PID algorithm used for dynamic flow control (Right) ATLAS Embedded Local Monitor Box (E-LMB) handling up to 64 analog sensors, with CanBus communication: supervised ATmega103 microcontroller – no DAC or PID routinely implemented

In a second study, a PID algorithm with a similar algorithm to that illustrated in eq (4.4) was implemented directly in the firmware of a microcontroller chip[52] (APPENDIX 2) of the same family as that used[53] for system programming and monitor functions in the ATLAS "Embedded-LMB" [58] currently deployed in large numbers around ATLAS for slow control activities. The performance of this algorithm was very similar to that of the commercial PID controller, which it was intended to replace much more cheaply using electronics already dispersed around the ATLAS inner detector for temperature monitoring etc.

[51] Model G9FTE-R*E1R-88-N: Mfr: RKC Instrument Co, 16-6 Kugahara 5-Chome Ohta-Ku, Tokyo, Japan
[52] AT90S8515; Mfr: ATMEL Corp, San Jose CA 95131, USA: programmed from C via GNU toolkit
[53] ATMEL ATmega103 128k RISC flash □controller

Figure 4.30 shows a typical on-line display of temperatures on the simulated silicon modules along a thermo-structure based on a series pair of barrel SCT staves equipped with 24 dummy silicon modules with maximum power of 10 Watts per module. The rapid cool-down of the 8 stopped modules towards the cooling tube wall temperature of around -22ºC is evident: the extent of the horizontal scale is around 20 seconds. This illustrates the order of reaction time needed in any dynamic flow control algorithm.

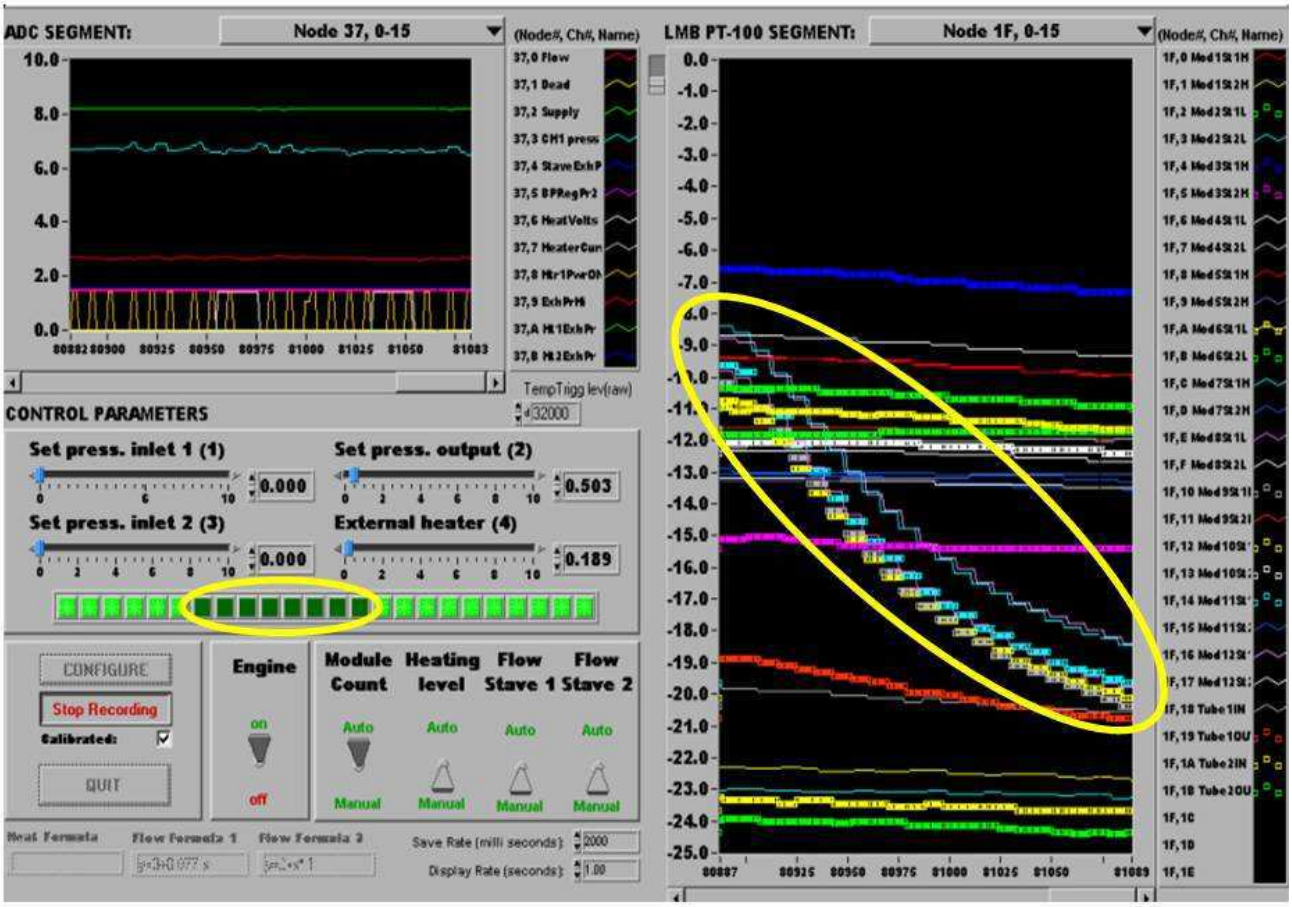

Fig. 4.30. Illustration of the rapid cool-down of 8 stopped modules to near the tube wall temperature on a thermostructure based on two SCT staves in series. Horizontal scale extent around 20 seconds

4.4.2 Configuring the exhaust for dynamic flow operation

Figure 4.26 illustrated the exhaust test stand. An important element of the exhaust study was to determine the temperature profile along the exhaust tube under conditions of :

- dynamic flow control where no, or very little, unevaporated liquid should enter it;
- simulated fault conditions (failure of the cabled PID link between the exhaust temperature sensor and the liquid C_3F_8 flow regulator) allowing unevaporated liquid to enter the exhaust.

The usefulness of the first, vertical, insulated Plexiglass tube has already been described; it showed that no unevaporated liquid was entering the exhaust with the microcontroller-based PID algorithm operating, even under full power ➔ zero power transitions. This tube was followed by a two-metre section copper tube with a double-layered Kapton foil heating surface around it. The inner Kapton layer was intended to boil any unevaporated liquid under fault conditions, while the outer Kapton layer was glued to an aluminium foil jacket covering 5mm of Armaflex foam insulation and was intended to keep the outer surface of the insulated tube above the expected ATLAS cavern dew point of 18ºC. Following the heated section of exhaust was a second two-metre coaxial vacuum-insulated Plexiglass tube used to observe whether unevaporated liquid remained in the exhaust line – effectively testing of the efficacy of the inner Kapton heater in the preceding length of heated tube.

Under maximum flow fault conditions the innermost Kapton heater was found to be relatively ineffective in boiling unevaporated liquid, at least over a length of 2 metres, even when given the equivalent power of the unpowered upstream thermostructure (around 240 Watts). However it was found that even with all the upstream silicon modules unpowered, and passage of the full unevaporated C_3F_8 mass-flow of the upstream thermostructure, that the outer heater *alone* could keep the external surface of the insulation above the expected ATLAS cavern dew point of 18ºC, even for relatively modest applied powers of 10Watts per metre. In some ways this is unsurprising: the external Kapton heater is only compensating the cold leak through the Armaflex insulation arising from the temperature difference between the tube (at T_{EVAP} ~ -25ºC) and the ambient temperature of ~22ºC. Although under such fault conditions the external Kapton heater would have been incapable of evaporating any remaining C_3F_8 liquid (meaning that it could eventually travel through the exhaust tube up to 30 m to the back pressure regulator) it would be a simple matter to add another level of interlock to the flow control system, with a temperature sensor under the exhaust tube insulation at a point several tens of metres distant from the SCT or pixel detector, capable of interrupting the signal to the V2P actuator in the case of such an anomaly. Heat exchangers could also have been added to the individual exhaust tubes immediately upstream of the BPRs if it was considered that their membranes were at risk of exposure to unevaporated liquid or exhaust gas close to the evaporation temperature. This fault heat exchanger might have taken the form of a common heated ethylene glycol bath through which the individual exhaust tubes passed before entering their BPRs. This was a configuration already used extensively in ATLAS cooling installations.

It was decided that the next step should be to add external active insulation with aluminium and resistive Kapton foil heaters to the exterior surfaces of the inlet and exhaust multi-tube bundles of the 3-D demonstrator shown in Fig 4.23, allowing a typical power capacity of 15Watts/metre per input/exhaust tube in each bundle. In the case of the C_3F_8 input liquid tube bundle where the liquid was pre-cooled almost to the evaporation temperature, the same power density was likely to be needed at all times along the entire tube bundle length - from the pressure regulator rack through the ATLAS magnet to the start of the inner detector cold volume. In the case of the exhaust tubes, which - except under fault conditions - would contain only cold vapour warming up on its way through the tubing - a longitudinal 'zoning' system was planned with certain zones (of a few metres length) powered by variation of the duty cycle of a fixed DC voltage, based on the signals from local temperature sensors on the outer surface of the cooling tube bundles.

An inexpensive multi-channel switching circuit based on zero crossing AC relays followed by full wave rectifiers and smoothing capacitors (Fig. 4.31) to provide soft start DC for use in the ATLAS magnetic field,

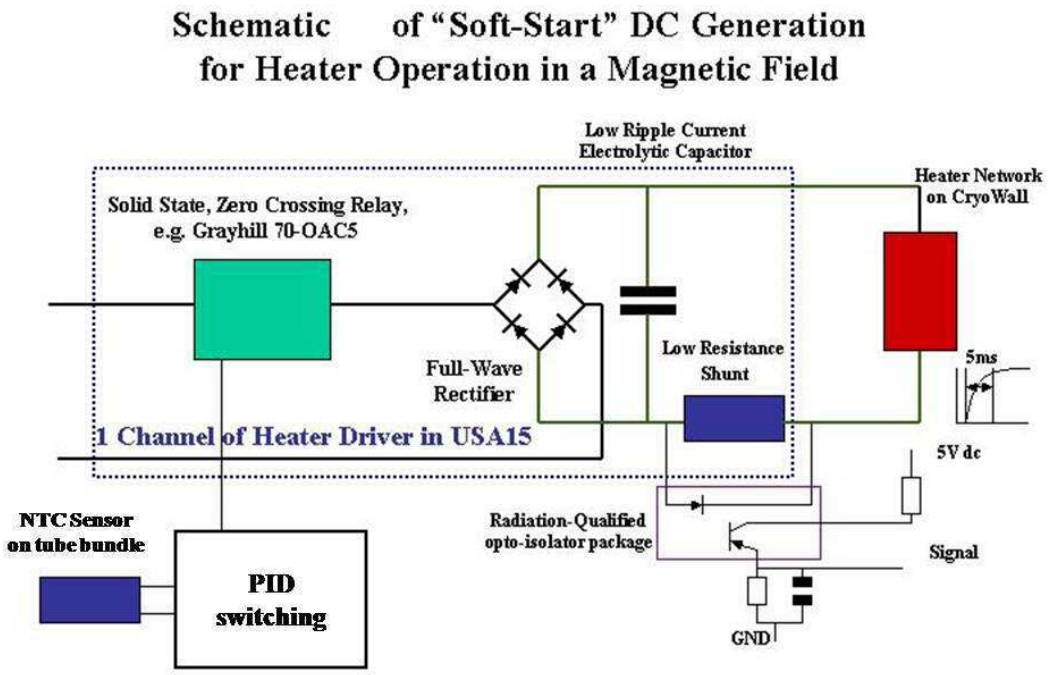

Fig. 4.31. Circuit for 'soft-start' DC heater powering in a B-field - for example on tube bundle active insulation.

based on the heater drivers used in the SLD CRID [42] was under consideration. The zero-crossing AC relay[54] only allows the output to be switched on or off as the input AC phase passes through zero. The DC generated from the rectifier therefore has an intrinsic up ON/OFF ramp time of ¼ of the AC cycle, or 5ms for 50Hz AC, reducing switching transient "BLI" (Tesla-metre-Ampere) forces on the heater wiring.

The presence of current in the heater circuit (not its analog value) was detected using an inexpensive optoisolator circuit with the LED emitter across a low resistance current shunt in each heater circuit.

Further positive considerations included the very compact nature of the heater switching channels (32 being accommodated in a 6U 19" chassis for the SLD CRID (Fig.4.32) and the noise immunity: noise on the DC generated from 50Hz AC is much further from the typical 50 ns RC-CR bandpass of the pixel and SCT front end electronics than the 500kHz or higher chopper frequencies associated with DC switching supplies. This circuit was therefore an attractive, robust and inexpensive candidate for adaptation to the ATLAS application.

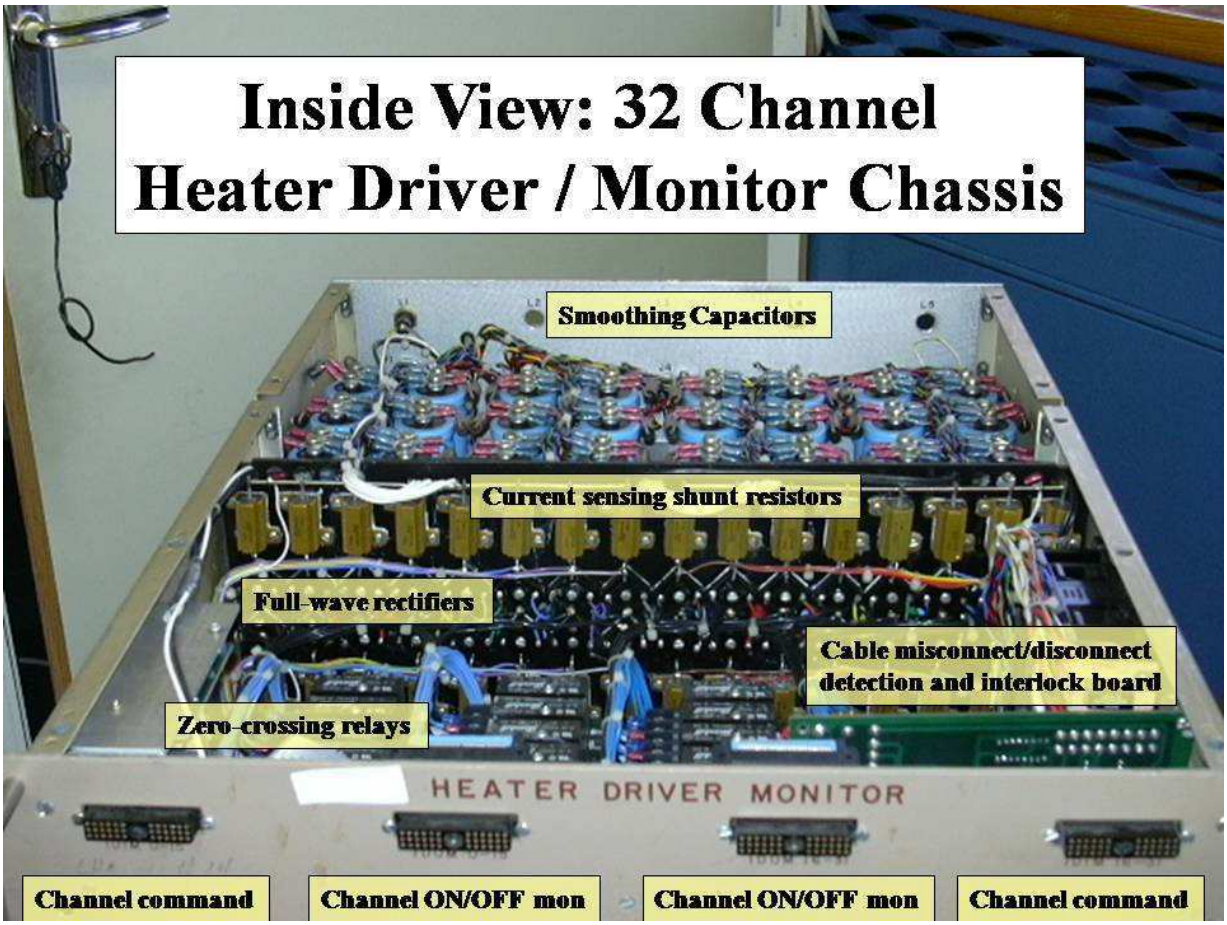

Fig. 4.32. Compact implementation (32 channels in 6U 19" chassis) of zero-crossing AC powered heater driver.

4.4.3. The plan: Proportional, Integral & Derivative (PID) firmware for the ATLAS E-LMB

Figure 4.29 illustrated the ATMEL microcontroller used in the ATLAS E-LMB monitor node, into which we proposed to add a PID algorithm for dynamic C_3F_8 flow control adapted to instantaneous variation of the load on each cooling circuit. Although E-LMBs are daisy-chained to each other and the computers using the industrial field-bus CAN [70] all PID- related activities - sensor acquisition and responses- would be strictly local. This local concept is viable since E-LMBs are specified to tolerate a radiation dose of 1 Gy and 10^{11} neutrons $yr^{-1}cm^{-2}$ and a magnetic field of 1.5T, and can hence be placed everywhere in the ATLAS experimental cavern outside of the calorimeter.

It was estimated that enough memory space remained in the E-LMB controller (given the firmware existing in 200/2001) for 4 separate PID blocks each implementing an algorithm based on a formula similar to eq. (4.4), [APPENDIX 2] allowing 4 cooling channels to be locally controlled. The cooling demonstrator of Table 4.3 and Fig

[54] 70 OAC5: Grayhill Inc., LaGrange IL 60525, USA.

4.23 would thus require 7 ELMBs. In its present form the E-LMB has 64 analog inputs and 24 digital I/O bits. It is not equipped with DAC outputs although these can (and more recently have been) be added using a port connection to an additional mezzanine card. At the time of the successful demonstration of dynamic flow control with pre-cooled liquid there was considerable interest in adding both DAC functionality and of programming a PID algorithm into the E-LMB microcontroller [71], [72]. Collaborators at NIKHEF were beginning to consider this, as evidenced in Fig. 4.33. The DACs proposed would be either LVDC (0-10V output) or 4-20mA output for driving long distance current loops.

ELMB-PID CANopen system v0.1 20-May-2002

ELMB
PID-controller
(framework)

ELMB-based multiple PID-controller
with CANopen interface

software user manual,
version 0.1 (draft)

20 May 2002

Henk Boterenbrood
boterenbrood@nikhef.nl

NIKHEF

1

DAC-module for the ELMB v0.0 18-Feb-2002

ELMB-DAC
16-channel 12-bit DAC-module

for the ELMB

user manual, version 0.0

18 Feb 2002

Jaap Kuijt, Piet de Groen, Paul Timmer,
Daniel Tascon Lopez, Sander Schouten, Henk Boterenbrood

NIKHEF
Amsterdam, NL

Table of Contents

Fig. 4.33. Front pages of proposals to add PID and DAC functionality to the ATLAS E-LMB.[71],[72]

With these additions all the elements for dynamic evaporative flow regulation of pre-cooled C_3F_8 evaporant would have been in place for the development of a multichannel system to meet the combined SCT and pixel circuit modularity of 204 cooling circuits (116 SCT & 88 pixel) and power requirement of ~63kW as indicated in table 4.5.

Sadly, this promising situation was not allowed to continue (for reasons probably best only verbalized). The work on the E-LMB & DAC extensions was also abandoned – the need for it 'evaporated'.

4.5 The as-built ATLAS C_3F_8 evaporative cooling system and its shortcomings

Table 4.5 illustrates the evaporative cooling circuit modularity & power requirement of the as-built ATLAS SCT and pixel detectors. Strenuous claims were made that dynamic control of evaporative coolant flow in such a system was too complicated, too error prone, too counter-intuitive to be workable, and that a simpler system based on a fixed flow – including a 20% 'safety factor' in excess of the worst case silicon consumption - to each cooling circuit, irrespective of its instantaneous power consumption, was preferable -the possibility being to boil off all the un-evaporated liquid in each circuit in a local electric heater in the exhaust tubing located within the inner detector cold volume.

Table 4.5 Evaporative Cooling Circuit modularity & power requirement for the ATLAS SCT and pixel detectors.

Tracking Surfaces (final system)	**Capillaries /circuit**	**No. circuits**	**Power load / circuit (W)**	**Subtotal power load (kW)**	**Nominal mass flow / circuit (g/s)**
SCT Barrel (4 layers)	2	44	504	22.2	7.8
SCT EC (3 circuit disks : 16)	3	64	347	22.2	5.7
SCT EC (2 circuit disks : 2)	2	8	242	1.9	4.5
Pixel Barrel (staves in series)	1	56	220	12.4	4.1
Pixel Discs (sector pairs in series: 6 disks)	1	24	110	2.7	2.1
Pixel service panels	1	8	220	1.8	4.1
TOTAL		**204**	**63040**	**63.2**	**1057**

The concept of 'pre-cooling' liquid C_3F_8 in insulated tube bundles was a ripe candidate for sacrifice. If the cooling were done locally in the inner detector volume it could be argued that the insulation around the liquid supply bundles could be eliminated, saving space in the services passages through the magnet – *value added*. Likewise the use of a vapour-liquid heat exchanger in each circuit close to the detector would allow the cold vapour to cool the incoming liquid *in the same circuit* – a concept called 'sub-cooling'[55] in standard refrigeration terminology. Furthermore, if this heat exchanger were followed by an electric heater inside each exhaust tube, in principle any liquid remaining after the heat exchanger could be evaporated and the temperature of the vapour in the now un-insulated exhaust tube brought to a temperature exceeding the local 18ºC dew point, using the *same* electric heater.

The main selling point of this fixed-flow philosophy was the elimination of all insulation around the liquid supply and return services. The problem with this approach was that as the now-uninsulated tubes passed through service channels containing low mass cables of high heat dissipation, the C_3F_8 liquid would in some places be exposed to temperatures as high as 35-40ºC. At these temperatures, the s.v.p. of the C_3F_8 liquid in the supply tubing would be around 15bar $_{abs}$. It would therefore be necessary to deliver the C_3F_8 liquid to the capillaries at a greater pressure than this to avoid premature boiling in the liquid delivery lines. New-found necessity being the mother of invention, it was – nonetheless - chosen to increase the condenser pressure - and with it the compressor output pressure - from the 8-9 bar_{abs} used in all previous small scale tests and in the demonstrator programme - to around 17bar_{abs}, resulting in a change of compressor from a single stage to two-stage version. Longer capillaries would be needed in the new circulator philosophy, but that was a fairly benign change compared with the others, which passed a final design review in May 2003 [73].

Figure 4.34 shows the schematic of a cooling circuit and the positions of the sub-cooling heat exchanger between the exhaust C_3F_8 vapour and the incoming liquid, and the exhaust electric heater intended to boil any unevaporated remaining liquid upstream of the un-insulated exhaust tubing leading the 30 metres or so to the backpressure regulator rack (effectively the region between the middle and lower boxes in Fig. 4.34). Figure 4.35 [74] illustrates the corresponding thermodynamic cycle with letter references to the various parts of the implemented circuit.

The same-circuit sub-cooling principle as usually implemented (for example in a domestic fridge) is that the cold evaporated vapour leaving the evaporator imparts its cold energy to the liquid arriving at the input of the capillary. This exploits the approximate equality in C_p (the specific heat at constant pressure) of a refrigerant in its liquid and vapour phases (in the case of the SFCs this is around 1000 $J.kg^{-1}.K^{-1}$). It is generally sufficient – viewed on a pressure-enthalpy representation such as Fig 4.10 or Fig 4.35 - that the temperature differences (delineated by vertical isotherms) of the liquid subcooling between the condensation temperature to the input of the capillary and between the vapour warm-up from the evaporation temperature to the start of the compression

[55] In this work 'precooling' refers to the cooling of incoming liquid to a temperature as near the evaporation temperature as possible by an independent external cooling circuit, while 'subcooling' refers to exhaust➔ input cooling in the same refrigerant circuit as that used to extract heat from silicon modules.

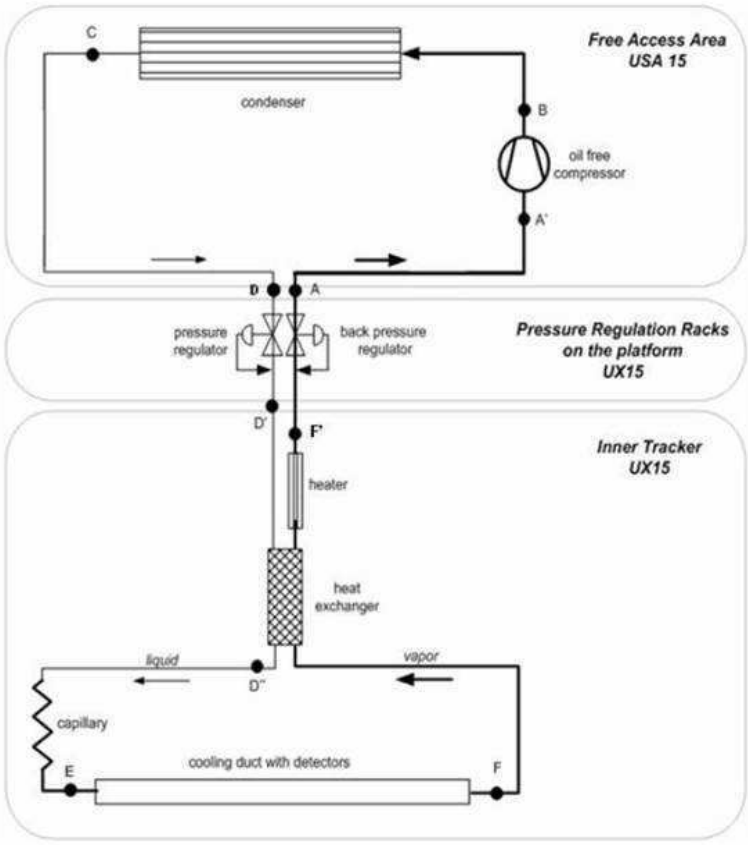

Fig. 4.34. Schematic of an ATLAS fixed flow evaporative C_3F_8 with local heat exchanger and exhaust heater

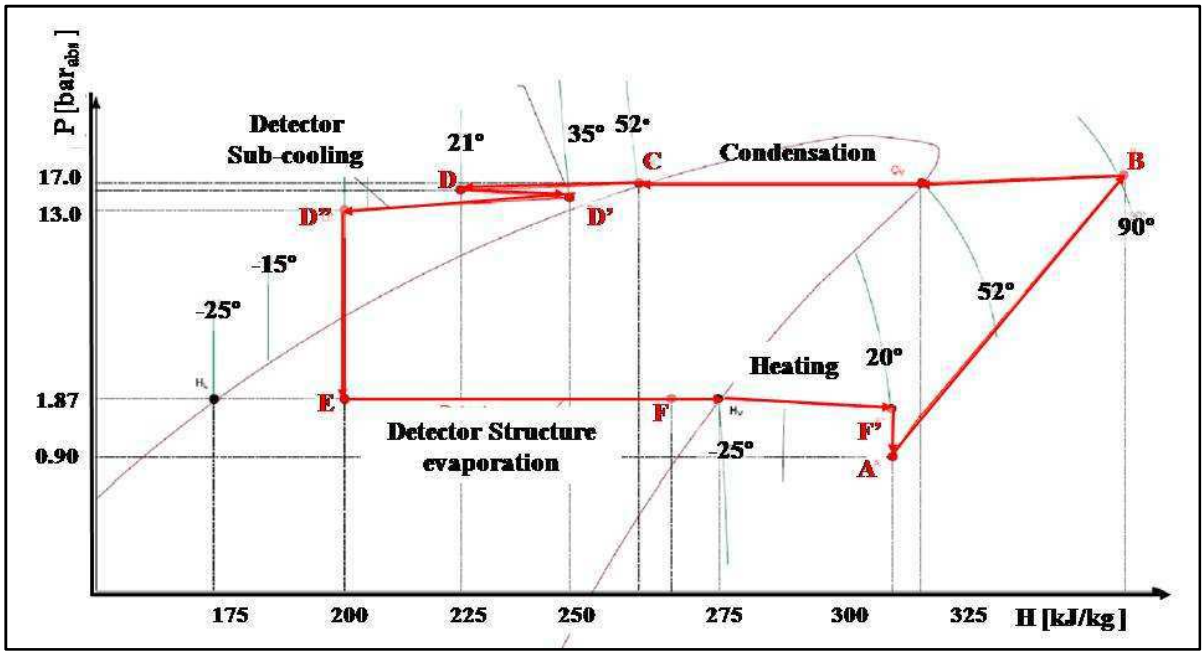

Fig. 4.35. Thermodynamic diagram of the implemented ATLAS fixed flow evaporative C_3F_8 cooling system with uninsulated services, local heat exchanger and exhaust heater.

phase are equal. This is manifested, for example in Fig 4.10, by lengths **FG** and **BC** being equal at a ΔT of 45ºC, although here the pre-cooling would have been achieved by C_3F_8 counter-evaporating in a separate common circuit,

with the combination of dynamically-controlled flow, relatively modest exhaust active insulation and vapour temperature-raising heat exchangers (overflow fault protection) near the back pressure regulator racks on the ATLAS service platforms.

In the ATLAS fixed flow implementation, by contrast, the efficiency of local subcooling vapour/liquid heat exchangers (Fig 4.31) was compromised by local space constraints, resulting in a minimum liquid injection temperature to the capillaries of no lower than -10ºC; 15ºC higher than the optimum (point **E** in Fig 4.35).

Defining the heat exchanger efficiency η [74] by:

$$\eta = \frac{T_0 - T_1}{T_0 - T_2}$$

where T_0 is the temperature of the liquid C_3F_8 arriving through the uninsulated delivery tubes (assumed at 35ºC), T_1 is the temperature of the liquid leaving the heat exchanger to enter the capillaries (taken to be -10 ºC) and T_2 is the evaporation temperature in the silicon structure (taken to be -25ºC).

By this definition the heat exchanger efficiency was taken to be 75%, thereby requiring an additional flow of coolant to compensate.

Fig. 4.36 illustrates the configurations of subcooling heat exchangers for SCT (2-capillary, 1-exhaust) barrel 'quartets' (a), SCT (2- or 3-capillary, 1-exhaust) disk sectors (b) and pixel (one- capillary, one-exhaust) cooling circuits (c). Exact geometries were circuit dependent, due to space constraints within the inner tracker volume.

However in the case of the SCT heat exchangers, the liquid tubes passed through a portion of the exhaust tube while in the case of the pixels the liquid supply tubes were simply glued to the outside of the corresponding thin wall aluminium exhaust tube.

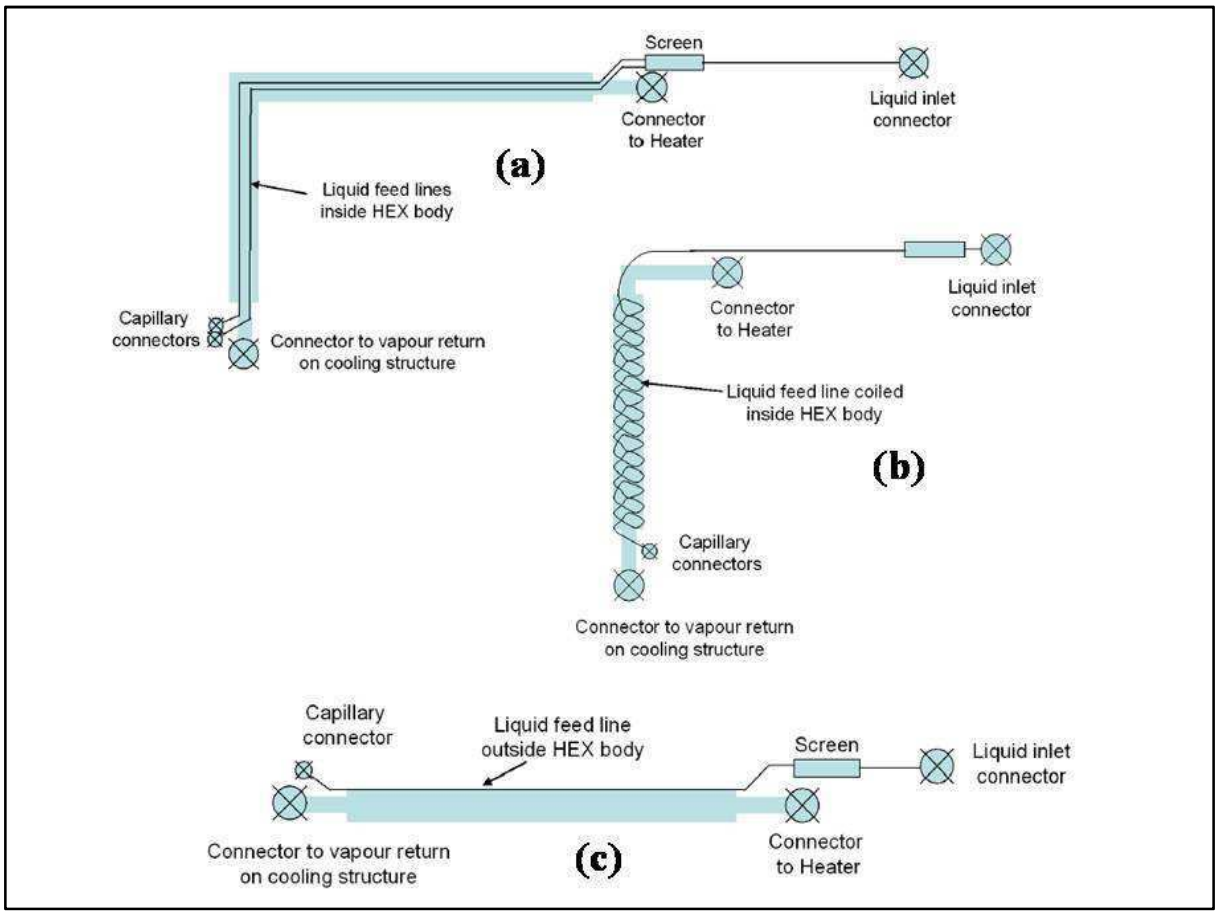

Fig. 4.36. Configurations of subcooling heat exchangers for SCT barrel 'quartets' (a), SCT disk sectors (b) and pixel (one-in, one-out) cooling circuits (c).

This extra flow to compensate the heat exchanger inefficiency is discernable from Fig 4.35: although the lengths **D'D"** and **FF'** in Fig 4.35 are approximately equal, zone **F➔Hv** is biphasic, rather than vapour-only: the cold energy in the fluid entering the exhaust in the combined form of unevaporated liquid/cold vapour (the combined zones F➔H_v and H_v➔F' respectively in fig 4.35) exceeds that which can be absorbed by sub-cooling the incoming liquid in the zone D'➔D''. A significant power overcapacity is required for the exhaust heater of each circuit, even when all the silicon

modules in the circuit are operating at full dissipation. This situation is illustrated in table 4.6 for the case of an SCT barrel stave 'quartet' with 504 W maximum silicon load cooled with a constant mass flow of 7.8g.s^{-1} (including safety factor: see also table 4.5) for evaporation at -25ºC as illustrated in Fig 4.35. For a liquid temperature at the capillary input of -10ºC, the available enthalpy is 75 J.gm^{-1} (**EH$_v$**, equivalent to 585 Watts cooling capacity at 7.8g.s^{-1}); giving a roughly 16% excess (roughly equivalent to **FHv)** to for the maximum silicon power to be evacuated.

Table 4.6 Exhaust heater power requirements: different silicon power dissipations in SCT barrel stave 'quartet'.

Silicon. Power (504W max)	% C_3F_8 liquid evaporated	Exhaust heater power to boil unevaporated liquid	Exhaust heater power to raise fully evaporated coolant from T_{evap} ➔20ºC (for η_{Hex} = 75%)	Total required exhaust heater power: varying Si. loads	Heater power as % max Si. power
504	86.3	81	88	169	33.5
400	68.3	185	88	273	54.1
300	51.3	285	88	373	74.0
200	34.1	385	88	473	93.8
100	17.1	485	88	573	113.7
0	0	585	88	673	133.5

It can be seen that in standby conditions the exhaust heater power exceeds the silicon power dissipation by a factor of 33%, representing a total heater power for all the 204 circuits in the SCT and pixel tracker of ~ 85kW.

Fig 4.37 illustrates the positioning of individual circuit subcooling heat exchangers and exhaust heaters devices in the ATLAS inner tracker volume in a quadrant view. The barrel SCT and pixel subcooling heat exchangers were mounted horizontally while those of the SCT disks were mounted vertically at varying azimuthal orientations (Fig. 4.38), as were the exhaust heaters which followed the heat exchangers.

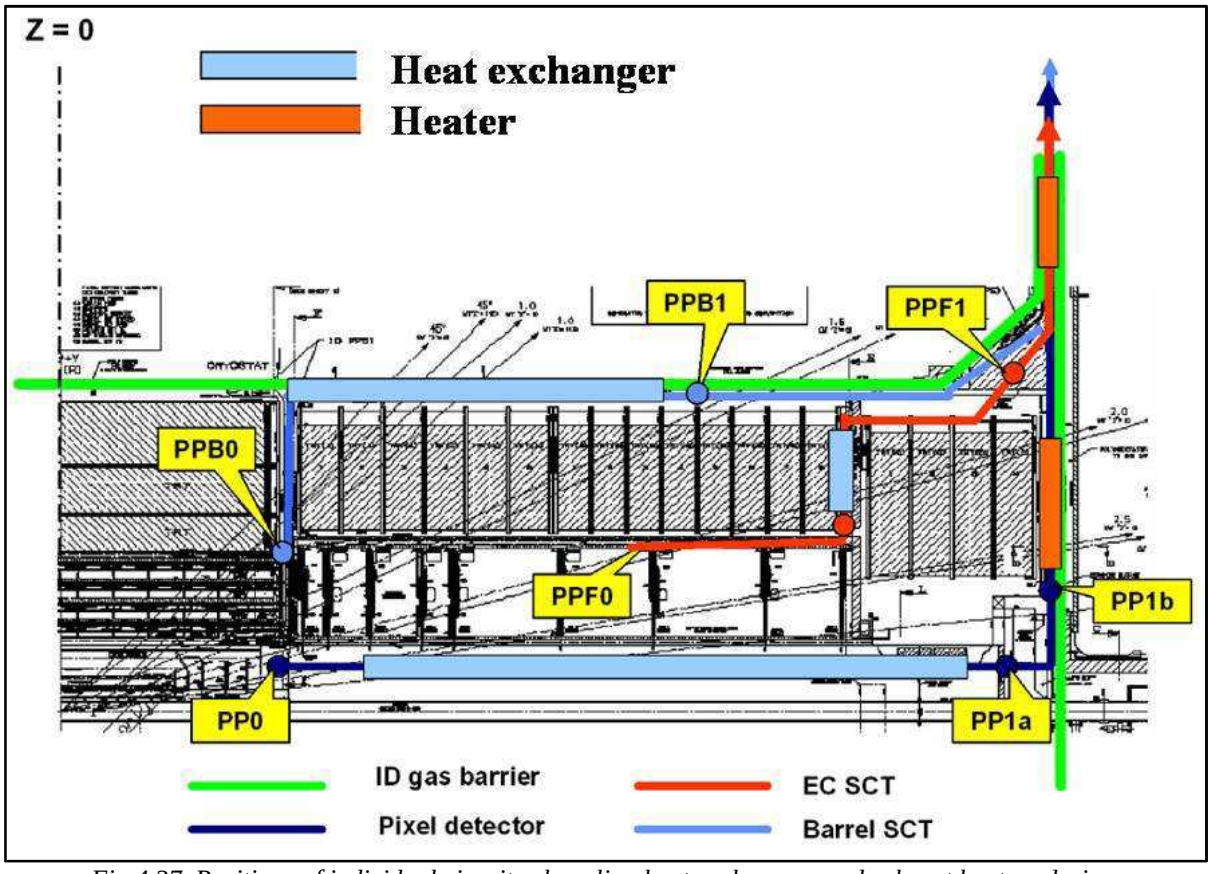

Fig 4.37. Positions of individual circuit subcooling heat exchangers and exhaust heaters devices in the ATLAS inner tracker volume.

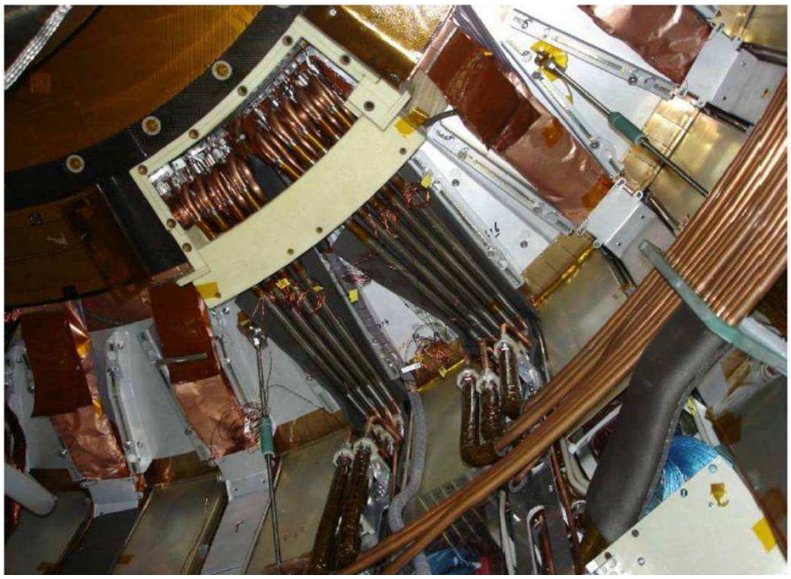

Fig 4.38. Example of (9) SCT disk cooling circuit subcooling heat exchangers installed in the ATLAS ID volume.

The exhaust heaters were located downstream of the subcooling heat exchangers using as short a length of tubing as possible. In some cases this had to be insulated – for example when exhaust heaters were mounted on the liquid argon calorimeter end flange or outside the N_2-purged inner detector cold volume (Fig. 4.37).

Figure 4.39 illustrates an exhaust heater (in this case a barrel SCT 'quartet' version). A coiled heating element of 80/20 Constantin/.Ni wire is embedded in an insulating magnesium oxide carrier bonded to the inside wall of a section of the exhaust tube[56]. The element was intended not operate above 100ºC (for sufficient safety margin against the decomposition of the C_3F_8 fluid which is believed to be significant at temperatures above 200ºC). Its direct contact with the fluid was expected to confer high thermal efficiency; an early demonstration with a heater for an SCT barrel stave 'quartet' circuit having been shown to boil all the passing C_3F_8 liquid when no power was applied to the silicon modules; also raising the C_3F_8 vapour to 20ºC with a maximum element temperature of < 80ºC.

Although interesting, this turned out to be a necessary but insufficient test, since electrical immersion heaters (rod-like or cylinder-like as in this case) are intended to heat liquids with the *whole* length of the element immersed. In varying orientations to the horizontal, with partial wetting of the element surface, (for example in conditions of low content of unevaporated C_3F_8 liquid) very high temperatures (> 120ºC) could be reached on the unwetted downstream ends of the heating element, necessitating a duplicated thermal interlock. The thermal interlock was in addition to a temperature sensor on the exhaust tube around 50cm downstream of the heater used for PID regulation of the heater duty cycle using switched 110V DC in response to the variation in the sensed temperature. The PID algorithm (an equation of similar form to eqn (4.4)) was programmed into channels of an industrial process controller. It was found necessary, however to set different values for the Proportional, Integral and Derivative terms, not only for different heater power ratings (as in Table 4.6) but also in different azimuthal orientations of heaters with the same power density. The latter was due to the differences in liquid wetting of the heater tube wall due to the effects of gravity.

The heaters turned to be one of the most unreliable components of the implemented evaporative cooling system. In addition to over-temperature problems with dried out sections of the element, there were repeated failures and short circuit breakdowns at the points where the heating element penetrated the heater tube wall to connect to short copper conductor extensions terminating in connectors. After extensive tests it was concluded that it was an intrinsic problem of electrical breakdown at the interface between the epoxy sealing the connector and the mineral-insulated heater cable, probably caused by trapped humidity in the magnesium oxide heater cable cladding.

This problem caused significant cost and time overruns to the commissioning phase of the project starting in early 2007, requiring the setting up of a task force and repeated visits to the manufacturer. Finally a new design of splice connector was supplied by the manufacturer which solved the problem. However, the problems had already caused significant modifications in the ID installation sequence and schedule and the overall mechanical configuration of the cooling system within the ID volume. Confidence in the heater reliability had become so low that all 204 heaters were moved from their original inaccessible locations (Fig 4.37) to new accessible locations outside the inner detector cold

[56] Custom design by Thermocoax SAS, 40 bd Henri Sellier ,92156 Suresnes Cedex, France

volume, their original locations being closed with blank tubes. In many cases the heaters had to be mechanically modified to fit in their new locations [75].

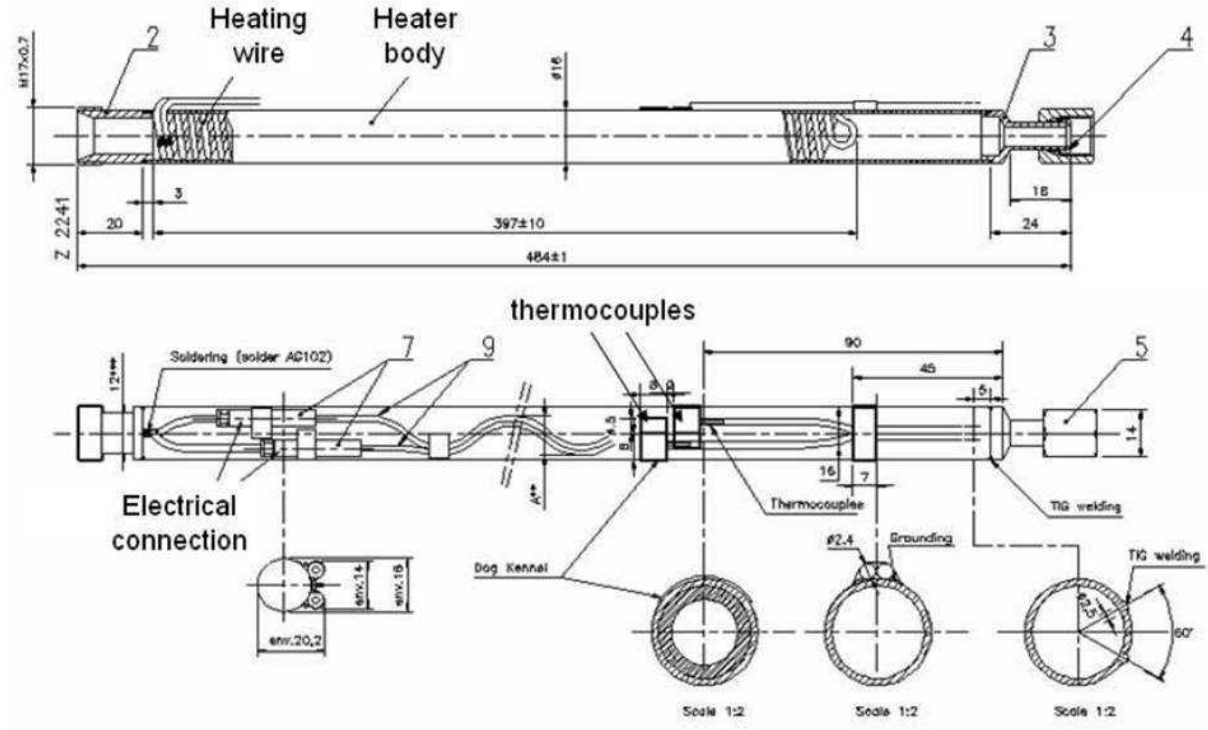

Figure 4.39. Example of an exhaust heater in this case a barrel SCT 'quartet' version.

Table 4.7 Original exhaust heater configurations for the SCT and pixel cooling circuits.

Circuit	Nominal circuit power (W)	Heater design power (W)	Tube I.D./O.D (mm).	Wire diameter (mm)	Element hot length (cm)	Free internal diameter
SCT Barrel	504	960	14/16	2	331	10
SCT Disk	347	650	11/13	1.15	363	8.7
Pixel Barrel	220	480	11/13	1	373	9
Pixel Disks	110	260	11/13	1.15	402	8.7

As previously discussed, the choice of uninsulated C_3F_8 supply tubing and its exposure to temperatures in the range 35-40ºC in the vicinity of low mass cables of high heat dissipation required an increase in the liquid delivery pressure to > 15bar $_{abs}$ prevent premature boiling in the tubes. This is illustrated in the zone **CDD'** in Fig. 4.35 where the C_3F_8 temperature drops from the condensation temperature of ~52ºC (the C_3F_8 vapour from the compressors having been condensed at a pressure of ~ 17bar $_{abs}$ via counter-flow with water) to around 21ºC on its way from the ATLAS technical cavern USA15 to the distribution racks on the ATLAS service platforms (**CD**). From here the liquid heats to around 35ºC in proximity with the cables (**DD'**). Figure 4.40 illustrates the two stage compressors[57] installed in USA15. These operate in parallel, with one compressor in reserve and another usually undergoing maintenance – to circulate and compress around 1kgs^{-1} of C_3F_8 vapour from an input pressure of 900mbar$_{abs}$ to the condensation pressure of 17bar$_{abs}$. Also visible in Fig. 4.40 is the C_3F_8 condenser (blue- centre view) and the C_3F_8 storage tank, which could recover and store approximately 1 tonne of C_3F_8 liquid. The various elements of the system are illustrated in the 'off-detector' schematic of Fig 4.41.

[57] Model QTOGX-160/80, Input pressure 0.8-1.4bar$_{abs}$, output pressure 17 bar $_{abs}$ 80-160m^{3}hr^{-1} C_3F_8; Mfr: Haug, St Gallen, Switzerland

Fig.4.40. Compressor installation in ATLAS USA15 technical cavern for the C_3F_8 evaporative cooling system.

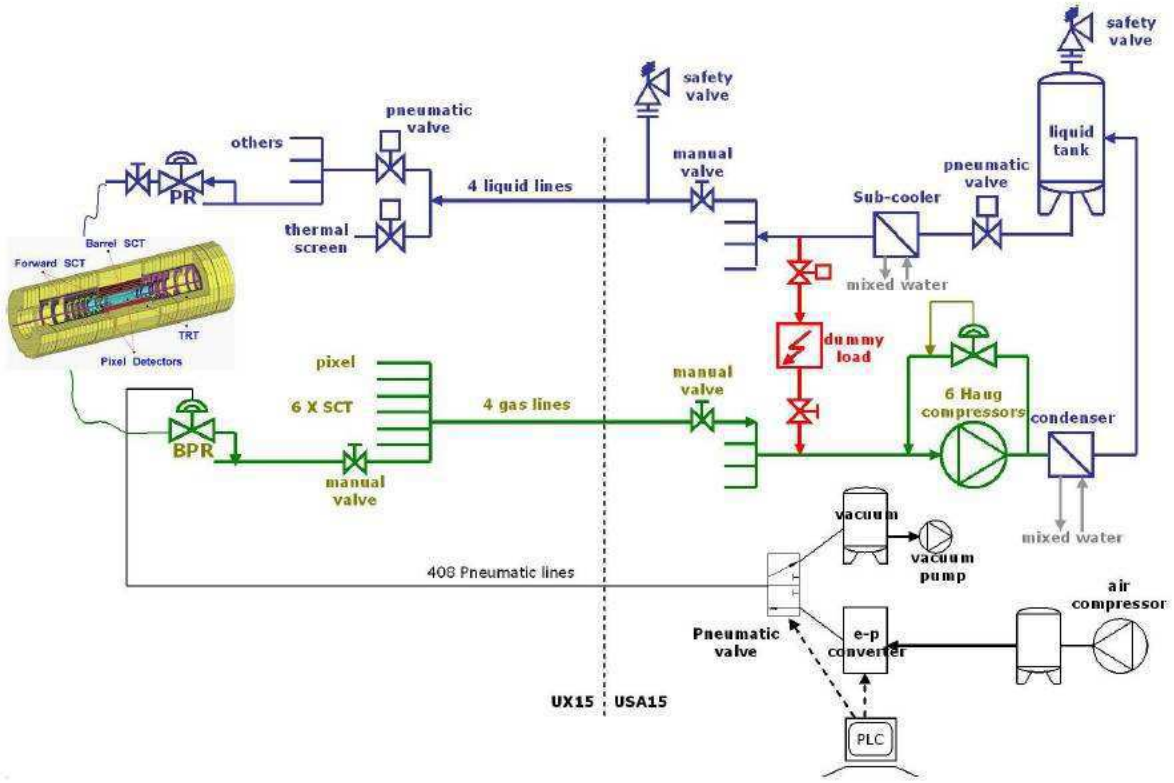

Fig. 4.41. Schematic of the ATLAS inner detector C_3F_8 evaporative cooling system concentration on the 'off-detector' elements in the USA15 technical cavern and on the ATLAS service platforms.

The cooling plant was partially installed in June 2006. The commissioning of the cooling system (following the heater problems) started with the SCT barrel in November 2007, before the completion of the external cooling installation, to confirm the heater modification and to advance the detector commissioning schedule.

In April 2008, the installation of all cooling circuits was completed. However in May 2008, during the commissioning of the pixel detector, the system experienced a catastrophic failure of three of the seven Haug compressors, after 22, 70 and 370 hours of service. An investigation showed that this was caused by an extended period of running with the magnetic couplings between the motor and the crank to the four pistons intermittently slipping, causing (eddy current heating) damage to the non-magnetic domes separating the motor magnet and the crank magnet. Unfortunately these domes also isolated the low pressure (~800-900 $mbar_{abs}$) C_3F_8 process gas in the crank case from the external air. This damage resulted in a loss of 100 kg of C_3F_8 and considerable particulate contamination of the compressor end of the cooling system, in addition to necessitating removal of the three compressors.

After the repair of the damaged compressors and cleaning of the plant, the commissioning restarted in August 2008. The cooling system was operated fully until the end of 2008, achieving 96% availability during the last three months of that year. However it was soon found that excessive vibrations induced cracking and leaks in the external pipework linking the eight cylinder segments of each compressor. The pipe work was completely redesigned and qualified by stress and vibration analysis. This modification was applied to all six compressors during the shut-down at the beginning of 2009. The cause of the vibration has been the subject of much discussion; a rapid consumption of the non-metallic piston rings in the high pressure zones of the cylinders is likely to cause a progressive asymmetric thrust on the central crank, which is supported by only two bearings. Since this reciprocating geometry resembled more a radial engine (with only one piston in each azimuthal position) than (for example) a 'V' engine with multiple cylinders the two azimuthal positions, any cylinder with a partial loss of compression had no partner at the same azimuth to help compensate. It was also commented that the piston ring wear was unsurprising in a device with the compression ratio of a diesel engine but none of its lubrication.

The complete cooling system was in operation again in June 2009, but the high maintenance overhead of the compressors continues to cause concern, and has led to the setting up of a task group to examine alternative means of circulation. This is discussed in section 5.3.

The renewed operation of the complete cooling system from June 2009 also allowed a systematic study of the operational temperatures on the inner detector silicon. It was found that the SCT Barrel 'quartet' circuits could not be made to operate at their lowest specified temperatures of -7°C [56] through excessive pressure drops in the exhaust heat exchanger and electrical heater combination. Indeed, their temperatures were routinely 10°C above the -7°C target [74], the result of an effective, unwanted, increase in evaporation pressure of 1.2 bar. Although it is claimed in some quarters that this problem doesn't cause any adverse effect yet and will not for many years (though it will affect the leakage current at the end of the life of the detector) [75], these claims are based on an accumulation of radiation dose based on smooth projections of LHC luminosity increase ➔10^{34} $cm^{-2}s^{-1}$ without any beam loss incidents during either proton or periodic heavy ion running.

To operate the SCT barrel silicon toward the specified -7ºC operating temperature, the lowest pressure part of the system - the aspiration pressure of the compressors - would have to be reduced. The problems with this are threefold:

- the present aspiration pressure is ~0.8 $bar_{abs.}$ There is insufficient '*footroom*' for a 1.2bar reduction;
- the vapour volumetic pumping requirement would increase substantially, since the evaporation at lower temperature would result in higher liquid➔ gas expansion ratios. This can be seen for example in a comparison of Tables 4.2 and 4.3 for C_3F_8;
- for a fixed compressor discharge pressure the compressor pumping speed drops with decreasing aspiration pressure (as the compression *ratio* increases), as illustrated in Fig 4.42 for the Haug Model QTOGX-160/80, at a fixed (unchangeable) output pressure of 17 bar_{abs} and an aspiration temperature around 20ºC. The arrow shows the ATLAS operating point, where the aspiration volume flow for a single compressor is around $80m^3hr^{-1}$ At this temperature the superheated vapour density is around $9kgm^{-3}$. The corresponding aspiration mass flow is therefore $200gms^{-1}$ for a single compressor. Six such compressors are needed for the full flow of the silicon tracker.

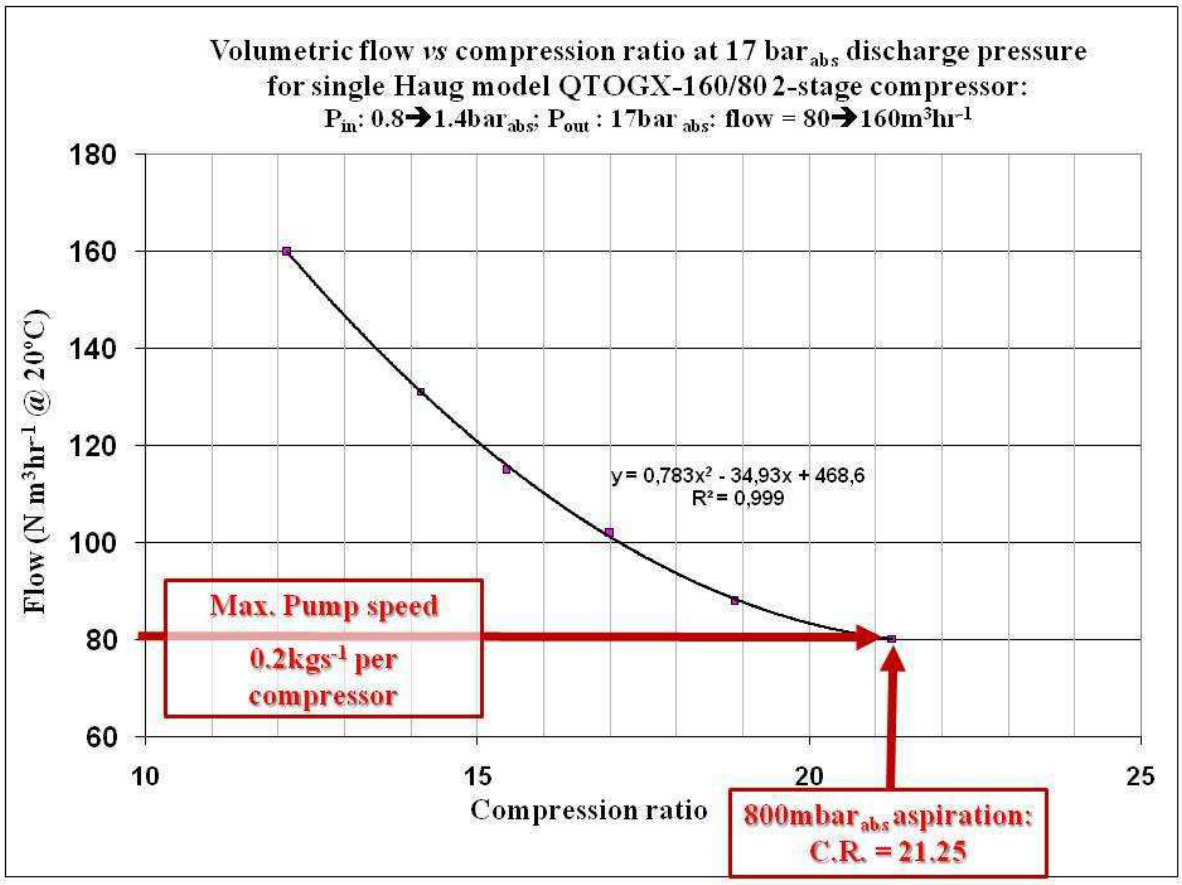

Fig 4.42 . Volumetric aspiration flow rate vs compression ratio for a single Haug QTOGX-160/80 compressor. At 800mbar$_{abs}$ (Compression Ratio = 21.25) the aspiration mass flow is 200gs^{-1}

Table 4.5 indicated that the total expected mass flow of the ATLAS silicon tracker would be around 1.05kgs^{-1}.

The original total pressure drop in an SCT barrel stave 'quartet' thermal test structures was 330mbar. Later this rose, for 504Watts dissipation, in the installed system, to 520 mbar with the following break-down:

- SCT barrel stave 'quartet' evaporator output TEE: 100mbar
- subcooling heat exchanger: 170 mbar
- exhaust electric heater: 160mbar
- tubing to backpressure regulator on ATLAS service panel (16mm ID tube): 90 mbar

This budget was exceeded due to the excessive impedance (limited tube diameters) in the SCT barrel stave 'quartet' exhaust TEEs carrying the highest flow of coolant (table 4.5), the corresponding sub-cooling heat exchangers and exhaust electric heaters. Additional pressure drops were also introduced through the necessity of moving the exhaust heaters to more accessible positions on the inner detector end flange, with the replacement of a length of larger ID tube with that of the electrical heaters. The high flow (C_v =1.0) Tescom backpressure regulators also exhibited a positive offset of their C_3F_8 operating pressure and the dome command pressure. This was typically ~100 mbar with the original 50µm stainless steel diaphragm at the full flow of around 8gs^{-1} and an operating pressure around 1000mbar$_{abs}$. This was the only impedance problem that could be easily addressed, the BPRs being on accessible service platforms: once their membranes had been changed to a softer material ('Gylon' ®) which had been 'pressure trained' the offset pressure could be reduced to an average of 50mbar.

Given the impossibility of lower aspiration pressure the author had proposed two methods [76] to circumvent the rising trend in expected exhaust pressure drop and compressor stress problems. These are both now the subject of intense effort in ATLAS and are discussed in the following sections.

5 Changes to the present ATLAS evaporative cooling system for it to cool the silicon tracker to the ID and Pixel TDR specification

The methods proposed by the author [76] to circumvent the exhaust pressure drop and compressor unreliability problems were;

(i) *raising the evaporation pressure while maintaining the same evaporation temperature through the use a of a blend of SFCs with a higher combined s.v.p.*. The blend ratio would be tuned to accommodate the existing pressure drop. In addition the blending would reduce the vapour flow rate, since the lower boiling temperature (more volatile) component would have a smaller liquid➔ vapour expansion ratio at the evaporation temperature than its partner, reducing the volumetric vapour flow by a factor depending on its molar concentration in the blend. The natural partner for C_3F_8 is the next lightest SFC – hexa-fluoroethane (C_2F_6). The higher evaporation pressure of such a blend would have the added advantage of operating the compressor at a higher aspiration pressure (lower compression ratio) where its pumping throughput would be greater. Fewer compressors of the present type (if retained) would be needed in simultaneous operation: MTBF (Mean Time Between Failures) would probably be increased;

(ii) *further reducing the compression ratio* - the principal limit on throughput (and reliability in the ATLAS implementation) with the use of a surface condenser. With a surface condenser a large fraction of the high pressure of 17bar required for liquid supply through the uninsulated tubes would be provided by exploitation of the ρgh hydrostatics of a 80-95 m column of liquid C_3F_8 or mixture descending the ATLAS pit. The large difference in liquid (vapour) densities of ~1650 (6.5) kgm^{-3} implies a ρgh pressure drop of ~60 mbar for C_3F_8 vapour ascending the deep pit to the surface condenser. Compressors could be retained in the underground cavern, as at present, but operating at a much lower compression ratio (output pressures < $10bar_{abs}$) for greater reliability, or could be eliminated entirely from the primary coolant loop if the surface condenser were to be operated at a lower temperature than the on-detector evaporation in a '***thermo-siphon***' mode of operation.

These approaches are the subject of intensive study, as discussed in the following sections.

5.1 Operation with C_2F_6/C_3F_8 evaporative blends

As a means of increasing the evaporation pressure for a given required evaporation temperature around -25°C, the author proposed the evaluation of blends of C_2F_6 and C_3F_8. The increased exit pressure at the exit of the SCT and pixel detector structures would mitigate the effects of pressure drop in the exhaust heat exchangers and electric heaters and in the tubing linking the SCT and pixel structures with the back pressure regulator racks on the ATLAS service platforms.

A mixture adding 10-20% of C_2F_6 to C_3F_8 is foreseen. The PC-SAFT equation of state has been used ([77], APPENDIX 1) to calculate the pressure-enthalpy diagram (and with it the s.v.p., critical temperature and pressure) of various mixture combinations, as illustrated in Figs 5.1-5.3. It can be seen that the evaporation of the mixture is not isobaric: as the concentration of C_2F_6 in the mixture increases so does the pressure difference between the input end of the evaporator (immediately following the capillary) and the end of the structure (upstream of the exhaust heat exchanger and electric heater). Figure 5.1 shows the evolution (for example) of the -23ºC evaporation isotherm for 10% C_2F_6/90% C_3F_8, which varies in the range (~2.5 bar_{abs}➔~1.8bar_{abs}).

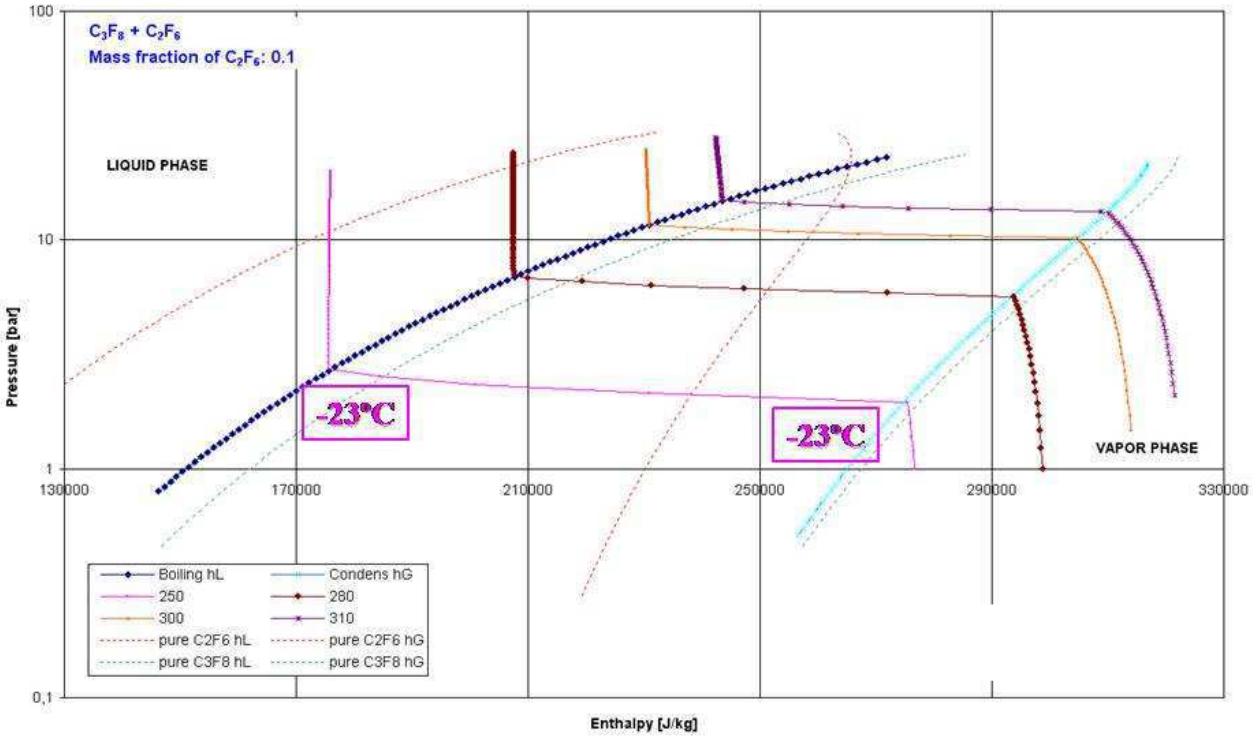

Fig 5.1. Pressure-enthalpy diagram for an evaporating mix of 10% C_2F_6/90% C_3F_8 (PC-SAFT)

Figure 5.2 shows the evolution of the same -23ºC evaporation isotherm for 20% C_2F_6/80% C_3F_8 , which varies in the range (~3 bar_{abs}➔~1.8bar_{abs}), while Fig. 5.3 shows the evolution of the -23ºC & -43ºC evaporation isotherms for a mixture of 50% C_2F_6/50% C_3F_8. At -23ºC this varies in the range (~ 6.5 bar_{abs}➔ ~4 bar_{abs}). It can be seen for the 50% C_2F_6/50% C_3F_8 mixture that much lower temperatures of evaporation can be conveniently reached at convenient evaporation pressures. For example at -43ºC the evaporation isotherm varies in the range (~4 bar_{abs}➔~1.5 bar_{abs}). Such a mixture might be of interest in an upgraded tracker where lower operating temperatures might be necessary to protect silicon detectors from type inversion and leakage current – induced thermal runaway at higher radiation fluencies than foreseen at the $10^{34}cm^{-1}s^{-1}$ intensity of LHC phase 1 running.

This *mémoire*, however, is restricted to the developments currently under way to evaluate cooling mixtures in the range 10-20% C_2F_6 in C_3F_8 to allow operation of the present ATLAS configuration of inaccessible on-detector cooling, exhaust heat exchangers and electric heaters in the time preceding the LHC luminosity upgrade. With these new mixtures in mind, a dedicated C_2F_6 /C_3F_8 blend circulator has been commissioned in the ATLAS SR1 surface building, while a new test bench for measuring heat transfer coefficients in these mixtures – an indispensible measurement of their cooling performance - is also presently under construction. As part of the evaluation programme for C_2F_6 /C_3F_8 mixtures, a combined ultrasonic flowmeter/ gas mixture analyzer is under development, as discussed in section 5.2.

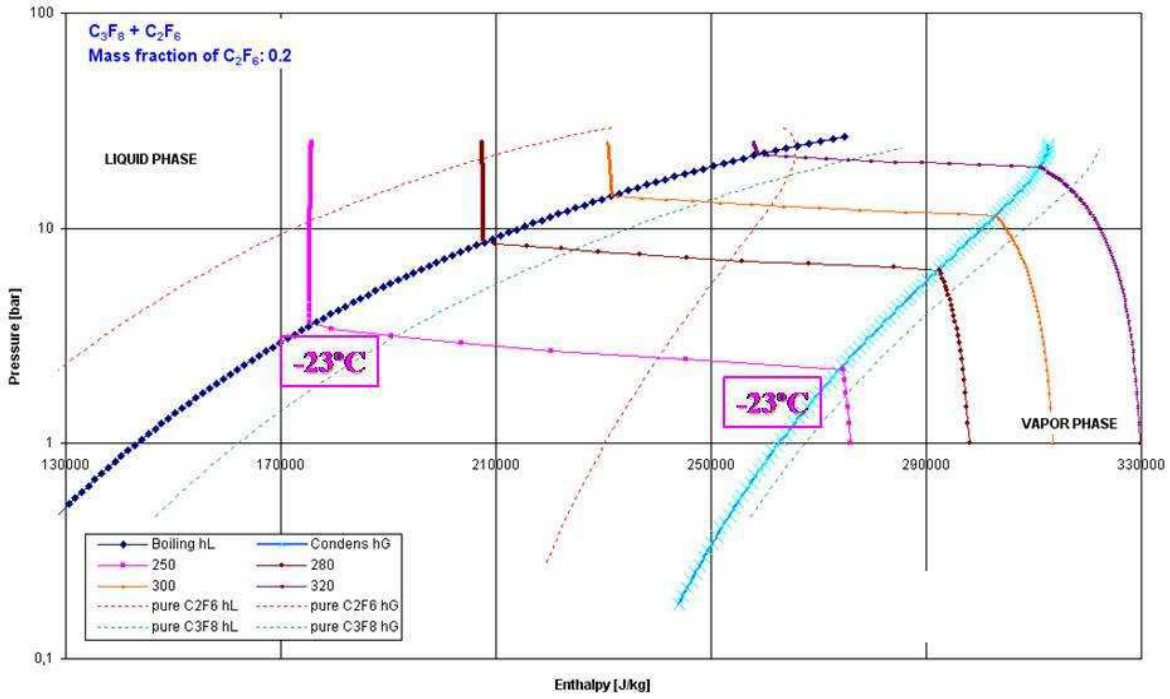

Fig 5.2. Pressure-enthalpy diagram for an evaporating mix of 20% C_2F_6/80% C_3F_8(PC-SAFT).

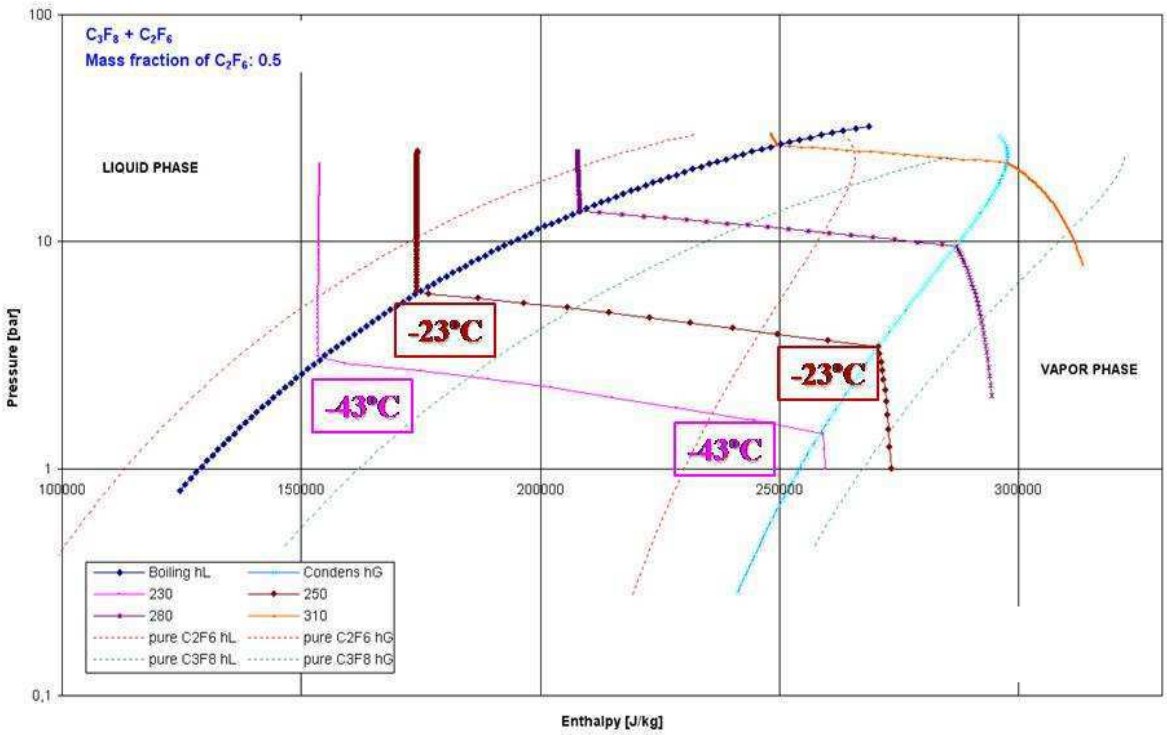

Fig 5.3. Pressure-enthalpy diagram for an evaporating mix of 50% C_2F_6/50% C_3F_8 (PC-SAFT).

5.2 Sonar analysis/flowmetry of C_3F_8/C_2F_6 mixtures

With the serious consideration of C_3F_8/C_2F_6 mixture for cooling the ATLAS silicon tracker it was natural to require a system to monitor the circulating mixture. Concerns were raised that the mixture might decline in concentration of C_2F_6 with time, as the more volatile component might be more likely to escape through leaks. It is not easy to quantify these concerns so it was decided to develop a more modern version of the SLD CRID sonar for this. This device would combine mixture analysis and flowmetry in the same instrument, which could be installed at a convenient point in the grouped vapour exhaust returning to the external circulation plant. An instrument of this kind was installed in the SLD barrel CRID radiator recirculator, as shown in Fig 5.4.

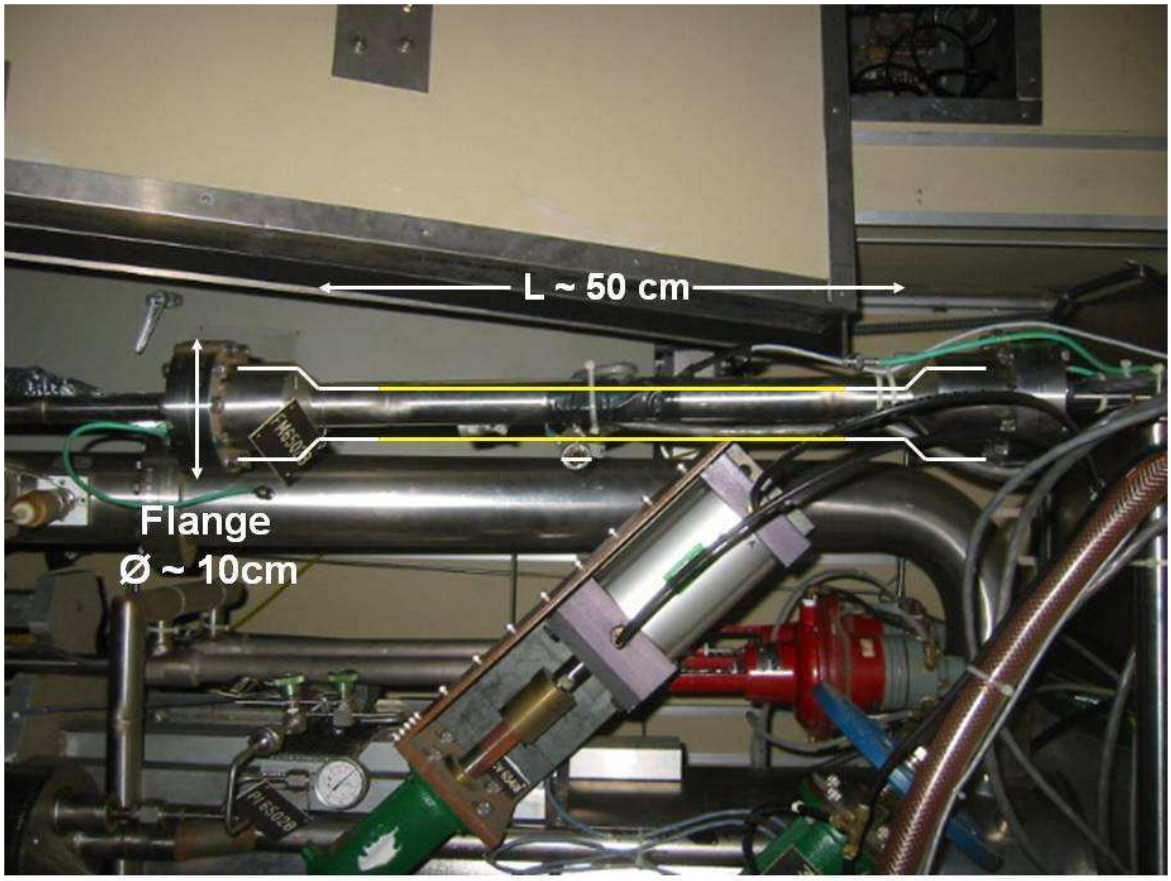

Fig. 5.4 Ultrasonic flowmeter installed in the SLD barrel CRID C_5F_{12}/N_2 radiator recirculator.

Three examples of the instrument were recreated, with more modern electronics with a 20MHz transit time clock and connection via USB or CANbus to a supervisory and monitoring computer running PVSS-II[58] – the CERN LHC standard for SCADA (Supervisory, Control and Data Acquisition) systems. The instrument combined analysis functions with those of a conventional ultrasonic flowmeter (UFM), in which difference in sound transit time in directions aligned at angles (< 90º) to the vapour flow can yield the flow velocity. Figure 5.5 illustrates the general UFM incarnation: the transit times t_{down} and t_{up} of sound pulses transmitted over path length L through the gas flow in opposing directions aligned at an angle Φ to the flow in a tube of cross sectional area A are given by:

$$t_{down} = L / (c + v \cos\Phi) , \qquad t_{up} = L / (c - v \cos\Phi) \tag{5.1}$$

were v is the gas linear flow velocity (ms^{-1}) and the c the speed of sound in the gas. The gas flow velocity can therefore be inferred from the two transit times by:

[58] By ETM professional control GmbH, A-7000 Eisenstadt, Austria (http://www.etm.at/index_e.asp?id=1&sb1=1)

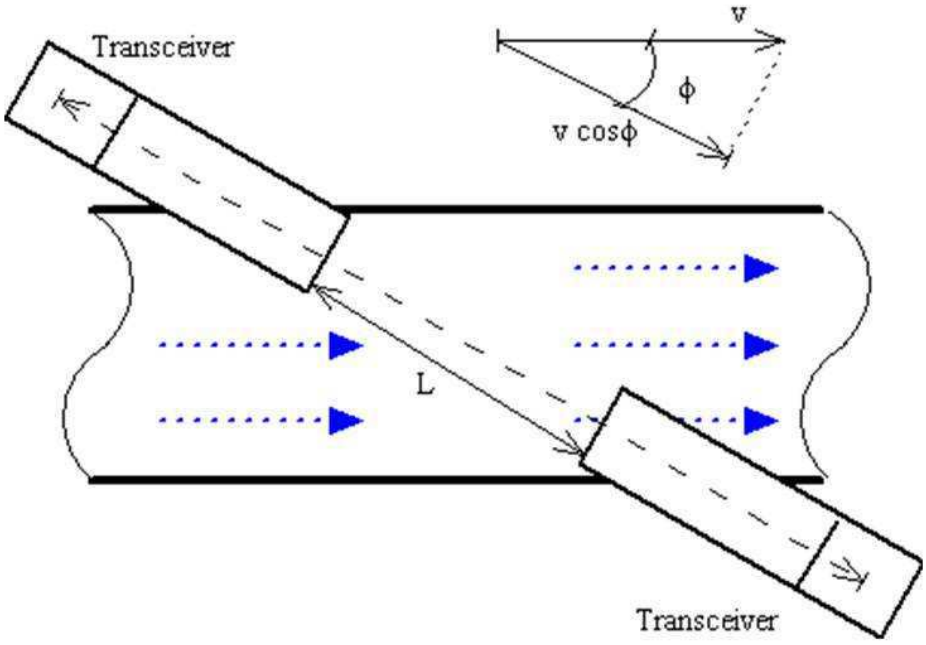

Fig. 5.5 Ultrasonic flowmeter: generalized layout and principle.

$$v = L/2\cos\Phi * ((t_u - t_d)/ t_{u*} t_d) \qquad (5.2)$$

and the volume flow V (m^3s^{-1}) from;

$$V = v * A \qquad (5.3)$$

The sound velocity *c* is inferred from the two transit times via:

$$c = L/2 * ((t_u + t_d)/ t_{u*} t_d) \qquad (5.4)$$

It can be seen that (contrary to the case in gas mixture analysis) it is not necessary to know the absolute temperature of the gas in the UFM in order to measure the flow velocity. The geometry of Fig. 5.5 presents little resistance to the flow of the gas, but is more difficult to construct. Corrections must also be made for the extra unswept legths of the process gas between the ultrasonic transducers – a calibration that can be made at zero flow. We decided in the prototype instruments, which were not intended for particularly high flow rates, to adopt a simpler sound path parallel and anti-parallel with the gas flow direction. As in the SLD instrument the ultrasonic transducers were centred in larger diameter 'blisters' at each end of the UFM tube, separated by a central tube whose inner diameter was similar to the transducer diameter. The ultrasonic transducers were separated by around 666 mm and equipped with PEEK conical deflectors. The annular area between the transducer and the inside of the wider region of tube at each end was chosen to be as close as possible (given the restricted choice of stock tube diameters) to that of the thinner central tube, as illustrated in Fig. 5.6. The mechanical envelope was of welded stainless steel with Conflat® flanges. Lateral ports were installed for the injection and pump-out of calibration gases. Six internal NTC thermistor temperatures sensors were installed: their wiring, together with the screened twisted pairs for the ultrasonic transducers, terminating in hermetic multipin connectors on lateral tubes at each end of the housing.

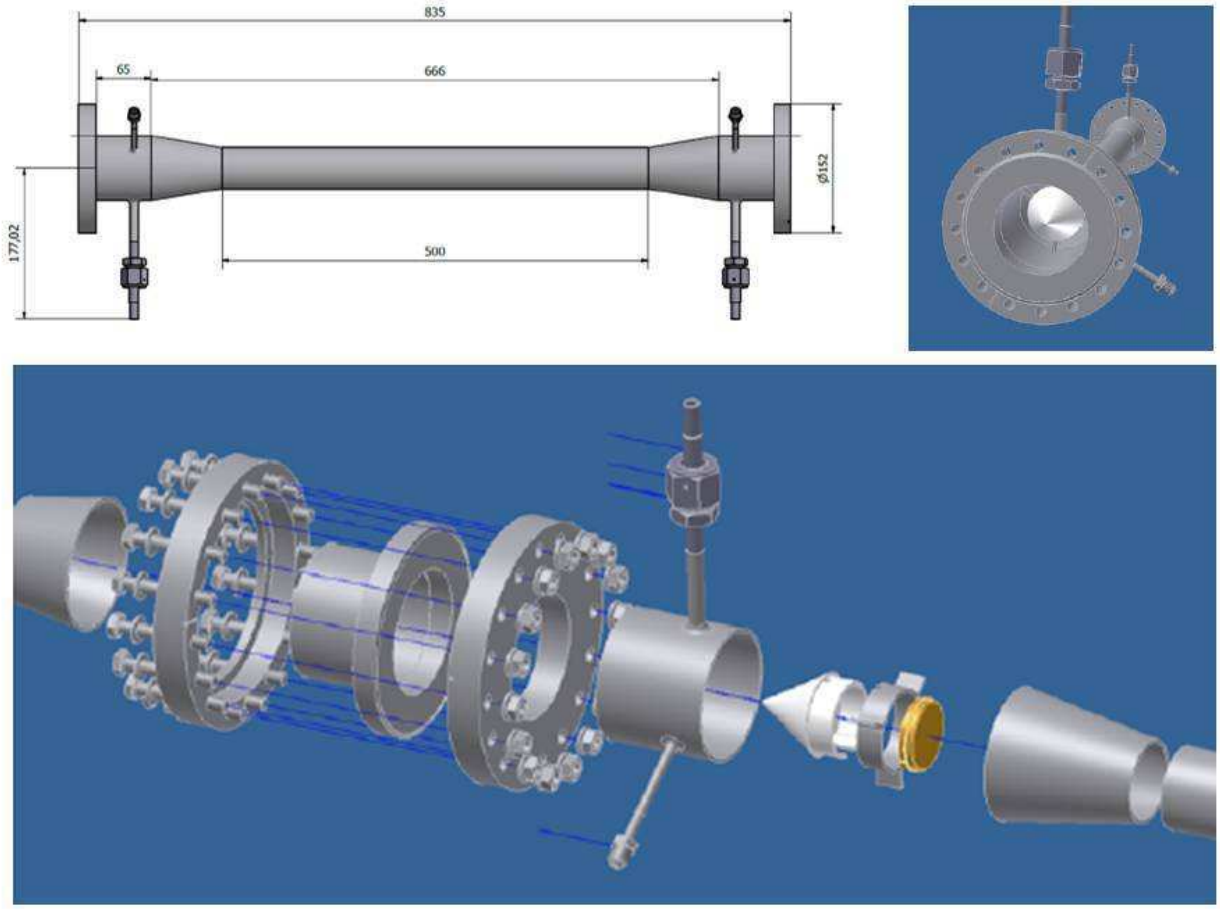

Fig. 5.6 Dimensional and component views of Ultrasonic flowmeter/analyzer for C_2F_6/C_3F_8 mixtures.

Of the three tubes built, one has been extensively investigated for range and linearity as a flowmeter in comparison with two other instruments:

- a Gill Instruments "Spirocell" medical ultrasonic flowmeter with a maximum advertised full scale range of 150 $l.min^{-1}$ equipped with RS232 readout;
- a Schlumberger Delta G16 rotor gas meter with a with a maximum advertised full scale range of 25m^3hr^{-1} (~7 $l.s^{-1}$), equipped with interrupted optical beam readout.

The linearity vs flow rate for the new instrument is compared with the two instruments (Fig. 5.7), which work on completely different principles. While the slopes differ from unity in both cases the linearity is good up to the maximum practicable range of the comparison instrument. Above ~110 $lmin^{-1}$ the Gill UFM reading was unstable, probably due to the high flow and turbulence in its 1cm diameter sound-and-gas path, while at flow rates above 20m^3hr^{-1} the microphonic noise pickup in our own instrument from the spinning rotors of the adjacent Delta G16 gas meter was a problem, necessating a reduction in the selectable gain in the custom-developed UFM electronics. The deviations from unity slope in the comparisons need further investigation. We did notice that the signal from the downstream transducer showed a progessive reduction in amplitude with increasing flow (not seen in the upstream transducer) – possibly due to the slab obstruction presented by the front face of the transducer to the gas flow. It is probable in installations requiring greater flow than ~ 25m^3hr^{-1} (as in the case of the full size 60kW thermo-siphon installation presently under consideration (section 5.3) that an angled transducer configuration with partially-withdrawn transducers (as in Fig. 5.5) may be necessary. This is a common geometry in large industrial UFMs, and we may be able to adapt such an instrument, or at least its insertion spoolpieces, adding temperature sensors to arrive at an instrument capable also of binary mixture analysis.

Figure 5.8 shows the UFM in a trial installation in the dedicated C_2F_6/C_3F_8 blend circulator recently completed. The short section of blank tube downstream is intended for a Delta G16 gas meter. Microphonic pickup from the nearby compressor has not been a problem up to the maximum compressor flow rate of

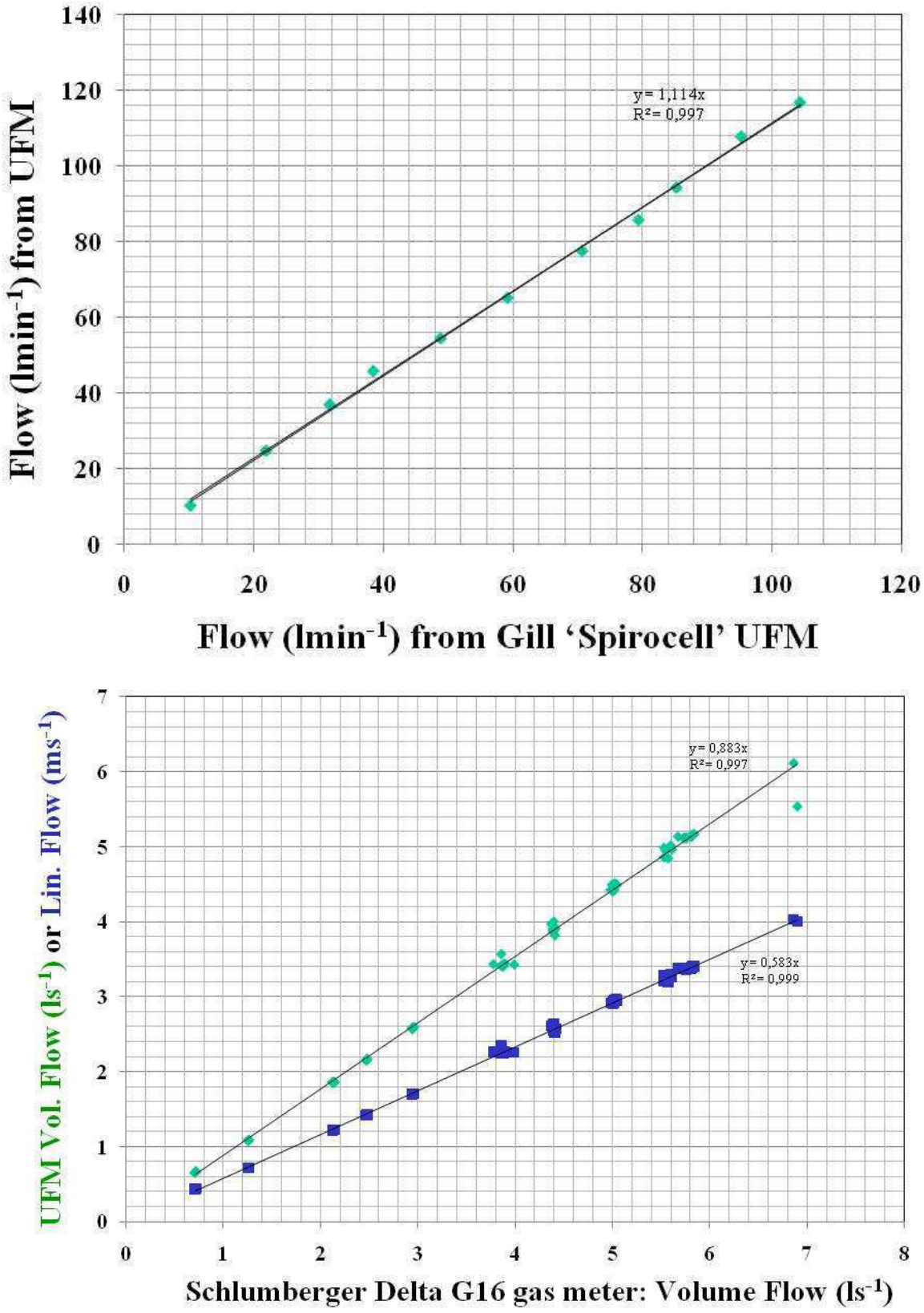

Fig.5.7 Linearity vs flow rate for the new instrument compared to a low flow UFM and a rotor gas meter

~13.75 m^3hr^{-1}: it is probable that this can be partially eliminated by the Armaflex® closed cell thermal necessary in the analyzer function.

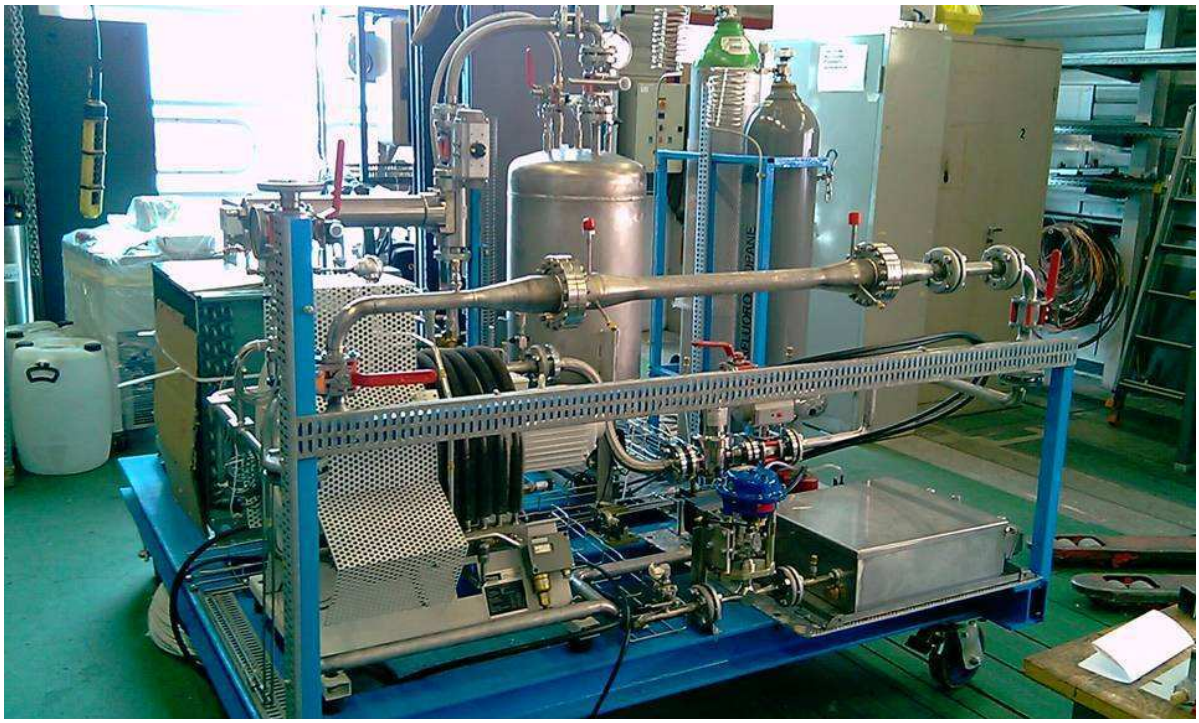

Fig.5.8 The ultrasonic flowmeter in a trial installation in the dedicated C_2F_6/C_3F_8 blend recirculator.

In parallel with the development of the instrument mechanics comparisons have been made between PC-SAFT-predicted sound velocity in C_2F_6/C_3F_8 mixtures and our measurements. Figure 5.9 shows such a comparison over the full dynamic range of C_2F_6/C_3F_8 mixtures at $1bar_{abs}$ and 21°C. The agreement between prediction with the PC-SAFT equation of state and measurements in created mixtures is good - especially when compared to the poor predictive power of theory for fluorocarbon mixtures twenty years ago - though some parameter

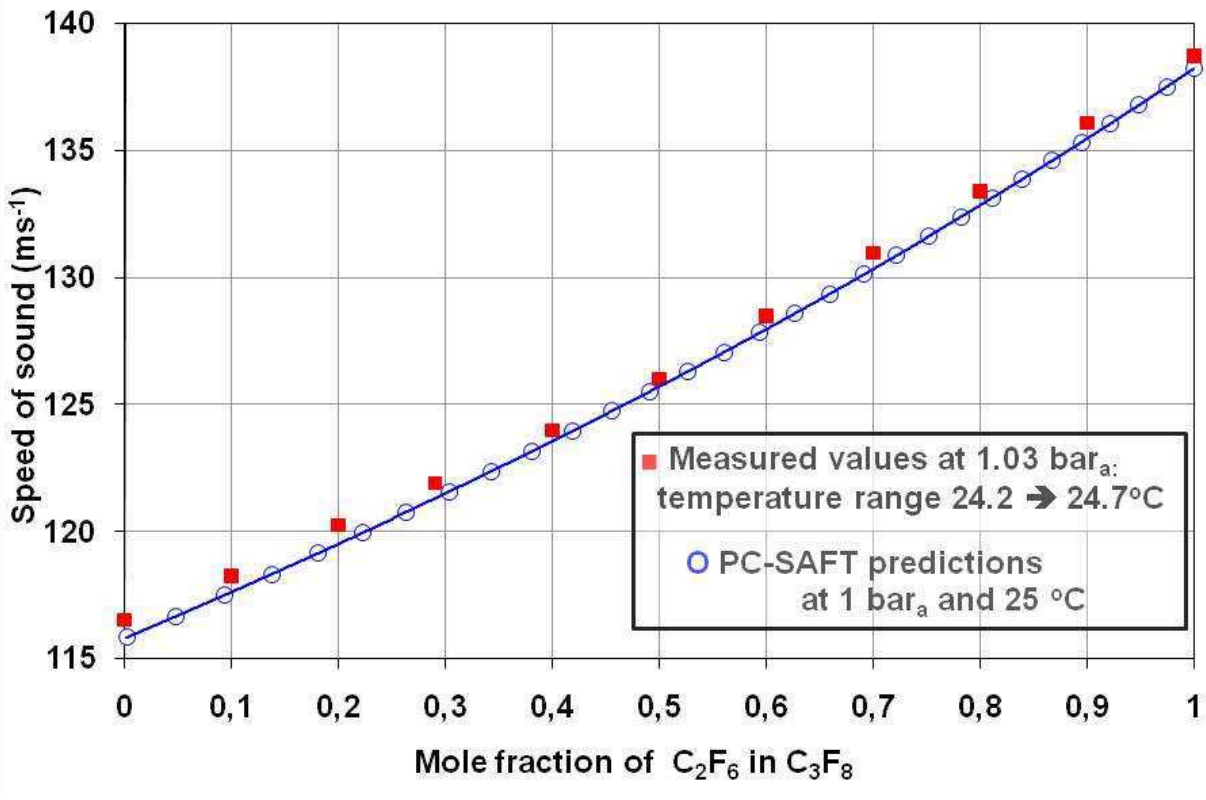

Fig. 5.9 Comparison of PC-SAFT prediction with sound velocity measurements over the full C_2F_6/C_3F_8 range.

tweaking in the PC-SAFT model may still be necessary**.**

Unlike in the situation that existed for the C_5F_{12}/N_2 mixtures of the SLD barrel CRID radiator (Fig .3.5), for which theoretical predictions of sound velocity *vs* mixture ration were far from reality, it is now possible to decide between a look up table based on measurements *or* quite accurate predictions from an EOS with parameters adapted to fluorocarbons.

Look-up tables, whether created from predictions or fits to measurements need not correspond exactly to the temperature of the process gas, since the speed of sound V_s varies over a Celsius temperature range $(T_1\text{-}T_0)$ – which can be defined as the difference between the temperature of the process gas and that at which the look up table was created - according to:

$$V_{S\,(T_1)} = V_{S\,(T_0)} \cdot \sqrt{\frac{(T_1 + 273.2)}{(T_0 + 273.2)}} \qquad (5.5)$$

From Fig. 5.9 we can conclude the precision with which sound velocity needs to be measured to achieve a desired mixture resolution. In the range between 0 and 25% C_2F_6 concentration in C_3F_8 the average gradient is ~0.16 $ms^{-1}\%^{-1}$. Sensitivity to 1% mixture variations requires a sound velocity measurement precision ($\delta V/V$) of around 1.6 10^{-3}. In a sonar tube with typical length 60cm this implies a sound flight time variation of around 10μs in 5ms (the transit time for V_s = 120ms^{-1}). The time variation of 10μs is around half a cycle of 50 kHz ultrasound and is easily within the 50ns intrinsic resolution of the new transit time clock.

Taking a conservative figure for the sound transit time resolution of 100ns, the minimum mixture resolution over the working range 0 ➔25% C_2F_6 concentration in C_3F_8 will be around 2.10^{-5}. Such small variations can be masked by temperature fluctuations in the tube: the tube temperature must be read along with the sound transit time.

In addition to new electronics a graphical user interface (GUI) running under PVSS-II has been created for the sonar instrument. This logs transit times, temperatures and pressure, calculates the sound velocity from the known inter-transducer distance and can calculate the mixture concentration at regular intervals using stored look-up tables generated according to the PC-SAFT EOS. All data are recorded to the ATLAS central slow control system database. The GUI has been under development since early 2010, and has been in use almost continuously since that time with a sonar tube installed in a gas sampling rack in the gas 'hut' of the ATLAS USA15 underground service cavern. This sonar tube has been 'sniffing' the N_2 environmental gas - using a small vacuum pump to aspirate the vapour through 150m of tube from the environmental barrier around the pixel detector for changes in C_3F_8 concentration from pre-existing known leaks. The sound velocity in the gas was constant over a considerable period, but between September 13 and 16, 2009 - during an abort shutdown of the pixel cooling system - a decrease (increase) in sound transit time (sound velocity) in the 496.9 mm sonar tube was seen, as illustrated in Fig 5.10, an extract from the pixel on-line logbook[78].

The increase in sound velocity of 0.56ms^{-1} is a manifestation of the disappearance of the normal contamination level of ~ 0.05% of C_3F_8 in the pixel environmental gas aspirated by the sonar. Figure 5.11 shows the calibration lookup table for C_3F_8/N_2 mixtures at the nearby temperature of 25°C. The agreement of the PC-SAFT predictions with the measurements on mixtures set up in the sonar tube is very satisfying. In the (0-5%) C_3F_8content region the calibration curve sensitivity is around 10$ms^{-1}\%^{-1,}$ due to the large difference in molecular weight of the two components (28 and 188 units).

The observed C_3F_8 concentration change of ~ 5.10^{-4} is a dramatic demonstration of the sensitivity of this simple instrument to small changes of concentration of a heavy vapour in a light carrier.

This sensitivity has been verified by the author [79] in collaboration with colleagues at CERN and at the anaesthesia department of the Centre des Hôpitaux Universitaires de Genève in August 2001 studies of the sensitivity of a combined ultrasonic gas analyzer/flowmeter to concentrations of the heavy anaesthetic vapours;

- Halothane (C_2HF_3ClBr: MW=197);
- Enflurane & Isoflurane ($C_3H_2F_5OCl$: MW=184);
- Desflurane ($CF_2H\text{-}O\text{-}CHF\text{-}CF_3$: MW=168);
- Sevoflurane ($CFH_2\text{-}O\text{-}CH[CF_3]_2$: MW=200).

which must be carefully maintained in percent-scale ranges in a light carrier composed of mixtures of nitrous oxide (N_2O: MW = 44) and Oxygen (O_2: MW=32).

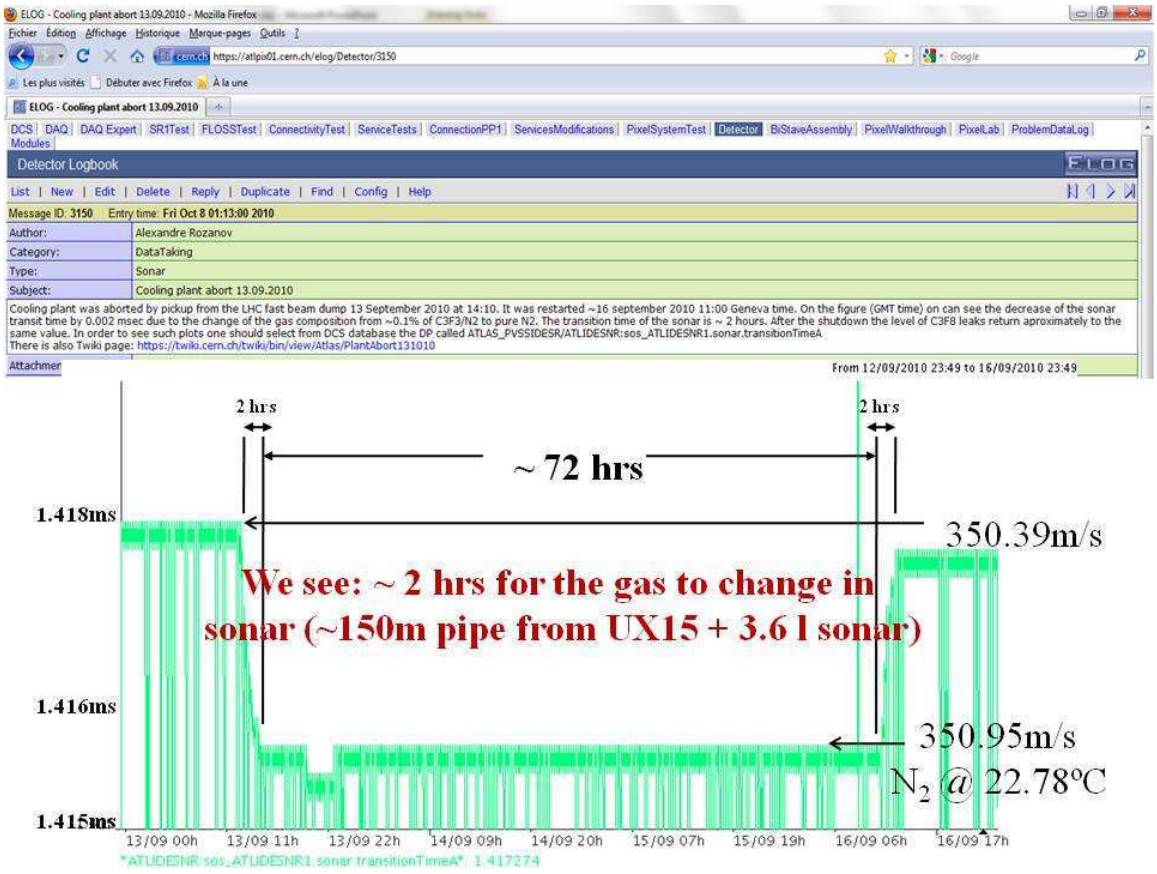

Fig 5.10. Change in sound velocity seen in the environmental N_2 gas surrounding the ATLAS pixel detector during the C_3F_8 cooling shutdown 13-16/9/2010 due to cessation of C_3F_8 leak into the environmental volume

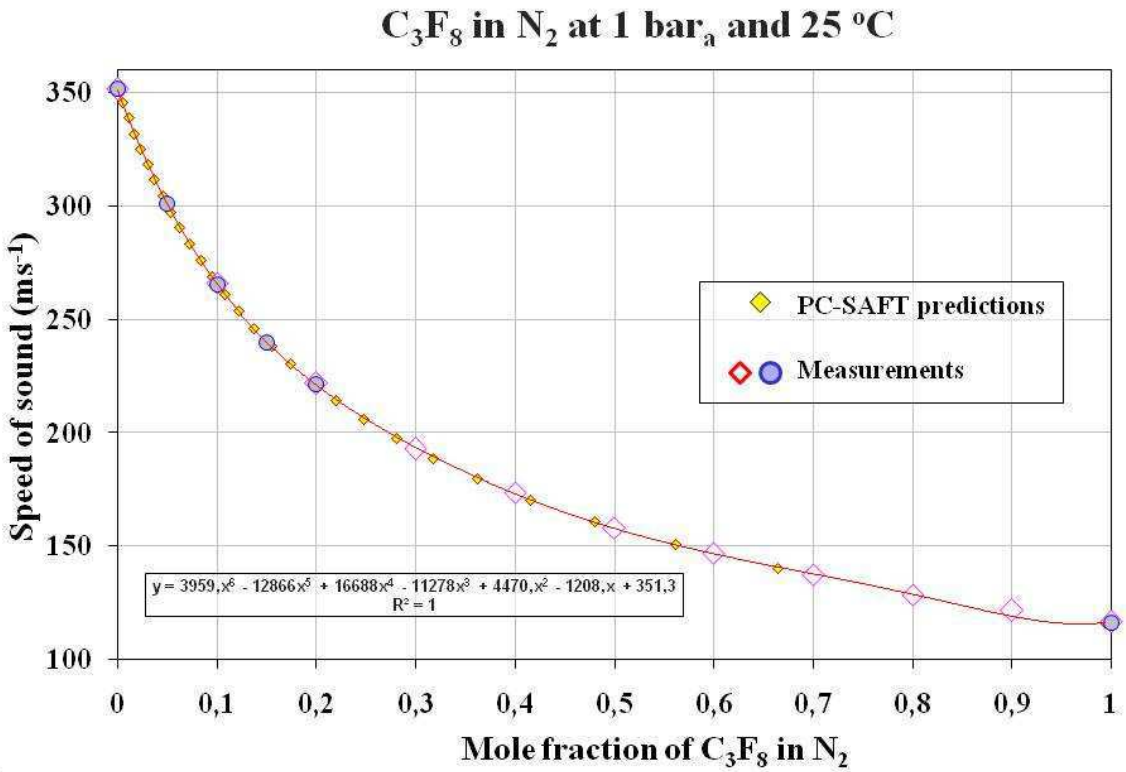

Fig. 5.11 Comparison of PC-SAFT prediction with sound velocity measurements over the full N_2/C_3F_8 range.

5.3 The proposal for a surface condenser to reduce or eliminate compressor stress

As previously mentioned, several options exist for the elimination of the stress seen by the present Haug compressors of the ATLAS ID tracker C_3F_8 evaporative cooling system. Given that the uninsulated liquid supply tubing is inaccessible until a possible future upgrade, and the lack of insulation requires delivery to the injection capillaries at a pressure of ~ $17bar_{abs}$ to avoid premature boiling in the liquid delivery lines, this pressure, presently delivered by the compressors in a 2-stage configuration, must be provided by other means. This could be done by liquid booster pumps, but these have had a less than satisfactory reputation in use at CERN, and such pumps with graphite gears or palettes have been found to produce particulate contamination requiring filtration.

The proposed solution [76] is a dramatic amplification of the SLD CRID thermo-siphon principle, using a substantial fraction of the 90 m depth of the ATLAS pit to generate the liquid pressure presently generated by the compressors located in the USA15 underground service cavern. To do this, the condenser, running C_3F_8 or a mixture of C_2F_6/C_3F_8 would be located at the surface. Vaporised coolant leaving the ATLAS tracker would ascend to the surface. Three configurations of such a system are possible:

- A system retaining reciprocating compressor(s) in the USA15 cavern, but with substantially reduced compression ratio, probably being of single-stage configuration with a likely output pressure in the range 5-$9bar_{abs}$. Vapour condensation at the surface would take place at the output pressure of the compressors minus the small static- and flow- related pressure drops seen by the compressed vapour on its ascent to the condenser. The condenser would probably be cooled with standard water;

- A system eliminating the present reciprocating compressors altogether (and with them most of the unreliable and potentially polluting moving parts including piston rings etc). It this case the condenser would need to be the coldest part of the cooling system, probably requiring a powerful industrial refrigeration plant;

- A system integrating a different oil-less (turbine) compressor technology. One promising candidate is offered by the Turbocor® direct drive supercharger technology.

These alternatives are considered in the following sections.

5.3.1. Moves toward a 'compressorless' thermo-siphon SFC circulation system

Figure 5.12 illustrates a simplified layout for a passive compressorless thermo-siphon circulation system employing a surface condenser [80]. The inaccessible internal coolant distribution within the service-ways through the ATLAS magnets would be unchanged from the present configuration shown in Fig. 4.41. The changes, indicated in the right-hand side of Fig 5.12 are confined to the USA15 service cavern, the new tubing linking it to the surface, and the new surface condenser with its low-temperature chiller installation.

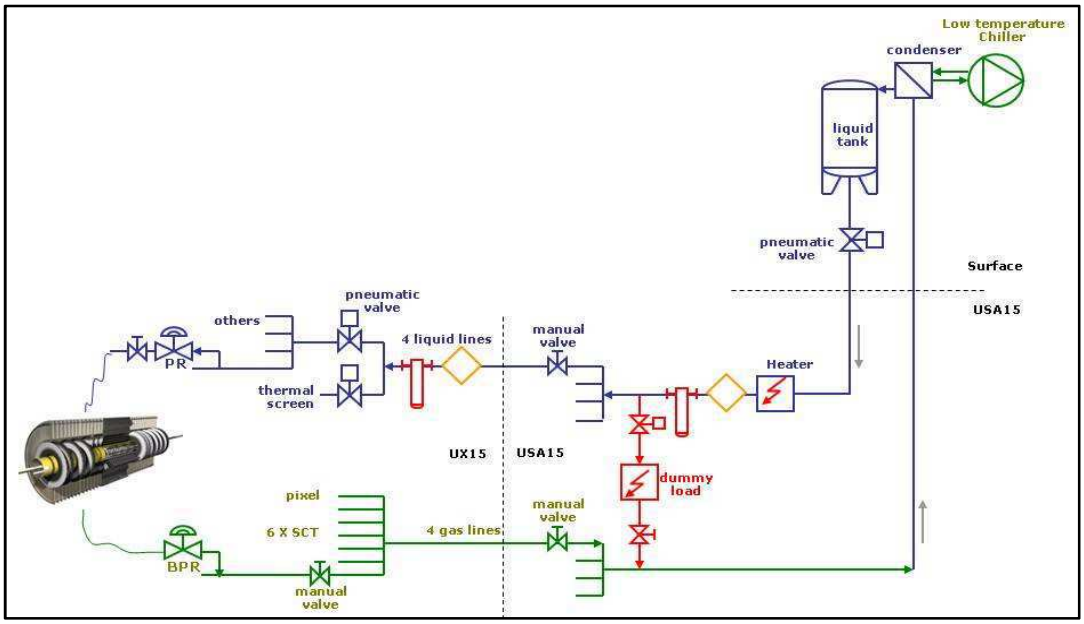

Fig 5.12. A possible compressorless thermo-siphon circulation system employing a surface condenser.

The layout of Fig. 5.12 has been arrived at following successful recent tests on a small-scale (18 m height difference) thermo-siphon shown in Fig. 5.13, together with its thermodynamic cycle diagram.

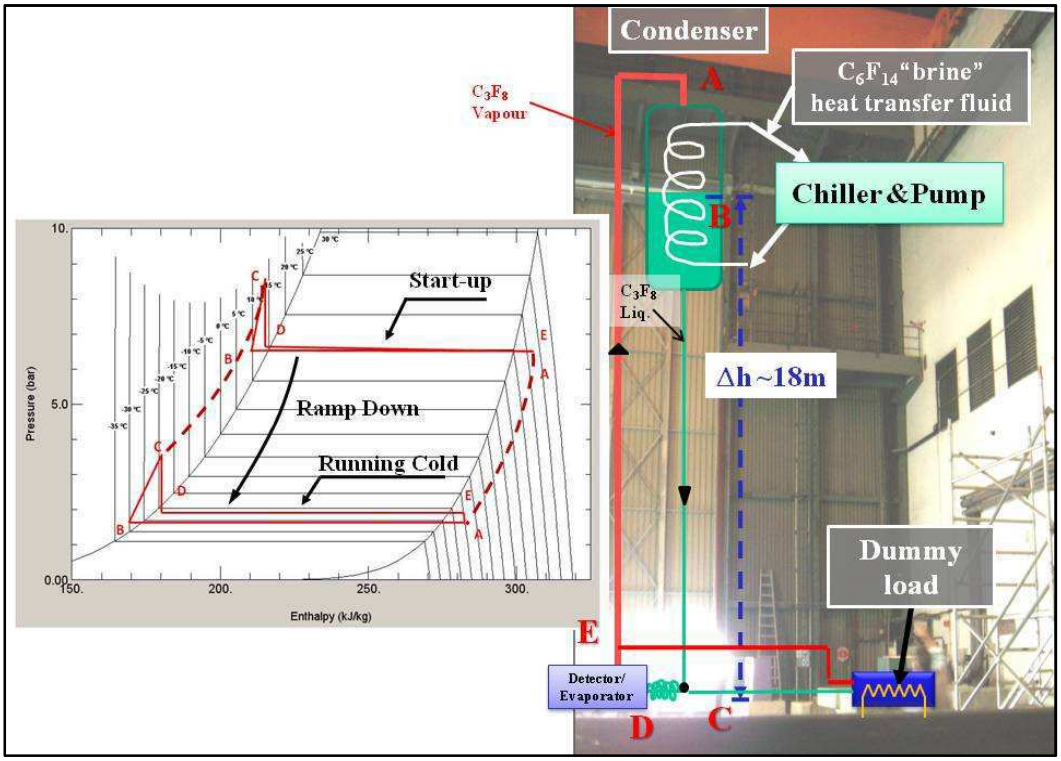

Fig 5.13. Miniature (18m) compressorless thermo-siphon circulation test system.

The miniature thermo-siphon successfully demonstrated all the phases of operation, including start-up from warm, normal operation at a variety of power levels and adapted liquid flow rates, normal shutdown and recovery from 'abnormal' shutdowns caused by (for example) simulated power failures to the chiller which circulated the C_6F_{14} 'brine' coolant to the heat exchanger in the elevated condenser.

The thermo-siphon demonstrated long-term stable operation over many tens of hours at constant performance, for example evacuating 1.6kW of heat through evaporation at -28°C with a mass flow of 16gms^{-1} C_3F_8. Evaporation at -25°C(-5°C) at mass flows of 21gms^{-1}(30gms^{-1}) could respectively recover 2.1kW (3kW), through the use of almost all the enthalpy available at the evaporation temperatures.

With the simple fixed-flow liquid circulation pump of the C_6F_{14} chiller and the single coil heat exchanger used in this condenser an important criterion for operation was that the temperature of the saturated vapour in the headspace $T_{sat(tank)}$ above the liquid remained at least 1°C above the bulk liquid temperature $T_{sat(liq)}$. At very low C_3F_8 flow rates where there was less condensation work for the heat exchanger this temperature difference could collapse, causing the flow to stall. A minimum flow through a switchable dummy load in parallel with the normal load was considered an advantage. A more sophisticated variable flow chiller and dual coil condenser is foreseen in the next development system; a 70m demonstrator being installed between the ATLAS surface building and a 2kW load installed in the USA15 underground service cavern. This system makes use of an existing stairwell for tube passage. The control system will link the speed of the C_6F_{14} 'brine' liquid pump to the condenser coil temperature via a PID controller and a variable frequency motor drive.

A dummy load is necessary also to start circulation to allow priming of the condenser for the ($T_{sat(tank)} > T_{sat(liq)}$) circulation criterion to be established before flow is sent to silicon detectors. The dummy load is itself primed by virtue of its depth with respect to the condenser.

Depending whether the final system serves as a compression booster or a pure thermo-siphon, its surface condenser cooling configuration and surface power requirements will differ greatly. Figure 5.14 illustrates a possible thermodynamic loop for a compressorless thermo-siphon system adapted to 60kW on detector cooling and using the ATLAS pit depth [81].

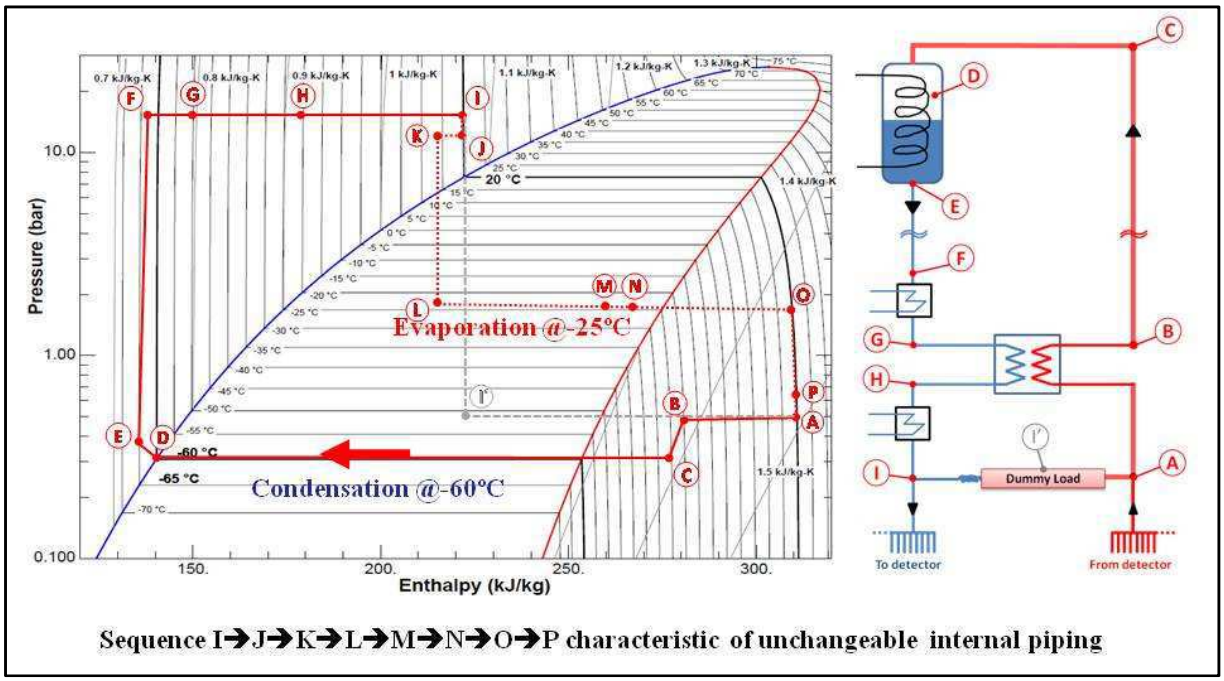

Fig. 5.14 A thermodynamic loop under consideration (November 2010) for a thermo-siphon system

In this scheme it is planned to mount the C_3F_8 condenser at a high point in a surface building (equivalent height ~ 3 storeys). This elevation, when added to the useable pit depth, results in a probable 95m vertical liquid column. It is proposed to insulate the liquid down pipe over most of its length to avoid water condensation on the outer surface, but to install heaters near the base of the column (F➔G➔H➔I) to raise the liquid temperature to ~20ºC for passage through the uninsulated pipes linking the USA15 service cavern to the liquid distribution racks on the ATLAS service platforms. At the base of the liquid column C_3F_8 bubble formation is prevented by the 15bar ρgh compression of the 95 m of C_3F_8 liquid. The sequence I➔J➔K➔L➔M➔N➔O➔P is not shown in the circuit diagram of Fig 5.14, as it is based on the unchangeable *innards* already shown in Fig. 4.34.

The ρgh hydrostatic advantage of exploiting the ATLAS pit depth is clear: the density difference between C_3F_8 liquid from the condenser and warm returning vapour (respectively ~1650 & ~6.5 kgm^{-3}) means that the hydrostatic pressure drop for vapour returning to the surface is only ~ 60mbar. The ascent tube is sized to give a total pressure drop (hydrostatic + dynamic) of around 160 mbar for a C_3F_8 vapour flow of around 1.2 kgs^{-1}

Condensation takes place at the relatively low pressure (temperature) of 300$mbar_{abs}$ (-60ºC), requiring a very powerful cooling plant for the intermediate C_6F_{14} 'brine', as shown in fig 5.15

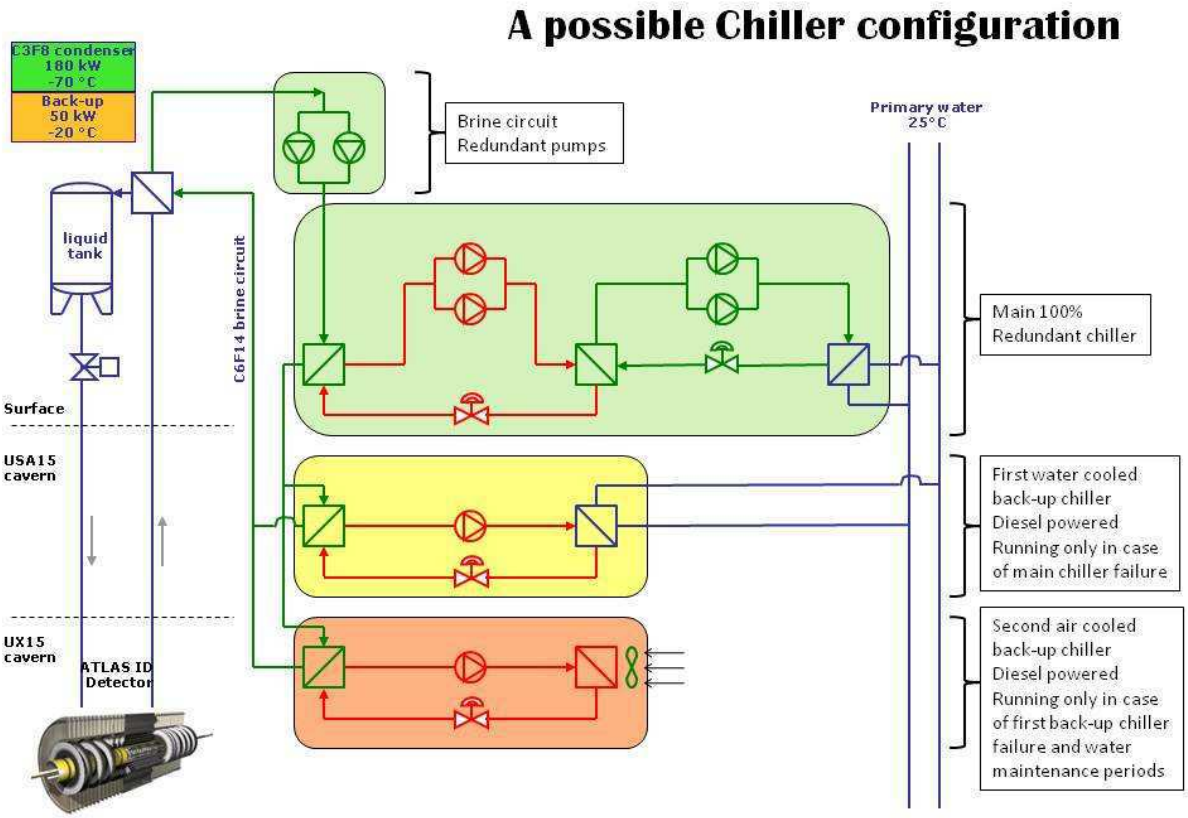

Fig 5.15 A possible brine chiller / circulator for the C_3F_8 surface condenser (after [81]).

This proposed chiller (based on commercial units with two cascaded refrigeration stages) draws ~ 180kW of electrical power to cool and circulate the required C_6F_{14} liquid delivery of 20(40) kgs^{-1} - for a temperature rise of 10(5)°C in the C_6F_{14} - in the range (-60➔-70°C) necessary to condense around 1.2 kgs^{-1} of C_3F_8. The heat gained by the C_6F_{14} in this process is extracted through a 'primary water' feed at 25°C from the nearby ATLAS water cooling tower. Power gains could be made by increasing the condensation temperature, but the uninsulated internal tubing and finite pit depth (short of mounting the condenser on a pylon) greatly limit this margin. The ~15bar (condenser exit ➔ capillary exit) pressure difference of the original system of Figs. 4.35 & 4.41 must be respected since the lengths of the inaccessible capillaries are determinant.

The thermodynamics of circulating a C_3F_8/C_2F_6 blend with a cold surface condenser and would be very similar to that shown in Fig 5.14, the main difference being the raising of the on-detector evaporation line from 1.67bar_{abs} to pressures in the range 2.5-3 bar_{abs}, depending on the final blend chosen. The condensation pressure would be expected to rise by a small amount; probably a few hundred mbar. The pressure generated by the ρgh column of a liquid with a (10-30%) admixture of C_2F_6 in C_3F_8 would be reduced very slightly (by around 3% in a blend containing 30% C_2F_6 compared to the pressure generated in a column of pure C_3F_8), and would have little effect on the circulation, which would in any case be substantially improved by the higher evaporation pressure to counter the losses in the present internal configuration.

Temperature profiles along dummy SCT and pixel structures will soon be measured in a variety of C_3F_8/C_2F_6 blends. Should these measurements, together with those of heat transfer coefficient prove promising, it is likely that C_3F_8/C_2F_6 blends will be recommended for use in a reconfigured circulation system with a surface condenser and reduced (or no) underground compression.

5.3.2 Déjà-vu? the turbine compressor ...

Figure 5.16 (a) illustrates the internal construction of the Danfoss Turbocor® direct-drive centrifugal turbine compressor[59] which has recently entered the industrial market as a retrofit to conventional reciprocating installations and which uses innovative oil free gas and magnetic bearings for the shaft carrying the dual impellers. First calculations suggest that one such compressor – the Turbocor TT-300 operating at 45,000 rpm could replace the entire bank of Haug reciprocating compressors, however at the lower discharge pressure of 7-8bar_{abs} [80]. The remaining pressure would be provided by the vertical liquid column from the surface condenser. A Turbocor TT-300 has been purchased by CERN, together with an evaporator and condenser in a combined test stand (Fig. 5.16 b). An extensive study of this compressor is planned to assess its suitability for the circulation of C_3F_8. Perhaps the circle is closing on the alarming SLD experience with the Paxton supercharger and its flailing belts... it will be interesting to see how this story develops.

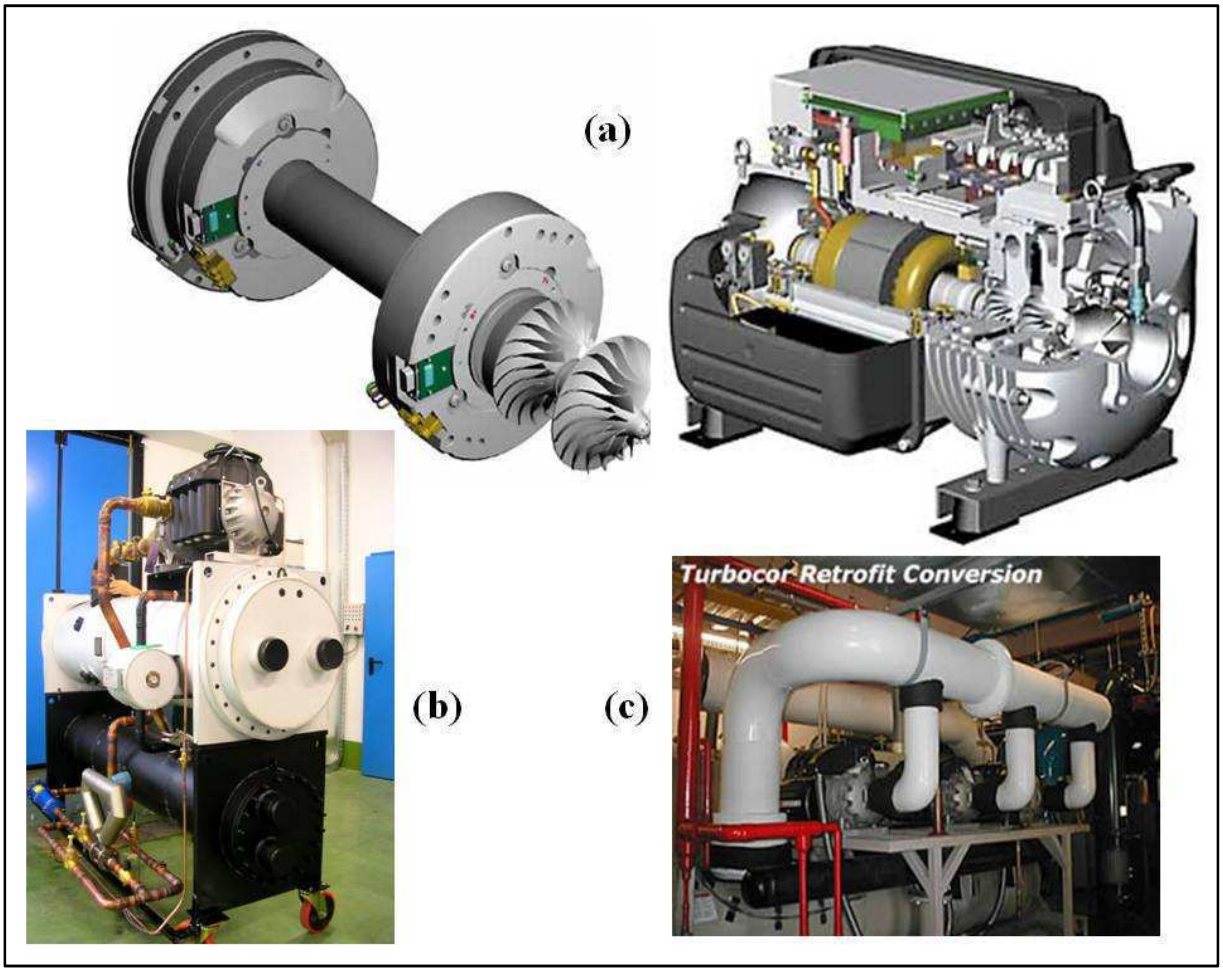

Fig 5.16 Turbocor dual-impeller centrifugal compressor. Internal components (a). including central shaft with innovative dual magnetic / gas floating bearings directly driven from the electric motor. A Turbocor test stand recently bought by CERN (b) and an example of a large industrial installation (c).

Figure 5.17(a) illustrates the use of an underground compressor running C_3F_8 - with a discharge pressure around 8 bar_{abs} - in combination with a surface condenser. The compressor could be a Turbocor or a single stage oil-less reciprocating type (or parallel bank): the thermodynamic situation would be identical, as shown in Fig 5.17(b). Both would use a surface condenser running at ~ 20°C on a standard chiller or standard water. The tortuous sequence **EFGH** on the enthalpy-pressure diagram if Fig 5.17(b) represents the inaccessable subcooling and capillary *innards* of the present incarnation (Figs 4.34, 4.35). The thermodynamic diagram of Fig 5.17(b) is independent of whether the compressor retained in the underground cavern is a turbine or an oil-less single-stage reciprocating type, of which several Haug models have been successfully employed at CERN for many years.

The thermodynamics of circulating a C_3F_8/C_2F_6 blend with a surface condenser and would be very similar to that shown in Fig 5.17(b), the main difference being the raising of the on-detector evaporation line from 1.67bar_{abs} to pressures in the range 2.5-3 bar_{abs}, depending on the final blend chosen.

[59] http://www.turbocor.com/

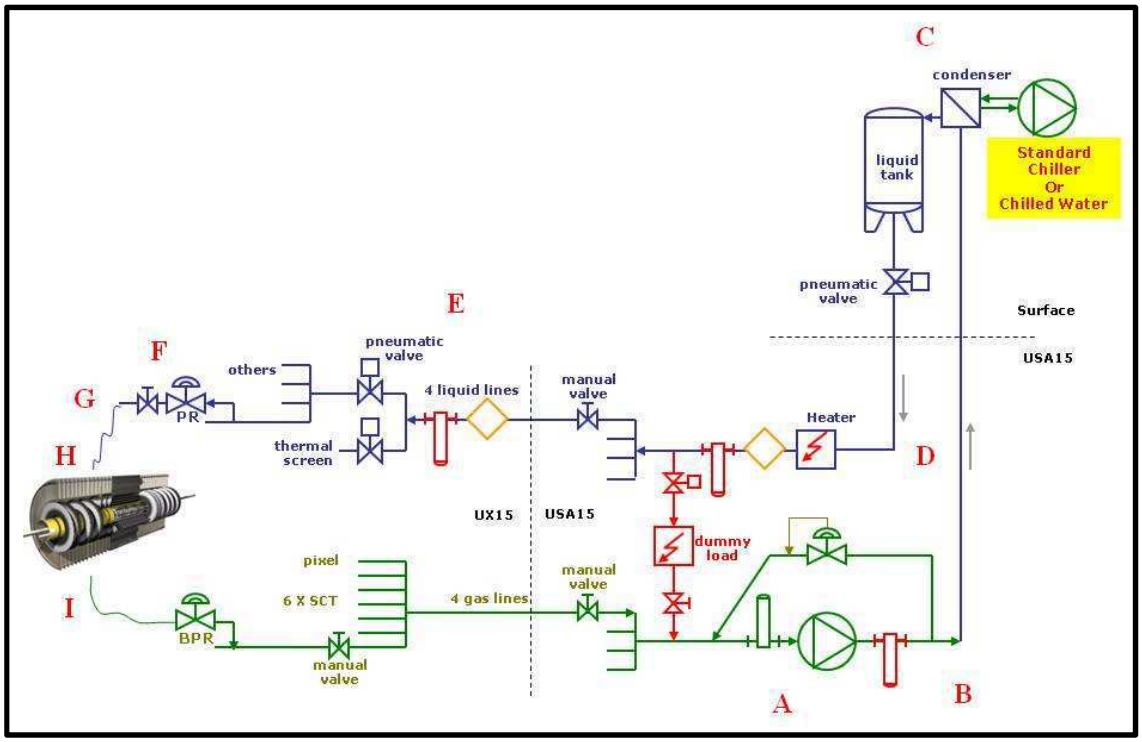

Fig 5.17 (a) Schematic of a cooling plant with of an underground compressor combined with a surface condenser running on a standard chiller or chilled water.

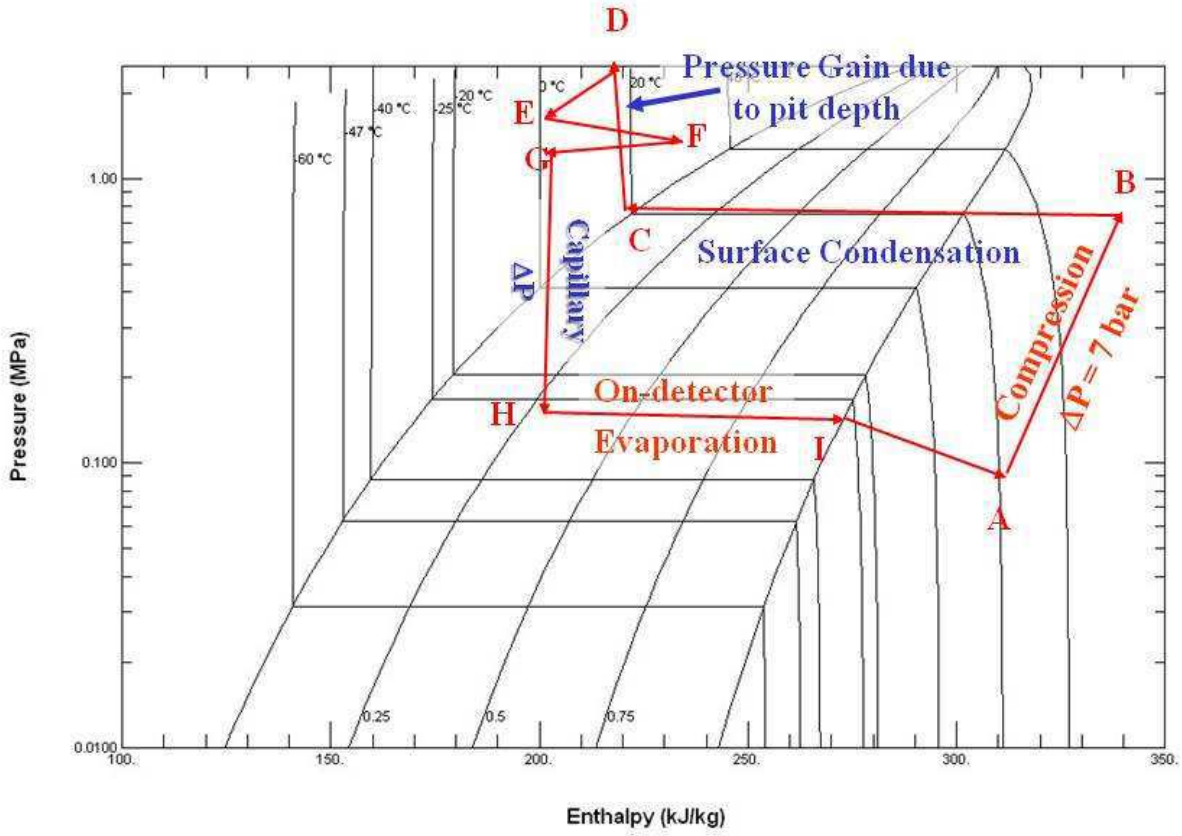

Fig 5.17 (b) Thermodynamic cycle of a cooling plant with of an underground compressor combined with a surface condenser running on a standard chiller or chilled water.

6. Fluorocarbon tracker cooling in other LHC experiments

The CMS, ALICE and TOTEM experiments at LHC use SFCs as coolants for their inner trackers due to their desirable properties of radiation tolerance, non-flammability and non-conductivity.

CMS operates a C_6F_{14} mono-phase cooling system. The system consists of three parts as shown in Fig 6.1:

- a commercial chiller plant using R507 refrigerant, located in a service cavern and cooling an intermediate fluid via a heat exchanger; ;
- the detector cooling units which circulate C_6F_{14} to the detectors. The C_6F_{14} liquid is cooled in local heat exchangers on the CMS experiment service platforms ;
- a 150m heat transfer line between the chiller and detector cooling units using C_6F_{14}

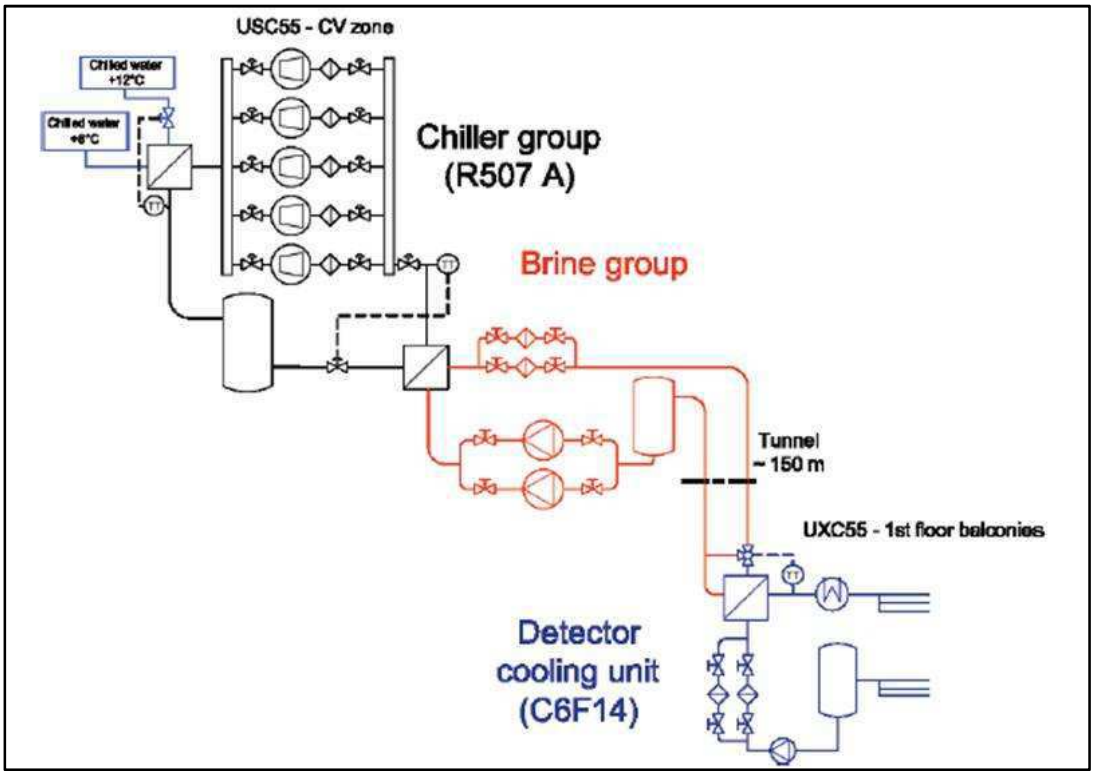

Fig. 6.1. CMS tracker liquid C_6F_{14} cooling plant schematic.

Each sub-tracker system has an independent cooling unit [75] which controls operation temperature for each sub-tracker separately. The systems subdivide and circulate the liquid to 198 cooling circuits for strip and pixel detectors with a total flow rate of 18 l/s^{-1}. CMS began its silicon tracker commissioning in 2008. During the 7 month commissioning period the leak rate of the cooling fluid from the detector cooling units increased to around 50 kg/day. Investigations revealed many leaks at multiple locations, many due to the use of resins, elastomers and plastic tubes and fittings incompatible with C_6F_{14} – avoidable problems perhaps, since extensive libraries of material compatibility data had been compiled by the DELPHI RICH [37] and SLD CRID groups.

Since the leaks were so widespread, the CMS collaboration decided to refurbish all the external cooling units at the beginning of 2009 with SFC-compatible materials and to implement a very thorough QA plan including visual inspection and X-ray imaging of at least 10% of the welds, together with leak and pressure tests at every stage of the assembly process. In parallel, a leak test was done on the internal and inaccessible detector circuits to check the leak rate, which became the reference point for later leak tests. In addition to the leak problems, other defects of the system, including an inability to purge gas, were remedied at the same time. Control and monitoring was also improved. The cooling system was restarted in June 2009 with a greatly reduced leak rate.

The ALICE silicon pixel detector (SPD) uses an evaporative C_4F_{10} cooling system [82] , whose schematic and thermodynamic cycle are shown in Fig. 6.2. The systems uses an oilless vapour compressor and a liquid pump[60].

[60] Caster Model MPA114316W1 with graphite impeller.

Pumped liquid enters 0.5mm ID capillaries and extracts heat from the pixel tracker at ~12°C at an evaporation pressure of ~1.7 bar_{abs}. The compressor raises the exhaust vapour pressure to ~2.1 bar_{abs} for condensation in a water –cooled condenser. The cooling flow rate is around 36gms^{-1}.

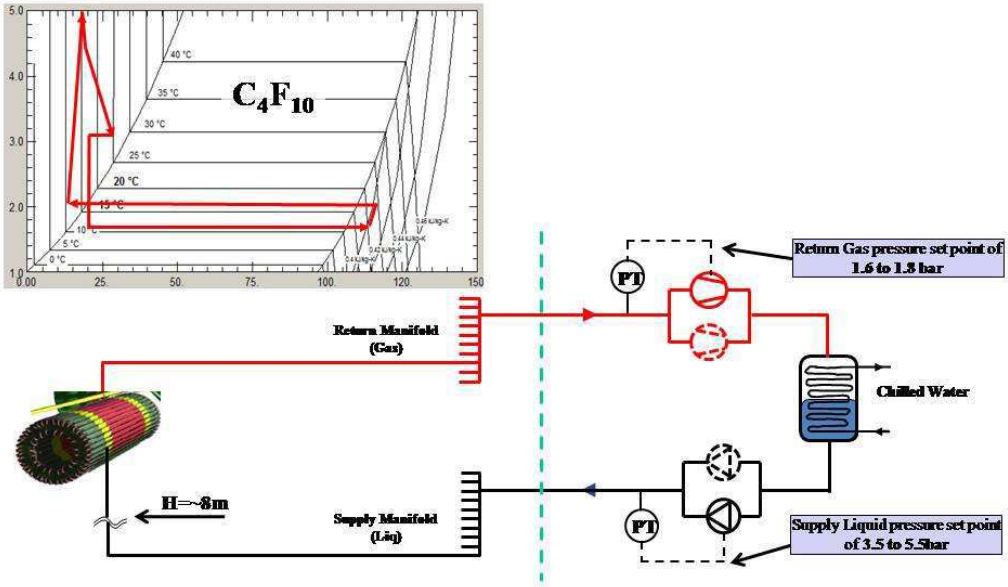

Fig. 6.2. ALICE silicon pixel detector evaporative C_4F_{10} cooling schematic and thermodynamics.

A possible upgrade to a thermo-siphon mode of operation is also being considered (Fig. 6.3). There have been problems with fragmentation of the impellers of the liquid pump presently in use, and compressor maintenance has been labour intensive. Compressor-less thermo-siphon operation, profiting from the 30m depth of the ALICE pit to generate the liquid supply pressure - rather than a liquid pump - is an attractive upgrade option.

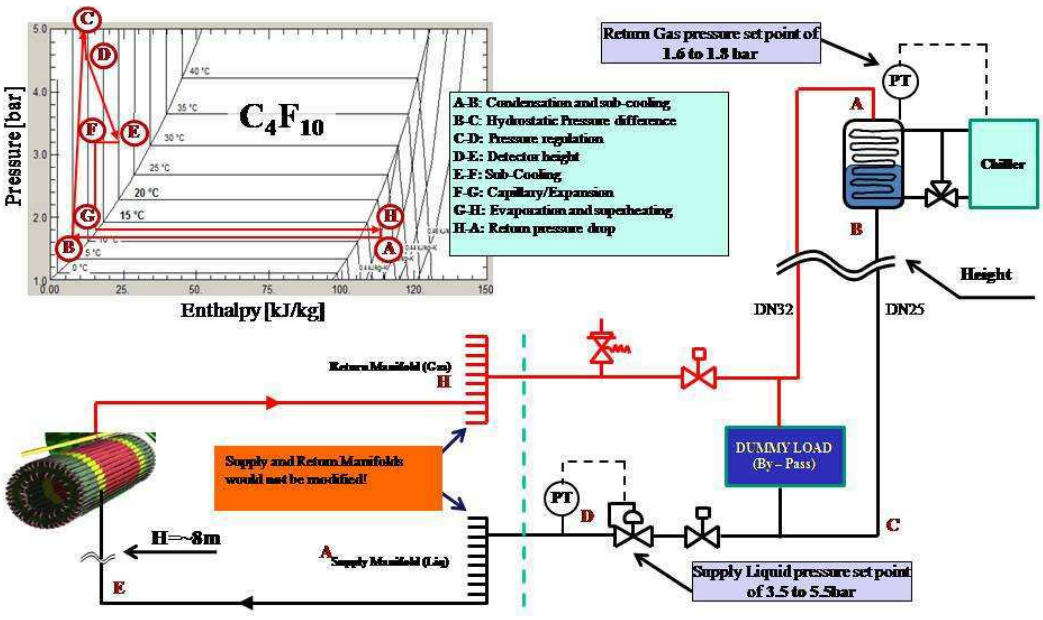

Fig. 6.3 Possible upgrade of the ALICE silicon pixel detector evaporative C_4F_{10} cooling system to thermo-siphon operation.

The TOTEM experiment will measure elastically scattered protons at angles of a few μrad with respect to the circulating LHC beams at IP5. To do this the experiment will position 240 silicon detectors in 24 Roman pots to within10σ of the beams. The silicon modules will be cooled by the evaporation of C_3F_8 at -15ºC; around 30W will be extracted from each Roman pot [83]. Figure 6.4 illustrates the circulation system, the capillaries and silicon detector cooling channels in the Roman pots.

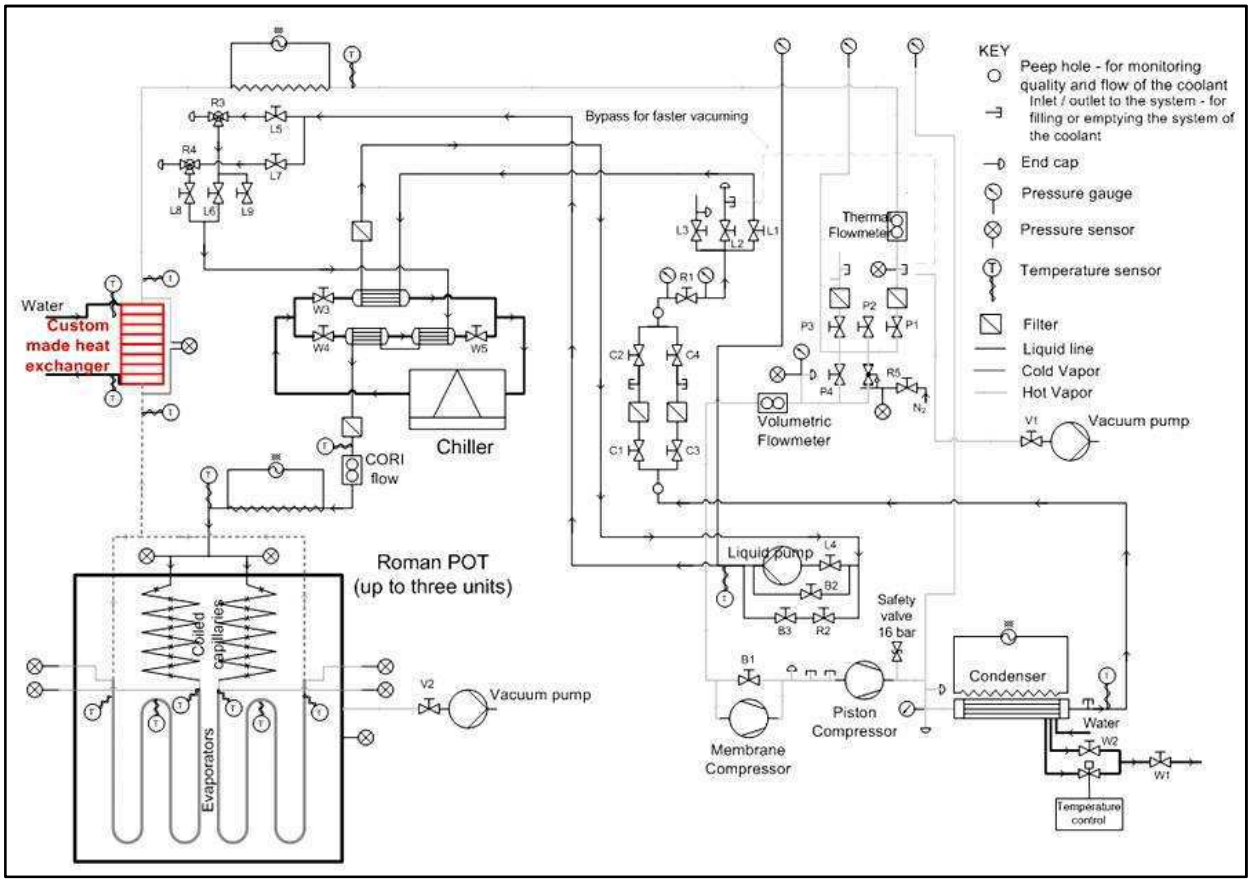

Fig 6.4. The C_3F_8 evaporative cooling system for silicon detector cooling channels the TOTEM Roman pots.

The Roman pot stations are at symmetrical distances of 147 and 220 m from LHC IP5 interaction point 5, and more importantly, more than 300m away from the USC55 underground service area. Because of the high radiation environment of the LHC tunnel, very little of the refrigeration system can be installed close to the Roman pots, with the exception of the capillaries and piping. USC55 is a protected and always accessible area, which hosts many of the technical services of the CMS experiment and of the LHC machine.

Evaporative fluorocarbon cooling was chosen since it allows fluid transport at ambient temperature over exceptionally long distances (in this case, round trips of 300 or 500m) at low flow and pressure drop. The evaporative cooling system provides a total cooling capacity of 1.2kW via a mass flow rate of 40 g/s uniformly shared among the 24 Roman pots. The fluid is supplied in liquid phase at a pressure of 11 bar_{abs} at the capillaries where the isenthalpic expansion decreases its pressure to the required evaporation temperature of -30ºC; a corresponding evaporation pressure of 1.35 bar_{abs}. At the Roman pot exhausts (dotted lines in Fig. 6.4) the evaporation process is completed and the gas is heated to a temperature above the tunnel dewpoint by means of a heat exchanger running demineralised water. The system uses oil-free compressors[61] as in the case of the other evaporative cooling systems discussed in this *mémoire.*

[61] Haug WTEGX 80/60 LM-L Pin 1 bar_{abs}; P_{out} 11-12bar $_{abs}$ 18m^3hr^{-1} C_3F_8

7 Irradiation studies on SFCs for the LHC cooling application.

Fluorocarbon fluids have been extensively studied under neutron and ionizing radiation as part of their qualification as LHC tracker coolants [84, 65]. Studies with neutrons included irradiation of small (<10 cm^3), static liquid samples of C_6F_{14}[62] to 3.10^{13} neutrons.cm^{-2} to simulate the expected environment at LHC. Studies showed the main longest-lived radioisotopes to be ^{18}F ($\tau_{1/2}$=110 min: 634 keV e^+ emitter). From neutron capture cross section data, the expected activity levels for these radionuclides are in the range 10^4-10^5 Bq.g^{-1} during circulation (for an instantaneous rate ~ 10^6 neutrons.$cm^{-2}s^{-1}$), which was considered be acceptable in a closed circuit system.

Samples were also exposed to ^{60}C γ irradiation. After an absorbed dose of 3 MRad, about 1% by weight of C_6F_{14} liquid had been chemically modified with chemical evidence for the production of reactive HF, due to impurities containing C-H groups. Scanning electron microscopy and Auger electron spectroscopy were used to characterize the morphologies and elemental compositions of C-, F- and O-containing polymeric deposits formed on stainless steel and aluminum samples immersed in liquid during irradiation. After 6 MRad, surfaces were almost uniformly covered with a polymeric layer of ~ 0.4 μm. Degradation and plate-out were greater in a sample of C_6F_{14} to which 3% (vol.) n-heptane had been added to act as a H-source and simulate the hydrogen containing impurities.

Since saturated fluorocarbons ($C_nF_{(2n+2)}$), are synthesized from alkane precursors, batch testing for residual H contamination (using the characteristic Fourier Transform Infra-Red signature of C-H bonds) is advisable. Techniques for the catalytic removal of $C_nF_xH_{(2n-x)}$ contamination were developed for the DELPHI RICH detector, where high fluid purity is needed for good UV transparency: similar techniques could be used in the present application.

Residually-hydrogenated and double carbon-bonded FC molecules can both be identified in Fourier Transform Infra Red spectroscopy via their respective characteristic absorptions near 3000 & 1784 cm^{-1}. Double carbon-bonded molecules also exhibit strong absorption in the UV range 190-200nm, allowing fairly straightforward batch qualification, as carried out for the DELPHI RICH detector. Techniques for the catalytic modification of these molecules were extensively investigated for DELPHI [35]: double carbon-bonded molecules can be reformed by a permanganate ($Mn0_4$) catalyst with the removal of the MnO_2 precipitated in the process.

The lack of inertness of the residually-hydrogenated molecules necessitated development of less aggressive methods of oxygen and water vapour removal through the use of porous membranes [35,36]. More recent techniques to remove hydrogenated molecules have centred on the use of activated carbon [85].

[62] Mfr.: 3-M Corp. Specialty Chemicals Division, St. Paul, MN, USA PFG 5060 grade >99%purity

8. An 'exotic' use of a Saturated Fluorocarbon for dark matter investigation.

The PICASSO experiment at SNOLAB is searching for dark matter via the detection of ionization-induced explosions of superheated droplets of C_4F_{10} in a modern twist on the bubble chamber [86]. The nuclear spin composition of ^{19}F makes it a favoured nucleus for direct detection of WIMPs undergoing spin-dependent interactions. The current detector employs 32 temperature-stabilised 4.5 litre acrylic cylinders located in the SNOLAB deep cavern to reduce cosmic ray background (Fig. 8.1). Each cylinder contains 4.5 litres of polymerized emulsion loaded with C_4F_{10} - droplets (Ø 50-280 μm peak ~ 200 μm), giving a C_4F_{10} effective target mass of 85g. Nine piezo sensors can triangulate a droplet exploding into a vapour bubble suspended in gel. The active part of each detector is topped with mineral oil connected to hydraulic manifold.

Each cylinder measures for a period of ~ 30 hours after which it is hydraulically re-primed to ~6 bar for ~15h to reform any vapour bubbles back to droplets.

Fig. 8.1. Two of the cylinders of the Picasso dark matter experiment. The connections the piezo acoustic sensors for the triangulation of C_4F_{10} droplet explosion sare shown, together with the tube for C_4F_{10} repressurization.

9. Conclusion

With good optical transparency and relatively low chromatic dispersion, saturated fluorocarbon fluids continue to enjoy an on-going thirty-year association with Cherenkov detectors. These advantageous properties are in addition to their attractive features of non -flammability, non-toxicity, good dielectric performance and compatibility with a wide range of materials used in detector construction. In the vapour phase SFCs can be mixed with other lighter gases to achieve blends in desired ranges of refractive index. Such blends have been exploited first at the OMEGA RICH (C_2F_6/N_2) during the mid 1980s and later at the SLD barrel CRID (C_5F_{12}/N_2) until the late 1990s. Liquid C_6F_{14} radiators were first used in the barrel detectors of the DELPHI RICH and SLD barrel CRID. This liquid has subsequently used in the STAR RICH at the Brookhaven Relativistic Heavy Ion Collider (RHIC) and in the ALICE HMPID detector at LHC. The end-caps of the DELPHI RICH and SLD CRID detectors were the first detectors to employ C_4F_{10} as a gaseous radiator. it has been subsequently used in the RICH detector of COMPASS and the LHCb RICH-1; the former with a CsI photocathode and the latter with hybrid photon detectors with P20 photocathode. Saturated fluorocarbon gaseous radiators, C_2F_6 and C_4F_{10} have also been flown in high altitude balloon-borne RICH detectors. The lightest of the saturated fluorocarbons, CF4 has been the most recent to be employed, in the LHCb RICH-2 and in a windowless RICH in the PHENIX detector at the Brookhaven RHIC. In the PHENIX detector CF4 is also the active gas in the imaging chamber, which uses a CsI photocathode in combination with Gas Electron Multiplier (GEM) stack.

Saturated fluorocarbon gaseous radiators are susceptible to ultrasonic analysis exploiting the variation of sound velocity with gas mixture at known temperatures and pressure. Sonar gas analyzers have been developed for the continuous real time monitoring of radiator mixtures and for monitoring the changeover from the radiator vessel passivation gas to the active Cherenkov radiator, and *vice versa*.

Techniques for the optimization of the UV transparency of saturated fluorocarbon fluids include the use of molecular sieves, porous membranes and active catalysts for water vapour and oxygen removal. Techniques for the analysis of delivered fluid batches to reveal residual hydrogen contamination, (including the presence of non-fully fluorinated molecules) were highly developed in the DELPHI RICH detector and have assumed even greater importance more recently in LHC detector cooling applications where such fluids can be subject to very high radiation doses.

Starting from their use as Cherenkov radiators, Saturated fluorocarbon have also progressed - due to their low viscosity and unmatched radiation tolerance – into cooling fluids for silicon tracker elements closest to the interaction points in LHC experiments. The use of evaporative cooling substantially reduces the coolant mass flow, allowing a lower mass cooling system and a reduces %X0 in the silicon tracker. They are now used as evaporative coolants in the silicon trackers of three LHC experiments, ATLAS< ALICE and TOTEM, and in liquid phase for the cooling of the CMS silicon tracker. Additionally C_6F_{14} is used as a liquid coolant for the electronics of the ATLAS Transition Radiation Tracker (TRT). Thermodynamic (evaporation and condensation cycle) techniques for *continuous* circulation of SFCs in particle physics experiments were pioneered at the SLD CRID detector at SLAC, since then, such techniques have been expanded to the much higher mass flow systems required for the cooling of silicon trackers.

These thermodynamic developments will continue with the exploitation of blended SFC mixtures and the hydrostatic advantages of deep detector pits to enhance reliability by eliminating moving parts such as compressors from the primary cooling loops.

This memoire has reviewed many aspects of these versatile fluids.

In addition, a novel and fascinating application using acoustic triangulation of exploding fluorocarbon liquid bubbles, which may help in the direct search for dark matter, is mentioned.

References

[1] R. Fowler et al., Ind. Eng. Chem. **39** (1947) 292.
[2] G. May, F2 Chemicals Ltd, Warrington, UK, (private communication).
[3] J. H. Simons & W. J. .Harland, J. Electrochem. Soc. **95** (1949) 47.
[4] D. L. Cochran; "Boiling Heat Transfer in Electronics" Proc. National Electronic Packaging & Production Conference (NEPCON68) New York, 4-6 June 1968.
[5] R. D. Danielson, N. Krajewski & J. Brost, "Cooling a Superfast Computer" Electronic Packaging & Production, July 1986, pp 44-45 (Cahners).
[6] N. Kramer, "Liquid burn-in testing cuts TWT supply failures"; Electronic Packaging & Production, November 1982, pp. 29-30 (Cahners).
[7] T. Thompson, "Condensation/Vapor-Phase Reflow Soldering" Assembly Engineering; June 1977 pp 44-47 Hitchcock Publishing Company Inc.
[8] P.A. Cherenkov, Dokl. Akad. Nauk. SSSR **2** (1934) 451, & Phys. Rev. **52** (1937) 378.
[9] J. V. Jelley, "Cherenkov radiation and its applications", Pergamon Press, 1958.
[10] I. E. Tamm & I.M. Frank, Dokl. Akad.Nauk SSSR 14 (1937) 107.
[11] E. Anassontzis et al., Nucl. Instr. & Meth. A **323** (1992) 351
also E. Albrecht et al., Nucl. Instr. & Meth. A 433 (1999) 47 & G. Lenzen et al. Nucl. Instr. & Meth. A 343(1994) 268
[12] R. Apsimon et al., IEEE Trans. Nucl. Sci. **34** (1987) 504.
[13] K. Abe et al., Nucl. Instr. & Meth. A **343** (1994) 74 also K. Abe et al., IEEE Trans.Nucl.Sci.40 (1993), 593
[14] B. Lasiuk et al., Nucl. Phys. A 698 (2002) **452**. STAR
[15] J. Baechler, et al., Nucl. Instr. and Meth. A **343** (1994) 213. NA35
[16] P. Martinengo, Proc 7th Intl. Workshop on RICH detectors, Cassis, France May 3-7 2010, to be published in Nucl. Instr & Meth A. ALICE
[17] A. Roberts; Nucl. Instr. Meth **9** (1960), 55.
[18] S. Poultney, G. Reynolds & J. Waters, Rev Scien. Instr **33** (1962), 574, Nucl. Instr. Meth **20** (1963), 267.
[19] J. Seguinot & T. Ypsilantis, Nucl Instr. Meth A **142** (1977) 377
also J. Seguinot et al., Nucl Instr Meth A **173** (1980) 283 also E. Barrelet et al Nucl Instr Meth A**200** (1982) 219.
[20] R. Bouclier et al, Nucl Instr. Meth A**205** (1983) 403 also R. McCarthy et al, Nucl. Instr. Meth A **248** (1986) 69.
[21] M. Davenport et al., IEEE Trans Nucl Sci **NS-30**(1983)35 also RAL PPESP/82/24, proposal 231, addendum 4 (1982).
[22] E. Nappi & J. Seguinot, Rivista del Nuovo Cimento 28, No. 8-9 (2005) 1.
[23] A. Augusto Alves et al., 'The LHcb Detector at the LHC', JINST3:S08005 (2008) 1
[24]I. Tserruya, Proc 7th Intl. Workshop on RICH detectors, Cassis, France May 3-7 2010, to be published in Nucl. Instr & Meth A.
[25] G. Barbiellini et al., Nucl. Instr. &. Meth. A 461 (2001) 269.
[26] E. Diehl, D. Ellithorpe, D. Muller & S. Swordy, Proc. 26th International Cosmic Ray Conference (ICRC 99), Salt Lake City, Utah, 17-25 Aug 1999: Vol. 3 pp 89-92.
[27] F. Tessarotto, Proc 7th Intl. Workshop on RICH detectors, Cassis, France May 3-7 2010, to be published in Nucl. Instr & Meth A.
[28] K. Zeitelhack et al., Nucl Instr & Meth A 433 (1999) 201. (HADES)
[29] N. Akopov et al., Nucl. Instr. & Meth. A 479 (2002) 511. (HERMES]
[30] I. Arino et al., Nucl. Instr. & .Meth. A516 (2004) 445-461. HERA-B
[31] S. Horikawa et al., Nucl. Instr. & Meth. A 595 (2007) 212 DIRAC
[32] M. Bosteels et al, LHCb RICH Gas System Proposal: LHCB-IG-EN-0003 version 1.0: INFRASTRUCTURE/GAS SYSTEMS Engineering Note, 6 August 2000, also C. Frei (private communication)
[33] E. Albrecht, et al., Nucl. Instr. and Meth. A 510 (2003) 262 & P. Fauland "The COMPASS Experiment and the RICH-1 Detector" PhD Thesis, University of Bielefeld, 3/2004; CERN-THESIS-2009-071 02/03/2004
[34] C. Pastore; Proc 7th Intl. Workshop on RICH detectors, Cassis, France May 3-7 2010, to be published in Nucl. Instr & Meth A.
[35]S. Ilie, G. Lenzen, Perfluorocarbon liquid. Specific chemical aspects for use within the DELPHI RICH, DELPHI internal note 93-33 RICH54, 30 March 1993
[36] O. Ullaland, Nucl. Instr. and Meth. A 553 (2005) 107
[37] E. Albrecht, S. Ilie & S. Jääskeläinen ; "Per-fluorocarbon effects on composite and polymeric materials used within RICH detectors" DELPHI internal note, 1989.
[38] M. Bosteels and S. Ilie "An inert cleaning system for Liquid Fluorocarbons" CERN MT-SM-93-02 (1993).
[39]"The distillation plant of the DELPHI Barrel RICH Detector" C. Joram, DELPHI 98-53 RICH94, 26 May 1998, also. H. Furstenau, et al., Nucl.Instr. and Meth.A371 (1996) 263.
[40] The Fluid systems for the SLD Cherenkov ring imaging detector. K. Abe *et al.* SLAC-PUB-5988, Oct 1992. Proc. IEEE Nuclear Science Symp., Orlando, FL, Oct 25-31, 1992.
[41] K. Abe *et al.* SLAC-PUB-95-6693, Oct 1994 and IEEE Trans.Nucl.Sci.42:518-523, 1995.
[42] "Monitor and Control Systems for the SLD Cherenkov Ring Imaging Detector." P. Antilogus et al. SLAC-PUB-5105, Oct 1989. Proc. Int. Conf. on Accelerator and Large Experimental Physics Control Systems, Vancouver, Canada, Oct 30 - Nov 3, 1989 (ICALEPS89): Nucl.Instr. and .Meth.A293 (1990) 136.
[43] "A sonar-based instrument for the ratiometric determination of binary gas mixtures": G. Hallewell et al: Nucl. Instr. & Meth A 264 (1988) 219.
[44] "The Performance of the barrel CRID at the SLD: Long term operational experience." K. Abe et al; IEEE Trans.Nucl.Sci.45:648-656,1998.

[45] M. Andrieux et al Nucl. Instr. & Meth. A 371 (1996) 259.
[46] E. Albrecht et al: Nucl.Instr. & Meth. A 502 (2001) 266.
[47] A. Papanestis LHCb internal note 2004-043 28 Feb 2005.
[48] C. Arrighi et al.; "A Radiation Hard Detector for Tracking and Secondary Vertex Finding for the EAGLE detector at the CERN LHC", EAGLE Internal note INDET 009, April 30, 1992
[49] "Two phase liquid-gas cooling for silicon Pixel Detectors": A. Fallou et al., Proc. 1st international workshop on electronics and detector cooling (WELDEC), Lausanne Oct 4-7, 1994
[50] K. Woloshun et al., Proc 1st international workshop on electronics and detector cooling (WELDEC), Lausanne Oct 4-7, 1994
[51] R. Apsimon and G. Tappern, Proc 1st international workshop on electronics and detector cooling (WELDEC), Lausanne Oct 4-7, 1994
[52] see for example "Liquid cooling systems (LCS2) for LHC detectors" P. Bonneau et al., Proc. 5th Workshop on Electronics for LHC Experiments (LEB99), Snowmass, Colorado, 20-24 Sep 1999. Snowmass 1999; pp 416-420
[53] ATLAS Inner detector technical design report Vol. 2 CERN/LHCC/97-17 ATLAS TDR 5, 30 April 1997 pp 401-404, 464
also ATLAS pixel technical design report CERN/LHCC/98-13 ATLAS TDR 11, 31 May 1998 pp 39-42
[54] See: ATLAS Inner detector technical design report Vol. 2 CERN/LHCC/97-17 ATLAS TDR 5, 30 April 1997, pp 497-509
[55] See: ATLAS Inner detector technical design report Vol. 2 CERN/LHCC/97-17 ATLAS TDR 5 30 April 1997, pp 358-364
[56] See: ATLAS pixel technical design report CERN/LHCC/98-13 ATLAS TDR 11, 31 May 1998 pp 206-214
[57] See: ATLAS Inner detector technical design report Vol. 2 CERN/LHCC/97-17 ATLAS TDR 5 30 April 1997, p 364
[58] "A Low Cost I/O Concentrator Using the CAN Field- Bus" B. Hallgren et al; CERN-EP-99-159, Oct 1999 Proc. International Conference on Accelerator and Large Experimental Physics Control Systems, Trieste, Italy, 4-8 Oct 1999 http://atlasinfo.cern.ch/ATLAS/GROUPS/DAQTRIG/DCS/LMB/SB/elmb_1.html
[59]. Reviewers' report on ATLAS Inner Detector Cooling Review, CERN 30 November 1997
Also contributions by R. Budinský, G. Hallewell, G. Lenzen, T. Niinikoski, J.Thadome & V. Vacek:,
Proc. ATLAS Cooling Review, CERN (18-19 September, 1997)
[60] "Direct Evaluation of Vapour-Liquid Equilibria of Mixtures by Molecular Dynamics Using Gibbs-Duhem Integration" M.Lísal, & V. Vacek Molecular Simulation, **18** (1996) 75.
[61] Custom mixture: properties with "REFPROP": Database of thermodynamic and transport properties of refrigerants and refrigerant mixtures: Version 6.01 National Institute of Standards and Technology, Gaithersburg MD 20899 USA (1998): C_4F_{10}, C_3F_8, mix & CF_3I extensions by V.Vacek.
[62] Fluorocarbon Evaporative Cooling Developments for ATLAS Pixel and Semiconductor Tracking Detectors. E. Anderssen et al Proc 5th Workshop on Electronics for LHC Experiments, Snowmass, USA CERN 99-09/LHCC99-33 Oct 30,1999 pp 421-426
[63] "Characteristics of Heat Transfer Coefficient During Nucleate Pool Boiling of Binary Mixtures", T. Inoue, N. Kawae & M. Monde: Heat & Mass Transfer **33** (1998), 337
[64] M. Lísal, R. Budinský, V. Vacek: "Vapour-liquid Equilibria for Dipolar Two-Centre Lennard-Jones Fluids by Gibbs-Duhem Integration" Fluid Phase Equilibria, 135 (1997), 193
[65] V. Vacek, G. Hallewell, S. Ilia and S. Lindsay; Fluid Phase Equilibria 174 (2000) 191
[66] V. Vacek, G. Hallewell and S. Lindsay; Fluid Phase Equilibria 185 (2001) 305
[67] NIST Database of Thermodynamic and Transport Properties of Refrigerants and Refrigerant Mixtures-REFPROP PACKAGE (with extensions by V.Vacek for C_4F_{10}, C_3F_8, mix & CF_3I) Version 6.01, NIST, Gaithersburg MD 20899 USA, (1998)
[68] M. Price et al., Reviewers' report on ATLAS Inner Detector Cooling Review, CERN 26-28 May 1999
[69] Development of Fluorocarbon Evaporative Cooling Controls for the ATLAS Pixel and Semiconductor Tracking Detectors C. Bayer et al, Proc 6th Workshop on Electronics for LHC Experiments, Kracow, Poland, September 2000 CERN 2000-101 CERN/LHCC/2000-041, 25 Oct 2000.
[70] ISO 11898:1993 Controller area network (CAN) for high-speed communication (1993)
also DS301, CANopen Application Layer & Communication Profile Version 4.0, June 2000, CAN in Automation e. V.
also CANopen Working Draft 404 "Device Profile for Measuring Devices and Closed Loop Controllers".
[71] H. Boterenbrood E-LMB PID-controller Framework Software User Manual (Draft) NIKHEF 20 May 2002.
[72] J. Kuijt, P. de Groen, P. Timmer, D. Tascon Lopez, S. Schouten, H. Boterenbrood: E-LMB DAC 16-channel 12-bit DAC module Framework Software User Manual (Draft) NIKHEF 18 February 2002.
[73] ATLAS Inner Detector Thermal/Gas Final Design Review May 12-13, 2003. Chair B. Szeless
[74] D. Attree et al. The evaporative cooling system for the ATLAS inner detector. 2008. JINST 3:P07003(2008) 1.
R.Adolphi et al., JINST 3:S08004 (2008) 1
[75] R.Adolphi et al., JINST 3:S08004 (2008) 1
Also K. Nagai, "Cooling: Experience from ATLAS & CMS" Proc VERTEX 2009 (18th workshop on Vertex detectors) Veluwe, Netherlands September 13-18 2009
[76] G. Hallewell; presentation at ATLAS High Luminosity Upgrade Tracker Workshop, Liverpool University, December 6-8, 2006. http://indico.cern.ch/conferenceDisplay.py?confId=9131
[77] V. Vacek – Private communication
[78] ATLAS Pixel Detector On line Log https://atlpix01.cern.ch/elog/Detector/3150
[79] G. Hallewell, S. Lindsay, M. Streit-Bianchi "Interim report on a sonar gas analyzer for anaesthesia, based on the "Spirocell" Ultrasonic flowmeter. Results of tests at Hôpital Cantonal de Genève, August 6-10 2001."
CERN Distribution: H. Hoffmann, J-M le Goff, J-A Rubio, S. Stapnes.
H.U.G. Distribution: F. Clergue, C. Klopfenstein
[80] M. Battistin, J. Bothelo-Direito & G. Hallewell: Presentations at 3rd ATLAS ID cooling thermo-siphon Cooling workshop, 28 May 2010 http://indico.cern.ch/conferenceDisplay.py?confId=95414 Chair: M. Battistin CERN EN-CV.
[81] J. Bothelo-Direito: Presentation at 4th ATLAS ID cooling thermo-siphon Cooling workshop, 19 November 2010
[82] V. Manzari – private communication also A. Pepato et al., Nucl. Instr. & Meth. A565 (2006)
also J. Direito: Presentation at 3rd ATLAS ID cooling thermo-siphon Cooling workshop, 28 May 2010 http://indico.cern.ch/conferenceDisplay.py?confId=95414 Chair: M. Battistin CERN EN-CV.

[83] M. Oriunno et al. Nucl. Instr. and Meth. A 581 (2007) 499 also CERN EDMS TS-CV 778214-v2 4/10/2006. Also: G. Antchev et al., Nucl. Instr. & Meth. A617 (2010
[84] S. Ilie, "Tests on Cooling Fluids: Radiation Resistance" Report to the ATLAS Inner Detector Cooling Review, 26-28 May 1999.
[85] M. Battistin, et al., Chemical and radiolytical characterization of some perfluorocarbon fluids used as coolants for LHC experiments: chemical characterization, CERN TS-Note2006-010, 30 October 2006
[86] F. Aubin et al; New Journal of Physics 10 (2008) 103017 doi:10.1088/1367-2630/10/10/103017

APPENDIX-1: Perturbed-Chain Statistical Associating Fluid Theory

PC-SAFT equation of state formalism [A1-1]

The use of empirical or semi-empirical equations of state (EOS) requires knowledge of many parameters derived from extensive and time-consuming thermo-physical measurements on the fluids of interest. Such measurements are made for the frequently used substances in the petro-chemical and refrigeration industries, with the result that "special" or "minor" applications (loosely defined as being less than millions of tonnes of usage per year) generally lack adequate experimental data needed to derive EOS predictions of thermodynamic behaviour.

Nevertheless over the last 8 years thermophysical properties of the three saturated fluorocarbons of main interest R218 (C_3F_8), R116 (C_2F_6) and R610 (C_4F_{10}) were collected and have already been added to the REFPROP 8.0 database[63] or the NIST Web book of Chemistry[64])

The main advantage of the theoretically-based EOSs (SAFT or PC-SAFT) is their quite accurate approximation of complex multicomponent mixtures. We therefore decided to use the PC-SAFT model [A1-2] to predict also the thermophysical properties of several saturated fluorocarbon binary mixtures. In this way we substitute simplistic traditional EOS (for example the ideal gas and Van Der Waals EOS, shown at the time to be incapable of modeling fluorocarbon-nitrogen mixtures by Hallewell et al [A1-3]) and also the empirically or semi-emprically based EOS, including the extended Benedict Webb Rubin EOS.

The PC-SAFT EOS models long chain molecules using the following parameters:

- segment number ***m***;
- segment diameter ***σ*,**
- segment attraction parameter ***e***, or the more complex and more often used so-called segment energy parameter ***ε*/*k*$_B$,**

Despite this seeming simplicity, this molecular model accounts for the essential characteristics of real molecules;

- repulsive interactions;
- non-spherical shape of molecules (chain formation);
- attractive interactions (dispersion);

For our application no pre-existing PC-SAFT molecular parameters for SFCs were found in the literature. Therefore the parameters *m*, *σ*, and *ε* had to be determined by fitting the saturated vapor pressure and liquid density *(both from experimental data sources in the literature)*

The Perturbed-Chain SAFT EOS adopts a hard-sphere chain fluid as a reference fluid. The EOS consists, thus, of a reference hard-chain EOS and a perturbation contribution.

$$\frac{A}{NkT} = \frac{A^{hc}}{NkT} + \frac{A^{pert}}{NkT}, \qquad Z = Z^{hc} + Z^{pert} \tag{A1.1}$$

where $Z = P.v/R.T$ is the compressibility factor, P is the pressure, v is the molar volume, R denotes the gas constant, T is the absolute temperature, A is the Helmholtz free energy, N is the total number of molecules, k is the Boltzmann constant, and superscripts ^{hc}, and ^{pert} denote the hard-sphere chain reference EOS, and the perturbation contribution, respectively. In this terminology the reference EOS reduces to ideal-gas behavior at the zero-density limit.

[63] http://www.nist.gov/data/nist23.htm
[64] http://webbook.nist.gov/chemistry/

The hard-chain contribution

Based on Wertheim's thermodynamic perturbation theory of first order Chapman et al. developed an equation of state, which for hard-sphere chains comprising ***m*** segments is given by

$$\frac{A^{hc}}{NkT}-\frac{A^{ideal}}{NkT}=\overline{m}\cdot\frac{A^{hs}}{N_s kT}-\sum_i x_i(m_i-1)\cdot ln\, g_{ii}^{hs}(\sigma_{ii}) \tag{A1.2}$$

$$Z^{hc}=1+\overline{m}(Z^{hs}-1)-\sum_i x_i(m_i-1)\rho\frac{\partial ln\, g_{ii}^{hs}}{\partial\rho} \tag{A1.3}$$

$$\overline{m}=\sum_i x_i m_i \tag{A1.4}$$

where $\mathbf{x_i}$ is the mole fraction of chains of component **i**, $\mathbf{m_i}$ is the number of segments in a chain of component **i**, **r** is the total number density of molecules, $\mathbf{g_{ii}^{hs}}$ is the radial pair distribution function for segments of component **i** in the hard sphere system, and superscript '**hs**' indicates quantities of the hard-sphere system. The expressions of Boublik, Mansoori et al. are used for mixtures of the hard-sphere reference system in Eqs. (A1.2) and (A1.3), given by;

$$\frac{A^{hs}}{N_s kT}=\frac{1}{\zeta_0}\left[\frac{3\zeta_1\zeta_2}{(1-\zeta_3)}+\frac{\zeta_2^{\,3}}{\zeta_3(1-\zeta_3)^2}+\left(\frac{\zeta_2^{\,3}}{\zeta_3^{\,2}}-\zeta_0\right)\cdot ln(1-\zeta_3)\right] \tag{A1.5}$$

$$g_{ij}^{hs}=\frac{1}{(1-\zeta_3)}+\left(\frac{d_i d_j}{d_i+d_j}\right)\frac{3\zeta_2}{(1-\zeta_3)^2}+\left(\frac{d_i d_j}{d_i+d_j}\right)^2\frac{2\zeta_2^{\,2}}{(1-\zeta_3)^3} \tag{A1.6}$$

$$Z^{hs}=\frac{1}{(1-\zeta_3)}+\frac{3\zeta_1\zeta_2}{\zeta_0(1-\zeta_3)^2}+\frac{3\zeta_2^{\,3}-\zeta_3\zeta_2^{\,3}}{\zeta_0(1-\zeta_3)^3} \tag{A1.7}$$

$$\text{Where}\qquad \zeta_m=\frac{\pi}{6}\rho\sum_i x_i m_i d_i^{\,m} \qquad m=\{0,1,2,3\} \tag{A1.8}$$

with d_i being a temperature dependent segment diameter of component i , according to

$$d_i=\sigma_{ii}\cdot\left(1-0.12\cdot\exp\left(-3\cdot\varepsilon_{ii}/kT\right)\right) \tag{A1.9}$$

Mixture management in PC-SAFT

Mixtures are investigated in PC-SAFT using the conventional Berthelot-Lorentz combining rules. The parameters between the pair segments are given as follows;

$$\sigma_{ij}=\frac{1}{2}\left(\sigma_i+\sigma_j\right),\qquad \varepsilon_{ij}=\sqrt{\varepsilon_i\varepsilon_j}\left(1-k_{ij}\right) \tag{A.1.10}$$

where $\boldsymbol{k_{ij}}$ is the unknown binary interaction parameter that is to be defined on the basis of the available experimental data. It can be considered to be equal to zero for mixtures of SFCs with two and three carbons since

Table A1-1 Complete set of parameters of gases and saturated fluorocarbons for the PC-SAFT EOS [A1-4]

Formula	M [g·mol^{-1}]	m [-]	σ [Å]	ε/k_B [K]	T_{min} [K]	T_{max} [K]	Data source	$AD(p)$ [%]	$AD(\rho_L)$ [%]	$SD(p)$ [%]	$SD(\rho_L)$ [%]
O_2	31.999	1.0740	3.2598	117.729	73	147	[95]	0.132	-0.122	0.380	0.882
Xe	131.290	0.9147	4.0747	237.682	163	276	[95]	0.012	-0.008	0.310	0.491
N_2	28.013	1.2053	3.3130	90.960	63	126	*				
CF_4	88.004	2.2326	3.1050	120.998	128	216	[95]	0.073	-0.069	0.134	0.657
C_2F_6	138.012	2.8108	3.3128	140.512	175	279	[95]	0.030	-0.028	0.156	0.281
n-C_3F_8	188.019	3.2747	3.4579	155.080	196	328	[95]	0.036	-0.033	0.350	0.322
n-C_4F_{10}	238.027	3.7325	3.5567	164.583	225	367	[95]	0.095	-0.082	0.566	0.946
n-C_5F_{12}	288.034	4.3437	3.5851	169.208	253	400	[95]	0.054	-0.044	0.943	0.390
n-C_6F_{14}	338.042	4.8562	3.6440	173.414	288	333	[107]	0.003	-0.002	0.090	0.207
n-C_7F_{16}	388.049	5.4127	3.6739	176.403	278	333	[108]**	0.004	-0.003	0.078	0.376
n-C_8F_{18}	438.057	5.6756	3.7618	182.796	288	377	[109]	0.069	-0.009	2.383	0.478
n-C_9F_{20}	488.064	6.1774	3.7973	185.597	288	333	[107]	0.005	-0.001	0.581	0.084

* parameters taken from Gross and Sadowski, [103] ** only vapor pressure

they have a similar (n- only; no iso) structure.

The partial vapor pressures of the components of ideal solution of two liquids are related to the composition of the liquid mixture in terms of Raoult's law:

$$P_A = x_A.P_{satA} \quad \text{and} \quad P_B = x_B.P_{satB} \tag{A1.11}$$

where $\mathbf{x_i}$ is the molar concentration of component i in solution.

The total vapour pressure of the mixture is defined by Dalton's law;

$$P = P_A + P_B \tag{A1.12}$$

The mixture composition can be defined e.g. by the overall mole fraction z_B of component *B*, defined as

$$z_B = N_B/(N_A + N_B). \tag{A1.13}$$

Combining Raoult and Dalton's laws:

$$p = \frac{p_{sat,A}\,p_{sat,B}}{p_{sat,A} + \left(p_{sat,B} - p_{sat,A}\right)y_A} \tag{A1.14}$$

The amount of the liquid phase (*L*) and the vapor phase (*V*) can be determined from the compositions of phases x_A and y_A by the so called 'Lever rule'

$$N_L\left(x_A - z_A\right) = N_V\left(z_A - y_A\right) \tag{A1.15}$$

The phase equilibrium of the two-component mixture is usually interpreted on a pressure–composition diagram.

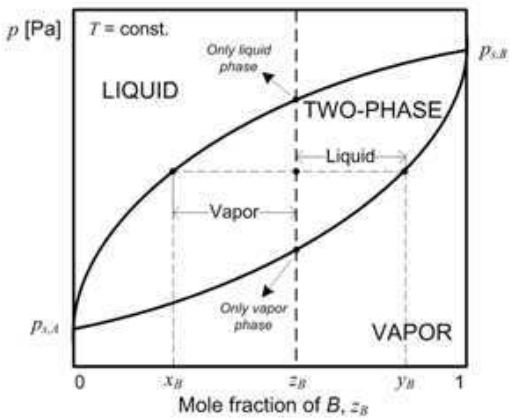

Before any calculations can be made a *tie line* is drawn on the phase diagram to determine the percent weight of each element. This tie line is drawn horizontally at the composition's temperature from the liquid to the vapour. The percent weight of element B at the liquid is given by w_l and the percent weight of element B at the vapour is given by w_v. The percent weight of vapour and liquid can then be calculated using the following lever rule equations:

Percent weight of the liquid phase: $$X_l = (w_0 - w_v)/(w_l - w_v) \quad \text{(A1.16)}$$

Percent weight of the vapour phase: $$X_v = (w_l - w_0)/(w_l - w_v) \quad \text{(A1.17)}$$

where w_o is the percent weight of element B for the given composition.

An example of the outcome of calculation sof this type is the p-H diagram for a bicomponent mixture : Fig A1-1.

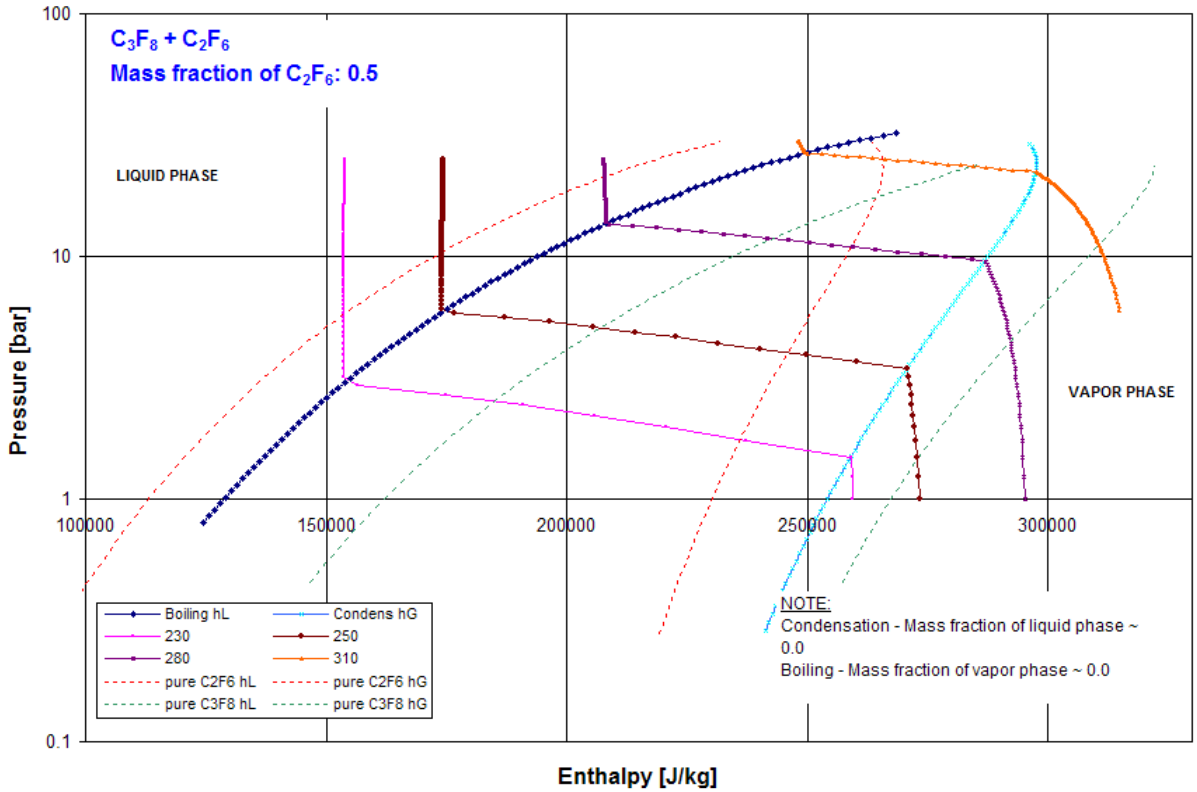

Fig A1-1 Pressure enthalpy phase diagram generated for the evaporation of 50% C_2F_6/50% C_3F_8 using PC-SAFT

Table A1-2 Calculated speed of sound in C_2F_6/C_3F_8 and C_3F_8/N_2 calculated using PC-SAFT **(see** section 5.2**)**

C3F8 + C2F6 — T[K] = 298.15, p[bar] = 1. Results (component 2 / B): Binary interaction parameter kij = 0.

z_B[mol/mol]	m_B[kg/kg]	Phase	d[kg.m3]	h[J.kg-1]	s[J.kg-1.K-1]	cv[J.kg.K-1]	cp[J.kg.K-1]	SoS[m.s-1]	*ideal gas at reference state* h_0[J.kg-1]	*ideal gas at reference state* s_0[J.kg-1.K-1]
0.001361849	0.001	Vap	7.75738541	313551.45	1471.22127	743.906365	792.210398	115.816363	*55493.3104*	*264.154183*
0.047634464	0.035413793	Vap	7.65714094	313318.752	1473.83735	742.78493	791.582931	116.65089	*54767.2623*	*261.390562*
0.092781557	0.069827586	Vap	7.55952271	313077.921	1476.42262	741.664125	790.957953	117.479811	*54057.4451*	*258.688651*
0.1368437	0.104241379	Vap	7.4644261	312828.696	1478.97595	740.543772	790.335196	118.303291	*53363.2242*	*256.046015*
0.179859538	0.138655172	Vap	7.37175208	312570.763	1481.496	739.423986	789.714689	119.121486	*52683.9852*	*253.460297*
0.221865903	0.173068966	Vap	7.2814069	312303.783	1483.98134	738.304667	789.096254	119.934548	*52019.1383*	*250.929236*
0.262897917	0.207482759	Vap	7.19330169	312027.396	1486.43047	737.185809	788.47981	120.74262	*51368.1179*	*248.450663*
0.302989091	0.241896552	Vap	7.10735216	311741.215	1488.84179	736.06729	787.865164	121.54584	*50730.3795*	*246.02249*
0.342171419	0.276310345	Vap	7.02347828	311444.833	1491.21362	734.949118	787.252261	122.344339	*50105.3998*	*243.642712*
0.380475458	0.310724138	Vap	6.94160406	311137.923	1493.54458	733.831465	786.641209	123.138243	*49492.693*	*241.309466*
0.417930412	0.345137931	Vap	6.86165722	310819.635	1495.83132	732.714048	786.031667	123.927674	*48891.707*	*239.020641*
0.454564205	0.379551724	Vap	6.78356902	310489.823	1498.07317	731.597091	785.423807	124.712747	*48302.031*	*236.774662*
0.490403547	0.413965517	Vap	6.70727401	310147.797	1500.26739	730.480502	784.817484	125.493573	*47723.1827*	*234.569683*
0.525474006	0.44837931	Vap	6.63270985	309792.954	1502.41158	729.364313	784.212679	126.27026	*47154.7147*	*232.403994*
0.55980006	0.482793103	Vap	6.55981711	309424.62	1504.50306	728.248081	783.608906	127.042913	*46596.1873*	*230.275913*
0.593405163	0.517206897	Vap	6.48853911	309042.058	1506.53894	727.132418	783.006732	127.811628	*46047.1697*	*228.183794*
0.626311791	0.55162069	Vap	6.41882175	308644.453	1508.51603	726.017044	782.405836	128.576502	*45507.2362*	*226.126013*
0.658541498	0.586034483	Vap	6.35061337	308231.057	1510.43141	724.901929	781.80615	129.337627	*44975.9896*	*224.101055*
0.690114957	0.620448276	Vap	6.28386459	307800.744	1512.28073	723.787105	781.207668	130.095091	*44452.9908*	*222.107248*
0.72105201	0.654862069	Vap	6.21852823	307352.497	1514.06005	722.672506	780.610288	130.848982	*43937.8348*	*220.14305*
0.751371707	0.689275862	Vap	6.15455914	306885.12	1515.76479	721.558147	780.013994	131.59938	*43430.106*	*218.206884*
0.781092344	0.723689655	Vap	6.09191411	306397.256	1517.38977	720.444059	779.418784	132.346367	*42929.3813*	*216.297144*
0.810231503	0.758103448	Vap	6.03055177	305887.461	1518.9295	719.33011	778.824496	133.090019	*42435.2414*	*214.412243*
0.838806081	0.792517241	Vap	5.97043246	305353.97	1520.37729	718.216545	778.231346	133.83041	*41947.2364*	*212.550482*
0.866832331	0.826931034	Vap	5.91151821	304794.864	1521.72591	717.103073	777.639018	134.567615	*41464.9112*	*210.710146*
0.894325886	0.861344828	Vap	5.85377256	304207.926	1522.96704	715.989954	777.047744	135.301701	*40987.7856*	*208.88943*
0.92130179	0.895758621	Vap	5.79716056	303590.605	1524.09114	714.87691	776.457222	136.032737	*40515.35*	*207.086425*
0.947774526	0.930172414	Vap	5.74164864	302939.882	1525.08695	713.764024	775.867512	136.76079	*40047.0481*	*205.299051*
0.973758042	0.964586207	Vap	5.68720458	302252.272	1525.94154	712.651474	775.278768	137.485921	*39582.2789*	*203.525071*
0.999265775	0.999	Vap	5.63379742	301523.565	1526.63935	711.538902	774.690613	138.208195	*39120.364*	*201.761968*

C3F8 + N2 — T[K] = 298.15, p[bar] = 1. Results (component 2 / B): Binary interaction parameter kij = -0.0166

z_B[mol/mol]	m_B[kg/kg]	Phase	d[kg.m3]	h[J.kg-1]	s[J.kg-1.K-1]	cv[J.kg.K-1]	cp[J.kg.K-1]	SoS[m.s-1]	*ideal gas at reference state* h_0[J.kg-1]	*ideal gas at reference state* s_0[J.kg-1.K-1]
0.006674449	0.001	Vap	7.71415404	124370.1	686.668022	743.891764	792.409241	116.171346	*0*	*0*
0.19771857	0.035413793	Vap	6.40783157	128093.074	711.6367	743.64076	800.18549	128.56882	*0*	*0*
0.335066552	0.069827586	Vap	5.48467661	131770.163	736.503665	743.462041	808.270541	139.978135	*0*	*0*
0.438567262	0.104241379	Vap	4.79615678	135420.793	761.312431	743.324054	816.526904	150.666951	*0*	*0*
0.519359862	0.138655172	Vap	4.26228968	139054.827	786.084894	743.210749	824.887551	160.799749	*0*	*0*
0.584178836	0.173068966	Vap	3.83594887	142677.782	810.833237	743.11345	833.316266	170.48676	*0*	*0*
0.637335262	0.207482759	Vap	3.48748014	146292.98	835.564756	743.027173	841.791901	179.806422	*0*	*0*
0.681716923	0.241896552	Vap	3.19725767	149902.539	860.284083	742.948671	850.301103	188.817038	*0*	*0*
0.719330895	0.276310345	Vap	2.95176071	153507.868	884.994294	742.876125	858.835418	197.563401	*0*	*0*
0.751615503	0.310724138	Vap	2.74136411	157109.945	909.697512	742.807992	867.388764	206.08084	*0*	*0*
0.77962846	0.345137931	Vap	2.55902606	160709.464	934.395247	742.74294	875.956601	214.397809	*0*	*0*
0.804164947	0.379551724	Vap	2.39947409	164306.938	959.088603	742.680942	884.536572	222.537605	*0*	*0*
0.82583431	0.413965517	Vap	2.25868116	167902.748	983.778407	742.620814	893.125757	230.519618	*0*	*0*
0.84511135	0.44837931	Vap	2.13351784	171497.186	1008.46529	742.562291	901.722573	238.360157	*0*	*0*
0.862371515	0.482793103	Vap	2.02151503	175090.481	1033.14974	742.505447	910.326078	246.073086	*0*	*0*
0.877915595	0.517206897	Vap	1.92069836	178682.81	1057.83213	742.449667	918.934854	253.670329	*0*	*0*
0.891987401	0.55162069	Vap	1.82946997	182274.319	1082.51279	742.394712	927.548025	261.162202	*0*	*0*
0.904786648	0.586034483	Vap	1.74652281	185865.122	1107.19196	742.340773	936.165269	268.557689	*0*	*0*
0.916478489	0.620448276	Vap	1.67077729	189455.316	1131.86983	742.28763	944.785945	275.864689	*0*	*0*
0.927200688	0.654862069	Vap	1.6013338	193044.978	1156.54658	742.234918	953.409342	283.090184	*0*	*0*
0.937069063	0.689275862	Vap	1.53743669	196634.174	1181.22235	742.183052	962.035589	290.240341	*0*	*0*
0.946181697	0.723689655	Vap	1.47844656	200222.96	1205.89726	742.131585	970.663998	297.320698	*0*	*0*
0.954622202	0.758103448	Vap	1.42381872	203811.382	1230.5714	742.080433	979.294281	304.336203	*0*	*0*
0.962462297	0.792517241	Vap	1.37308626	207399.479	1255.24486	742.029269	987.925937	311.291319	*0*	*0*
0.969763844	0.826931034	Vap	1.32584664	210987.287	1279.91771	741.979097	996.559824	318.190011	*0*	*0*
0.976580493	0.861344828	Vap	1.28175098	214574.834	1304.59001	741.928709	1005.19461	325.035983	*0*	*0*
0.982958994	0.895758621	Vap	1.24049539	218162.146	1329.26182	741.878743	1013.83081	331.832509	*0*	*0*
0.988940275	0.930172414	Vap	1.20181391	221749.245	1353.93319	741.829395	1022.46853	338.58259	*0*	*0*
0.994560322	0.964586207	Vap	1.16547282	225336.151	1378.60415	741.779647	1031.10667	345.28905	*0*	*0*
0.999850899	0.999	Vap	1.13126588	228922.881	1403.27475	741.730469	1039.74613	351.954355	*0*	*0*

References

[A1-1] Mainly from slides by V. Vacek ATLAS ID 9th sonar meeting: 22/4/2010, http://indico.cern.ch/conferenceDisplay.py?confId=91912

[A1-2] "Perturbed-Chaim SAFT: An Equation of State Based on a Perturbation Theory for Chain Molecules". Gross, Joachim; Sadowski, Gabriele; *Ind. Eng. Chem. Res.* 2001, *40*, 1244-1260.

[A1-3] "A sonar-based instrument for the ratiometric determination of binary gas mixtures": G. Hallewell et al: Nucl. Instr. & Meth A 264 (1988) 219.

[A1-4] "Properties of saturated fluorocarbons: Experimental data and modeling using perturbed-chain-SAFT" G. Hallewell, V. Vacek & V. Vins, Fluid Phase Equlibria, 292, (2010) 64

APPENDIX-2: Flow Control PID program for ATMEL micro-controller chip

(implemented July 2000 by C. Bayer, Univ. Wuppertal): pre-gnu conversion to machine code (page 1 of 4)

```
#include <io.h>
#include <interrupt.h>
#include <math.h>
#include <sig-avr.h>
#include <timer.h>
#include <wdt.h>
#include <eeprom.h>
#include "mfc.h"
uint8_t volatile dispch, map, input, ziff, flash, fon;
int16_t volatile temp, disp[DISPLAYS], par[PARAMS], aktpar, aktsig
n;
int16_t last_error, acc_error, lastout;
static int16_t dummy_attribute_((section (“.eeprom”))) = 0;
static int16_t savepar[PARAMS] _attribute_((section (“.eeprom”))
) = {
        PAR1, PAR2, PAR3, PAR4, PAR5, PAR6, PAR7
} ;
void delay( uint8_t anz ) {
        uint8_t i;
        uint16_t j, k;

        for ( i = 0; i < anz; i++ )
                for ( j = 0;  j < 32768; j++ ) k += j;
}
int16_t round (float t ) {
        t *= 10;
         if ( fabs( t ) == t ) return (int16_t) ( t - 0.5 ) ;
         else return return (int16_t) ( t + 0.5 ) ;
}
void display( int16_t n) {
         uint8_t tmp;

        if  ( n < 0) {
        n = -n ;
        sbi( PORTC, CMINUS ) ;
        }
        else cbi ( PORTC, CMINUS) ;
        if ( input && aktsign && (  ziff ! =4 || fon ) )
        sbi( PORTC, CMINUS ) ;
        if  ( n > 999 ) n = 999;
        tmp = ( n / 100 ) ;
        if ( ziff  == 1 ) FLASH ( SEG1, tmp ) ;
        else {
                if ( tmp == 0 && ! ziff )
                        SEG ( SEG1, SEGBLANK ) ;
                else
                        SEG ( SEG 1, tmp ) ;
        }
        tmp = ( n / 10) % 10 ;
        if ( ziff == 2 ) FLASH ( SEG 2, tmp ) ;
                 else
                 SEG( SEG2, tmp ) ;
        tmp = n % 10;
        if ( ziff == 3 ) FLASH(  SEG3, tmp ) ;
        else
                SEG( SEG3, tmp ) ;
}
inline uint8_t getbyte( void )  {
        loop_until_bit_is_set( SPSR, SPIF ) ;
        return inp( SPDR ) ;
}
```

APPENDIX-2: Flow Control PID program for ATMEL micro-controller chip (page 2 of 4)

```
int16_t readadc ( uint8_t t ) {
                uint8_t t1,  t2 ;
                float t ;
                cli () ;
                cbi( PORTC, CCSADC ) ;
                outp( SPIADCGET I ( rot3( i ) « 4 ), SPDR ) ;
                getbyte() ;
                outp( SPINULL, SPDR ) ;
                t1 = getbyte() ;
                outp( SPINULL, SPDR ) ;
                t2 = getbyte() ;
                sbi( PORTC, CCSADC ) ;
                sei () ;
                t = ( t1 « 5 ) + ( t2 » 3 ) ;
                t /= ( RESOLUTION / VREF ) ;
                t = ( RESISTOR * t ) / ( VREF – t ) ;
                t = log ( t ) ;
                t = inverse ( A0 + A1 * t + A3 * t * t * t ) + KELVIN ;
                return round( t ) ;
}
                void initdac( uint16_t v ) {
                cbi( PORTC, CCSDAC ) ;
                outp( high( v) I SPIINITDAC, SPDR ) ;
                getbyte() ;
                outp( low( v) , SPDR ) ;
                getbyte() ;
                sbi( PORTC, CCSDAC } ;
}
                void setdac( uint8_t ch, int16_t value ) {
                int16_t v;
                if ( value < 0 ) v = 0;
                 else {
                                if ( value > RESOLUTION )  v = RESOLUTION;
                                else v = value;
                }
                cbi( PORTC, CCSDAC ) ;
                outp ( high ( v) I (ch « 6  ) I SPISETDAC, SPDR  );
                getbyte() ;
                outp( low( v ), SPDR );
                getbyte() ;
                sbi( PORTC, CCSDAC ) ;
}
SIGNAL( SIG_INTERRUPT1 ) {
                uint8_t *p, *e;

                if  (input) {
.                               if ( ziff ) {
                                                if ( ++ziff == 5) {
                                                 ziff = 0;
                                                 par[input - 1] = aktsign ? -aktpar : aktpar ;
                                                 e = (uint8_t *) &savepar[input -1] ;
                                                 p = (uint8_t *) &par[input -1] ;
                                                 eeprom_wb( (uint16_t) e, *p ) ;
                                                 eeprom_wb( (uint16_t) ( e + 1 ) , *++p ) ;
                                                }
                                }
                                else ziff = 1;
                }
                else {
                                 if ( ++dispch == DISPLAYS ) dispch = 0;
                }
}
```

APPENDIX-2: Flow Control PID program for ATMEL micro-controller chip (page 3 of 4)

```
SIGNAL ( SIG_INTERRUPT0 ) {
        If ( input && ziff ) {
        switch (ziff ) {
                case 1 :
                if ( aktpar / 100 ! = 9 );aktpar +=100;
                else aktpar = -=900;
                break;
                case 2 :
                if ( (aktpar / 10 ) % 10 ! = 9 );aktpar +=10;
                else aktpar  -= 90;
                break;
                case 3 :
                if ( aktpar %10 ! = 9 );aktpar ++;
                else aktpar = -= 9;
                break;
                case 4 :
                aktsign = !aktsign ;
                break ;
        }
}
 else {
        if ( input++ == PARAMS ) input = 0 ;
        else {
        aktsign = par[input –1] < 0 ? 1 : 0 ;
         aktpar = aktsign ? -par[input -1] : par[input – 1] ;
        }
    }
}
SIGNAL ( SIG_OVERFLOW0 ) {
        if ( input)  {
                if ( flash % FL_MOD == FL_ON  ) {
                        SEG( SEGM, input ) ;
                        fon = 1;
                }
                else
                if ( flash% FL_MOD == FL_OFF ) {
                        SEG( SEGM, SEGBLANK ) ;
                        fon = 0;
                }
        flash++ ;
        display  ( aktpar  ) ;
        }
        else {
                flash = FL_INIT;
                SEG( SEGM, dispch + 1 ) ;
                display( disp[dispch] ) ;
                }
                timer0_start() ;
}
SIGNAL( SIG_OUTPUT_COMPARE1A ) {
         int16_t error;
        int32_t output, tmp;
        error = ( temp -par[1] ) ;
        if ( abs( error ) < DEADBAND ) error = 0 ;
        tmp = (long) error * (long ) par[2] ;
        if ( tmp > 32767L ) tmp = - 32767L;
        else if ( tmp < -32768L ) tmp = -32768L;
        output = tmp;
        output += ( (long) ( error – last_error ) * (long) par [4] );
        if ( ! ( ( error < 0 && lastout == OUT( par[5] ) ) ||
                ( error > 0 && lastout == OUT( par[6] ) ) ) ) {
                 tmp = (long) acc_error;
                 'tmp += (long) error;
                 if ( tmp > 32767L ) tmp = 32767L;
                else if ( tmp < -32768L ) tmp = -32768L;
                acc_error = (short) tmp;
        }
```

APPENDIX-2: Flow Control PID program for ATMEL micro-controller chip (page 4 of 4)

```
            tmp = ( (long) acc_error * par[3] );
            if ( tmp > 32767L ) tmp = 32767L;
            else if ( tmp < -32768L ) tmp = -32768L;
            output += tmp;
            disp [ 2] = ( ( short) tmp ) / 33;
            if ( output < 0L ) output = 0L;
            else if ( output > 32767L ) output = 32767L;
            last_error = error;
            lastout = ( (short) output ) » 3;
            if ( lastout > OUT( par[6] ) ) lastout = OUT( par[6] ); .
            else if ( lastout < OUT( par[5] ) ) lastout = OUT( par[5] ) ;
            setdac ( 2 , lastout ) ;
            disp[1] = lastout » 2;
}
int main( void ) {
             uint8_t i, anz;
            int32_t sum;
            outp ( DIRA, DDRA ) ;
            outp ( DIRB, DDRB ) ;
            outp ( DIRC, DDRC ) ;
            outp ( DIRD, DDRD ) ;
            outp( AINIT0, PORTA );
            outp( CINIT0, PORTC ) ;
            outp( DINIT0, PORTD ) ;
            delay( 50 );
            SEG( SEGALL, SEGBLANK ) ;
            outp( CINIT1, PORTC ) ;
            outp( DINIT1, PORTD ) ;
            outp( BV( SPE ) I BV( MSTR ), SPCR ) ;
            outp( BV( INT1 ) I BV( INT0 ), GIMSK ) ;
            outp( BV( ISC11 ) I BV( ISC01 ) , MCUCR ) ;
            outp( BV(OCIE1A ) I BV( TOIE0 ) , TIMSK ) ;
            outp( BV( CTC1 ) I CK64, TCCR1B );
            __outw( PIDSAMPLE, OCR1AL ) ;
            timer0_source( CK1024 ) ;
            timer0_start() ;
            eeprom_read_block( (uint8_t * ) par, uint16_t) savepar, PARAMS
             « 1 );
            initdac( 0 );
            setdac( 0, IOFFSET ) ;
            setdac( 1, IOFFSET ) ;
#if FL_INIT ! = 0
            flash = FL_INIT;
#endif
            temp = readadc( par[0]  - 1 ) ;
            disp [0] = temp ;
            sum = 0L;
            anz = 0;
            sei( ) ;
            while ( 1 ) {
                        sum += (long) readadc( par[0] -1 ) ;
                         for ( i = 0 ; i < 255; i ++ ) nop() ;
                         if ( ! ++anz ) {
                        cli() ;
                        temp = (short) ( sum / 256 ) ;
                        disp[0] = temp;
                        sei ();
                        sum = 0L;
                        }
                        wdt_reset() ;
            }
}
```

APPENDIX-3 Material safety data sheet for a typical SFC

(Page 1 of 4)

AIR LIQUIDE	SAFETY DATA SHEET	Page : 1 / 4 Revised edition no : 1 Date : 15/7/2005 Supersedes : 0/0/0
Hexafluoroethane (R116)		AL064

Label 2.2 : Non flammable, non toxic gas.

1 IDENTIFICATION OF THE SUBSTANCE / PREPARATION AND OF THE COMPANY / UNDERTAKING

Trade name : Hexafluoroethane (R116)
MSDS No : AL064
Chemical formula : C2F6
Company identification : AIR LIQUIDE SA
France
See paragraph 16 "OTHER INFORMATION"
Emergency phone nr : See paragraph 16 "OTHER INFORMATION"

2 COMPOSITION / INFORMATION ON INGREDIENTS

Substance / Preparation : Substance.

Substance name	Contents	CAS No	EC No	Index No	Classification
Hexafluoroethane (R116)	100 %	76-16-4	200-939-8	—	

Contains no other components or impurities which will influence the classification of the product.

3 HAZARDS IDENTIFICATION

Hazards identification : Liquefied gas.
In high concentrations may cause asphyxiation.

4 FIRST AID MEASURES

First aid measures
- Inhalation : In high concentrations may cause asphyxiation. Symptoms may include loss of mobility/consciousness. Victim may not be aware of asphyxiation.
In low concentrations may cause narcotic effects. Symptoms may include dizziness, headache, nausea and loss of co-ordination.
Remove victim to uncontaminated area wearing self contained breathing apparatus. Keep victim warm and rested. Call a doctor. Apply artificial respiration if breathing stopped.
- Skin/eye contact : Immediately flush eyes thoroughly with water for at least 15 minutes.
In case of frostbite spray with water for at least 15 minutes. Apply a sterile dressing. Obtain medical assistance.
- Ingestion : Ingestion is not considered a potential route of exposure.

5 FIRE-FIGHTING MEASURES

Flammable class : Non flammable.
Specific hazards : Exposure to fire may cause containers to rupture/explode.
Hazardous combustion products : If involved in a fire the following toxic and/or corrosive fumes may be produced by thermal decomposition : Carbonyl fluoride. Carbon monoxide. Hydrogen fluoride.
Extinguishing media
- Suitable extinguishing media : All known extinguishants can be used.

APPENDIX-3

Material safety data sheet for a typical SFC (page 2 of 4)

AIR LIQUIDE	SAFETY DATA SHEET	Page : 2 / 4 Revised edition no : 1 Date : 15/7/2005 Supersedes : 0/0/0
Hexafluoroethane (R116)		AL064

5 FIRE-FIGHTING MEASURES (continued)

Specific methods : If possible, stop flow of product.
Move away from the container and cool with water from a protected position.

Special protective equipment for fire fighters : Use self-contained breathing apparatus and chemically protective clothing.

6 ACCIDENTAL RELEASE MEASURES

Personal precautions : Evacuate area.
Wear self-contained breathing apparatus when entering area unless atmosphere is proved to be safe.
Ensure adequate air ventilation.

Environmental precautions : Try to stop release.
Prevent from entering sewers, basements and workpits, or any place where its accumulation can be dangerous.

Clean up methods : Ventilate area.

7 HANDLING AND STORAGE

Storage : Keep container below 50°C in a well ventilated place.

Handling : Suck back of water into the container must be prevented.
Do not allow backfeed into the container.
Use only properly specified equipment which is suitable for this product, its supply pressure and temperature. Contact your gas supplier if in doubt.
Refer to supplier's container handling instructions.

8 EXPOSURE CONTROLS / PERSONAL PROTECTION

Personal protection : Ensure adequate ventilation.
Do not smoke while handling product.

9 PHYSICAL AND CHEMICAL PROPERTIES

Physical state at 20 °C	: Liquefied gas.
Colour	: Colourless.
Odo(u)r	: No odour warning properties.
Molecular weight	: 138
Melting point [°C]	: -101
Boiling point [°C]	: -78.2
Critical temperature [°C]	: 19.7
Vapour pressure, 20°C	: 30 bar
Relative density, gas (air=1)	: 4.8
Relative density, liquid (water=1)	: 1.23
Solubility in water [mg/l]	: No reliable data available.
Flammability range [vol% in air]	: Non flammable.
Other data	: Gas/vapour heavier than air. May accumulate in confined spaces, particularly at or below ground level.

APPENDIX-3

Material safety data sheet for a typical SFC (page 3 of 4)

AIR LIQUIDE	SAFETY DATA SHEET	Page : 3 / 4 Revised edition no : 1 Date : 15/7/2005 Supersedes : 0/0/0
Hexafluoroethane (R116)		AL064

10 STABILITY AND REACTIVITY

Stability and reactivity : Stable under normal conditions.
Thermal decomposition yields toxic products which can be corrosive in the presence of moisture.

11 TOXICOLOGICAL INFORMATION

Toxicity information : No known toxicological effects from this product.

12 ECOLOGICAL INFORMATION

Ecological effects information : No known ecological damage caused by this product.
Effect on ozone layer : Not covered by the 'Montreal Protocol'.
Global warming factor [CO2=1] : 9200

13 DISPOSAL CONSIDERATIONS

General : Do not discharge into any place where its accumulation could be dangerous.
Contact supplier if guidance is required.

14 TRANSPORT INFORMATION

UN No. : 2193
H.I. nr : 20
ADR/RID
- Proper shipping name : HEXAFLUOROETHANE (REFRIGERANT GAS R 116)
- ADR Class : 2
- ADR/RID Classification code : 2 A
- Labelling ADR : Label 2.2 : Non flammable, non toxic gas.
Other transport information : Avoid transport on vehicles where the load space is not separated from the driver's compartment.
Ensure vehicle driver is aware of the potential hazards of the load and knows what to do in the event of an accident or an emergency.
Before transporting product containers :
- Ensure that containers are firmly secured.
- Ensure cylinder valve is closed and not leaking.
- Ensure valve outlet cap nut or plug (where provided) is correctly fitted.
- Ensure valve protection device (where provided) is correctly fitted.
- Ensure there is adequate ventilation.
- Compliance with applicable regulations.

15 REGULATORY INFORMATION

EC Classification : Not included in Annex I.
Not classified as dangerous preparation/substance.
EC Labelling : No EC labelling required.
- Symbol(s) : None.
- R Phrase(s) : None.
- S Phrase(s) : None.

APPENDIX-3

Material safety data sheet for a typical SFC (page 4 of 4)

AIR LIQUIDE	SAFETY DATA SHEET	Page : 4 / 4
		Revised edition no : 1
		Date : 15/7/2005
		Supersedes : 0/0/0
Hexafluoroethane (R116)		AL064

16 OTHER INFORMATION

Asphyxiant in high concentrations.
Keep container in well ventilated place.
Do not breathe the gas.
Ensure all national/local regulations are observed.
Contact with liquid may cause cold burns/frostbite.
The hazard of asphyxiation is often overlooked and must be stressed during operator training.

This Safety Data Sheet has been established in accordance with the applicable European Directives and applies to all countries that have translated the Directives in their national laws.

Before using this product in any new process or experiment, a thorough material compatibility and safety study should be carried out.
Details given in this document are believed to be correct at the time of going to press. Whilst proper care has been taken in the preparation of this document, no liability for injury or damage resulting from its use can be accepted.

Recommended uses and restrictions : This SDS is for information purposes only and is subject to change without notice. [Prior to purchase of products, please contact your local AIR LIQUIDE office for a complete SDS (with Manufacturer's name and emergency phone number).]

End of document

APPENDIX-4: Perfluorocarbons and global warming

This appendix puts in perspective the contributions of per-fluorocarbons to global warming, based on recent DOE figures.

DOE/EIA-0573(2000)

Emissions of Greenhouse Gases in the United States 2000

November 2001

Energy Information Administration
Office of Integrated Analysis and Forecasting
U.S. Department of Energy
Washington, DC 20585

APPENDIX-4 (cont)

Executive Summary

Table ES2. U.S. Emissions of Greenhouse Gases, Based on Global Warming Potential, 1990-2000
(Million Metric Tons Carbon Equivalent)

Gas	1990	1991	1992	1993	1994	1995	1996	1997	1998	1999	P2000
Carbon Dioxide	1,355	1,341	1,367	1,399	1,425	1,438	1,488	1,509	1,511	1,536	1,583
Methane	199	200	200	194	194	195	188	186	181	180	177
Nitrous Oxide	94	96	98	98	106	101	101	99	99	100	99
HFCs, PFCs, and SF_6	30	28	29	30	32	35	39	42	46	45	47
Total	1,678	1,665	1,694	1,722	1,757	1,770	1,815	1,836	1,836	1,860	1,906

P = preliminary data.

Note: Data in this table are revised from the data contained in the previous EIA report, *Emissions of Greenhouse Gases in the United States 1999*, DOE/EIA-0573(99) (Washington, DC, October 2000).

Sources: **Emissions:** Estimates presented in this report. **Global Warming Potentials:** Intergovernmental Panel on Climate Change, *Climate Change 2001: The Scientific Basis* (Cambridge, UK: Cambridge University Press, 2001), pp. 38 and 388-389.

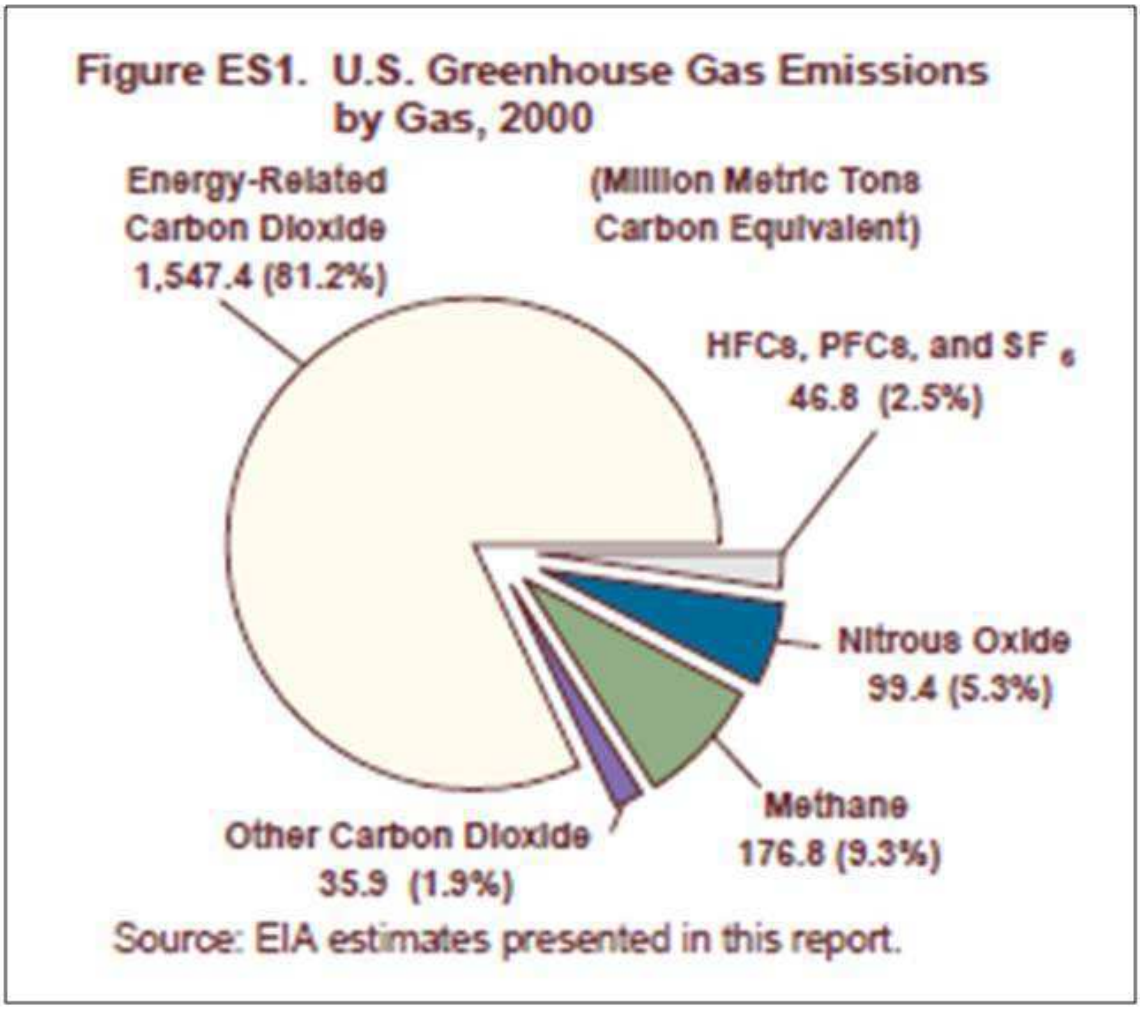

APPENDIX-4 (cont)

IPCC Calculates New Global Warming Potentials in 2001

Global warming potentials (GWPs) provide a means of comparing the abilities of different greenhouse gases to trap heat in the atmosphere. The GWP index converts emissions of various gases into a common measure, described as the ratio of the radiative forcing that would result from the emissions of one kilogram of a greenhouse gas to that from emissions of one kilogram of carbon dioxide (CO_2) over a period of time.[a]

In 2001, the Intergovernmental Panel on Climate Change (IPCC) Working Group I released its Third Assessment Report, *Climate Change 2001: The Scientific Basis*. Table 6.7 in the IPCC report gives revised GWPs for a number of the "other gases" included in this chapter.[b] In the table below, the revised GWPs are compared with those published in 1996 in the IPCC's Second Assessment Report, *Climate Change 1995: The Science of Climate Change*.[c]

The 2001 direct GWPs are based on an improved calculation of CO_2 radiative forcing and new values for the radiative forcing and lifetimes of a number of halocarbons.[d] One significant revision, drawn from a 1999 report by the World Meteorological Organization, *Scientific Assessment of Ozone Depletion*, is the radiative efficiency (per kilogram) of CO_2, updated to a value that is 12 percent lower than the IPCC's 1995 estimated value, at 0.01548 Wm^{-2}/ppmv (watts per square meter per part per million by volume).[d] Another significant revision is the updating of several radiative efficiencies (per kilogram), most notably, that of CFC-11. The radiative forcing estimates for halocarbon replacement gases, which are scaled relative to that of CFC-11 when their GWPs are calculated, are also affected by this change.[e]

Comparison of 1996 and 2001 IPCC Values for the Global Warming Potentials (GWPs) of "Other Gases"

Gas	1996 IPCC GWP	2001 IPCC GWP
HFC-23	11,700	12,000
HFC-125	2,800	3,400
HFC-134a	1,300	1,300
HFC-143a	3,800	4,300
HFC-152a	140	120
HFC-227ea	2,900	3,500
HFC-236fa	6,300	9,400
Perfluoromethane (CF_4)	6,500	5,700
Perfluoroethane (C_2F_6)	9,200	11,900
Sulfur Hexafluoride (SF_6)	23,900	22,200

[a]The GWPs shown here are based on a time horizon of 100 years.
[b]Intergovernmental Panel on Climate Change, *Climate Change 2001: The Scientific Basis* (Cambridge, UK: Cambridge University Press, 2001), pp. 388-389.
[c]Intergovernmental Panel on Climate Change, *Climate Change 1995: The Science of Climate Change* (Cambridge, UK: Cambridge University Press, 1996), p. 121.
[d]*Climate Change 2001*, p. 386.
[e]*Climate Change 2001*, p. 387.

Total U.S. Emissions of Hydrofluorocarbons, Perfluorocarbons, and Sulfur Hexafluoride, 1990-2000

Estimated 2000 Emissions (Million Metric Tons Carbon Equivalent)	46.8
Change Compared to 1999 (Million Metric Tons Carbon Equivalent)	2.0
Change from 1999 *(Percent)*	*4.5%*
Change Compared to 1990 (Million Metric Tons Carbon Equivalent)	17.1
Change from 1990 *(Percent)*	*57.8%*

APPENDIX-5 Some (incomplete) guidelines to SFC materials compatibility

(Page 1 of 2)

Table A5-1. liquid SFC compatibility with various tube materials and valve seal elastomers:
(C_6F_{14} liquid immersion unless stated otherwise)
Radiation data in addition to finding in section 7 and references therein.

Sources http://detector-cooling.web.cern.ch/detector-cooling/fluidmaterial.html
including compilation by M. Capaens, CERN, November 2001), 3M Corp., DELPHI-RICH SLAC-SLD etc.

See Note

	Rad Hard[65]	Compatibility[66]	Gas Permeability $Px10^{10}$(cm^3mm/cm^2 s cm Hg) (DATA: Angst+Pfister)	GLOBAL RESULT
St. Steel	**OK**	**OK**	0	**OK**
Aluminium	**OK**	**OK** (if fluid is pure) Not well know if fluid is contaminated with H_2O, O_2, C-H due to F-production	0	**OK**
Copper (free of hydraulic drawing oil)	**OK**	**OK** (if fluid is pure) Not well know if fluid is contaminated with H_2O, O_2, C-H due to F-production	0	**OK**
PEEK	10^8 rad (Data: TIS/CFM /MTR/96-17)	**OK** (Data: 3M)		**OK**
PUR	**10^7 rad** (Data: Angst+Pfister)	**OK** (Data: 3M)	5 N_2 , 15-50 O_2 , 140-400 CO_2	**OK**
Polypropylene PP	**10^7 rad** (Data: Angst+Pfister)		3-5 N_2 , ~10 O_2 , ~ 35 CO_2	?
Polyethylene PE	**10^8 rad** (Data: CERN 82-10)	**OK** (Data: DELPHI 95-21 RICH 66)	0.1 N_2 , ~ 1 O_2 ,1-6 CO_2 ,8 H_2	**OK**
Nylon (Polyamide 6)	**10^7 rad** (Data: CERN 82-10)	**OK** (Data: 3M)	~ 2 N_2 ,~ 1 O_2 ,1-6 CO_2 , 8 H_2	**OK**
Rilsan (polyamide 11)		**OK** (Data: 3M) Discolaration, Weight loss, but mechanical prop. OK (Data DELPHI95-21RICH66)		**BAD**
Teflon (PTFE)		**BAD** **Absorbs SFCs**		**BAD**
PVC	**10^8 rad** (Data: Angst+Pfister)	Some effect (Data: 3M)	0.3N_2 , ~1 O_2 , 1-10 CO_2 , 33H_2	**BAD**
Araldite 2100		**OK** (Data:ALICE HMPID)		**OK**
3M-DP190epoxy		**OK** (Data : SLAC-SLD)		**OK**
Kalrez® seat elastomer		**OK** (Data : SLAC-SLD)		**OK**
Kel-F® seat elastomer		**OK** (Data : SLAC-SLD)		**OK**
Vespel® C_3F_8 sat vap		**OK** (Data: ILK-Dresden 2004)		**OK**
Gylon ® in C_3F_8 sat vap		**OK ?** (Data: ILK-Dresden 2007)	Weight, dimension gain, reduced tensile strength, probably better in superheated vap (BPR membrane)	**OK ?**

Note: fluorocarbons as they remove the plasticiser from certain plastics making the product brittle. Source: G. Lenzen, DELPHI RICH and 3M Sources:

[65] OK means that material does not show any damage up to the indicated dose. BAD means it is affected well below 10^5 rad.
[66] Effect means change of weight and/or volume after > 72h immersion in C_6F_{14}. Some effect means > 1%. BAD means >4%.

APPENDIX 5 – (Cont)

(Page 2 of 2)

A very good summary of SFC compatibility with a variety of polymers is given in ref
http://detector-cooling.web.cern.ch/detector-cooling/data/Fluoro_Compatibility.htm
from which this material is copied.

3M and various materials manufacturers were contacted by the CERN EN-CV group regarding compatibility of their products with Fluorinert SFCs:

GOOD

- Acrylic (Acrylite / Acrysteel / Aristech / Cyrolite / Diakon / Kamax) *possible
- Buna-N - Nitrile rubber (NBR=Acrylonitrile butadiene rubber - Perbunan-NT / Hycar / Butacril / Chemigum / Isr-N / Stansolv / Sol-Vex) *good
- Nalgene - Polyurethane (PU/PUR=Polyurethane rubber - Vulkollan / Adiprene) *possible
- Neoprene W (CR=Polychloroprene rubber - Baypren / Neox / Stanzoil) *prohibited
- Silicone (SIR=Silicone rubber - Silastic) *possible

BAD

- Nylon (PA=Polyamid - Stanyl / Capron / Ultramid / Maranyl / Zytel / Orgamid / Grilon / Rilsan / Reny / Vestamid) *possible
- Polypropylene (PP=Polypropylene - Celmar / Coprax / Giacogreen / Hostelen PP / Novolen / Appryl / Lacqtene / Propathene / Ektar FB / Fortilene / Marlex / Polyfine / Pro-Fax / Tenite) *possible
- PVC (PVC=Polyvinyl chloride - Betaglas / Darvic / Fiberlok / Trovidur / Hostalit / Vestolit / Tygon) *prohibited
- Teflon (PTFE=Polytetrafluoroethylene - Flubriflon / Fluon / Teflon TFE / Valflon F / Hostaflon TF / Furon / Gortex / Tfm / Rulon) *prohibited
- Tygon (PVC) *prohibited
- Viton (FKM=Fluoroelastomer - Fluorel) *prohibited
- (from our test) EPDM (Ethylene propylene rubber - Keltan / Nordel / Vistalon / Buna-AP / Pyrofil) *possible

*CERN IS 41 classifications

APPENDIX 6 Selected physical data for saturated fluorocarbons

This appendix is a compilation from various sources of relevant parameters and properties for saturated fluorocarbon fluids, with the exception of specific pressure-enthalpy curves already included in preceeding chapters. The most pertinent properties are:

- Saturated vapour pressure as a function of temperature;
- Liquid and gas phase density as a function of temperature;
- Liquid Viscosity as a function of temperature;
- Solubility of various gases in the fluorocarbon liquids;
- Refractivity *vs.* wavelength;
- Optical transparency *vs.*wavelength.

Figure A-6.1 shows the saturated vapour pressures vs temperature for the SFCs currently considered in Cherenkov radiator and detector cooling applications. The low volatility heavier fluids C_7F_{16} and C_8F_{18} (known via their 3M Corp. appellations as PF5070 and PF5080), though commercially marketed, are not currently in common use in high energy physics applications.

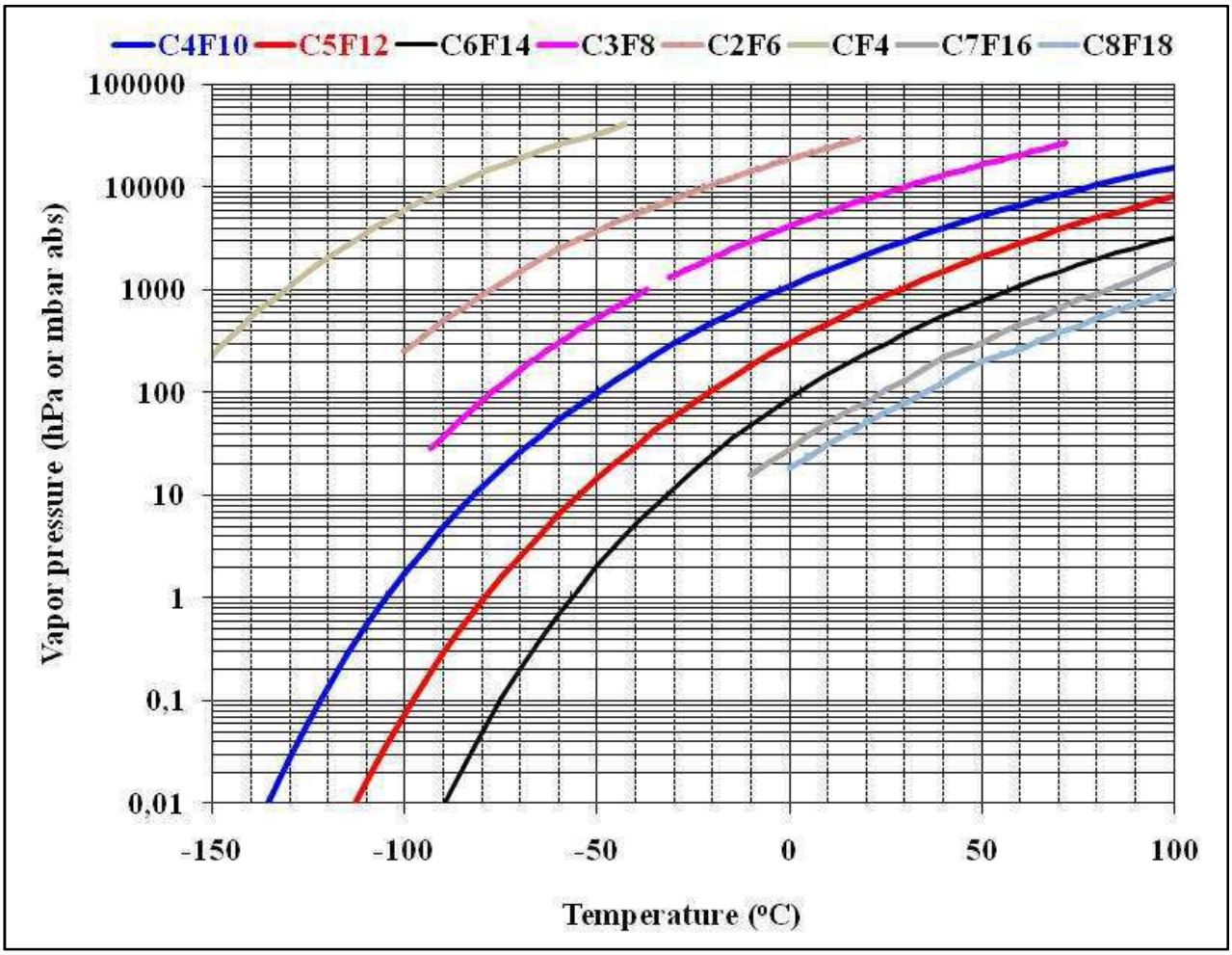

Fig. A6-1. Vapour pressure curves of the saturated fluorocarbons currently used in high energy physics Cherenkov and detector cooling applications.

Sources:

- *Dirk Wiedner : Presentation on LHCb RICH detectors at RICH2007:* http://rich2007.ts.infn.it [A6.-1]
- *S.Pignato (3M Corporation): private communication* [A6-2]
- *Air Liquide Gas Encyclopaedia (Air Liquide/Elsevier*), ISBN-10: 0444414924, ISBN-13: 978-0444414922 [A6-3]
- http://detector-cooling.web.cern.ch/Detector-Cooling/data/TABLE4-1.HTM [A6-4]

Figure A6-2 illustrates the kinematic viscosity of various SFC liquids as a function of temperature. The kinematic viscosity in cSt (centistokes: 1 cSt = 10^{-6} m^2s^{-1}) can be converted to the dynamic or absolute viscosity in units of Pa.s or $kgm^{-1}s^{-1}$ by multiplication by the liquid density.

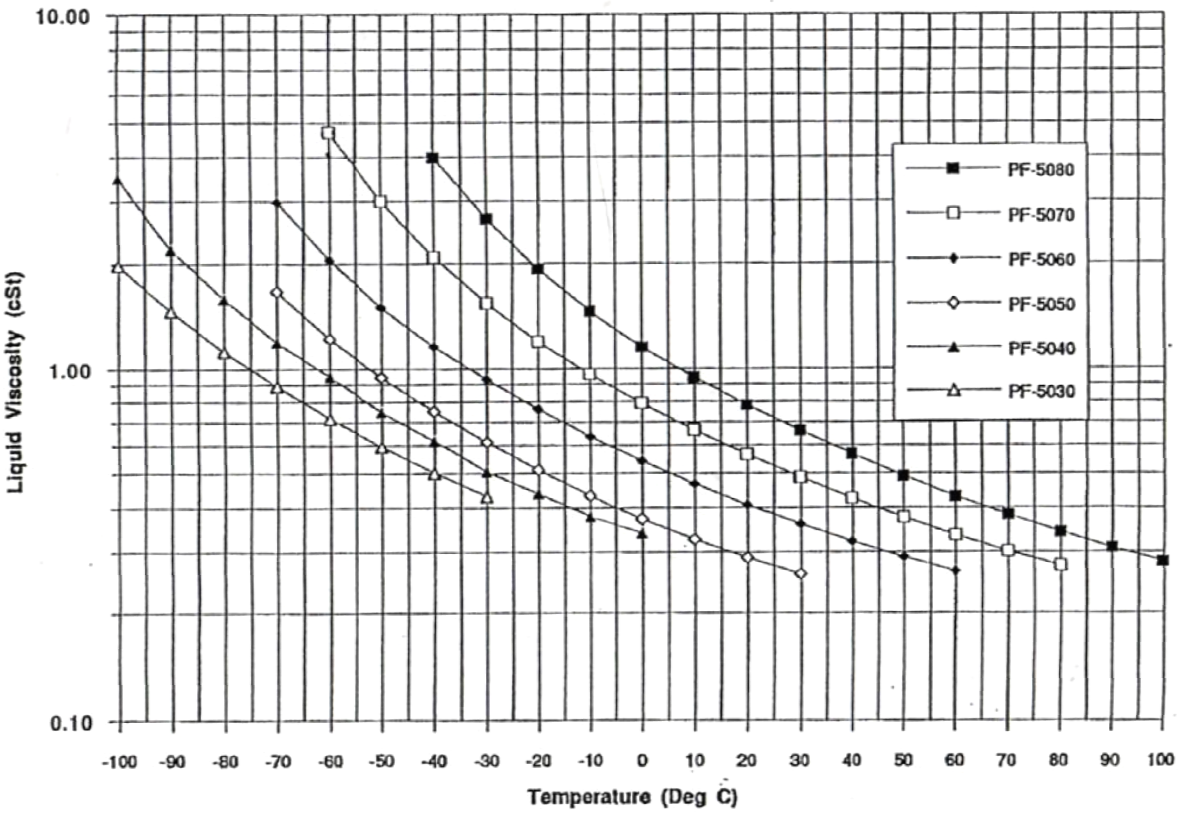

Fig. A6-2. Kinematic viscosity curves of 3M Corp. – manufactured fluorocarbon "performance fluids"): the third number in the index refers to the number of carbon atoms in the molecule. Source: S.Pignato (3M Corporation): private communication [A6-2.]

Figure A6-3 illustrates the density of various SFC liquids as a function of temperature, while Fig. A6-4 illustrates the superheated vapour density of the various SFCs as a function of temperature at atmospheric pressure . The very large temperature range spans from the boiling temperature at 1 bar abs to 50 C. While the superheated vapour density at temperatures in the range 15-40° C at atmospheric pressure is of interest in the context of large Cherenkov radiator enclosures, the density at low temperatures has significance in the design of the recirculator tubing, particularly if a condensation/evaporation cycle is employed.

Fig A6-5 illustrates the variation of superheated vapour density vs temperature over a wide range of pressures for the fluid C_3F_8, which has been extensively studied for evaporative cooling the ATLAS silicon tracker. The density in varying pressure bands is of interest to the design of exhaust tubing, where – depending on the evaporation pressure - the superheated vapour following evaporation of all the injected liquid may be above atmospheric pressure. All data for figs A6-4 & A6-5 is calculated using the NIST on-line database http://webbook.nist.gov/chemistry/fluid/

Figure A6-6 shows the typical heat capacity of the 3M Corp. "Fluorinert" liquid SFCs in liquid phase; data relevant to liquid phase cooling and heat exchange in condensers: *source 3M Corp*. As noted, these are similar, to within 5%, over the fluid range.

Table A6-1 indicates the solubility of commonly-encountered gases at atmospheric pressure into a liquid SFC at a temperature of 25°C. Their solubility into water at the same temperature is shown for comparison. It can be seen that the solubility into the SFC liquid is much greater than into water under the same conditions.

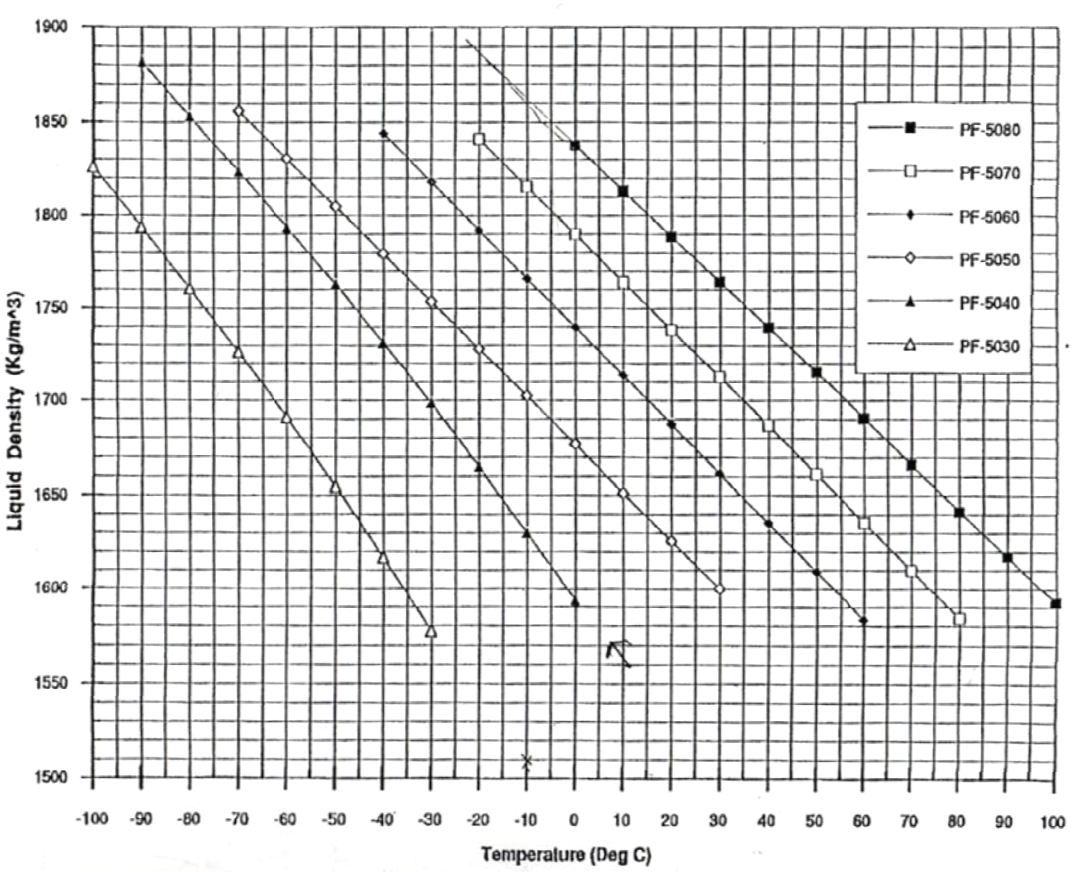

Fig. A6-3. Liquid density curves of 3M Corp. – manufactured fluorocarbon "performance fluids"): the third number in the index refers to the number of carbon atoms in the molecule. Source: S.Pignato (3M Corporation): private communication [A6-2].

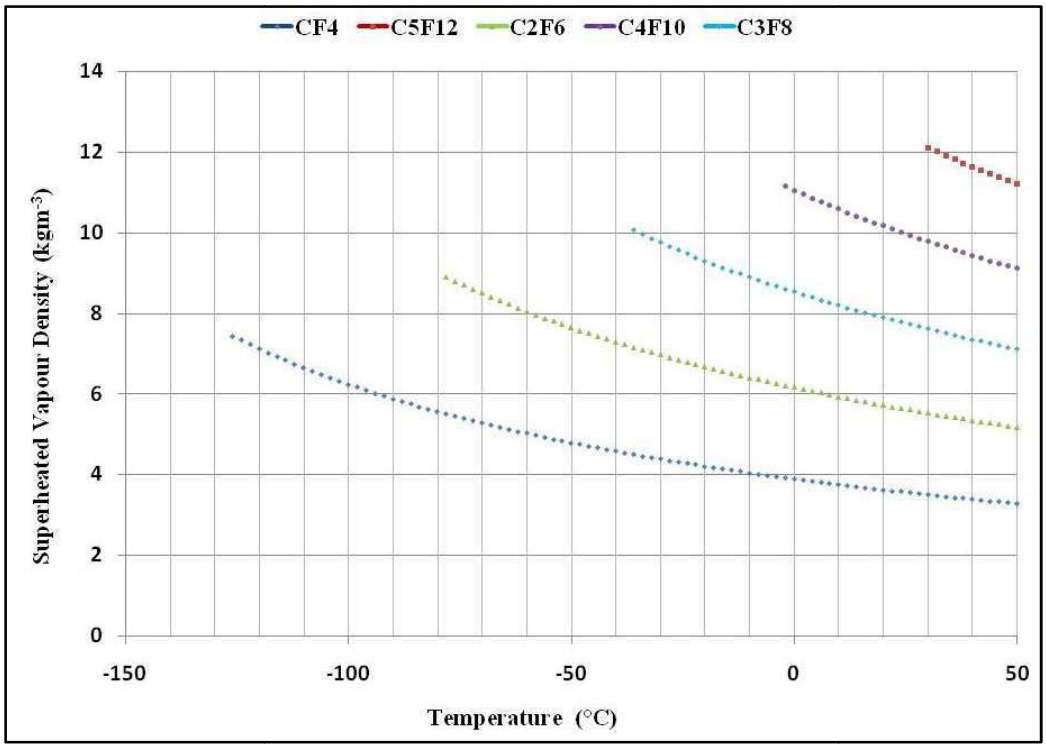

Fig. A6-4. Superheated vapour density curves for SFCs used as Cherenkov radiators: Source: U.S. National Institute of Standards (NIST) chemistry database: http://webbook.nist.gov/chemistry/fluid/ [A6-5].

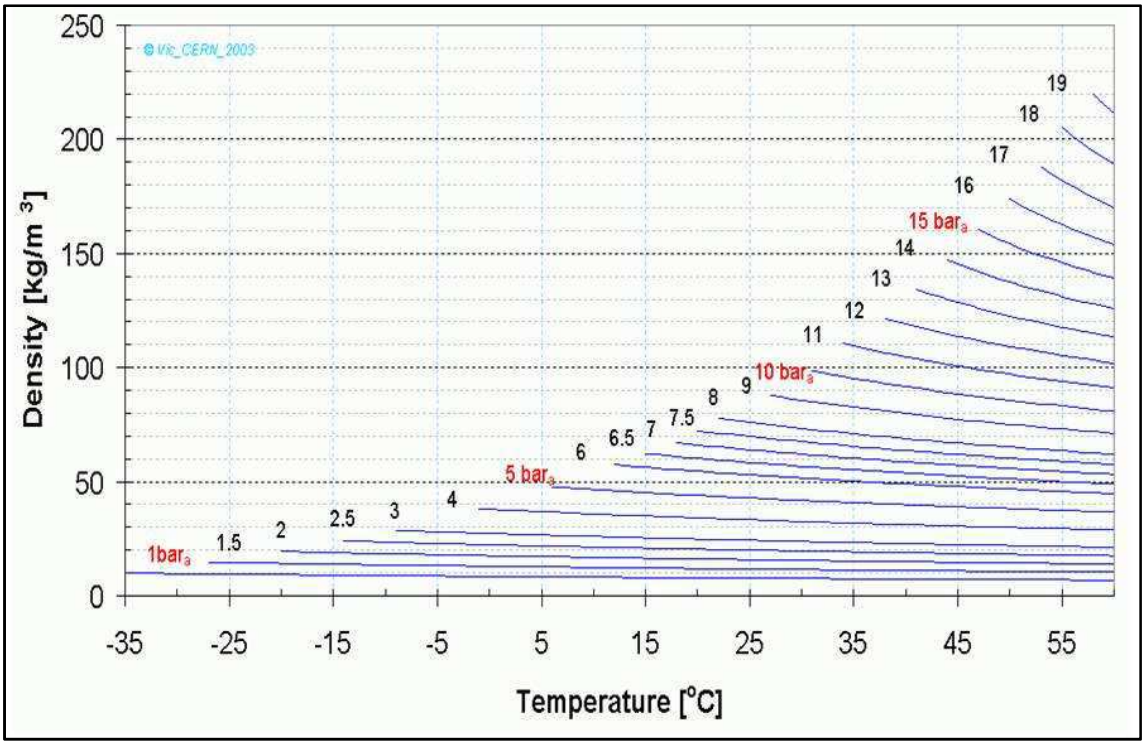

Fig. A6-5. Superheated vapour density curves for C_3F_8 as applicable to evaporative cooling application. Source: U.S. National Institute of Standards (NIST) chemistry database: http://webbook.nist.gov/chemistry/fluid/ [A6-5].

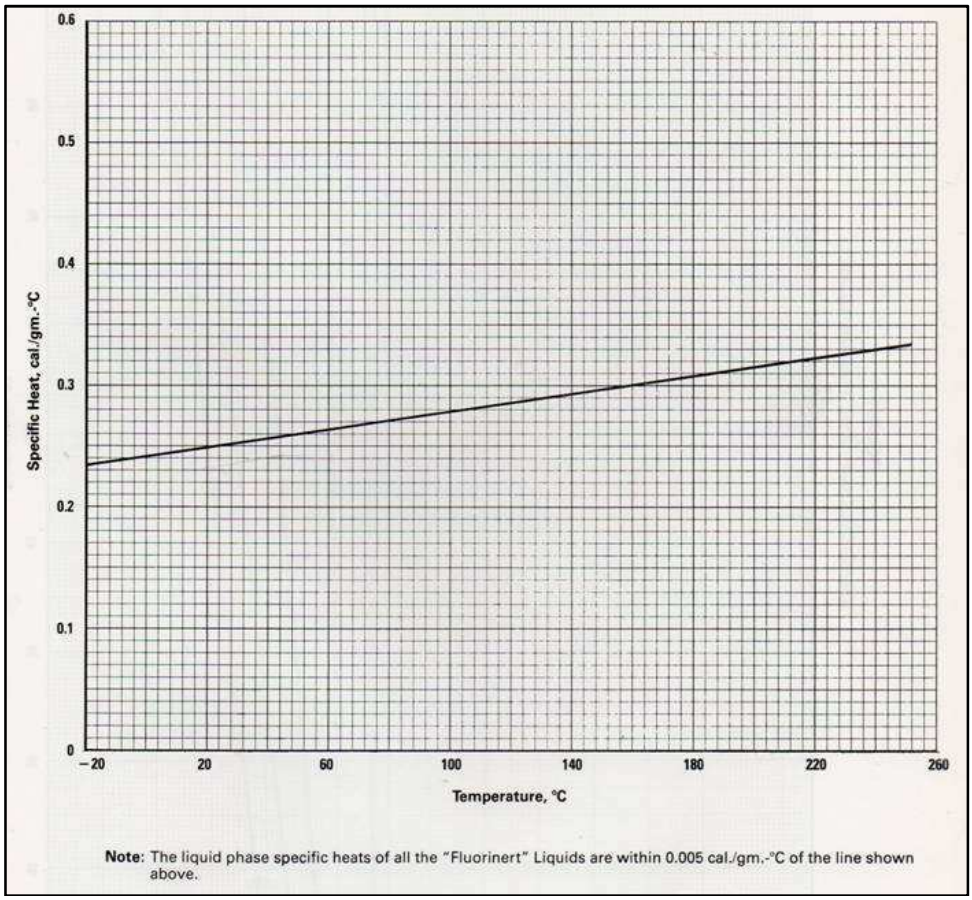

Fig. A6-6. Specific heat capacity of the 3M Corp. "Fluorinert" liquid SFCs in liquid phase: relevant to liquid phase cooling and heat exchange in condensers: source 3M Corp.[A6-2]

Table A6-1. Solubility of various common gases into a liquid SFC (3M FC-72: C_6F_{14}) at 25°C, with comparison with water under the same conditions: source 3M Corp.

Dissolved Gas (P = 1 bar_{abs})	Into Water ml gas per ml liquid at 25°C	Into 3M FC-72 (C_6F_{14}) ml gas per ml liquid at 25°C
Helium	0.09	11
Argon	5.6* (at 0°C)	65
Hydrogen	1.9	17
Nitrogen	1.6	43
Oxygen	3.2	65
Carbon Dioxide	80.5	248
Air	1.9	48

The Cherenkov threshold and optical detection bandwidth for various SFC fluids used as Cherenkov radiator are shown in Fig. A6-7. Both the refractive index and optical transparency are strongly dependent on the purity of the fluids, as has been seen in the preceding sections.

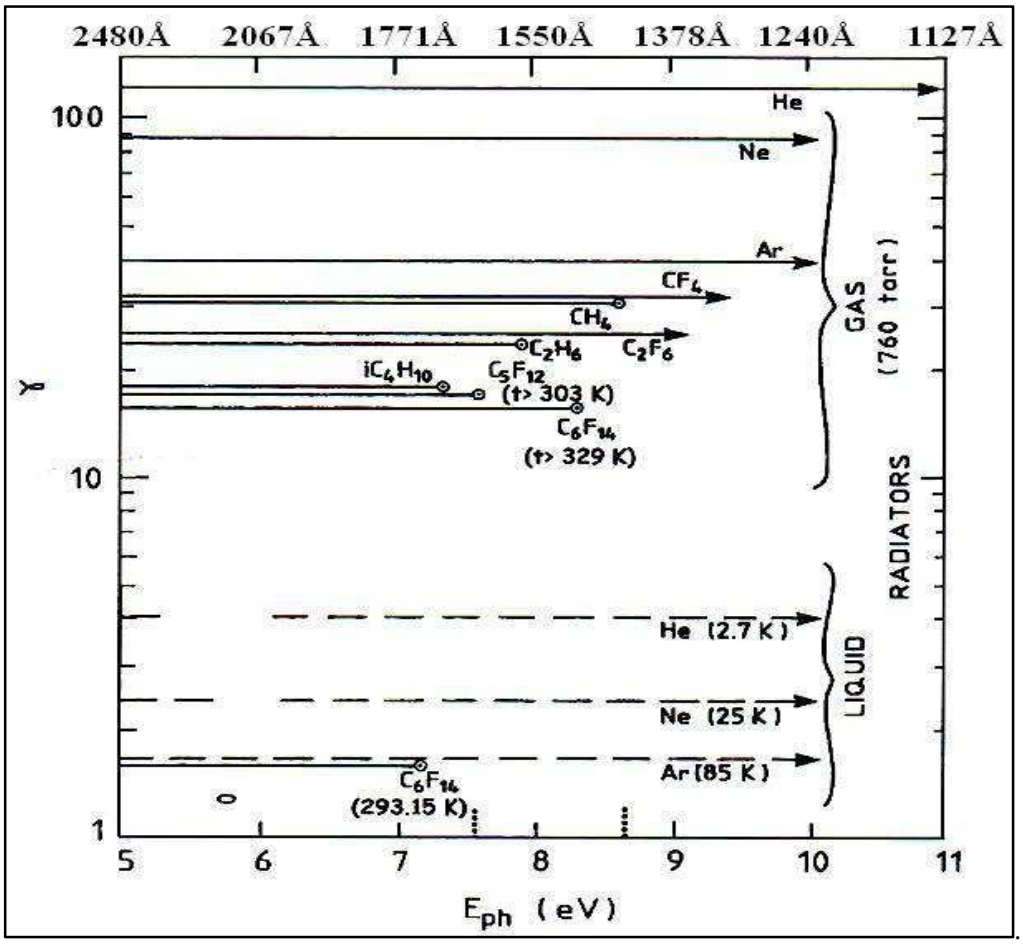

Fig. A6-7. Cherenkov threshold and optical detection bandwidth for various SFC fluids used as Cherenkov radiators: source: E. Nappi & J. Seguinot, Rivista del Nuovo Cimento 28, No. 8-9 (2005) 1. [A6-5]

Fig A6-8a, b illustrates the refractive index of CF_4, C_2F_6, C_4F_{10}, C_5F_{12} and C_6F_{14} in both liquid form (at varying temperatures) and for CF_4, C_2F_6, C_4F_{10}, C_5F_{12} also in vapour phase (at 25°C and 1 bar abs). The refractive indices in the two states are linked via the Lorentz-Lorenz formula:

$$\frac{(n^2-1)_{VAP}}{(n^2+2)_{VAP}} = \frac{P}{RT_{VAP}} * \frac{M}{\rho_{LIQ}} * \frac{(n^2-1)_{LIQ}}{(n^2+2)_{LIQ}} \qquad \text{(A6-1)}$$

Where P is the vapour phase pressure (Pa), R is the molar gas constant (8.314 $Jmol^{-1}.K^{-1}$), T is the absolute temperature of the vapour phase radiator (K), M is the molar mass (kg) and ρ is the liquid density (kgm^{-3}). The left and right hand sides of eq (A6-1) are equivalent and linked to the molar refractivity which is independent of the medium phase. It can be seen that the first two product terms on the right hand side of eq. (A6-1) have a familiar PV/RT form.

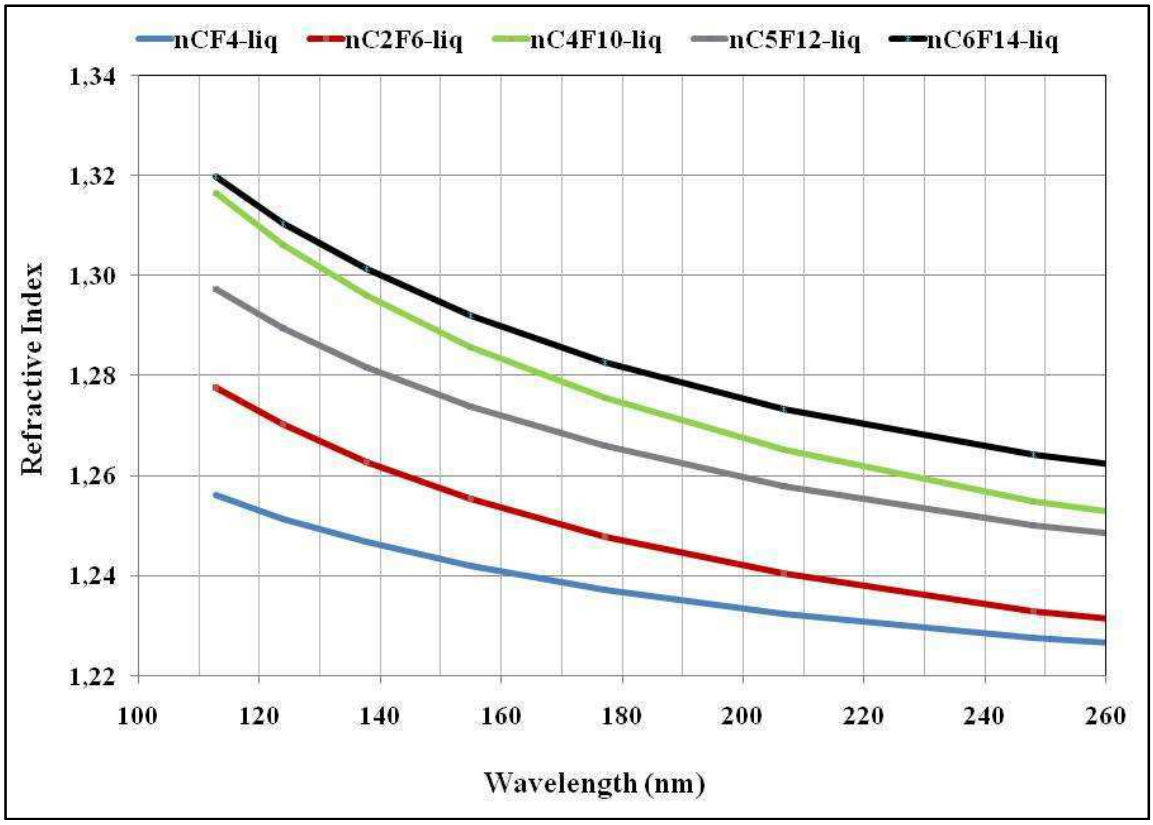

Fig. A6-8a Liquid refractive index of CF_4, C_2F_6, C_4F_{10}, C_5F_{12} & C_6F_{14}; respectively 146, 195, 265, 303 & 329K. source: E. Nappi & J. Seguinot, Rivista del Nuovo Cimento 28, No. 8-9 (2005) 1. [A6-5]

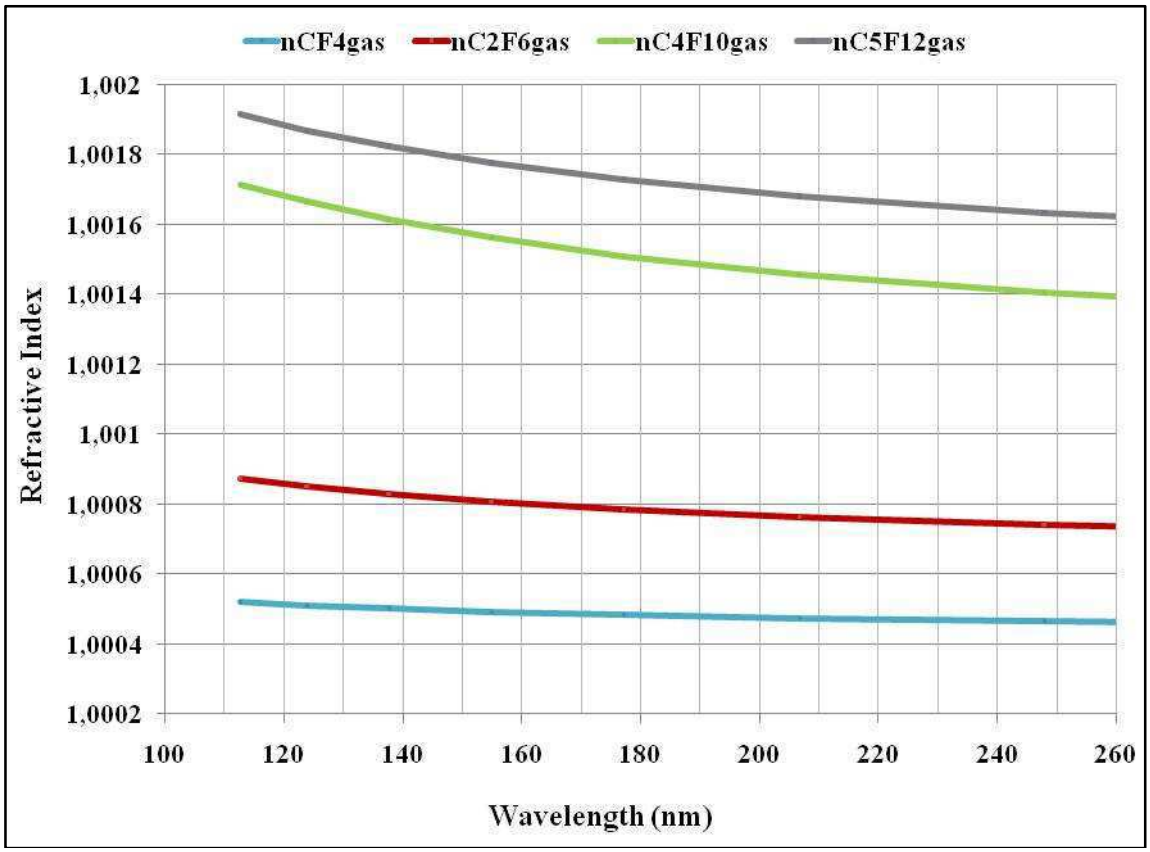

Fig. A6-8. Refractive index of CF_4, C_2F_6, C_4F_{10} and C_5F_{12} in vapour phase at 35°C and 1 bar abs. Derived from liquid phase refractive indices of Fig. A6-8a via eq. (A6-1)

Fig A6.6 illustrated the detection bandwidth of the saturated fluorocarbon radiators in a rather approximate way.

Their maximum transparent detection bandwidth is very dependent on their cleanliness and the techniques used to purify them, as discussed in sections 2.4.2, 2.4.4 and 2.5.2.

Pure CF_4, whose transparency has not been explicitly discussed in the context of LHCb or PHENIX, has the widest light transmission down to VUV wavelengths of any saturated fluorocarbon. Absoprtion begins at ~ 100nm [A6-6] meaning that in windowed photon detection chambers (unlike the PHENIX windowless application) very expensive Calcium Fluoride or Magnesium Fluoride windows would be needed to exploit the full Cherenkov photon bandwidth. In LHCb however, CF_4 is chosen more for its convenient refractive index than its full bandwidth, which is not exploitable at wavelengths <200nm with the S20 photocathodes and quartz windows of the HPD (Hybrid Photon Detector) tubes.

In addition to the effects of cleaning on maximizing optical transparency already seen in samples of C_4F_{10} and C_6F_{14} (figures 2.21 and 2.23/2.24 respectively), results for the cleaning of C_5F_{12} in the context of the SLD-CRID thermodynamic circulator are shown in figs A6-9a and A6.9b [A6-7]. Fig A6-9a shows the transmission of 87%C_5F_{12}/13% N_2 radiator gas mixture extracted from the radiator return and measured in the 20 cm gas cell of Fig 2.38. The transmissions in the 20cm cell are compared with scaled measurements from a typical Cherenkov photon path length of 67cm and also from DELPHI RICH measurements in pure C_5F_{12} made in a 1cm liquid cell [A6-8]. Figure A6-9b shows the transparencies various 1cm liquid samples extracted from the -80°C C_5F_{12} reservoir tank. These transmissions are compared with measurements taken in the DELPHI RICH in November 1998 [A6-8].

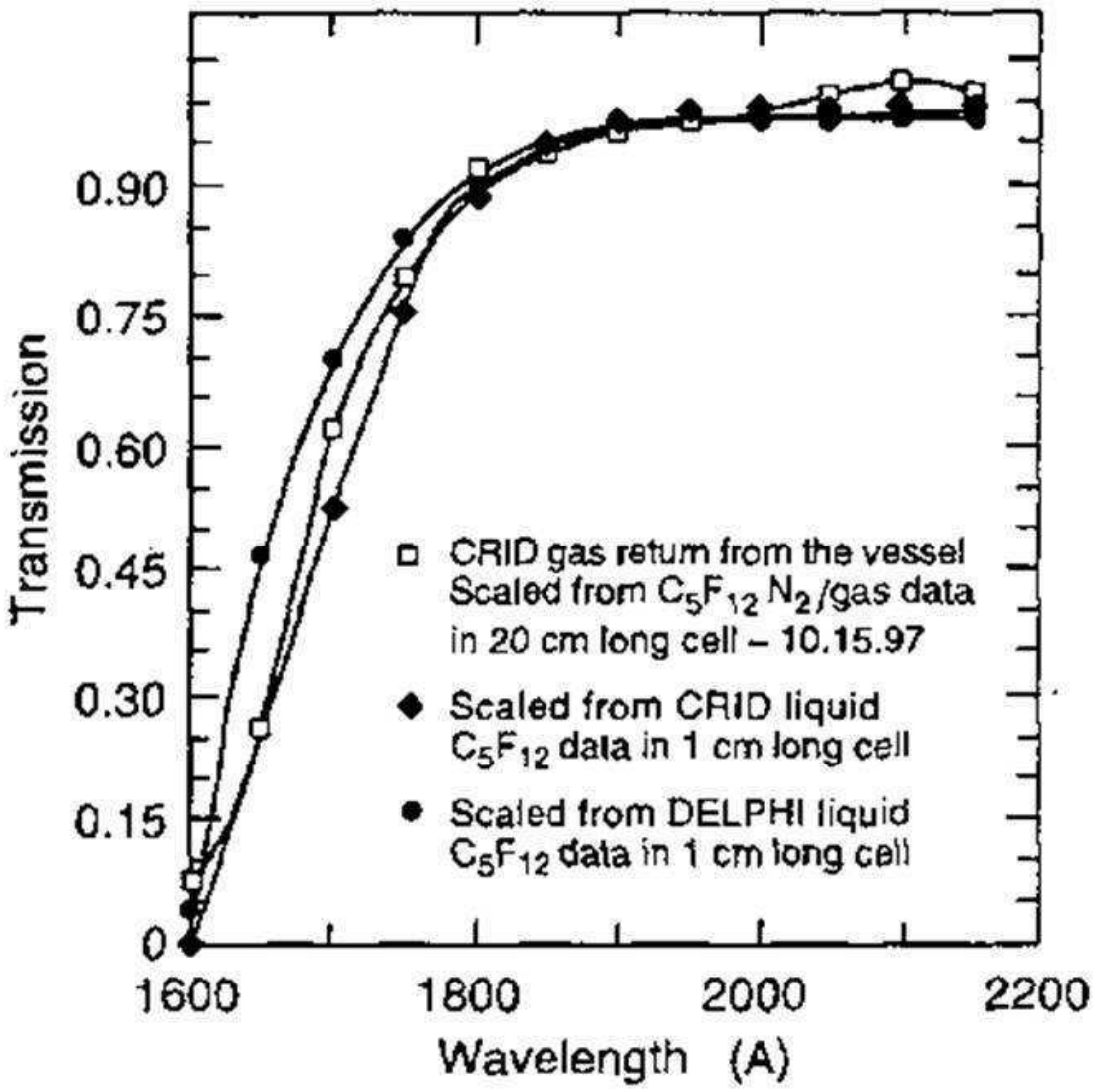

Fig A6-9. Transmission in 87%C_5F_{12}/13% N_2 radiator gas mixture extracted from the radiator return and measured in a 20 cm gas cell, compared with scaled measurements from typical Cherenkov photon path length of 67cm and also from DELPHI RICH measurements in pure C_5F_{12} made in a 1cm liquid cell.

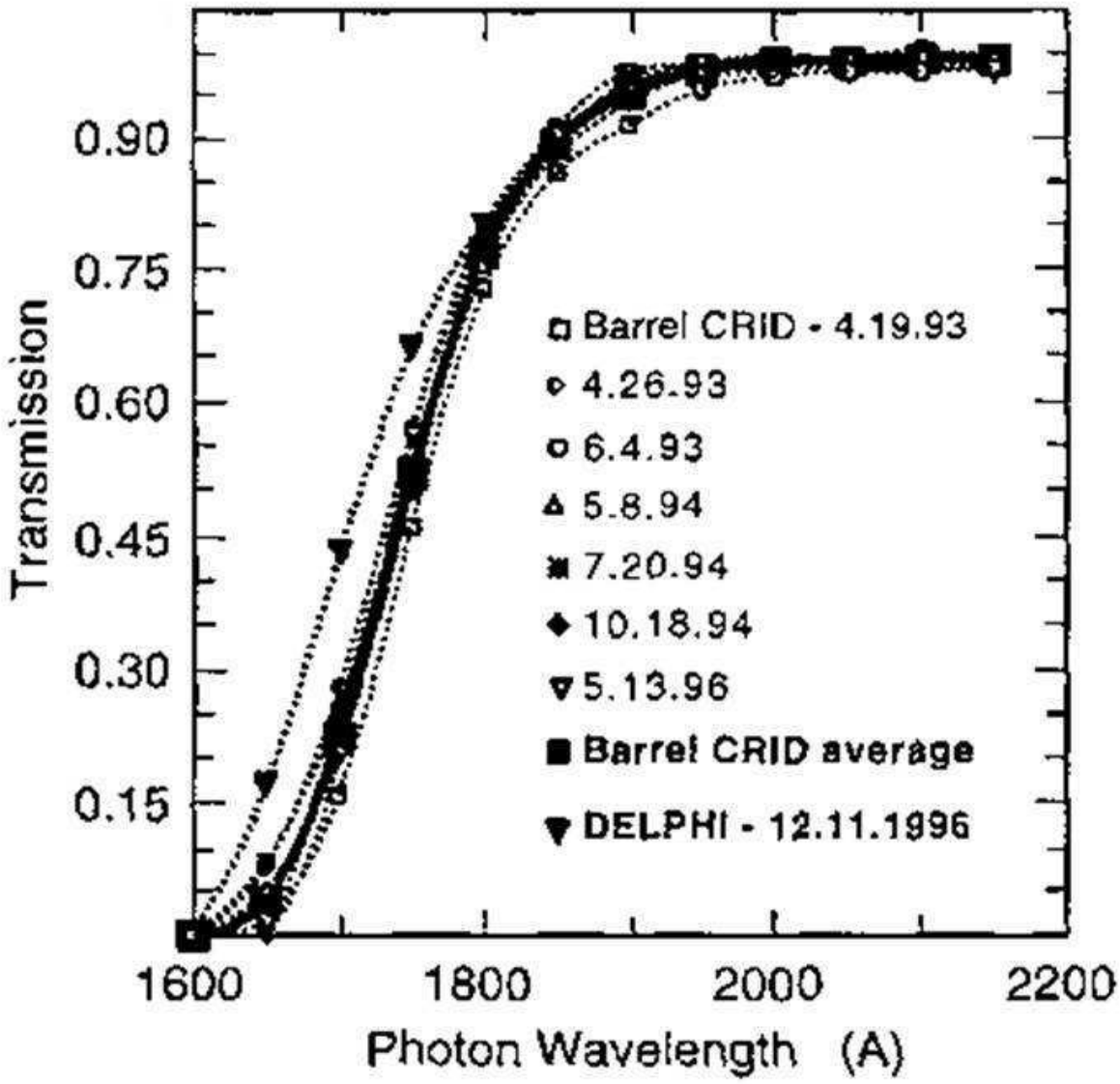

Fig. A6-9b. Transparencies of 1cm C_5F_{12} liquid samples extracted from the SLD-CRID -80°C C_5F_{12} reservoir tank, compared with measurements taken in the DELPHI RICH in November 1998.

The combination of data shown in figures A6-9a,b in this appendix, taken together with figures 2.21, 2.23 and 2.24 of previous sections probably summarize the best achieved transparent bandwidths of C_4F_{10}, C_5F_{12} and C_6F_{14} seen in large-scale operational RICH detector systems.

References

[A6-1] Dirk Wiedner : Presentation on LHCb RICH detectors at RICH2007: http://rich2007.ts.infn.it
[A6-2] S.Pignato (3M Corporation): private communication
[A6-3] Air Liquide Gas Encyclopaedia (Air Liquide/Elsevier), ISBN-10: 0444414924, ISBN-13: 978-0444414922
[A6-4] http://detector-cooling.web.cern.ch/Detector-Cooling/data/TABLE4-1.HTM
Source: U.S. National Institute of Standards (NIST) chemistry database: http://webbook.nist.gov/chemistry/fluid/
[A6-5] E. Nappi & J. Seguinot, Rivista del Nuovo Cimento 28, No. 8-9 (2005) 1.
[A6-6] "Radiator gases with small refractive indices": Olav Ullaland, Presentation at Intl. RICH-Workshop of the CBM Experiment at FAIR Gesellschaft für Schwerionenforschung Darmstadt, Germany, March 6 -7, 2006
[A6-7] Performance of the Barrel CRID at the SLC, Long Term Operational Experience.
K. Abe et al SLAC PUB 7705, Nov. 1997 **IEEE Trans.Nucl.Sci.45:648-656,1998**.
[A6-8] G. Lenzen private communication: see also earlier data in. E. Schyns PhD thesis,
University of Wuppertal, 1997 WUB-DIS-92-22

ANNEXE A: Curriculum Vitae: Gregory David Hallewell

(1) État civil

- Né le 18 septembre 1955, Cardiff, Pays de Galles, GB ; Marié, 3 enfants

(2) Études Universitaires

- 1974-77 : études pour diplôme 'Bachelor of Science' en Physique et Astrophysique, Queen Elizabeth College, Université de Londres
- 1977-82 : études pour thèse 'Docteur en Philosophie' en Physique des Particules, Westfield College, Université de Londres

(3) Diplômes Universitaires

- juillet 1977 : 'Bachelor of Science' en Physique et Astrophysique, de l'Université de Londres ;
- le 12 mai 1982 : Doctorat de l'Université de Londres :
  Thèse ; « Étude du canal $\pi^+ p \rightarrow K^+\Sigma^+$ entre 1.4 et 2.5 GeV/c »
  cadre de l'expérience RMS (« Rutherford Multiparticle Spectrometer ») :
  analyse du canal $\pi^+ p \rightarrow K^+\Sigma^+$ par la technique « Barellet Zéros ».

(4) Mobilité professionnelle

- 1982➔1985 : Laboratoire Rutherford-Appleton, Oxford, GB ; Post-doc;
- 3/1985➔10/1991 : Stanford Linear Accelerator Center (SLAC), Stanford University, Californie, USA: Post-doc (3/85–6/90; puis physicien permanent jusqu'en 10/91);
- (10/1991➔) : Centre de Physique des Particules de Marseille (CPPM) CNRS/IN2P3 ; UMR 6550
  - 10/1991 : Intégration comme ingénieur de recherche classe 1 en instrumentation ;
  - 10/1998➔3/2000 : Attaché scientifique CERN en disponibilité IN2P3 (sur l'expérience ATLAS) ;
  - 3/2000➔3/2001 « Visiting Scientist » Rutherford Appleton Laboratory, Didcot, GB., en mise à disposition IN2P3 (présent au CERN sur l'expérience ATLAS) ;
  - 3/2001 : Réintégration comme ingénieur de recherche classe 1 en instrumentation ; (expériences ANTARES, KM3NeT et ATLAS)
  - promu ingénieur de recherche classe exceptionnelle jan. 2008.

(5) Diffusion de l'information scientifique et technique

- 239 publications dans des revues internationales visées par comité de lecture spécialisé dans la physique des particules et le développement des détecteurs pour la physique des particules et l'astrophysique. Auteur principal de 50 publications ;
- Env. 50 séminaires et présentations en conférences internationales, le plus récent en mai 2010 ;
- Corédacteur du TDR «Technical Design Report» KM3NeT
  ISBN 978-90-6488-033-9, mai 2010
- Corédacteur du CDR «Conceptual Design Report» KM3NeT
  ISBN 978-90-6488-031-5, avril 2008
- Chef du comité de publication et de communication du consortium « KM3NeT » depuis septembre 2006 ;
- Corédacteur du TDRs «Technical Design Reports» du détecteur à pixels pour l'expérience ATLAS au CERN. CERN/LHCC/98-13 ATLAS TDR 11 ; 31 mai 1998
- Corédacteur du TDRs «Technical Design Reports» du détecteur interne pour l'expérience ATLAS au CERN. CERN/LHCC/97-17 ATLAS TDR 5 ; 30 avril 1997
- Co-auteur de 15 notes techniques internes ATLAS et 7 notes techniques internes ANTARES;
- Auteur de 3 articules d'intérêt général sur les détecteurs de rayonnements Tcherenkov et le télescope a neutrinos ANTARES, tous diffusés dans la revue « Courrier CERN » ciblé au grand public (10/2010, 3/2003,7/2003) ;
- Chef de comité local d'organisation et membre de comite scientifique international du congrès RICH2010 (7th International Workshop on Ring Imaging Cherenkov Detectors), Cassis, France, 3-7 mai 2010 ;
- Chef de comite de rédaction des proceedings du congres RICH2010 (publication prevu dans la revue Nuclear Instruments & Methods A en 2011)
- Chef de comité local d'organisation et membre de comité scientifique international du congrès VLVnT08 (3^{d} International Workshop on a Very Large Volume Neutrino Telescope for the Mediterranean Sea) Toulon, France 22-24 avril 2008 ;
- Chef de comite de rédaction des proceedings du congrès VLVnT008 (publication dans la revue Nuclear Instruments & Methods A, Vol 602, (2009)) ;
- Membre du comité international scientifique de la conférence «RICH2007 »
  Trieste, Italie, 10/2007 ;
- Membre des comités internationaux d'organisation scientifique des congrès
  VLVnT1 (Amsterdam, NL ; oct. 2002) & VLVnT2, (Catane, Italie ; nov. 2005) ;
- Présentation sur le télescope a neutrinos ANTARES au colloque national « OPTO2005 » (Paris Expo le 28 septembre 2005) organise par POPSUD (« Pôle Optique et Photonique Sud »; un groupement des entreprises et laboratoires impliqués dans les développements photoniques et soutenu par les collectivités de la région PACA).

(6) Activités de revue et dans le financement de projets scientifiques

- Sollicité comme rédacteur des papiers scientifiques et reviewer de propositions de recherche: Nucl. Instr. Meth. A (Elsevier); Intern. J. Thermophysics (Springer).
  Agence Nationale de Recherche (Programmes blanc et jeunes chercheurs), CSF (Czech Science Foundation), Helmholtz Gemeinschaft (Allemagne), INTAS (E-U➔ 1/2007) ;
- Membre du comité d'écriture de la proposition pour un projet d'étude de faisabilité d'un télescope a neutrinos en mer Méditerranée avec volume ~ $1km^3$ (nommée « KM3NeT »), qui a été soumise à la communauté européenne au sein de la « 6^{me} programme cadre » en mars 2004 ;
- Membre du comité de négociation financière pour la cadence de financement du projet « KM3NeT » pendant ses 3 années de déroulement ; Cette proposition a demandé un financement de la part de la C.E. de €10m ; elle a démarré fév. 2006
  sous un base de €9m.

4

(7) Valorisation / Relations avec industrie et médicine

- Août 2000. Gestion d'une étude collaborative entre l'hôpital Cantonal de Genève et le CERN sur la faisabilité d'analyse par ultrasons de mélanges utilises dans l'anesthésie. Tests conclus avec succès au département de l'anesthésie de l'HCG en aout 2000, suivi par l'écriture du rapport.

.

- Membre du comité scientifique du GIS (Groupement Industriel – Scientifique) CNRS/IN2P3 – Photonis SA, Brive la Gaillarde.
  Partenariat pour le développement des nouveaux capteurs à photons pour les applications scientifiques, industrielle et dans l'imagerie médicale.

  Financement par Photonis d'un stagiaire et un thésard au CPPM dans le développement des nouveaux capteurs à photons dans le projet KM3NeT.

  Ce collaboration a terminé en mars 2009 suite a la cessation de fabrication de toutes formes de photomultiplicateurs par Photonis SA.

- Consultant à l'industrie (1987-1991) sur le développement des algorithmes pour l'analyse par ultrasons des mélanges de vapeurs utilisés en MOCVD («Metal Organic Chemical Vapor Deposition») pour la fabrication des semi-conducteurs et dans la pétrochimie.

(8) Rapport détaillé sur l'activité post-doctorale avec encadrements

(8.1) Laboratoire Rutherford-Appleton, Oxford, GB et CERN : Post-Doc (1982-1985)

Dans une collaboration Anglo-allemande pour le développement du premier grand détecteur «RICH » (Ring Imaging Cherenkov detector : identification des particules subatomiques par focalisation en anneau de l'onde de choc lumineuse par l'effet Tcherenkov dans un gaz. Responsabilité pour la réalisation du système électronique de lecture des signaux de simples photoélectrons vus dans le détecteur.

Encadrement : Direction d'une équipe de six électroniciens et techniciens en électronique : développement et évaluation des prototypes, réalisation et mise en marche du système final.

(8.2) Stanford Linear Accelerator Center, Californie, USA:
Post-doc (3/1985 – 6/1990 ; puis physicien permanent jusqu'en 10/1991)

Dans la Collaboration internationale SLD «SLC Large Detector» ; une expérience au collisionneur linéaire électron-positron «SLC» (SLAC Linear Collider).

Gestion d'une équipe d'environ 25 étudiants, physiciens appliqués, ingénieurs, mécaniciens et électroniciens pour le développement et mise en marche des systèmes de réglage et de contrôle du détecteur SLD «CRID» (Cherenkov Ring Imaging Detector) Budget ~ $1.6M.

- système de distribution et d'analyse de gaz à très haute pureté ;
- Développement d'un analyseur multifonctions de gaz en temps réel : sélection entre 60 canaux d'entrée pour contrôle du mélange, de la transparence UV, ppm O_2 et H_2O par machine d'état finie programmée en chip FPGA ;
- Développement d'une station de purification de la photocathode gazeuse « TMAE » (tetrakis-dimethylamino-éthylène) pour la conversion des simples photons de rayonnement Tcherenkov en photoélectrons ;
- Développement d'un analyseur ultrasonique de mélanges de gaz (par vitesse de son) pour le CRID SLD.

Autres responsabilités :

- Caractérisation de l'amplificateur CRID de faible bruit (1500e- @ RC-CR de 50ns) : mesures de gain, linéarité, rejet de bruit «ripple» dû aux alimentations de bas et de haute tension dès fonction de fréquence ;
- Coordination de l'alimentation en haute tension de tous les sous-systèmes du détecteur SLD : collaboration avec les fabricants pour l'évaluation des prototypes, mise en marche du système.
- Dans la collaboration SLD «SLC Large Detector» ; expérience au collisionneur linéaire électron-positron «SLC» (SLAC Linear Collider).
- Responsable d'une équipe d'environ 25 étudiants (stagiaires et thésards), physiciens appliqués, ingénieurs, mécaniciens et électroniciens pour le développement et mise en marche du système de réglage et de contrôle du détecteur SLD-CRID (« Cherenkov Ring Imaging Detector »).

Encadrement

Pendant ce période l'équipe a accueilli 8 stagiaires et 4 thésards en temps partiel.

- **Stagiaires**: David Barbat, Glenn Crawford, Michael Culhane, Sarah Darby, Craig Galloway, Paul Korff, Michael Marx, Leonid Sapozhnikov.
- **Thésards**: Jennifer Huber, Young Joon Kwon, Thomas Pavel, Fumihiko Suekane.

(8.3) Centre de Physique des Particules de Marseille (CNRS/IN2P3, UMR6550)

Intégré en octobre 1991 comme ingénieur de recherche classe 1 en instrumentation

- ***Collaboration ATLAS-Pixel (depuis octobre 1991)***

Collaboration pour la réalisation et mise en service d'une expérience au collisionneur LHC (« Large Hadron Collider ») au CERN. Co-auteur de la proposition (avril 1992) du groupe CPPM pour un détecteur à très haute granularité (pixels 50 x 400 μm), avec lecture en technologie sous-micron durci contre radiation, pour les couches internes du trajectographe ATLAS.

Activités

- Co-coordinateur du groupe mécanique pixels ATLAS (1995 - 1999). Membre des comités de pilotage du détecteur interne et du détecteur à pixels ATLAS.
- Corédacteur du TDRs «Technical Design Reports» du détecteur à pixels ATLAS et du détecteur interne ATLAS. Auteur de 15 notes techniques internes ATLAS ;
- Concepteur du système de refroidissement du détecteur à pixels par l'évaporation de fluides fluoro-carbones, adopté pour tout le trajectographe silicium ATLAS (pixels et micropistes) ;
- Coordinateur (basé au CERN septembre 1998 - février 2001) du développement du système de refroidissement et de réglage automatique pour le trajectographe silicium ATLAS. Responsabilité d'un groupe de 8 ingénieurs en mécanique, techniciens et étudiants chargé de développer un système de refroidissement par l'évaporation de octafluoro-butane (C_3F_8), jusqu'au niveau d'un démonstrateur ;

Encadrement (refroidissement du trajectographe ATLAS)

Pendant ce période le groupe a accueilli 4 stagiaires et 4 thésards en temps partiel.
Stagiaires: Christophe Bayer, Per Peterssen, Heidi Sandaker
Thésards: Bogdan Gorski, Käre Langedrag, Scott Lindsay, Thomas Tic

Activités Actuelles (novembre 2010)

- Gestion d'un groupe (11 personnes) qui développe un instrument ultrasonique (combinaison débit-mètre ultrasonique+ analyseur de mélanges de gaz) pour l'étude des mélanges de hexafluoro-éthane (C_2F_6) avec octafluoro-propane (C_3F_8) pour le refroidissement évaporatif du trajectographe ATLAS ;

Encadrement (développement instrument ultrasonique**)**

Le groupe accueillit 1 stagiaires et 4 thésards en temps partiel
Stagiaires: Martin Doubek,
Thésards: Alexandre Bitadze, Nicolas Bousson**,** Vaclav Vins, Michal Vitek

- Développement d'un système de circulation d'un mélange de fluides C_3F_8 et C_3F_8 pour le refroidissement évaporatif du trajectographe ATLAS sans l'utilisation de compresseur a vapeur. (Remplacement du compresseur par un condenseur à la surface et l'exploitation du colonne gravitationnel de 92m de liquide fluorocarbure pour alimenter le trajectograhe ATLAS en fluide caloporteur Réalisation de deux prototypes (2kW, 15 et 92m d'hauteur, 2010/11), suivi par système plein échelle (60kW, 92m d'hauteur) pour 2013.

- ***Collaboration ANTARES (depuis mars 2001)***

Collaboration internationale [France, Allemagne, Espagne, Pays-Bas, Italie, Russie], pour la réalisation, mise en service et operation (depuis 2007), d'un télescope sous-marin à neutrinos cosmiques situé au large de Toulon par 2400m de fond. Détection des particules par enregistrement de l'onde de choc lumineuse par l'effet Tcherenkov dans l'eau de mer

Activités

- Coordinateur pour la réalisation et mise en service de la boîte de jonction sous-marine du détecteur ANTARES : (noyau de connexion électrique et fibre-optique de l'expérience) qui associe la mécanique - pour résister la pression de 256bar – avec différentes technologies ;

l'électronique pour le pilotage et la surveillance, l'électrotechnique pour la distribution de la puissance et l'optique pour la distribution d'horloge et la récupération des données. La boîte de jonction a été mise à l'eau en 12/2002, et branchée en intervention bathyscaphe en 3/2003. Exploitée depuis 46 mois, elle est en communication continue avec la station côtière ;

- Réalisation du système de très haute fiabilité pour l'alimentation en énergie du détecteur par câble électro-optique de longueur 40 km, avec 50% composants inaccessibles (enfermées dans la boîte de jonction) pendant la durée de vie de 10 ans du détecteur. Gestion du câble sous-marin 40km ANTARES dans la MECMA (« Mediterranean Cable Maintenence Agreement » ; mutuelle de 39 operateurs des câbles sous-marins en mer Méditerranée) ; « contact-person » MEMCA pour ANTARES.;
- Impliqué dans la mise en marche du système de « slow control » pour l'alimentation de l'expérience depuis la station côtière ;
- Coordinateur pour la réalisation d'une ligne mécanique prototype de pleine échelle ANTARES. L'expérience avec cette ligne a proposé des améliorations du câble vertical électro-optique utilisé depuis avec succès dans les deux lignes ANTARES opérationnelles (10/06).

Encadrement

- **Thesard :** Sonia Karkar (temps partiel : caractérisation des photomultiplicateurs)

- ***Projet « KM3NeT » (depuis mars 2004)***

Collaboration de 10 pays européennes de pour une étude (à partir de 01/02/2006) pour la réalisation et mise en service d'un télescope sous-marin à neutrinos cosmiques de très grand volume (>1 km^3), situé par grand fond en mer Méditerranée.

Activités

- Corédacteur du TDR (mai 2010) et du CDR KM3NeT (avril 2008)
- Membre du comité d'écriture de la proposition pour un projet d'étude de ce détecteur, (nommée « KM3NeT »), qui a été soumise à la communauté européenne au sein de la « 6^{me} programme cadre » en mars 2004.
- Membre du comité de négociation financière pour la cadence de financement du projet « KM3NeT » pendant ses 3 années de déroulement ; Cette proposition a demandé un financement de la part de la C.E. de €10m ; elle a démarré en février 2006 sous un base de €9m;
- Chef du comité de publication et de communication KM3NeT ;
- Développement des «hybrid photon detectors » ; capteurs sensibles aux simples photons : (photocathode de grande format hémisphérique, amplification de lumière utilisant des cristaux scintillantes, avec lecture par photomultiplicateur ou pixels semi-conducteurs, pour donner une amélioration en efficacité quantique) en partenariat avec Photonis SA (jusqu'en mars 2009)

Encadrement

Thesard : Imen Al Samarai (temps partiel : caractérisation des photomultiplicateurs hybrides - thèse cofinancée par Photonis SA)

Séminaires et présentations en conférences

Séminaires

- KM3NeT: a cubic kilometre-scale deep-sea telescope for neutrino astronomy in the Mediterranean Sea
  Département de Physique et Astronomie, Université de Bristol (GB) le 11 mars 2009
- KM3NeT: a cubic kilometre-scale deep-sea telescope for neutrino astronomy in the Mediterranean Sea
  Département de Physique, Université d'Oxford (GB) le 31 octobre 2007
- KM3NeT: a cubic kilometre-scale deep-sea telescope for neutrino astronomy in the Mediterranean Sea
  Rutherford Appleton Laboratory, Chilton, Didcot, (GB) le 30 octobre 2007
- KM3NeT: a cubic kilometre-scale deep-sea telescope for neutrino astronomy in the Mediterranean Sea
  Département d'Astronomie, Université de Cardiff (GB) le 16 février 2006
- Fluorocarbon evaporative cooling of the ATLAS silicon tracker, and the enthalpy transistor
  RAL Seminar, Rutherford Appleton Laboratory, février 2001
- The ATLAS pixel detector at LHC
  Département de Physique, Rutgers University, New Jersey, USA, juin 1999
- The ATLAS pixel detector development
  SLAC seminar, Stanford Linear Accelerator Center, USA, mars 1994
- The ATLAS pixel detector development
  Département de physique, Université de New Mexico, Albuquerque, NM, USA, mars 1994
- Development of active pixel detectors for the ATLAS experiment for LHC
  Institut Paul Scherrer, Villigen, Suisse, juin 1993
- Development of active pixel detectors for the ATLAS experiment for LHC
  Max-Planck-Institut fur Kernphysik, Heidelberg, Allemagne, juin 1993
- Development of the SLD CRID
  Cornell University Journal Club, Cornell, Ithaca, New York, USA (avril 1989)
- Development of the SLD CRID
  Fermilab Seminar, Fermi National Accelerator Laboratory, Batavia, Illinois USA (avril 1989)
- Ultrasonic Analysis of Drift Chamber Gases
  Département de Physique Université de Californie Santa Cruz,(USA) mai 1988
- Ultrasonic Gas Analysis – a competitor in chromatography applications?
  SRI International, Menlo Park, Californie (USA), juin 1988
- Ultrasonic Gas Analysis in Drift Chamber and Cherenkov Counter Appplications
  Lawrence Berkeley Laboratory, Californie (USA) aout 1988
- Ultrasonic Gas Analysis for the SLD CRID detector
  Rutherford Appleton Laboratory, GB, juillet 1988
- Ultrasonic Gas Analysis for the SLD CRID detector
  Département de Physique, Université Brunel, GB, juillet 1988
- The SLD Cherenkov Ring Imaging Detector
  Rutherford Appleton Laboratory, GB, juillet 1988
- The SLD Cherenkov Ring Imaging Detector
  Royal Holloway College, GB, juillet 1988
- The OMEGA Ring Imaging Cherenkov Detector
  Brookhaven Seminar, Brookhaven National Laboratory, Long Island, New York, USA, novembre 1982
- The OMEGA Ring Imaging Cherenkov Detector
  SLAC Seminar, Stanford Linear Accelerator Center, Stanford, Californie, USA, novembre 1982
- Development of he OMEGA Ring Imaging Cherenkov Detector
  Physics Department, Université de Liverpool UK, juin 1982

Présentations orales en conférences

- The use of saturated fluorocarbons in high energy physics, G. Hallewell, CPPM
  7th Intl. Workshop on Ring Imaging Cherenkov Counters, Cassis, France, 3-7 mai 2010
- Data Transfer in the KM3NeT deep sea Neutrino Telescope
  G. Hallewell, CPPM, pour le consortium KM3NeT
  Topical Workshop on Electronics for Particle Physics (TWEPP09), Paris 21-25 septembre 2009
- New Developments of Scintillating Crystal-Based Hybrid Single Photon Detectors (X-HPDs) for Charged Particle and Neutrino Detection Applications
  G. Hallewell, CPPM, pour le consortium KM3NeT
  1st International Conference on Advancements in Nuclear Instrumentation, Measurement Methods and their Applications (ANIMMA09) Marseille 7-10 juin 2009
- Scintillator-based hybrid photon detector development for the KM3NeT (km3-scale) deep sea neutrino telescope. G. Hallewell, CPPM, pour le consortium KM3NeT
  VLVnT08; 3rd international Workshop on a Very large volume neutrino telescope for the Mediterranean Sea, Toulon, France, 22-24 avril 2008
- Construction and operation of the ANTARES underwater neutrino telescope
  G. Hallewell, CPPM, pour la collaboration ANTARES:
  6th Intl. Workshop on Ring Imaging Cherenkov Counters, Trieste, Italie, 15 - 20 octobre. 2007
- Status report on cooling R&D with light fluorocarbons : report of the Tracker Upgrade Thermal Management Group: G. Hallewell, CPPM
  ATLAS High Luminosity Upgrade Tracker Workshop Liverpool (GB): 6-8 decembre 2006
- Large Underwater Neutrino Detectors: Photon Detector Challenges, G. Hallewell, CPPM
  LIGHT06: Large Area Photon Detectors Workshop, Kibbutz Eilot, Eilat, Israel, 8-12 janvier 2006
- The status of Cherenkov Detectors in Astrophysics, G. Hallewell, CPPM (Presentation invite):
  5th Intl Workshop on RICH Detectors: (RICH 2004), Cancun, Mexique, 6-10 decembre, 2004
- The ANTARES Junction box and deep sea connection hub
  2nd international Workshop on a Very large volume neutrino telescope for the Mediterranean Sea, Catane, Italie, 22-24 novembre 2005
- Le câble et boite de jonction sous-marin du télescope à neutrinos ANTARES ; retour d'expérience
  Réunion des électroniciens CNRS, Carry-le-Rouet, mai 2003
- Status of the ANTARES Underwater Neutrino telescope. G.D. Hallewell, CPPM
  pour la collaboration ANTARES
  4th Intl Workshop on RICH Detectors: (RICH 2002), Pylos, Grèce, 5-10 juin 2002.
- Development of Fluorocarbon Evaporative Cooling Controls for the ATLAS Pixel and Semiconductor Tracking Detectors: G. Hallewell, CPPM
  6th Workshop on Electronics for LHC Experiments, Crackow, Pologne, septembre 2000
- Fluorocarbon Evaporative Cooling Developments for ATLAS Pixel and Semiconductor Tracking Detectors. G. Hallewell, CPPM
  5th Workshop on Electronics for LHC Experiments, Snowmass, USA, septembre 1999
- The Present Status of Pixel Detector Development for High Energy Physics Collider Applications.
  G. Hallewell, CPPM, Presentation invitee; 2nd International Symposium on Development and Application of Semiconductor Tracking Detectors, Hiroshima, Japon, 10-13 octobre, 1995
- Two Phase Liquid-Gas Cooing for Silicon Pixel Detectors. G. Hallewell, CPPM
  1st Intl Workshop on Electronics and Detector Cooling (WELDEC), Lausanne, Suisse, 4-7 oct. 1994
- Smart High Precision Pixel Detectors for Particle Physics at High Luminosity. G.D. Hallewell
  Presentation invitée 2nd International Workshop on B-Physics at Hadron Machines,
  (Beauty 94), Le Mont-Saint-Michel, France, 25-29 avril, 1994
- A Simplified Formula for the Analysis of Binary Gas Containing a Low Concentration of a Heavy Vapor in a Lighter Carrier. G. Hallewell, CPPM & L. Lynnworth, Panametrics Inc.,
  1994 IEEE Ultrasonics Symposium, Cannes, France, novembre 1994

- Development of Active Pixel Vertex Detectors for High Luminosity Particle Physics Applications.
  G. Hallewell, CPPM
  1994 London Conference on Position Sensitive Detectors, Brunel University, GB., octobre 1994
- Long Term, Efficient RICH Detector Operation with TMAE. G.D. Hallewell, CPPM
  1st Workshop on Ring Imaging Cherenkov Detectors (RICH 93), Bari, Italie, 2-5 juin 1993.
- Commissioning of the SLD Cherenkov Ring Imaging Detector G. Hallewell, SLAC
  1991 Conference on Frontier Detectors for Frontier Physics , La Biodola, Elba, Italie, juillet 1991
- The Ring Imaging Cherenkov Detector: A Single Particle Telescope for Particle Identification:
  G. Hallewel, SLAC: Invité 37th Scottish Universities Summer School in Physics: ¨Pattern Recognition and Image Processing in Physics¨, Université de Dundee, écosse, juillet 1990
- Monitor and Control Systems for the SLD Cherenkov Ring Imaging Detector. G. Hallewell, SLAC
  Intl Conf. on Accelerator and Large Experimental Physics Control Systems, (ICALEPS89)
  Vancouver, Canada, 30 oct - 3 nov 1989.
- Construction and status of the SLD Cherenkov Ring Imaging Detector G. Hallewell, SLAC
  1989 Vienna Wire Chamber Conference, Vienne, Autriche, février 1989
- The Recent Performance of the CERN Omega Ring Imaging Cherenkov Detector.
  G.Hallewell, SLAC & RAL, 1985 IEEE Nuclear Science Symposium, San Francisco, USA nov. 1985.
- The CERN OMEGA Ring Imaging Cherenkov Detector: G. Hallewell (RAL)
  1984 Intl. Symposium on Cherenkov Detectors in Science and Technology, Dubna, URSS, juillet 1984.
- Construction of the OMEGA Ring Imaging Cherenkov Detector, G. Hallewell, RAL
  UK Institute of Physics Meeting on Nuclear and Particle Physics, Liverpool University, juillet 1983
- A Ring Image Cherenkov Detector for the CERN Omega Spectrometer. G. Hallewell (RAL)
  1982 IEEE Nuclear Science Symposium, Washington DC.
- Barrelet Zeros Analysis of the reaction $\pi^+ p \rightarrow K^+ \Sigma^+$ between 1.27 & 2.50 GeV/c.
  G. Hallewell, Westfield College Univ. London
  UK Institute of Physics Meeting on Nuclear and Particle Physics, Oxford University, juillet 1981

Publications les plus pertinents au mémoire HDR ➔ 1/2011

239) Editorial: 7rd International workshop on Ring Imaging Cherenkov Detectors,
Proceedings 7rd International workshop on Ring Imaging Cherenkov Detectors, Cassis, France, May 3-7, 2010.
To be published in Nucl. Instrum. Meth. A.

238) Aspects of the use of saturated fluorocarbon fluids in high energy physics.G. Hallewell.
Proc. 7rd Intl workshop on Ring Imaging Cherenkov Detectors, Cassis, France, May 3-7, 2010.
To be published in Nucl. Instrum. Meth. A.

237) Properties of saturated fluorocarbons: Experimental data and modelling using perturbed-chain SAFT:
G. Hallewell, V. Vacek & V. Vins **Fluid Phase Equilibria 292, 64 , 2010**

236) Novel and Simple sonar gas analyzers G. Hallewell, V. Vacek & M. Doubek
Proc. 9th Asian Thermophysical Properties Conference Oct. 19-22, 2010
(Published by University of Science and Technology Beijing), Beijing, China, , Paper No: 10-92-96, 6pp.

234) Rich Pickings in Cassis, G. Hallewell, D. Hoffmann & E. Nappi: CERN Courrier, Oct 2010.
http://cerncourier.com/cws/article/cern/43812

219) The evaporative cooling system for the ATLAS inner detector. D Attree et al. (95 co-authors)
JINST 3:P07003,2008.

208) The status of Cherenkov Detectors in Astrophysics, G. Hallewell
Invited presention at 5th Workshop on RICH Detectors: (RICH 2004), Cancun, Mexico, Dec 6-10, 2004
Nucl. Instr. & Meth A553: 242-255 (2005)

181) Development of a Detector Control System for the ATLAS pixel Detector
S. Kersten et al; Proc 8th International Conference on Accelerator and Large Experimental Physics
Control Systems (ICALEPS2001) November 27-30, 2001 San Jose, California USA pp 445-447

177) Interim Report on a Sonar Gas Analyser for Anaesthesia Based on the "Spirocell" Ultrasonic Flowmeter:
Results of Tests at Hopital Cantonal de Geneve, Aug 6-10 2001.
G Hallewell (CPPM), S. Lindsay (U. Melbourne), M. Streit-Bianchi (CERN/ETT)
Rapport Interne Division ETT, CERN, Genève, November 2001

176) Studies for a Detector Control System for the ATLAS pixel Detector: C. Bayer et al;
Proc 7th workshop on Electronics for LHC Experiments, Uppsala, Sweden, Sept 2001, pp 396-400

175) Development of Fluorocarbon Evaporative Cooling Recirculators and Controls for the ATLAS
Inner Silicon Tracker C. Bayer et al (15 co-authors; principal author: G. Hallewell)
Proc. IEEE Nuclear Science/Medical Imaging Symposium, Lyon, France, October 2000

174) Development of Fluorocarbon Evaporative Cooling Controls for the ATLAS Pixel and
Semiconductor Tracking Detectors C. Bayer et al (17 co-authors; principal author: G. Hallewell)
Proc 6th Workshop on Electronics for LHC Experiments, Crackow, Poland, September 2000
CERN 2000-101 CERN/LHCC/2000-041, 25 Oct 2000

173) Velocity of Sound Measurements in Gaseous per-fluorocarbons and their Mixtures
G. Hallewell, S. Lindsay and V. Vacek **Fluid Phase Equilibria, 185 (2001) 305-314**

167) Perfluorocarbons and their use in Cooling Systems for Semiconductor Particle Detectors
V. Vacek et al (3 co-authors): **Fluid Phase Equilibria 174 (2000) 191-201**

163) Fluorocarbon Evaporative Cooling Developments for ATLAS Pixel and Semiconductor Tracking
Detectors. E. Anderssen et al (27 co-authors): **ATLAS INDET-NOTE 99-016, Oct 29,1999**
Paper Presented (by G.H.) at 5th Workshop on Electronics for LHC Experiments, Snowmass, USA
Proc 5th Workshop on Electronics for LHC Experiments CERN 99-09/LHCC99-33 Oct 30,1999 pp 421-426

160) A Low Cost I/O Concentrator Using the Can Field-Bus B. Hallgren et al (13 co-authors):
Proc. International Conference on Accelerator and Large Experimental Physics Control Systems,
Trieste, Italy, Oct 4-8, 1999 pp199-201 **CERN-EP-99-159, Oct 1999**

154) Evaporative Fluorocarbon Cooling for the ATLAS Pixel Detectors
G. Hallewell **FERMILAB-CONF-98-196L, 1998**
Presented (by G.H.) at International Pixel Detector Workshop (PIXEL98), Batavia, IL 7-9 May 1998

150) ATLAS Pixel Detector Technical Design Report **CERN/LHCC/98-13 ATLAS TDR 11**, **31 May 1998**
Co-Editors: G. Hallewell (CPPM), N. Wermes, Bonn University

148) The Performance of the Barrel CRID at the SLD: Long Term Operational Experience.
SLD CRID Collaboration: K. Abe et al. (49 co-authors): **SLAC-PUB-7705, Nov 1997**
Proc. IEEE Nuclear Science Symposium Albuquerque, NM, 9-15 Nov 1997.

146) ATLAS Inner Detector Technical Design Report **CERN/LHCC/97-16 ATLAS TDR , 30 April 1997**
Co-Editors of ATLAS Pixel Detector Chapter: M. Gilchriese, (LBNL), G. Hallewell (CPPM)

141) Obtaining Physics Results from the SLD CRID
K. Abe et al (67 co-authors) **Nucl.Instrum.Meth.A371:195-199, 1996**

140) Operational Status and Performance of the SLD CRID
K. Abe et al (67 co-authors): **Nucl.Instrum.Meth.A371:8-11, 1996**

Proc 1995 International Europhysics Conf. on High Energy Physics

106) The Endcap Cherenkov Ring Imaging Detector at SLD.
K. Abe et al, (68 co-authors); **IEEE Trans.Nucl.Sci.42:518-523, 1995**

103) Two Phase Liquid-Gas Cooing for Silicon Pixel Detectors. D. Labat, A Fallou and G. Hallewell
Presented at First International Workshop on Electronics and Detector Cooling (WELDEC),
Lausanne, October 4-7 1994: Also **ATLAS Internal Note INDET NO-065** (October 7, 1994)

102) ATLAS Technical Proposal for a General Purpose pp Experiment at the Large Hadron Collider at CERN
CERN/LHCC/94-43 LHCC/P2 15 December 1994

99) A Simplified Formula for the Analysis of Binary Gas Containing a Low Concentration
of a Heavy Vapor in a Lighter Carrier. G. Hallewell and L. Lynnworth
Presented at 1994 IEEE Ultrasonics Symposium, Cannes, France November 1994
Proc 1994 IEEE Trans Ultrasonics Symposium Vol 3 p 1311, 1994

75) Results from the SLD Barrel CRID Detector.
K. Abe et al (65 co-authors): **IEEE Trans.Nucl.Sci.41:862-865, 1994**

73) Long Term, Efficient RICH Detector Operation with TMAE.
G.D. Hallewell: **Nucl.Instrum.Meth.A343:250-257, 1994**
Presented paper at 1st Workshop on Ring Imaging Cherenkov Detectors (RICH 93), Bari, Italy, 2-5 Jun 1993.

72) Performance of the CRID at SLD. K. Abe et al (64 co-authors):
Proc. DPF meeting, Batavia, IL, Nov 10-17, 1992. **Nucl.Instrum.Meth.A343, 1994**

59) Performance of the SLD Barrel CRID during the 1992 Physics Data Run.
K. Abe et al (72 co-authors): **IEEE Trans.Nucl.Sci.40:589-592, 1993**

58) The Fluid Systems for the SLD Cherenkov Ring Imaging Detector.
K. Abe et al (72 co-authors): **IEEE Trans.Nucl.Sci.40:593, 1993**

54) The First Results from the CRID Detector at SLD.
J. Vavra et al, (64 co-authors). **SLAC-PUB-5945, Oct 1992.**
Proc. 26th Intl Conference on High Energy Physics, Dallas, TX, Aug 6-12, 1992.

46) Performance of the Frontend Electronics and Data Acquisition System for the SLD Cherenkov
Ring Imaging Detector. K. Abe et al (62 co-authors): **IEEE Trans.Nucl.Sci.39:897-900, 1992**

44) Progress and Commissioning of the SLD Cherenkov Ring Imaging Detector.
K. Abe et al (58 co-authors), **SLAC-PUB-5642**
Proc. 1991 Vancouver DPF Conference on Particles and fields '91, vol. 2 pp 1139-1141

43) The Ring Imaging Cherenkov Detector: A Single Particle Telescope for Particle Identification:
G. Hallewell Invited Paper at 37th Scottish Universities Summer School in Physics
¨Pattern Recognition and Image Processing in Physics¨, Ed: R. Vaughan (NATO Advanced Studies Series)
University of Dundee, Scotland July/August 1990; Published in Procedings, p283. Adam Hilger, 1991,

41) Component and System Tests of the SLD Cherenkov Ring Imaging Detector.
P. Antilogus et al (57 co-authors): **IEEE Trans.Nucl.Sci.38: 417, 1991**

40) Cherenkov Ring Imaging Detector Frontend Electronics.
P. Antilogus et al (52 co-authors): **IEEE Trans.Nucl.Sci.38:408-416, 1991**

38) Production of 400 Mirrors with High VUV Reflectivity for use in the SLD Cherenkov Ring Imaging Detector.
SLD-CRID Collaboration K. Abe et al (52 co-authors): **Nucl.Instrum.Meth.A300:501-510, 1991**

36) Electrostatic Design of the Barrel CRID and Associated Measurements.
SLD-CRID Collaboration K. Abe et al. (50 co-authors): **SLAC-PUB-5214, Apr 1990**
Proc. Int. Conf. on Instrumentation for Colliding Beam Physics, Novosibirsk USSR, Mar 15-21, 1990.

34) Construction and Testing of the SLD Cherenkov Ring Imaging Detector.
M. Cavalli-Sforza et al (51 co-authors): **IEEE Trans.Nucl.Sci.37:1132-1141, 1990**

33) Monitor and Control Systems for the SLD Cherenkov Ring Imaging Detector. P. Antilogus et al (57 co-authors): Presented (by G.H.) at Accelerator Control: Int Conf. on Accelerator and Large Experimental Physics Control Systems, Vancouver, Canada, Oct 30 - Nov 3, 1989. **Nucl.Instrum.Meth.A293:136-144, 1990**

32) Development and Construction of the SLD Cherenkov Ring Imaging Detector.
D. Aston et al (44 co-authors), Presented (by G.H.) at Int. Wire Chamber Conf.,Vienna, Austria, Feb 13-17, 1989. **Nucl.Instrum.Meth.A283:582-589, 1989**

31) Development of CRID Single Electron Wire Detector.
D. Aston et al (44 co-authors): **Nucl.Instrum.Meth.A283:590-595, 1989**

29) A Sound Method for Measuring Gas Concentrations. G.D. Hallewell (SLAC).
SLAC-PUB-4759, Sep 1988. Printed in Research & Development, Cahners, Sep 1988.

28) A Status Report on the SLD Data Acquisition System.
SLD Collaboration: M. Breidenbach et al. (255 co-authors): **IEEE Trans.Nucl.Sci.36:23-28, 1989**

27) Progress Report on Cherenkov Ring Imaging Detector Development.
D. Aston et al (42 co-authors): **IEEE Trans.Nucl.Sci.36:276-282, 1989**

25) Lorentz Angle Studies for the SLD Endcap Cherenkov Ring Imaging Detector.
P.A. Coyle et al (35 co-authors): **Nucl.Instrum.Meth.A273:858,1988**

24) ¨Ultrasonic Analysis of Binary Gas Mixtures¨ G. Hallewell:
ICFA Instrumentation Bulletin No. 4 p26 (March 1988)
International Committee for Future Accelerators & University of Siegen, Germany

23) Progress Report on the SLD Cherenkov Ring Imaging Detector System. G.D. Hallewell et al (34 co-authors), Presented (by G.H.) at 1987 Nuclear Science Symp. San Francisco, CA, Oct 21-23, 1987.
IEEE Trans.Nucl.Sci.35:398-403, 1988

22) Development of a Low Noise Preamplifier for the Detection and Position Determination of Single Electrons in a Cherenkov Ring Imaging Detector by Charge Division.
E. Spencer et al (20 co-authors): **IEEE Trans.Nucl.Sci.35:231-236, 1988**

21) Construction and Initial Operation of a Proportional Wire Detector for use in a Cherenkov Ring Imaging System. J. Vavra et al (22 co-authors): **IEEE Trans.Nucl.Sci.35:487-492, 1988**

20) ¨Solving Process Control Problems: Ultrasonic Analysis of Binary Gas Mixtures¨
Contributed Article (by G.H.) to ¨Technology 87¨: U.S. Department of Energy R&D Technology Transfer Program Annual Report **DOE/ER-0355, p 35 (Jan 1988**)

19) The Omega Spectrometer Ring Imaging Cherenkov Detector. Recent Detector Modifications and Event Analysis. R.J. Apsimon et al: (19 co-authors): **IEEE Trans.Nucl.Sci.34:504-510, 1987**

18) A Sonar-Based Technique for the Ratiometric Determination of Binary Gas Mixtures.
G.D. Hallewell et al (4 co-authors): **Nucl.Instrum.Meth.A264:219, 1988**

17) The SLD Cherenkov Ring Imaging Detectors.
R. Johnson et al (32 co-authors), Proc. 1987 Uppsala Conference High Energy Physics, Vol. 1, pp 122-123.

16) Progress Report on the SLD Cherenkov Ring Imaging Detector.
V. Ashford et al (29 co-authors): **IEEE Trans.Nucl.Sci.34:499, 1987**

15) Recent Progress in Cherenkov Ring Imaging for the SLD Experiment.
V. Ashford et al (27 co-authors): **SLAC-PUB-4064, August 1986**
Presented at 23rd Int. Conf. on High Energy Physics, Berkeley, CA, Jul 16-23, 1986.
Published in Proc. Berkeley High Energy Phys.1986: p1470

14) Development of the Cherenkov Ring Imaging Detector for the SLD.
V. Ashford et al (23 co-authors): **IEEE Trans.Nucl.Sci.33:113-121, 1986**

13) The Recent Performance of the CERN Omega Ring Imaging Cherenkov Detector.
R.J. Apsimon et al: (16 co-authors):
Presented (by G.H.) at 1985 IEEE Nuclear Science Symposium, San Francisco, CA.
IEEE Trans.Nucl.Sci.33:122-131, 1986

12) The Design of the Optical Components and Gas Control Systems of the
CERN Omega Ring Imaging Cherenkov Detector.
R.J. Apsimon et al, (17 co-authors): **Nucl.Instrum.Meth.A241:339, 1985**

11) A Ring Imaging Cherenkov Detector for the CERN Omega Spectrometer.
R.J. Apsimon et al (17 co-authors): **IEEE Trans.Nucl.Sci.32:674, 1985**

10) The CERN OMEGA Ring Imaging Cherenkov Detector: R.J. Apsimon et al (17co-authors):
Contributed Paper (by G.H.) to 1984 International Symposium on Cherenkov Detectors and their uses in
Science and Technology, Dubna, USSR, July 1984. **Nucl.Instrum.Meth.A248:76-85, 1986**

9) The Omega Ring Imaging Cherenkov Detector Readout System User's Guide.
G. Hallewell (CERN & Rutherford Appleton Laboratory). **RAL-85-009**, Nov 1984. 90pp.

6) A Ring Image Cherenkov Detector for the CERN Omega Spectrometer. M. Davenport et al: (17 co-authors)
Presented (by G.H.) at 1982 IEEE Nuclear Science Symposium, Washington DC.
IEEE Trans.Nucl.Sci.30:35, 1983

4) SLD: LETTER OF INTENT. (D. Axen et al.). **SLAC-PROPOSAL-SLC-09, 1982**